

Florida State University Libraries

Electronic Theses, Treatises and Dissertations

The Graduate School

Not Just Sinking Particles: Export and the Biological Carbon Pump in a Three-Dimensional Ocean Driven by Circulation and Vertical Migration

Thomas Bryce Kelly

FLORIDA STATE UNIVERSITY
COLLEGE OF ARTS AND SCIENCES

NOT JUST SINKING PARTICLES: EXPORT AND THE BIOLOGICAL
CARBON PUMP IN A THREE-DIMENSIONAL OCEAN DRIVEN BY
CIRCULATION AND VERTICAL MIGRATION

By

THOMAS BRYCE KELLY

A Dissertation submitted to the
Department of Earth, Ocean and Atmospheric Science
in partial fulfillment of the
requirements for the degree of
Doctor of Philosophy

2020

Thomas Bryce Kelly defended this dissertation on October 30, 2020.

The members of the supervisory committee were:

Michael R. Stukel
Professor Directing Dissertation

Alan G. Marshall
University Representative

Sven A. Kranz
Committee Member

Angela N. Knapp
Committee Member

Peter L. Morton
Committee Member

The Graduate School has verified and approved the above-named committee members, and certifies that the dissertation has been approved in accordance with university requirements.

To my family and friends. Life is about the connections we make and
the changes we leave behind.

ACKNOWLEDGMENTS

This page is not long enough to adequately acknowledge everyone that contributed over the past six years, 9 research expeditions, a dozen conferences, and more than a few late nights at the bar. Instead of attempting (and failing) to enumerate all persons who helped me along this journey, I will keep it short and simple.

I would first like to thank my PhD advisor, Mike Stukel, for showing me the priorities of a good scientist: 1) science, 2) fun, & 3) safety. Having sailed in seas around the world—and doing much of it without sleep—we have spent countless hours discussing science and life. I am thankful for these times.

To my family, I owe my love of science and the passion for what I do. Especially my mom who always knew that a job worth doing was worth doing right. Whether it was science, history or language, she taught me to recognize the amazing world and people around us. For her it is always about the journey, not the destination. Throughout this work I think of my brother, Ian, whom I am sure will grow up to be a great scientist and a great eccentric.

I especially thank my wife, Laura, for putting up with my eccentricities regarding numbers and computer models, and for putting up with my tirades about assumptions and black boxes. It has been an amazing couple of years with travel, romance, and work. You help we wake up refreshed and excited for the coming day. While not engineers by trade, *we may let the scaffolds fall, confident that we have built our wall* (Scaffolding by Seamus Heaney).

This work would not have been possible, or would be in a very different form, if it were not for several people that have believed in me and challenged me to improve. In particular, Bill Landing, Michael Landry, Ralf Goericke, Sven Kranz, Angie Knapp and Pete Morton. More than demonstrating traits that make a good scientist, you illustrate how to be a good person. Beyond this, many people have been instrumental in shaping this present dissertation and this scientist, so to all those who are reading this, “thank you”. And finally, remember to vote.

TABLE OF CONTENTS

List of Tables	viii
List of Figures	x
Abstract	xvi
1. INTRODUCTION	1
Background.....	1
Summary of Present Work.....	4
2. THE IMPORTANCE OF MESOZOOPLANKTON DIEL VERTICAL MIGRATION FOR SUSTAINING A MESOPELAGIC FOOD WEB	7
Introduction.....	7
Materials and Methods	9
Ecosystem Data.....	9
Linear Inverse Model.....	14
Analyses and Model Comparisons.....	16
Results.....	18
In Situ Ecosystem Observations	18
Model-Observation Mismatch	19
Epipelagic Ecosystem Model.....	19
New Production, Export and DVM	24
Mesopelagic Ecosystem.....	26
Discussion.....	27
Diel Vertical Migration & Active Transport in the CCE.....	27
Sensitivity Analysis and Ecological Connections.....	30
Linear Inverse Models	32
The Biological Carbon Pump and Mesopelagic Flux Attenuation	33
Conclusions.....	35
3. LATERAL ADVECTION SUPPORTS NITROGEN EXPORT IN THE OLIGOTROPHIC OPEN-OCEAN GULF OF MEXICO	37
Introduction.....	37
Methods	39
Sampling Plan and Environmental Sampling	39
<i>Trichodesmium</i> Abundance and N ₂ Fixation	39
Productivity & Nutrient Dynamics	40
Thorpe Scale Analysis	40
Zooplankton Abundance, Biomass, and Migrant Excretion.....	40
Export Production	41
Nitrogen Isotopic Signatures of New and Export Production	41

Remote Sensing Estimates of Transport	41
NEMURO-GOM Estimates of Transport	42
Field Observations and Dynamics	42
Lateral Supply of Bioavailable Nitrogen	46
Conclusions.....	52
4. SPATIAL AND INTERANNUAL VARIABILITY IN EXPORT EFFICIENCY AND THE BIOLOGICAL PUMP IN AN EASTERN BOUNDARY CURRENT UPWELLING SYSTEM WITH SUBSTANTIAL LATERAL ADVECTION.....	53
Introduction.....	53
Methods	55
Cruise Data.....	55
Remote Sensing Products	59
Model Framework & Hydrodynamic Model	59
Statistical Analysis.....	61
Results and Discussion	61
Spatial Patterns in Export Production	61
Observed Temperature and Export Production.....	63
NPP and Export Production.....	68
Interannual Variability in Satellite-Derived Export Production	72
Caveats, Future Research, and Other Mechanisms of Export	72
5. DECOUPLING OF PRIMARY PRODUCTION AND EXPORT PRODUCTION: SYNTHESIZING OBSERVATIONS FROM A MESOSCALE FILAMENT	78
Introduction.....	78
Materials & Methods	79
Field Data.....	79
Particle Model and Hydrodynamics.....	81
Results.....	85
Field Data from Lagrangian Cycles.....	85
Particle Production Model	88
Three-Dimensional Particle Advection and Export.....	89
Model Sensitivity and Controlling Parameters	92
Discussion.....	93
Carbon Export Production in the CCE.....	93
Impact of Mesoscale Filament on Export	95
Comparison to Other Model Approaches	96
Linking Particle Transport to <i>In Situ</i> or Remote-Sensing Particle Observations	97
Conclusions.....	98
6. CONCLUSIONS.....	100

Review	101
Additional Contributions	103
Biogeochemistry and Export Production	103
Broader Ecosystem Connections	104
Future Work.....	105
Autonomous Platforms	105
Zooplankton and the BCP.....	106
General Recommendations	106
APPENDICES	108
A. LINEAR INVERSE ECOSYSTEM MODEL CONSTRAINTS.....	108
B. SUPPLEMENTAL DISCUSSION ON LATERAL TRANSPORT IN THE GOM	119
C. SUPPLEMENT TO CHAPTER 4	122
D. SUPPLEMENT TO CHAPTER 5	125
References.....	127
Biographical Sketch.....	154

LIST OF TABLES

2.1 Overview of conditions for each cycle along with the attributed classifications: upwelling, transition region, and nutrient limited.....	11
2.2 Names and abbreviations of all model compartments. An abbreviation in the left column indicates inclusion in the epipelagic, while an abbreviation in the right column indicates inclusion in the mesopelagic. Each abbreviation is a distinct compartment in the LIEM with the prefix ‘vm’ signifying vertical migration and ‘d’ signifying the mesopelagic	12
4.1 Environmental conditions, water column parameters and sediment trap fluxes for each cruise cycle. NPP, Chl-a, POC are integrated over the euphotic zone. Export was calculated based on sediment trap derived flux and normalized to the base of the euphotic zone using a remineralization correction: $Export = SedTrap * \exp((Z_{SedTrap} - Z_{eu}) \cdot 0.0063)$. Export during P0605 cycles (*) was based on $^{234}Th:^{238}U$ disequilibrium profiles and not sediment traps. Data is available from the CCE Datazoo site.....	56
4.2 Summary and comparison of model formulations. Statistics were calculated from a type II ordinary least squares regression. Function f is the NPP model shown, function g was applied to the residuals of f(NPP), and f’ is a function predicting e-ratio from SST	66
4.3 Summary of CCE regional model results for select years. Shown are the modeled export production ($mg\ C\ m^{-2}\ d^{-1}$) for the region (entire CCE Domain), the coastal zone (< 150km offshore) and the Offshore zone (>250 km offshore) and averaged for the indicated year. Export efficiency is shown in the parentheses	74
5.1 Description and values of model parameters. Quantities determined by grid search optimization or directly from field data are noted as such.....	83
5.2 Summary of experimental conditions during each cycle. All values were averaged across all profiles taken during the cycle. Gross primary production and NCP values are from Kranz et al. (2020). *Values for “typical” coastal bloom and oligotrophic cycles were from previous CCE process studies from a 2008 costal cycle and an offshore 2016 cycle (P1604-4 and P1604-2, respectively). †Range indicates 95% confidence interval. **Values estimated as the mean of Cycle F1 and Cycle F3.....	87
A1 Measurement constraints used in the LIEM. Values given show the mean (μ) and 1 SD (σ) for each cycle except for min/max constraints which are blank. Marked values (*) were assumed values calculated from cycles of the same classification. All values are given in $mg\ C\ m^{-2}\ d^{-1}$	108
A2 Mesozooplankton biomass and minimum respiration estimates used in the LIEM. Respiration is given in $mg\ C\ m^{-2}\ d^{-1}$ and biomass in $mg\ C\ m^{-2}$	109

A3 Input equations for the model and the associated organisms where G = grazing, R = respiration, D = detritus production, E = excretion of DOC, GPP = gross primary production, and NPP = net primary production. Subscript x signifies organism x, and epi and meso signify the epipelagic or mesopelagic flux, respectively. Measured constraints and mass balance constraints are provided in Appendix A. Activity specific constraints for vertically migrating mesozooplankton include epipelagic and mesopelagic temperatures (T_{epi} and T_{meso} , respectively) and $a = 0.0648^{\circ}\text{C}^{-1}$ (Ikeda, 1985)117

C1 Summary of results from LTRANS particle simulation including the estimated age, fraction of particles that left the euphotic zone and the method used to calculate the age (“median” = median of all particle ages; “interpolation” = linear interpolation based on the fraction of particles with known ages and the total number of particles).....122

C2 Modeled NPP, Export and export efficiency for the CCE domain derived from remote sensing fields for the indicated years124

LIST OF FIGURES

1.1 Overview of carbon export pathways: (A) active transport, (B) gravitational settling, (C) mixing, (D) subduction, and (E) lateral transport	2
2.1 Schematic of model structure organized into distinct layers (epipelagic, DVM and mesopelagic) where arrows indicate a model flow. Mesozooplankton compartments are shown in aggregated boxes (i.e. small mesozooplankton consisting of SMZ, vmSMZ and dSMZ are shown together). For clarity, green arrows indicate grazing while red highlight mesozooplankton flows. Closure terms (“EXT”) are in grey. Production of DOC is not shown but would flow from each living compartment to DOC/dDOC. Losses to respiration are also not shown. See Table 2.2 for abbreviations.....	10
2.2 A) Bathymetric map of study region showing drift trajectories from each cycle (inset shows larger region). Numbers correspond to cycle for P0704 (purple) and P0810 (yellow). (B-F) Summary of in situ observations plotted against NPP: (B) protistan grazing, (C) export flux from sediment trap at 100 m, (D) observed rate of change of phytoplankton biomass, (E) mean mesozooplankton grazing and (F) epipelagic bacterial production. Values are colored by cruise (P0704 = green, P0810 = blue). Dashed lines for reference slopes of 1:1, 1:10, or no change as indicated and error bars are ± 1 SD.....	18
2.3 Model-observation comparisons for selected measurements: (A) net primary productivity, (B) protistan zooplankton grazing, (C) mesozooplankton grazing, (D) epipelagic bacterial production, (E) sediment trap carbon export (@ 100m), and (F) non-vertically migrating mesopelagic nekton mortality. Cruises are denoted by color (P0704 = green, P0810 = blue). Dashed line is 1:1 and error bars show 1 SD of uncertainty.....	20
2.4 A) Box and whisker plot of GGE for organisms in the LIEM. Red shaded boxes indicate the permitted range of values constraining the LIEM. (B) Box and whisker plot of trophic levels for each zooplankton assuming detritus and primary productivity are trophic level 1, and bacteria are trophic level 2. Box and whisker plots show inter-quartile range and 95% C.I. as determined using the mean solutions for each cycle. For reference the mesozooplankton compartments are shaded across both figures. Abbreviations are explained in Table 2.2	22
2.5 Composition of diet for (A) epipelagic, non-DVM mesozooplankton, (B) vertically migrating mesozooplankton, and (C) mesopelagic, non-DVM mesozooplankton. Diet is partitioned into herbivory (darkest), protistivory, detritivory, and carnivory (lightest). Cycles are as indicated.....	23
2.6 A) The sum of both passive and active carbon export flux from the epipelagic plotted against NPP. Cruises are color coded and error bars show the 95% CI for each value. (B) The total active flux due to DVM verses passive flux for each cycle (as in A). Dashed 1:1 line for reference. (C) The total export ratio (i.e. total epipelagic export / NPP) plotted against NPP and colored as in (A). All values are in $\text{mg C m}^{-2} \text{d}^{-1}$	24

2.7 The (A) net and (B) relative fate of vertically migrating mesozooplankton within the mesopelagic. Loss terms are color coded, and cruise and cycle are as shown. Abbreviations are explained in Table 2.2	25
2.8 A) Proportion of active transport relative to total export verses total mesopelagic respiration by residents (i.e. dBAC, dHNF, dMIC, dSMZ, dLMZ, dMYC, dGEL). Cruises are colored and cycles are as shown. (B) Relative proportions of carbon demand supplied by passive or active flux for the indicated mesopelagic groups. Source was calculated using indirect flux analysis (Section 2.3.1) to determine the indirect contribution epipelagic detritus (passive) and vertically migrating mesozooplankton (active). Error bars are ± 1 SD	27
2.9 Comparison between modeled mesozooplankton DVM flux without mesopelagic mortality and the predicted flux from Archibald et al. (2019) with CCE-specific parameterization following Stukel et al. (2015a). Cruises are as colored (P0704 = green, P0810 = blue) and dashed line is a 1:1 reference line. Fluxes are shown in $\text{mg C m}^{-2} \text{d}^{-1}$	29
3.1 Overview of in situ data. Study locations in the central GoM (colored drift trajectories) with a white outline indicating the integration volume from surface to 55 m considered as representative of the eastern Central GoM (depths >2000 m, outside the general flow of the Loop Current). (a) Vertical profiles of nitrate concentrations with inset detailing low surface concentrations. (b) Vertical profiles of chlorophyll concentrations as recorded by calibrated fluorometer. (c) Vertical profiles of NPP and (d) vertical profiles of particulate nitrogen export at three depths (UEZ, LEZ, 200 m). Colors correspond to Lagrangian experiments, and error bars indicate ± 1 SD of means for measurements during experiments	44
3.2 Vertical nutrient profiles and daily UEZ rates and inventories. (a-b) Nitrate and ammonium profiles averaged by Lagrangian experiment. (c-e) Timeseries of UEZ-integrated NPP and inventories of nitrate and ammonium for each day of an experiment	45
3.3 Calculation of vertical mixing of nitrate. (a) Vertical profiles of nitrate concentrations, (b) vertical eddy diffusivity, and (c) calculated nitrate flux. Values shown were averaged for each Lagrangian experiment	45
3.4 Summary of observed euphotic zone nitrogen fluxes from the oligotrophic GoM. (a) Sediment trap fluxes include export at the base of the UEZ and the LEZ (closed circles) (b) Zooplankton excretion below the euphotic zone. (c) Vertical mixing of nitrate into the LEZ. Mixing into UEZ not shown (~ 0). (d) N_2 -fixation rates modeled from observed Trichodesmium biomass (circles) and from $\delta^{15}\text{N}$ -based budgets for the entire euphotic zone as reported in Knapp et al. (submitted). Fluxes $< 0.1 \mu\text{mol N m}^{-2} \text{d}^{-1}$ are shown on left as open symbols	47
3.5 Map of GoM with UEZ nitrogen concentrations (NEMURO-GOM). Data are monthly averages for each respective year for depths 0 – 55 m depth and include all nitrogen containing state variables	48

3.6 Map of GoM with surface POC inventories (MODIS). Data are 8-day composites for mid-May with 8 km lateral resolution. Years are as indicated.....	49
3.7 Comparison of lateral nitrogen supply to observed export production in the UEZ. Satellite lateral PON flux was calculated from 8-day composite MODIS Terra/Aqua imagery during the month of May (2002 – 2019) with flow fields prescribed by OSCAR circulation. NEMURO-GOM fluxes were calculated separately for PON, DON and DIN and summed for total lateral fluxes. NEMURO-GOM vertical fluxes are integrated for the UEZ and include upwelling and turbulent mixing but not export by sinking particles. Positive flux values indicate net input into the integration volume. Flux values are normalized to lateral area	50
3.8 Schematic of transport mechanisms and fluxes of the NE GoM. (left) Arrows and values and fluxes observed or estimated from model relative to euphotic zone NPP. (right) A 3D depiction of the NE GoM illustrating possible sources and sinks of bioavailable nitrogen in the oligotrophic euphotic zone.....	51
4.1 CCE LTER Domain and Drifter Tracks. Each panel is a map of CCE domain (box outline) along with the CalCOFI survey grid (gray circles in A-E; white circles in F) and drifter tracks (numbered red lines) for each cycle: A. P0605, B. P0704, C. P0810, D. P1408, E. P1604. F. Bathymetric map of the study region. SSChl-a concentrations are shown in the shading for A-E while depth is shown in F.....	56
4.2 A. Plot of observed e-ratios against distance offshore. “Warm” and “Cool” years are shown as red circles and blue squares respectively. Line shows least-squares linear regression. B. Same as in (A) for predicted e-ratios. Points show the Dunne et al. (green squares), Laws et al. (orange squares) and Henson et al. (green open triangles) model predictions along with least-squares linear regressions. B. Plot of predicted e-ratio from Dunne et al. export model against observed e-ratios (same legend as A). Labeled line is 1:1 correspondence. D and E. Same as (C) for the Hensen et al. and Laws et al. export models, respectively. F. Same as (C, D, E) for the model proposed in this study. Linear regressions and 95% CI are shown for each of the models (C, D, E, F; grey)	62
4.3 Scatterplot of export efficiency against NPP for all cruise cycles. Warm cruise years and cool cruise years are shown in red and blue, respectively; while each cruise is indicated by the indicated symbol. Error bars show 1 SE of measurement uncertainty. Black dashed line is a type II MA linear fit with the 95% confidence interval shown by shading.....	64
4.4 Plot of e-ratio (Sed Trap Flux / ¹⁴ CPP) against SST (°C) for the indicated cruises. Colored bands indicated the 95% confidence intervals on the relationship for just the “warm” cruises (orange; P1604 and P1408) and for all cruises (blue).....	65
4.5 Scatterplot showing age of water parcel based on LTRANS-ROMS model results against the measured SST for each cycle of P1604, P1408, P0810 and P0605 (Table 1). Dashed line is type II MA linear regression with 95% confidence interval determined from a bootstrapped jackknife procedure (sample with replacement; shaded region).....	67

4.6 Comparison of carbon export flux and bulk pigment fluxes out of the base of the euphotic zone. Pigment flux consists of the sum of Chlorophyll-a and phaeopigment flux estimates. Colors and symbols are as in previous figures with red squares representing anomalously warm cruise years and blue circles for anomalously cool cruise years. Error bars show 1 standard error in the measurements. Regression is type II MA regression with 95% confidence intervals shown by shading	69
4.7 A. Export flux vs Net Primary Productivity along with type II major axis regression. Error bars indicate 1 SE of measurement. Grey band is 95% confidence interval for the regression on all data. Red squares indicate data from P1604 and P1408 (i.e. “warm” years) while blue circles indicate all other cruises (P0605, P0704, and P0810; i.e. “cold” years). B. Same as in (A) showing 95% confidence windows for regression on “autumn” (P0810) cruise and the other years only (orange squares and green circles, respectively). C. Same as (A) with 95% confidence windows for warm-year and cool-year cruises (red squares and blue circles, respectively).....	70
4.8 Spatial map of export production anomaly (%) for April & May of the indicated year across the CCE domain based on the NPP model. Climatological values were calculated from averaging export between 1998 and 2016. (A) 1998, (B) 2006, (C) 2007, (D) 2008, (E) 2014, (F) 2015, (G) 2016. H. Spatial map of climatological April-May carbon export production (1998-2016 mean; mg C m ⁻² d ⁻¹)	73
4.9 A) Time series of NPP (mg C m ⁻² d ⁻¹) within the CCE domain (black), the coastal CCE waters (green), the transitional CCE waters (magenta) and the offshore CCE waters (blue). (B) Same as A with NPP normalized (% anomaly) to the climatological mean from 1998 to 2016. (C) Same as A with export flux as calculated from the model (Eq. 4.2). (D) Same as C with export normalized (% anomaly) to the 1997-2016 climatological mean. Vertical red lines indicate each CCE-LTER cruise, while blue shaded regions are the 1997-98 and 2015-16 El Niños	75
5.1 Map of study region (A) colored with MODIS AQUA SSChl (mg Chl m ⁻³) for the month of June, 2017. Overlaid are drift tracks for the 5 Lagrangian Cycles. (B) Cycle averaged rate of NPP for U, F1, and F3. (C) observed chlorophyll inventories throughout the cruise. Rate of change in chlorophyll inventories for each cycle are shown by type-I linear regression with 95% confidence intervals (shading). (D) Cycled averaged export production as measured in trap closest to euphotic zone depth. All error bars indicate 95% confidence interval.....	86
5.2 (A) Relationships between NPP and EF in the CCE region for each CCE LTER process study. A linear type-I regression is shown separately for each cruise. Error bars shown are ±1 standard error of an observation. (B) Vertical profiles of gravitationally settling flux measured by PIT-style sediment trap. Black lines correspond to the indicated cycles of CCEP1706 while all previous CCE-LTER sediment trap deployments are in grey.....	88
5.3 Waterfall diagram showing the mean sinking speed of exported particles in the 1D model. Solid lines indicate depth and duration for sediment trap deployments for cycles U, F1, F2, and F3. Contours show 10 m d ⁻¹ increments.....	90

5.4	Original distance offshore of particles exported past 150 m. Darker colors indicate particles that started closer to shore while bright colors shown particles that began far offshore	91
5.5	Distribution of net lateral distance traveled by particles collected in each sediment trap deployment for the indicated cycle and depth. Additionally, 2 non-filament locations were investigated (E) Inshore and (F) Offshore	92
6.1	Overview of carbon export pathways: (A) active transport, (B) gravitational settling, (C) mixing, (D) subduction, and (E) lateral transport	100
A1	Selected modeled rates verses observations: (A) primary productivity and export, (B) small mesozooplankton grazing, (C) epipelagic bacterial production, (D) protistian zooplankton grazing, (E) large mesozooplankton grazing, and (F) sediment trap export at 100m. Dashed line in each panel is a 1:1 reference line and error bars show 1 SD. (G) Box and whisker plot of relative model deviations from observations for each cycle (box shows inter-quartile range and whiskers to 95% CI). The cycles are shown in chronological order for each equation, and observations are as labeled. The red shading shows 1 SD of the observation (i.e. σ_{obs}) ...	114
A2	A) Proportion of mesopelagic respiration carried out by each category of mesopelagic organism. (B) Relative proportion of mesopelagic respiration supplied by each of the export pathways: passive transport by SDT and LDT, active transport by vmSMZ, vmLMZ, and vmMYC. Each were calculated from the indirect analysis.....	115
A3	Vertical Distribution of mesozooplankton biomass and dissolved oxygen (DO) concentrations. Bars shown the fraction of total mesozooplankton biomass captured at that depth (MOCNESS, 202 μ m mesh) averaged over each cycle. Blue line shows a lowess smoothing of the raw oxygen data (grey). Cycles are as indicated	116
B1	Comparison of lateral nitrogen supply to observed export production for entire euphotic zone (UEZ + LEZ). Observed export was at the base of the euphotic zone. Satellite lateral PON and NEURO-GOM fluxes were calculated as in Figure 3.7. NEMURO-GOM vertical fluxes are integrated to 135 m (UEZ + LEZ) and include upwelling and turbulent mixing but not export by sinking particles. Positive flux values indicate net input into the integration volume. Flux values are normalized to lateral area	121
C1	Plots of each modification of the empirical NPP model. Lines indicate 1 SE of the measurement or model prediction. Models: (a) NPP. (b) NPP + SST. (c) NPP + Chl-a. (d) NPP + POC. (e) NPP + Distance Offshore.....	123
D1	Comparison plots between model and observations for (A) POC and (B) Export. Dashed line is 1:1	125
D2	Mesozooplankton grazing vs. chlorophyll for the indicated CCE LTER process cruises. Line Indicates best fit for grazing model parameters. Error bars show observational uncertainty.....	125

D3 Modeled export flux in 1D model with sediment trap deployments for Cycles U, F1 – F3 overlaid in the same scale ($\text{mmol C m}^{-2} \text{ d}^{-1}$). Contours are shown for every $100 \text{ mmol C m}^{-2} \text{ d}^{-1}$ increment.126

ABSTRACT

The marine biological carbon pump is a primary control on atmospheric carbon dioxide concentrations because it transports fixed organic carbon into the ocean's interior thereby isolating carbon from the atmosphere, often for years to centuries. The biological pump is also the first step to long-term marine carbon sequestration through burial of carbon in sediments. Although important, much of the marine carbon cycle remains poorly constrained, especially between the lit surface and darker mesopelagic where gradients and fluxes of organic matter are largest. Here we investigate, through several oceanographic process studies, the connections between the physical, chemical and biological environment and the biological carbon pump. We first estimate the biologically mediated transport of carbon across a range of productivities in the California Current ecosystem and find that vertically migrating mesozooplankton may be responsible for 18 – 84% (median: 42%) of carbon export in these waters—a number far greater than previously assumed and one which has immediate ramifications for regional carbon budgets. Following this, the nutrient sources supporting vertical export in the oligotrophic Gulf of Mexico are investigated. Based on our field data alone, there was an apparent imbalance between the rate of nitrogen supply and removal in these systems with far more nitrogen being exported than supplied through vertical processes such as mixing. Through independent modeling and remote-sensing approaches we identify the oligotrophic Gulf of Mexico as a net recipient of organic matter from nearby coastal environments. Due to the combination of enhanced surface currents and strong lateral gradients in organic matter concentrations, over 90% of export production in the oligotrophic Gulf of Mexico may be supported by lateral connections rather than through vertical mixing processes.

Back in the California Current ecosystem, long term patterns in export efficiency (i.e. the fraction organic matter exported vs. produced) were investigated by merging remote sensing data products with data from Lagrangian process studies. No statistically significant trends with El Niño state were found, although there was substantial interannual variability in export efficiency. We hypothesized, and illustrated, that sea surface temperature could be a predictor of export efficiency in the California Current due the importance that regional circulation and upwelling have in modifying primary production and export efficiency. To briefly summarize: cold waters tend to be more recently upwelled than warmer waters (i.e. waters off southern California tend to

gradually warm up while at the surface) leading the warmer ‘aged’ waters to have communities (and chemical environments, e.g. transparent exopolymers) with distinct export efficiencies. This pattern is validated through a simple Lagrangian particle model coupled to a 3D hydrodynamic ocean model.

Finally, we investigate export production along a mesoscale filament in the California Current and quantitatively assess patterns of lateral decoupling between particle production and export production. By integrated lessons learned in the prior chapters, we designed a novel particle model that includes gravitational settling, remineralization, and mesozooplankton fecal pellet production. From this model we estimate that particles were being advected nearly 100 km on average between formation and export from the euphotic zone during the lifespan of the filament. Taken together, we have found through these diverse approaches that small scale idiosyncrasies may be clues to important drivers of export production and that many first order approximations, which are adequate for global patterns, fail to capture regional patterns.

CHAPTER 1

INTRODUCTION

Background

The marine carbon cycle directly regulates atmospheric concentrations of carbon dioxide (CO₂), a major anthropogenic greenhouse gas, through both biological sequestration in a process known as the “biological carbon pump” (BCP) and through dissolution of CO₂ into undersaturated waters in a process known as the “solubility pump” (Volk & Hoffert, 1985). Current global estimates for the strength of the BCP vary by nearly 3-fold (5 – 13 Pg C yr⁻¹; Laws et al., 2000, 2011; Henson et al., 2011), with even greater discrepancies at regional scales (for perspective, global fossil fuel emissions exceeded ~10 Pg C yr⁻¹ for the first time in 2018; Friedlingstein et al., 2019). Yet, our inability to accurately estimate contemporary BCP processes directly corresponds to an inability to predict how climate change will impact the marine carbon cycle. To understand where this uncertainty comes from, consider that while the solubility pump is physically controlled by temperature, salinity, and CO₂ gradients (Ito and Follows, 2003); the BCP can be controlled by numerous physical, chemical and ecological processes (Ducklow et al., 2001 and references within), many of which vary in space and time. Simply framed, the BCP is driven by a combination of marine productivity, which forms and transforms organic matter within the ocean’s surface, and vertical transport processes, which convey organic matter into the ocean’s interior. Due to the complex interactions between (1) the environment and the organisms that inhabit it, (2) organisms and organic matter, (3) organisms and themselves, and (4) organic matter and the environment; our ability to accurately measure all relevant processes, let alone to predict how they may change, remains an active and productive area of research.

Within a given ecosystem, a unique combination of ecosystem processes (1 – 4 above) form the biogeochemical pathways by which organic matter is transported into the ocean’s interior, a BCP process known as “vertical export”. These ecosystem processes not only control the quantity of organic matter transport but also the composition and form of the material (Armstrong et al., 2001; Siegel et al., 2014a; Lyszka et al., 2019). A porous aggregation of sinking particles, for example, is likely to have a very different journey sinking through the water column than a dense fecal pellet (Stukel et al. 2014; Turner, 2015). Traditionally, the

measurement of vertical export flux was carried out by sediment traps, devices resembling rain gauges that can be placed at a fixed depth in the ocean and which catch sinking particles. While still one of the best approaches to estimating the flux of sinking particles (Baker et al., 2020), a sediment trap only intercepts one form of export: gravitational/sinking export. In addition to sinking particle flux, export includes active transport by organisms (e.g. diel vertical migrators and nekton; Morales, 1999; Steinberg et al., 2000; Davison et al., 2013; Archibald et al., 2019a), subducted organic carbon as an entire water mass is transported vertically (Levy et al., 2013b; Omand et al., 2015; Stukel et al., 2018e), organic matter that is vertically mixed to depth by turbulence (Carlson et al., 1994), and lateral transport of organic matter (Plattner et al., 2005; Letscher et al., 2016), which is conducted by ocean circulation (Figure 1.1). While lateral transport does not generally fit cleanly with otherwise vertical processes, it can be an important source of organic matter (e.g. Chapter 3) and even stimulate vertical export processes (e.g. Chapter 5). Ultimately, the mode of organic matter export (Figure 1.1) dictates how long the carbon is removed from the atmosphere (deeply sinking particles may be removed for 100's of years while laterally exported material may return to the atmosphere in a matter of days) and the impact it has on other ecosystems (e.g. benthic flux).

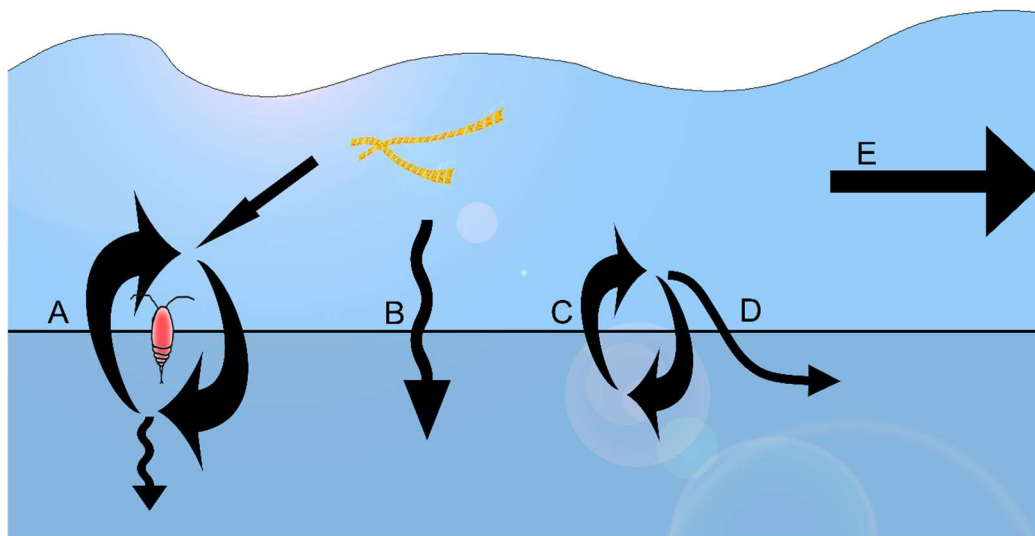


Figure 1.1. Overview of carbon export pathways: (A) active transport, (B) gravitational settling, (C) mixing, (D) subduction, and (E) lateral transport.

For export pathways that are not captured by sediment traps (i.e. “cryptic” export), other tools are required. Active biological transport has been estimated by comparing day-night net

tows and using estimates of respiration and excretion to calculate the net transport (e.g. Morales, 1999; Steinberg et al., 2002). Subduction and mixing, on the other hand, have often been inferred from hydrodynamic models or vertical gradients (Omand et al., 2015; Stukel and Ducklow, 2017). By using the fact that export (i.e. quantity of material leaving the surface ocean) should equal the difference of primary production and respiration ($\text{Export} = \text{PP} - \text{R}$) several complementary approaches can be used to estimate total vertical export (i.e., sinking + active transport + subduction + vertical mixing). Chemical tracers are regularly used to define the PP – R relationship (e.g. Juranek and Quay, 2013; Wang et al., 2020), yet uncertainty is often much larger than comparable sediment trap methods (Kranz et al., 2020). Such source vs. sink approaches have been widely applied since the approach does not require measurement of all export pathways simultaneously, yet the added challenges to interpretation due to high uncertainty must be recognized. Finally, explicit estimation of each term and processes can be used to quantify export, yet requires the combination of many independent measurements (Stukel and Landry, 2010; Forget et al., 2015; Kelly et al., 2019). While such an aggregative method may be the most compelling approach due to the numerous observations and constraints used, such approaches are difficult to generalize (since they require so many data) and can often end up with results that are as open to interpretation as the chemical tracer methods. Ultimately, the quantification of export flux remains an obstacle to global climate synthesis and prediction.

Thus far we have discussed the linkages between marine productivity and export as well as the general approaches used to estimate export in a nonspecific and broad-scale fashion. Now we will briefly turn to the question of scale and variability. Our understanding of global export is accurate enough to determine large scale patterns (Laws et al., 2000b; Henson et al., 2011a; Laws et al., 2011c) and to make useful predictions regarding climate sensitivities across a variety of spatiotemporal scales (e.g. Brun et al., 2019); yet those same global models will fail to resolve important regional dynamics (Maiti et al., 2013a) and will consistently misdiagnose environmental relationships. These issues are not just a reflection of uncertainty in the data (i.e. observations), but—and perhaps more importantly—are also a reflection of the fact that many distinct drivers impact export, which themselves vary significantly in space and time. For example, water temperature may be a good predictor of export globally (Dunne et al., 2005a; Henson et al., 2011a; Laws et al., 2011c): cold regions tend to have higher export than warmer regions. At finer spatial scales, however, these global relationships become less accurate. Indeed,

the opposite relationship is found when investigating export in the California Current system. These disparate results are not because the California Current is idiosyncratic but rather an indication that different drivers are important at different scales. In essence, the question changes in response to scale. Until we make progress in developing a uniform paradigm that incorporates all export pathways and the drivers that modulate them, our ability to predict how climate change impacts the BCP remains limited.

The present work investigates several of the aforementioned export pathways in detail (e.g. biological active transport) and attempts to synthesize multiple lines of evidence in order to improve the ways in which we assess relationships between ecosystems and the BCP. We investigate this relationship for multiple ecosystems and consider the specific drivers and mechanisms important to those systems.

Summary of Present Work

Chapter 2 inspects the ecological connectivity in a two-layer pelagic ecosystem (Kelly et al., 2019). Since carbon export in the California Current system is primarily a combination of gravitational particle flux (Stukel et al., 2018e) and active biological transportation (Figure 1.1), we developed a two-layer ecosystem model coupling the epipelagic ecosystem (i.e. where photosynthesis occurs) to the mesopelagic ecosystem. This lower-ecosystem model included everything from nutrients to micronekton and was constrained by *in situ* biomass and rate measurements taken during two cruises in the California Current Ecosystem (CCE). In addition to direct observations, the model was further constrained by literature-derived metabolic demands. The resulting model compared well to independent measurements of diel vertical migration (Archibald et al., 2019a) and revealed that active transport of mesozooplankton was often equal to or greater than the total passive carbon flux. Previous studies have suggested that approximately 20% of total export is mediated by active transport, yet we found this number to be as high as 80%. Such strong active transport was required in order to meet the metabolic demands of the resident mesopelagic mesozooplankton and micronekton, who were unable to meet their basal metabolism through consumption of sinking flux alone.

In addition to active biological transport, lateral advection of organic matter is generally neglected in biogeochemical budgets due to difficulty constraining these fluxes as well as a historical tendency to exclude lateral terms when integrating over sufficiently large areas or

times. In **Chapter 3** we first attempt to provide a closed nitrogen budget for the oligotrophic Gulf of Mexico (GoM) yet are unable to provide sufficient vertical nitrate fluxes to support observed export. To quantify lateral sources of nitrogen, two independent approaches are used: (1) remote sensing and circulation and (2) a 3D, coupled biogeochemical model (NEMURO-GoM; Shropshire et al., 2019). Both approaches suggest that lateral transport of organic matter (driven by the large spatial gradients and strong circulation found in the GoM) are of similar magnitude and sufficient to support observed export. Furthermore, we note a vertical decoupling of primary production and export production within the euphotic zone suggesting that the lower euphotic zone (i.e. around the deep chlorophyll max) is a zone of net particle attenuation rather than particle production as commonly assumed.

In **Chapter 4**, a compilation of *in situ* net primary productivity (NPP) and contemporaneous sinking particle fluxes collected off the coast of southern California shows an inverse relationship between primary productivity and export efficiency (Kelly et al., 2018). While contrary to prevailing global theories, we illustrate that this inverse relationship is consistent with a regional perspective when spatiotemporal decoupling is considered due to a combination of strong currents and slowly sinking particles. This perspective was validated using a 3D hydrodynamic model coupled to a Lagrangian particle model. Together, this coupled approach illustrated a strong relationship between “temporal progression” (i.e. age of the water mass since upwelling) and temperature within the study region and provided a simple quantitative assessment of our decoupling hypothesis. The relationship between NPP and sinking particle flux can serve as a regionally-optimized predictor, and, indeed, has already been used for this purpose (Smith et al., 2018; Kahru et al., 2019). Currently the algorithm is used to provide the community with a regional particle export product: <http://wimsoft.com/CC4km.htm>.

Lessons learned in the preceding chapters are applied to a biogeochemical analysis and synthesis of data collected in 2017 about a mesoscale filament. During the month-long cruise, we observed the formation, propagation and termination of a coastal filament off the coast of California. In **Chapter 5** we integrated productivity (GPP, NPP, nitrate uptake) and export production (sediment traps) into a particle production model to explicitly determine the biogeochemical progression of the filament. The particle production model is used to evaluate the degree of spatiotemporal decoupling within the filament and to determine the extent of lateral connectivity throughout the region.

The final chapter (**Chapter 6**) is dedicated to an outward look upon the major results of the four preceding chapters as well as a discussion on the recent technological advances that may impact the study of carbon biogeochemistry in the coming years.

CHAPTER 2

THE IMPORTANCE OF MESOZOOPLANKTON DIEL VERTICAL MIGRATION FOR SUSTAINING A MESOPELAGIC FOOD WEB

Introduction

*This chapter corresponds to an original research article published in *Frontiers in Marine Science* in 2019 with the following coauthors, who were invaluable to the project: Peter C. Davison, Ralf Goericke, Michael R. Landry, Mark D. Ohman, and my doctoral advisor Michael R. Stukel.*

Although mesopelagic food webs are believed to depend entirely on productivity generated in the euphotic zone, reconciling mesopelagic metabolic demand with estimates of export has been challenging (del Giorgio and Duarte, 2002a; Steinberg et al., 2008; Burd et al., 2010; Henson et al., 2011b; Hannides et al., 2015). Due to large uncertainties in rate measurements for meso- and bathypelagic organisms as well as low sampling resolution, steady-state budgets must either report wide ranges or otherwise exclude some processes, such as mortality and defecation of diel vertical migrators at depth. Even among recent studies, global carbon export budgets have been highly variable (Boyd and Trull, 2007; Henson et al., 2011b, 2015; Laws et al., 2011a; Siegel et al., 2014b). Compounding this issue, several analyses have reported carbon demands by mesopelagic bacteria alone that exceed calculated carbon export (Ducklow and Harris, 1993; Burd et al., 2010), sometimes by an order of magnitude (Steinberg et al., 2008). This apparent imbalance between carbon supply to the mesopelagic and estimated metabolic demand suggests either that export estimates fail to capture important dynamics or that metabolic calculations are highly biased (Burd et al., 2010).

Some work has demonstrated that diel vertical migrators are important for net transfer of organic carbon from the euphotic zone to the mesopelagic, a transfer not measured with traditional carbon export methods (Morales, 1999; Steinberg et al., 2000). Since export by mesozooplankton is not captured by sediment traps or radioisotope disequilibria methods, we must rely on net tows coupled to assumptions about *in situ* respiration rates or on indirect modeling syntheses. For example, using remote sensing fields and a size-structured ecosystem model, Archibald et al. (2019) found that global zooplankton diel vertical migration (DVM) can

increase export production by 14% annually. This is consistent with previous modeling exercises based on zooplankton behavior (Bianchi et al., 2013a) and community size structure (Aumont et al., 2018). Zooplankton behavior models argue that for DVM to be evolutionarily advantageous (Cohen and Forward, 2009), the energy expenditure should be offset by a commensurate reduction in predation risk. Using this modeled-behavior approach, Hansen and Visser (2016) found that 16 – 30% mid-latitude export production in the North Atlantic was likely due to DVM mesozooplankton. Each of these models note sensitivities to zooplankton biomass and the fraction of the zooplankton population that undergoes DVM, which are ecosystem metrics that are difficult to generalize.

Linear inverse ecosystem models (LIEM) have been shown to be a versatile and robust framework for integrating a wide range of ecosystem data (Vézina et al., 1988; Gontikaki et al., 2011; van Oevelen et al., 2012; Sailley et al., 2013; Stukel et al., 2018c). A LIEM combines an ecosystem network with observations and generalized constraints to determine possible energy flows through the ecosystem. Unlike a forward model (e.g., an NPZ model; Franks, 2002), the relationships between organisms are not prescribed by functional responses of model state variables (e.g., assuming a Monod functional form controls phytoplankton nutrient uptake responses or an Ivlev grazing formulation). Instead, the model includes all possible combinations of fluxes that are compatible with the assumed model structure and input constraints. The most likely ecosystem structure is then retrieved based on a random walk through the solution space (van den Meersche et al., 2009). This inverted approach has the advantage of not requiring *a priori* assumptions of functional ecological responses but instead relies on an assumed basic ecosystem structure (i.e., which functional groups should be included and who eats whom) and many independent constraints on the food web.

The California Current Ecosystem (CCE) is an eastern boundary current upwelling biome with extensive temporal and spatial variability. As a result of high mesozooplankton biomass and strong DVM (Stukel et al., 2013d; Powell and Ohman, 2015; Ohman and Romagnan, 2016), we expect a substantial contribution to export production by diel vertical migrators and a commensurately important role in satisfying the mesopelagic carbon demand. Stukel et al. (2013) suggested that active transport could be responsible for 1.8 – 29% of total export in the CCE. However, their study focused only on active transport fluxes due to zooplankton respiration and only included basal metabolism. To more thoroughly investigate the potential importance of

active transport, we designed a two-layer LIEM, which includes non-living organic matter, primary producers, zooplankton and planktivorous nekton organized into two layers: an epipelagic and a mesopelagic ecosystem. Using extensive data from two cruises of the CCE Long-Term Ecological Research (LTER) Program in the southern California Current region, our LIEM data synthesis suggests that active transport of carbon from the epipelagic down to depth is a significant mechanism supporting the mesopelagic carbon demand. Although previous studies have indicated that active transport may be responsible for 10% - 30% of total carbon flux (Yebera et al., 2005; Bianchi et al., 2013a; Hansen and Visser, 2016a; Aumont et al., 2018; Archibald et al., 2019b), our LIEM suggests that 20% - 80% of carbon export in the CCE can be attributed to mesozooplankton DVM.

Materials and Methods

Ecosystem Data

The data presented here (Appendix A) were collected during two cruises of the California Current Ecosystem Long Term Ecological Research (CCE LTER) program (P0704 in April 2007; P0810 in Oct. 2008). On these cruises, *in situ* drift arrays were used for quasi-Lagrangian tracking of water parcels for periods of 3-5 days (Landry et al., 2009a, 2012a), while the water column was repeatedly sampled for the following variables: CTD-derived physical data, phytoplankton diversity and biomass (flow cytometry, epifluorescence microscopy, and pigment analyses, (Taylor et al., 2012)), primary production ($H^{14}CO_3$ -uptake, (Morrow et al., 2018a)), mesozooplankton biomass and community analyses (paired day-night bongo and Multiple Opening and Closing Net with Environmental Sampling System, MOCNESS net tows, (Ohman et al., 2012a; Powell and Ohman, 2012), microzooplankton biomass (epifluorescence microscopy), microzooplankton grazing (dilution method, Landry et al., 2009), mesozooplankton grazing (gut pigment methods, Landry et al., 2009), meso- and epipelagic micronekton biomass and metabolic demands (Oozeki net trawls, multi-frequency EK60 echosounder, and individual-based metabolic model (Davison et al., 2013, 2015), bacterial production (3H -leucine uptake, Samo et al., 2012), and gravitational particle export (sediment traps and ^{234}Th : ^{238}U disequilibrium, Stukel et al., 2013). The use of a quasi-Lagrangian sampling framework also allowed us to assess net rates of change of phytoplankton biomass. Bulk rates and associated errors for the 3 – 5 day cycles were calculated by averaging vertically-integrated rates or

biomasses for each experimental cycle. The data and detailed methods can be found on the CCE LTER Datazoo website (<http://oceaninformatics.ucsd.edu/datazoo/data/ccelter/datasets>) and/or in published manuscripts cited above.

The quasi-Lagrangian experiments (hereafter ‘cycles’ of repeated measurements in the same water parcel) spanned much of the physical, chemical, and ecological variability of the CCE domain (Table 2.1, Figure 2.1) which allowed us to classify cycles according to nutrient conditions, the primary driver of ecosystem variability within the CCE (Landry et al., 2012a). Cycle classification was defined as: nutrient-limited cycles which were conducted in off-shore, low nutrient regions (P0704-2, P0810-2, P0810-6); transition region cycles which were characterized by low surface nutrient concentrations and intermediate NPP and biomass (P0810-1, P0810-3, P0810-4); and upwelling cycles in which surface nutrient concentrations and phytoplankton growth rates were highest (P0704-1, P0704-4, P0810-5; Table 2.1).

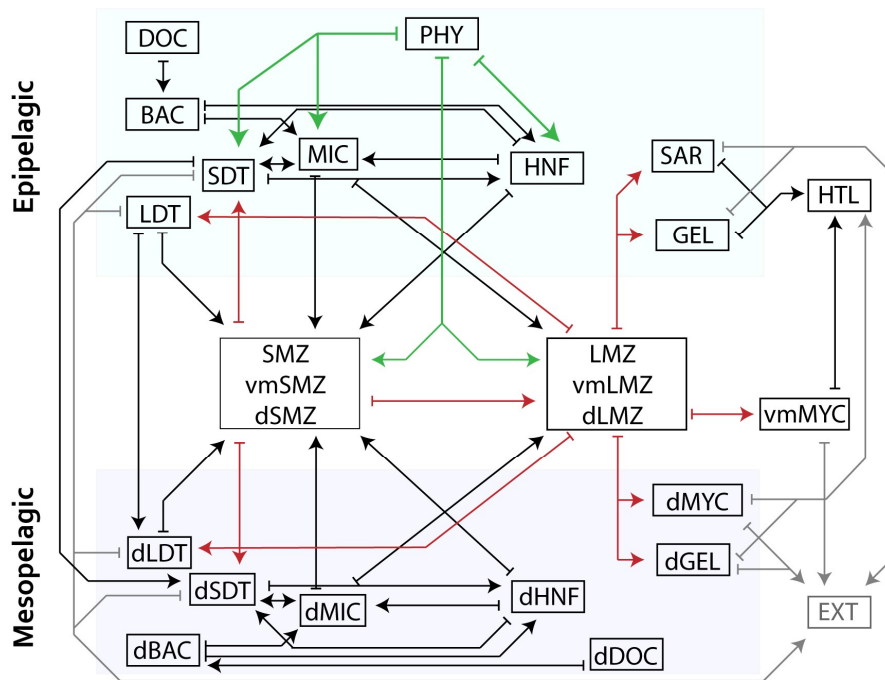


Figure 2.1. Schematic of model structure organized into distinct layers (epipelagic, DVM and mesopelagic) where arrows indicate a model flow. Mesozooplankton compartments are shown in aggregated boxes (i.e. small mesozooplankton consisting of SMZ, vmSMZ and dSMZ are shown together). For clarity, green arrows indicate grazing while red highlight mesozooplankton flows. Closure terms (“EXT”) are in grey. Production of DOC is not shown but would flow from each living compartment to DOC/dDOC. Losses to respiration are also not shown. See Table 2.2 for abbreviations.

Table 2.1. Overview of conditions for each cycle along with the attributed classifications: upwelling, transition region, and nutrient limited.

Cycle	Classification	Surface Chl ($\mu\text{g Chl a L}^{-1}$)	^{14}C Primary Productivity ($\text{mg C m}^{-2} \text{ d}^{-1}$)	Mesozooplankton Biomass (mg C m^{-2})
P0704-1	<i>Upwelling</i>	1.35	1,233	2,695
P0704-2	<i>Nutrient Limited</i>	0.22	587	391
P0704-4	<i>Upwelling</i>	0.99	2,314	1,715
P0810-1	<i>Transition region</i>	0.45	554	740
P0810-2	<i>Nutrient Limited</i>	0.20	484	528
P0810-3	<i>Transition region</i>	0.72	892	923
P0810-4	<i>Transition region</i>	1.05	674	832
P0810-5	<i>Upwelling</i>	1.47	1,672	1,098
P0810-6	<i>Nutrient Limited</i>	0.22	325	628

Daily *in situ* primary productivity measurements using $\text{H}^{14}\text{CO}_3^-$ uptake (^{14}CPP) were conducted at 6-8 depths spanning the euphotic zone using 4 L incubations subsampled in triplicate (Morrow et al., 2018a). A 250 mL dark bottle was used to correct for non-photosynthetic ^{14}C uptake. Contemporaneously, *in situ* dilution experiments, using the two-treatment approach of Landry et al. (2008), were conducted to measure protistan zooplankton grazing rates and chlorophyll-*a* growth rates (Landry et al., 2009a). Chlorophyll to carbon ratios were determined by the ratio of vertically integrated chlorophyll-*a* growth rates and ^{14}CPP . Euphotic zone primary production and protistan zooplankton grazing rates were vertically integrated and averaged by cycle.

Rates of ^3H -leucine incorporation into bacteria were measured in triplicate at multiple depths during each cycle (Samo et al., 2012). Each profile was vertically integrated and then averaged by cycle in order to determine production rates of epipelagic bacteria. Additionally, upper and lower bounds for mesopelagic bacterial production were calculated by integrating bacterial production attenuation curves and scaling by the epipelagic bacterial production (Eq. 1).

$$\text{Mesopelagic BP} = \text{BP}_{100} \int_{100}^{450} \left(\frac{z}{z_0}\right)^{-\alpha} dz \quad (\text{Eq. 1})$$

where BP_{100} is the measured BP rate at 100 m and α (BP attenuation factor) = 1.47 (Yokokawa et al., 2013) for the lower limit and $\alpha = 0$ (i.e., no attenuation) for the upper limit.

Table 2.2. Names and abbreviations of all model compartments. An abbreviation in the left column indicates inclusion in the epipelagic, while an abbreviation in the right column indicates inclusion in the mesopelagic. Each abbreviation is a distinct compartment in the LIEM with the prefix ‘vm’ signifying vertical migration and ‘d’ signifying the mesopelagic.

	Epipelagic Abbreviation	Name	Mesopelagic Abbreviation
Organisms	PHY	Phytoplankton	
	HNF	Heterotrophic Nanoflagellates	dHNF
	MIC	Microzooplankton	dMIC
	SMZ, vmSMZ	Small Mesozooplankton	dSMZ, vmSMZ
	LMZ, vmLMZ	Large Mesozooplankton	dLMZ, vmLMZ
	SAR	Sardines and other planktivorous fish	
		Non-DVM Myctophids	dMYC
	GEL	Gelatinous Predators	dGEL
	vmMYC	Vertically Migrating Myctophids	vmMYC
	BAC	Bacteria	dBAC
POC& DOC	SDT	Small Detritus	dSDT
	LDT	Large Detritus	dLDT
	DOC	Dissolved Organic Matter	dDOC
Closures	HTL	Higher Trophic Levels	HTL
	RES	Respiration	dRES
	EXT	Fecal Matter & External	EXT

Data for the mesozooplankton constraints comes primarily from day-night paired oblique bongo net tows through the epipelagic (for grazing rates) or day-night paired 202 μm mesh MOCNESS tows taken at 9 depth horizons spanning the upper 450 m (for biomass and metabolism estimates). MOCNESS samples were analyzed by ZooScan digital scanner (Gorsky et al., 2010; Ohman et al., 2012a), vignettes provisionally classified using machine learning methods, then 100% manually validated. Organisms were sorted (Stukel et al., 2013d) into groups including euphausiids, nauplii, copepods, appendicularians, siphonophores, and other crustaceans. For this study, we separated the mesozooplankton community into two size classes (<1 mm and >1 mm) of grazers and one compartment for gelatinous predators (siphonophores). We also partitioned the large and small mesozooplankton into non-vertically migrating epipelagic residents, vertical-migrators, or mesopelagic resident communities. Biomass estimates

of non-migrating epipelagic mesozooplankton were calculated from daytime net tows in the upper 100 m, while the non-migrating, mesopelagic biomass was calculated based on nighttime mesopelagic (100 m – 450 m) net tows (Stukel et al., 2013d). We note that epipelagic estimates are likely conservative due to net avoidance. Biomass estimates for the DVM mesozooplankton were calculated by averaging the difference in the night and day epipelagic biomass estimates with the difference in the day and night mesopelagic biomass estimates. This approach was used in order to be the most consistent with both the epipelagic and mesopelagic biomass estimates for non-vertically migrating biomass. For a list of abbreviations used for all model compartments, see Table 2.2.

Minimum respiration estimates for each mesozooplankton group were calculated using published temperature-length-basal respiration relationships (Ikeda et al., 2001). Oxygen consumption was converted to carbon units using the scale factor $9.88 \times 10^{-3} \text{ mg C d}^{-1} (\mu\text{L O}_2 \text{ hr}^{-1})^{-1}$. Mesozooplankton grazing on phytoplankton was calculated from gut pigment contents of oblique bongo net tow tows (202 μm mesh, $D = 0.71\text{m}$) and estimated gut passage rates (Dam and Peterson, 1988). Carbon-based grazing rates were then calculated from chlorophyll (Chl) consumption, and C:Chl ratios computed as the ratio of NPP to chlorophyll-specific growth rates obtained from the dilution experiments. Mesozooplankton grazing rates were size fractionated as above. Mesozooplankton gut contents samples were improperly frozen for P0810-5, P0810-6, and most of P0810-4. In order to provide estimates for these grazing rates, average grazing rates from the cycle with the same classification were used (e.g., P0810-5 was an upwelling cycle so grazing rates were averaged from the other upwelling cycles). Conservative uncertainty estimates were set to be 2x the error calculated by propagation of error. This higher level of uncertainty is a reasonable compromise given the data limitations. For additional details on gut pigment processing, see Landry et al. (2009).

Nekton biomass was estimated based on catches made by a 5 m² Matsuda-Oozeki-Hu net trawl (Davison et al., 2013). For each station, epipelagic net tows were conducted at night after the ascent of the deep scattering layer. Preserved specimens from each net tow were identified to species and measured. Fish were classified as either non-vertical migrating or vertically migrating based on species. An individual based model was then used to determine metabolic rates and requirements for each nekton population: resident epipelagic, diel vertical migrant, and resident mesopelagic (Davison et al., 2013).

VERTEX-style sediment traps consisting of 8-12 tubes per depth were deployed and recovered at the start and end of each cycle (Knauer et al., 1979a; Stukel et al., 2013d). Tubes were filled with a hypersaline, poisoned brine solution. Upon recovery >200- μm swimming mesozooplankton taxa were manually removed during inspection under a stereomicroscope. Samples for C and N or C: ^{234}Th ratios were filtered through pre-combusted glass fiber and quartz filters, respectively, prior to analysis on a CHN elemental analyzer or a RISO beta multi-counter.

^{234}Th : ^{238}U disequilibrium measurements were made at 12 depths spanning the upper 200 m at the start and end of each cycle using standard small-volume procedures (Benitez-Nelson et al., 2001a; Pike et al., 2005b). Thorium-234 export rates were then computed using a 1-box steady state model (Savoie et al., 2006a). The C: ^{234}Th ratio measured from sediment trap particles was used to convert to carbon export. For additional details, see (Stukel et al., 2019b).

Subduction of POC provides an alternative mechanism for the export of organic matter to the mesopelagic, that is not measured by either sediment traps or ^{234}Th profiles, which only record gravitational settling of particles. A three-dimensional particle advection model was used to determine a range of possible subduction rates (Stukel et al., 2018d). The maximum and minimum estimates of particle subduction were used as bounds on two size-fractionated subduction flows within the LIEM.

Linear Inverse Model

We developed a LIEM for the CCE to investigate mechanisms of epipelagic-mesopelagic coupling. The LIEM consists of 140 flows (i.e., ecosystem fluxes, Supp. Table 2) and 24 compartments (i.e. standing stocks; Table 2) organized into two layers: the surface epipelagic and a deeper mesopelagic ecosystem (defined as 100 – 450 m depth to match with *in situ* measurements). The epipelagic and mesopelagic ecosystems consist of 73 flows and 64 flows, respectively, with four explicit flows (particle sinking and subduction) and three implicit flows (active transport) directly linking the two layers (Figure 2.1). Three vertically migrating compartments (small and large mesozooplankton and nekton) connect the epipelagic and mesopelagic through a transfer associated with DVM (i.e. respiration, excretion, and mortality). Constraints consist of 24 mass balance equations, 18 approximate equations (i.e. *in situ* rate measurements) and 133 inequalities, which are provided in an online repository: https://github.com/tbrycekelly/Inverse_DVM.

The 18 approximate equations are ecosystem observations (Tables A1, A2), which can be directly compared to flows within the model. These equations are net primary productivity (NPP), phytoplankton biomass net rate of change, protistan grazing, size-fractionated grazing rates (<1-mm and >1-mm) for epipelagic resident and DVM mesozooplankton, sediment trap and ²³⁴Th-based export fluxes, bacterial production, and mesopelagic fish respiration, mortality and fecal pellet production rates. The model was provided an estimated value and associated uncertainty for each measurement.

Respiration, mesopelagic export, nekton fecal pellets, and losses to higher trophic levels were included as closure terms. Within the model, every organism loses carbon to respiration, DOC excretion, and defecation or mortality to detritus/fecal pellets. Grazing was allowed between organisms whose ecological roles and size ranges permit grazing (e.g., small mesozooplankton graze on nano- and microplankton; sardines consume only >1-mm mesozooplankton). Mass balance was required for each compartment. All compartments were assumed to be at steady state except for PHY, for which changes in biomass were measured (via Chl-*a* proxy) during each cycle and incorporated into the model. This flexibility was essential to capture the bloom phase of the ecosystem since dramatic shifts in Chl-*a* were observed during some cycles.

The formulas used in the inequality constraints are summarized in Table A3 and provided in an online supplement (https://github.com/tbrycekelly/Inverse_DVM). Upper and lower limit estimates of POC subduction from the epipelagic to the mesopelagic layer were taken from (Stukel et al., 2018d), and minimum fecal pellet fluxes were assigned based on the assumption that recognizable fecal pellets in sediment trap material represented a lower limit on total fecal pellet flux. Minimum and maximum Gross Growth Efficiencies (GGE) were assigned according to previously accepted literature values: 10% – 40% GGE for protistan zooplankton (HNF & MIC) and gelatinous predators (Straile, 1997); 10%-30% for mesozooplankton (Anderson et al., 2018); and 5% – 30% for bacteria (del Giorgio and Cole, 1998). The Absorption Efficiencies (AE) for all heterotrophs were limited to 50% – 90% (Conover, 1966).

Minimum respiration requirements were considered as both active respiration and basal respiration. Active respiration was set as a fraction of ingestion, and basal respiration was set as a function of biomass and temperature. Valid solutions fulfilled both criteria. Diel vertical migrator biomass, as determined from MOCNESS net tows, was used to calculate a minimum respiration

based on temperature. DOC excretion was required to be greater than 10% of ingestion (or 2% of NPP for phytoplankton) and less than respiration (or 35% of NPP). All inequality constraints are listed in Table A3.

Because the LIEM is under-constrained, infinite possible solutions satisfy the equality and inequality constraints. To choose mean solutions and determine uncertainties within the possible solution space, we use a Markov Chain Monte Carlo (MCMC) sampling method (Kones et al., 2009; van den Meersche et al., 2009; van Oevelen et al., 2010a), which has been shown to reconstruct unmeasured flows more accurately than the L_2 minimum norm approach (Stukel et al., 2012a; Saint-béat et al., 2013; Stukel et al., 2018a). Implementation details are given in Appendix A.

As a metric for discussing model results with respect to the approximation equations (i.e., the observations), we use the model-observation misfit relative to the model uncertainty: $\Sigma = (X_{model} - X_{obs})/\sigma_{obs}$. Here X_{model} is the model prediction, X_{obs} is the observed value, and σ_{obs} is the standard deviation of the observed value. The square of this quantity (Σ^2) is summed over all approximate equations yielding the solution cost function, and thus Σ is a proxy for disagreement between the LIEM and observations. Unless otherwise stated, LIEM solutions are given as ranges based on the mean solutions for each cycle as well as the median value for all cycles. Displaying data in this way allows us to highlight inter-cycle variability. For value and uncertainty in all rate constraints, see Appendix A.

Analyses and Model Comparisons

An indirect analysis permits investigation of the contributions of carbon between any two compartments through indirect linkages. By taking the normalized matrix of flows between compartments (G) and the identity matrix (I), the matrix $(I-G)^{-1}$ provides all the indirect flows data (Kroes, 1977). In this way the contribution of the surface compartments to the deep ones can be ascertained even when no direct flows exist. For example, if the food chain were $A \rightarrow B \rightarrow C$, an indirect analysis would reveal that 100% of the flows to C go through A.

A model to predict the export flux due to zooplankton DVM was recently published by Archibald et al. (2019), which adds a diel vertical migration module to the Siegel et al. (2014) ecosystem model. The Archibald et al. model parameterizes the export production based on NPP, size-fractionated grazing (i.e., protists and mesozooplankton), and the proportion of DVM

mesozooplankton. The export production attributed to vertical migrators who defecate at depth is a function of total grazing, the gut clearance rate, and the proportion of zooplankton undergoing DVM (Eq. 2).

$$Export_{twilight} = p_{DVM} \cdot (1 - f_{fec}) \cdot (m_{fec} \cdot G_m + n_{fec} \cdot G_n) \quad (2)$$

where p_{DVM} is the fraction of mesozooplankton that undergo DVM, and f_{fec} is the fraction of fecal pellets produced by diel vertical migrators in the euphotic zone. m_{fec} and n_{fec} are the proportions of grazing that are exported by mesozooplankton and protistan zooplankton, respectively. G_m and G_n are the grazing rates for mesozooplankton and protistan zooplankton, respectively.

The respiration conducted by vertically migrating zooplankton can be calculated based on the metabolic efficiency, fraction of mesozooplankton undergoing DVM, and their grazing rate (Eq. 3).

$$Export_{resp} = p_{met} \cdot p_{dvm} \cdot f_{met} \cdot \left[(1 - m_{fec}) \cdot G_m + \frac{n_{fec}}{m_{fec}} (1 - m_{fec}) \cdot G_n \right] \quad (3)$$

where p_{met} is the temperature dependent metabolic rate with ΔT , the temperature difference between the mesopelagic and epipelagic and $p_{met} = 2^{(\Delta T/10)} / (2^{(\Delta T/10)} + 1)$. f_{met} is the metabolic efficiency of the zooplankton, assumed to be 0.50. We calculated active transport from Equations 3 and 4 following Archibald, but using the CCE-optimized parameter set that Stukel et al. (2015) determined for the Siegel et al. (2014) model. The fraction of mesozooplankton undergoing DVM (p_{dvm}) was calculated as described above. Fecal pellet production for meso- and microzooplankton were set to $m_{fec} = 0.3$ and $n_{fec} = 0.06$ (Archibald et al., 2019b), respectively.

Since the Archibald et al. model does not include mortality at depth as export and excludes any mesopelagic ingestion or excretion, the total export flux is the sum of Eq. 2 and 3. To compare with the LIEM presented here, a modified LIEM active transport flux will be calculated using the total active transport for mesozooplankton and subtracting mesopelagic mortality.

Results

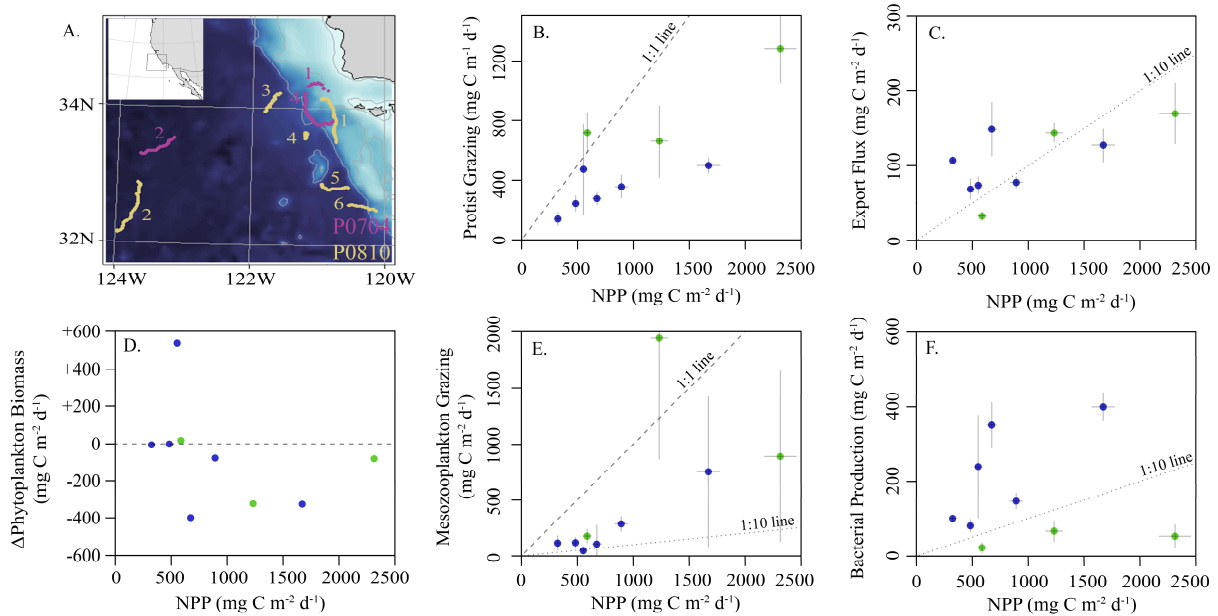


Figure 2.2. A) Bathymetric map of study region showing drift trajectories from each cycle (inset shows larger region). Numbers correspond to cycle for P0704 (purple) and P0810 (yellow). (B-F) Summary of in situ observations plotted against NPP: (B) protistan grazing, (C) export flux from sediment trap at 100 m, (D) observed rate of change of phytoplankton biomass, (E) mean mesozooplankton grazing and (F) epipelagic bacterial production. Values are colored by cruise (P0704 = green, P0810 = blue). Dashed lines for reference slopes of 1:1, 1:10, or no change as indicated and error bars are ± 1 SD.

In Situ Ecosystem Observations

The locations for each study site were chosen to maximize the range of environmental conditions (Figure 2.2). Sea surface chlorophyll *a* (Chl *a*) varied from 0.2 – 1.5 mg Chl *a* m⁻³ with vertically-integrated primary productivity varying from 325 – 2314 mg C m⁻² d⁻¹. Productivity and biomass typically declined with distance from the Point Conception upwelling center. Most cycles were in water masses with steady or declining phytoplankton biomass (Figure 2.2D), with the exception of P0810-1. Sediment trap-derived carbon export at 100 m depth varied from 32 – 170 mg C m⁻² d⁻¹ (Figure 2.2C), with observed e-ratios (i.e., sediment trap export / ¹⁴CPP) ranging from 5% - 33%. Standing stock of zooplankton correlated positively with NPP and export (Spearman correlations of 0.36 and 0.40, respectively). Protistan zooplankton were responsible for grazing ~50% of NPP (Figure 2.2B) while mesozooplankton grazed, on average, ~30% of NPP with one exception (Figure 2.2E). The proportion of

mesozooplankton biomass exhibiting DVM behavior ranged from 35% - 86% (median: 58%). Epipelagic bacterial production rates did not correlate with NPP but ranged from 22 – 400 mg C m⁻² d⁻¹ (Figure 2.2F), with the three lowest rates observed during the P0704 Cruise.

Model-Observation Mismatch

The LIEM solutions consistently show general agreement with all *in situ* observations except for modeled NPP, which is elevated by 18% - 56% (median: 22%) from ¹⁴CPP estimates (Figure 2.3A), or 3.0 – 9.3 Σ (median: 3.6 Σ). This degree of misfit corresponds to 18% – 82% (median: 46%) of the total model-observation misfit. Model agreement with the sediment trap was high (-33% – 25%; Figure 2.3E) with a modeled e-ratio (i.e. sediment trap export / NPP) of 5% – 35% (median: 14%), which compares well to the observed e-ratio of 5% – 33% (median: 11%). Modeled protistan grazing rates and mesozooplankton grazing rates were reasonably close to observations (Figure 2.3B). Modeled microzooplankton (MIC) grazing was lower than observed for cycles P0704-2 (-2.8 Σ) but agreed reasonably well (-1.5 – +0.1 Σ) for the other cycles (Figure A1). For P0704-1, mesozooplankton grazing rates were lower than observations for SMZ (-1.8 Σ), total non-DVM grazing (-1.8 Σ) and for vmSMZ grazing (-1.6 Σ). During the course of this cycle, phytoplankton biomass declined (-322 mg C m⁻² d⁻¹) and had high zooplankton grazing rates compared to the other cycles. This water parcel may have been in a declining bloom stage where observed grazing rates were unsustainable. Model-data agreement among the seven nekton-related observations (e.g., Figure 2.3F) was satisfactory ($|\Sigma| < 1$) except for P0810-1, which showed reduced vertically migrating nekton activity relative to estimates (vmMYC epipelagic respiration: -1.5 Σ , vmMYC mesopelagic respiration: -1.7 Σ , and vmMYC mesopelagic mortality: -1.1 Σ). This cycle was along the edge of an anti-cyclonic eddy, where lateral gradients were likely high.

Epipelagic Ecosystem Model

According to the LIEM, phytoplankton respired 18% - 39% (median: 30%) of GPP, lost 14% - 26% (median: 18%) as DOC, lost 2% - 42% (median: 6%) to non-grazer mortality and the remaining 5% - 54% (median: 45%) was grazed by zooplankton. Modeled NPP ranged from 421 mg C m⁻² d⁻¹ to 2750 mg C m⁻² d⁻¹ (median: 861 mg C m⁻² d⁻¹). The LIEM suggested that protists

and mesozooplankton had relatively similar grazing impacts on phytoplankton across all cycles,

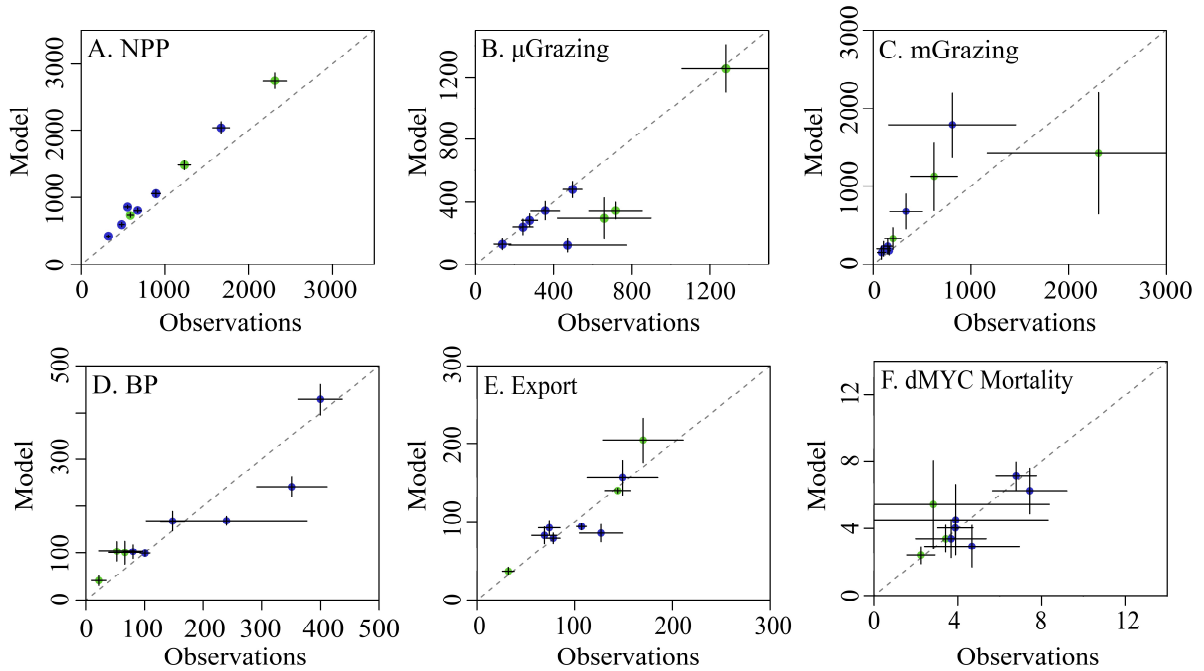


Figure 2.3. Model-observation comparisons for selected measurements: (A) net primary productivity, (B) protistan zooplankton grazing, (C) mesozooplankton grazing, (D) epipelagic bacterial production, (E) sediment trap carbon export (@ 100m), and (F) non-vertically migrating mesopelagic nekton mortality. Cruises are denoted by color (P0704 = green, P0810 = blue). Dashed line is 1:1 and error bars show 1 SD of uncertainty.

although the proportional role was greater for mesozooplankton in coastal regions and greater for protists under oligotrophic conditions. Between 14% and 47% (median: 33%) of NPP was grazed by protistan zooplankton (MIC + HNF) and 18% - 96% (median: 45%) by mesozooplankton (SMZ + vmSMZ + LMZ + vmLMZ). We note that protistan grazing rates normalized to NPP are slightly depressed relative to observations since model NPP was higher than observations while protistan grazing generally matched the observations (Figure 2.3; Figure A1). 57% - 82% (median: 74%) of mesozooplankton grazing was by small mesozooplankton (SMZ + vmSMZ). Vertically migrating mesozooplankton were responsible for 52% - 89% (median: 63%) of total mesozooplankton grazing, 58% - 85% (median: 77%) of which was done by vmSMZ (i.e. vmSMZ grazing / total vm grazing).

Mortality relative to ingestion for mesozooplankton was similar for the different epipelagic mesozooplankton (i.e. SMZ, LMZ, vmSMZ, and vmLMZ): SMZ: 24% - 25%, vmSMZ: 23% - 25%, LMZ: 22% - 25%, and vmLMZ: 24% - 27%, as was fecal pellet production (between 30% and 40% of ingestion).

Overall, 19% - 44% (median: 29%) of NPP was transferred from the epipelagic to the mesopelagic with 3% - 8% (median: 5%) of NPP leaving the epipelagic through higher trophic levels (SAR + vmMYC). Gravitational settling and subduction of POC accounted for 12% - 55% (median: 37%) and 2% - 32% (median: 14%) of epipelagic export, respectively, while 18% - 84% (median: 41%) was through active transport of DVM mesozooplankton (vmSMZ + vmLMZ). Vertically migrating myctophids (vmMYC) transferred 2% - 6% (median: 4%) of total export. Section 3.4 provides a more detailed description of export production.

The gross growth efficiencies (GGE) for each type of organism are shown in figure 2.4A. Overall, BAC GGE was 7% - 29% (median: 25%) with an upper bound set to 30%. Notably, BAC GGE differed based on cruise, with P0704 cycles ranging between 8% - 13% and P0810 ranging between 23% - 29%. MIC GGE was 35% - 38% (median: 37%), and HNF GGE ranged from 32% - 35% (median: 33%), which is slightly higher than typical estimates of protistan zooplankton GGE (Straile, 1997) although reported variability is high (Steinberg and Landry, 2017a). GGEs for epipelagic mesozooplankton were consistently above 20%.

Trophic levels for each organism (Figure 2.4B) were calculated by assuming that primary productivity, detritus and DOC were at trophic level 1. Trophic level indices were not affected by the overall cycle productivity (i.e. NPP), time of year, or by nutrient regime. The trophic level of small epipelagic mesozooplankton (SMZ) ranged from 2.2 to 2.5 (median: 2.2) and large mesozooplankton (LMZ) ranged from 2.2 to 2.9 (median: 2.6). The SAR trophic level was 3.3 - 3.8 (median: 3.5), and vmMYC was similar at 3.3 - 4.0 (median: 3.8). Modeling these higher trophic levels is important for structuring the ecosystem, and the nekton trophic levels found here are consistent with findings from ¹⁵N amino acid studies (Choy et al., 2015).

The modeled mesozooplankton ingestion can be classified into four distinct dietary types: (1) Herbivory = phytoplankton diet, (2) Protistivory = protistan zooplankton diet, (3) Detritivory = detrital diet (i.e. SDT or LDT), and (4) Carnivory = mesozooplankton diet. Using this partitioning, the relative contributions of each dietary component were assessed for large and small vertically migrating mesozooplankton compartments (Figure 2.5). The largest proportion of the diet for resident epipelagic mesozooplankton (i.e. SMZ & LMZ) was balanced between herbivory (19% - 57% median: 40%) and protistivory (26% - 59% median: 40%). Detritivory was 9% - 21% (median: 13%) of total diet. Inter-cycle variability in carnivory was low for resident epipelagic mesozooplankton and contributed 6% - 8% (median: 6%) of their diet.

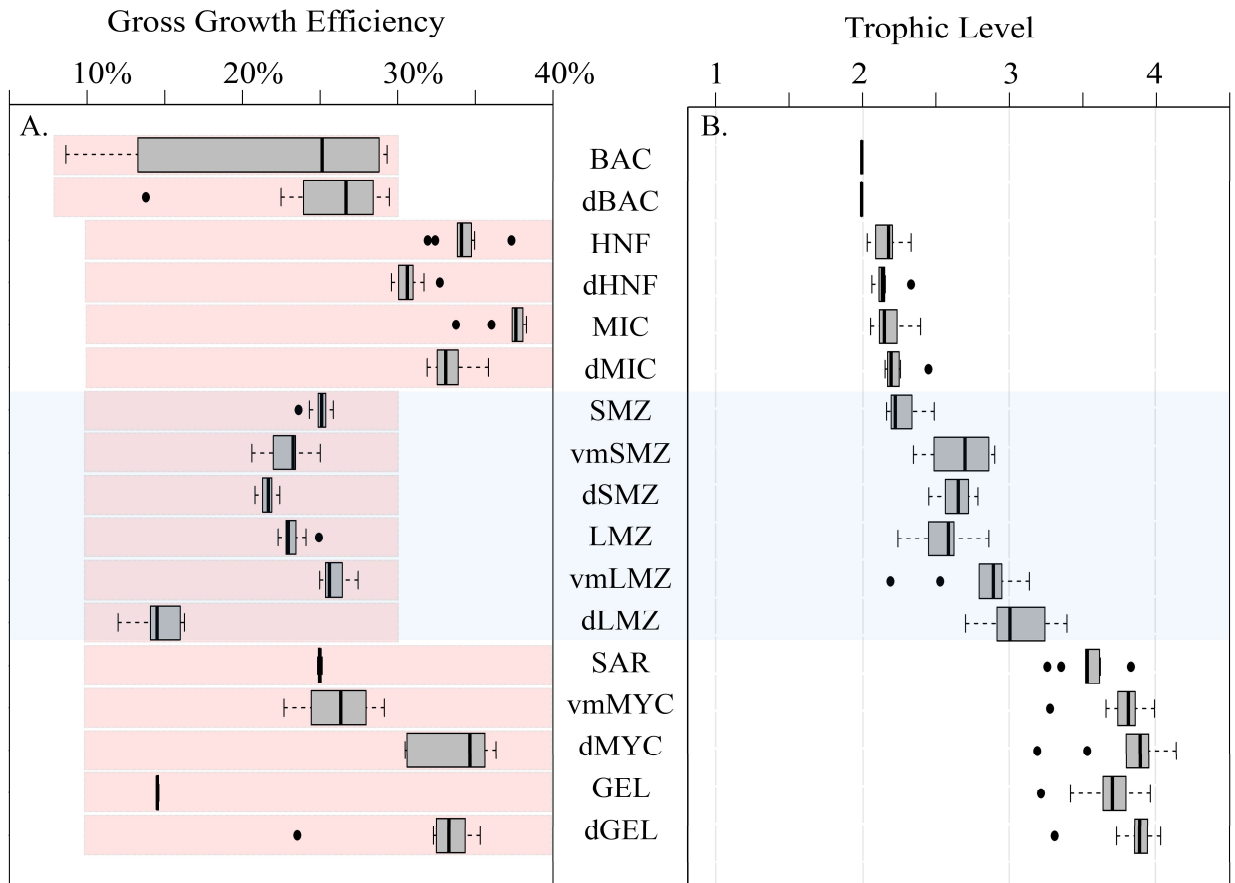


Figure 2.4. A) Box and whisker plot of GGE for organisms in the LIEM. Red shaded boxes indicate the permitted range of values constraining the LIEM. (B) Box and whisker plot of trophic levels for each zooplankton assuming detritus and primary productivity are trophic level 1, and bacteria are trophic level 2. Box and whisker plots show inter-quartile range and 95% C.I. as determined using the mean solutions for each cycle. For reference the mesozooplankton compartments are shaded across both figures. Abbreviations are explained in Table 2.2.

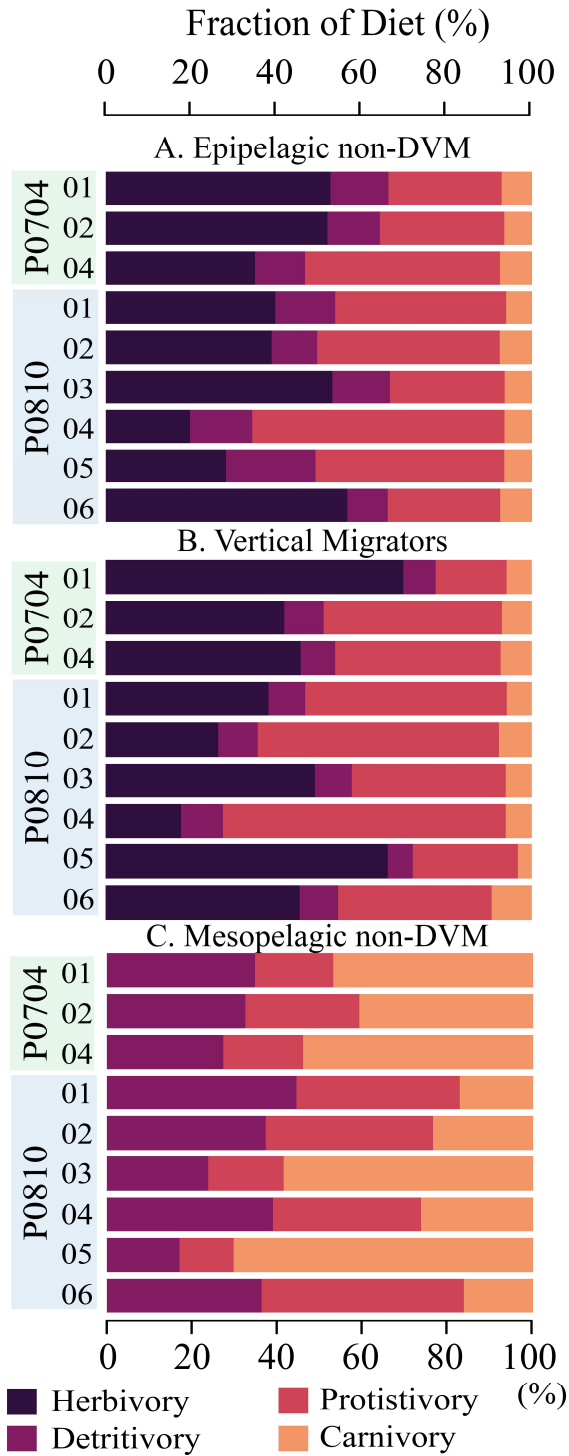


Figure 2.5. Composition of diet for (A) epipelagic, non-DVM mesozooplankton, (B) vertically migrating mesozooplankton, and (C) mesopelagic, non-DVM mesozooplankton. Diet is partitioned into herbivory (darkest), protistivory, detritivory, and carnivory (lightest). Cycles are as indicated.

Comparing the LIEM solutions between the nutrient limited and upwelling cycles, we found that large mesozooplankton (LMZ) grazing increased from 9% - 16% (median: 13%) in the nutrient limited cycles to 22% - 65% under upwelling conditions (median: 30%) of NPP. However, the overall diets of the mesozooplankton did not systematically change with nutrient condition.

New Production, Export and DVM

Total export ranged from 163 - 707 mg C m⁻² d⁻¹ (median: 282 mg C m⁻² d⁻¹), with distinctly elevated values associated with upwelling cycles (Figure 2.6A). The fraction of export attributed to mesozooplankton DVM (vmSMZ + vmLMZ) covaried with nutrient regime: mesozooplankton active transport contributed 14% - 37% of total export under nutrient limited conditions and 44% - 84% under upwelling conditions (Figure 2.6B). There was no significant relationship ($p < 0.1$) between the total export efficiency (i.e. total export / NPP) and NPP (Figure 2.6C).

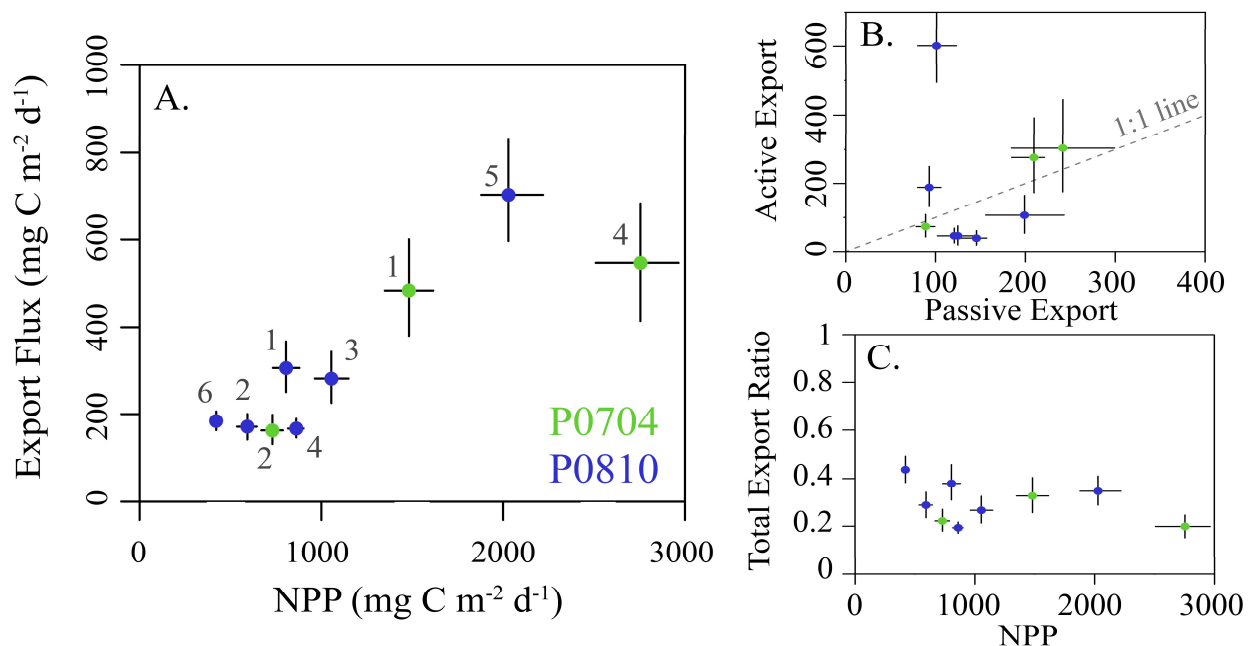


Figure 2.6. A) The sum of both passive and active carbon export flux from the epipelagic plotted against NPP. Cruises are color coded and error bars show the 95% CI for each value. (B) The total active flux due to DVM versus passive flux for each cycle (as in A). Dashed 1:1 line for reference. (C) The total export ratio (i.e. total epipelagic export / NPP) plotted against NPP and colored as in (A). All values are in mg C m⁻² d⁻¹.

For vmSMZ, 77% - 80% (median: 80%) of their respiration took place in the epipelagic, along with 67% - 87% (median: 85%) of their DOC excretion. This is consistent with the suggestion that mesozooplankton respiration and excretion are elevated in the warmer epipelagic waters (Ikeda, 1985a), where activity is highest.

The fate of active export flux is important for understanding the ecological impact of this carbon supply. Within the mesopelagic, mesozooplankton respired 11 – 104 mg C m⁻² d⁻¹ (median: 33 mg C m⁻² d⁻¹) and excreted 7 – 116 mg C m⁻² d⁻¹ (median: 20 mg C m⁻² d⁻¹; Figure 7A). Predation on vertically migrating mesozooplankton accounted for a loss of 23 – 352 mg C m⁻² d⁻¹ (median: 59 mg C m⁻² d⁻¹) in the mesopelagic. Mesozooplankton fecal pellet production in the mesopelagic was 8 – 29 mg C m⁻² d⁻¹ (median: 13 mg C m⁻² d⁻¹). Resident mesopelagic mesozooplankton were the dominant mortality term for the vertically migrating mesozooplankton (Figure 2.7B).

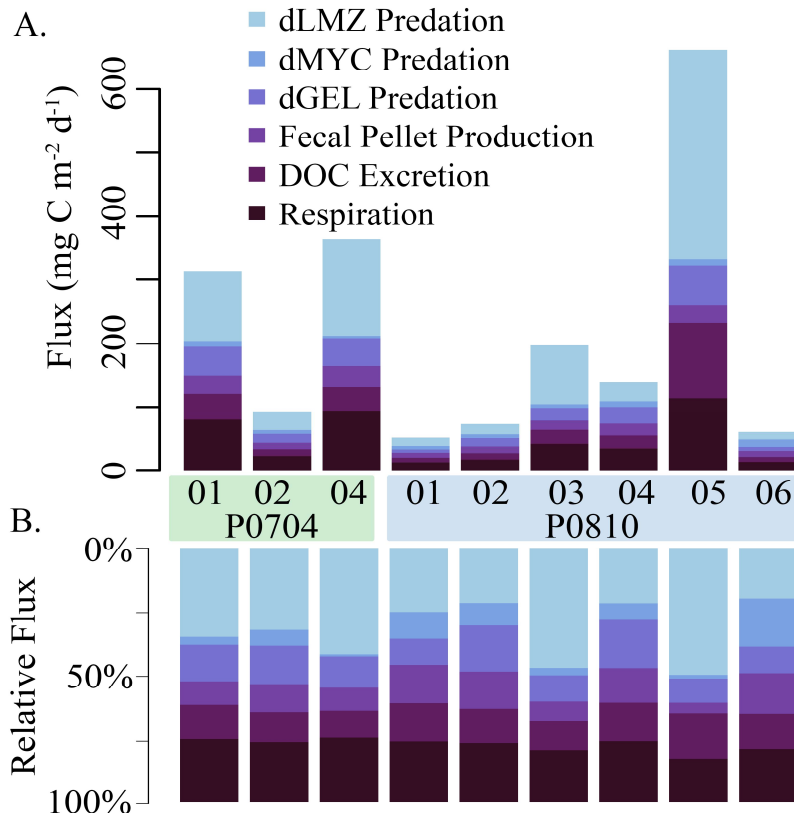


Figure 2.7. The (A) net and (B) relative fate of vertically migrating mesozooplankton within the mesopelagic. Loss terms are color coded, and cruise and cycle are as shown. Abbreviations are explained in Table 2.2.

Mesopelagic Ecosystem

Deep bacteria (dBAC) made up 6% - 30% (median: 11%) of the mesopelagic protistan zooplankton diet with the remainder supplied by detritus/fecal pellets. Mesopelagic mesozooplankton (i.e. dSMZ & dLMZ) had a more variable diet than the epipelagic mesozooplankton (Figure 2.5), with detritivory ranging from 17% - 43% (median: 39%) of their diet, protistivory at 14% - 51% (median: 30%) and carnivory at 10% - 68% (median: 33%).

Systematic increases in trophic level between the epipelagic and mesopelagic resident zooplankton and nekton were observed (Figure 2.4). The trophic level of epipelagic microzooplankton (MIC) was 2.0 – 2.3 while dMIC was 2.3 – 2.5. Similar increases between the epipelagic and mesopelagic were observed for mesozooplankton, where SMZ had a trophic level of 2.2 – 2.5 (median: 2.2) dSMZ had a trophic level of 2.5 - 2.8 (median: 2.6). Likewise, dLMZ trophic levels were elevated by ~0.4 relative to LMZ. The trophic level of dMYC (3.2 – 4.1) was more variable than the other micronekton (e.g. vmMYC: 3.5 – 4.0), illustrating a greater variability in diet.

Mesopelagic respiration is a useful diagnostic loss term for determining which organisms are responsible for the mesopelagic carbon demand (Figure A2). Mesopelagic bacteria accounted for the largest proportion of mesopelagic respiration (31%-41% median: 34%). High respiration of mesopelagic bacteria was found despite relatively high GGE for these organisms (median 26%, Figure 2.4A). Mesopelagic protistan zooplankton and resident mesozooplankton were responsible for 14% - 30% (median: 25%) and 14% - 24% (median: 15%), respectively. Resident gelatinous predators and myctophids are responsible for 4% - 8% of mesopelagic respiration combined. The proportion of export due to active transport covaried with resident mesopelagic respiration (Figure 2.8A), illustrating the coupling between active transport and mesopelagic activity in the LIEM. The effect of higher active transport relative to total export can be shown with an indirect analysis where the relative contribution of carbon from epipelagic detritus (i.e., a passive transport proxy) and vertically migrating mesozooplankton (i.e., an active transport proxy) in the diet of each organism can be measured. Indirect flux analyses show that a higher proportion of the carbon consumed by mesopelagic bacteria, protists, and mesozooplankton originated from passive rather than active transport (Figure 2.8B). However, mesopelagic nekton (dMYC) were predominantly supported by carbon derived from active transport pathways.

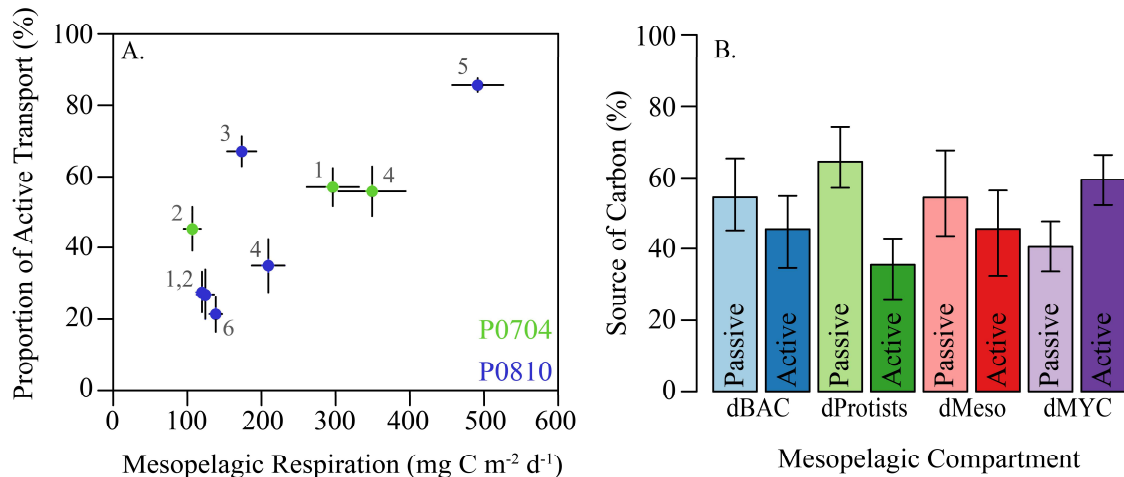


Figure 2.8. A) Proportion of active transport relative to total export versus total mesopelagic respiration by residents (i.e. dBAC, dHNF, dMIC, dSMZ, dLMZ, dMYC, dGEL). Cruises are colored and cycles are as shown. (B) Relative proportions of carbon demand supplied by passive or active flux for the indicated mesopelagic groups. Source was calculated using indirect flux analysis (Section 2.3.1) to determine the indirect contribution epipelagic detritus (passive) and vertically migrating mesozooplankton (active). Error bars are ± 1 SD.

Discussion

Diel Vertical Migration & Active Transport in the CCE

In contrast to common assumption about the processes driving the biological pump, our results suggest that active transport may be as, if not more, important than sinking particle flux. We found that active transport (mesozooplankton and fish combined) was responsible for 39 - 606 mg C m⁻² d⁻¹ (median: 107 mg C m⁻² d⁻¹), corresponding to 21% - 86% of total export to the mesopelagic, while sinking particles contributed 14% - 79%. This finding is not directly forced by an *a priori* assumption of the importance of active transport. Indeed, we placed no direct constraint on the amount of mesozooplankton mortality in the mesopelagic, and the minimum constraints on basal metabolism by zooplankton in the mesopelagic (Stukel et al., 2013d) implied that active transport could have been as low as 2% - 40% of sinking flux (median: 18%). Nevertheless, the importance of active transport was a robust result of the inverse analyses. For P0810-6, the cycle with the lowest relative contribution of active transport to total export (21%), the total flux was 184 ± 23 mg C m⁻² d⁻¹ (95% CI) and active transport was 39 ± 21 mg C m⁻² d⁻¹ (95% CI). This cycle was oligotrophic and had the lowest ¹⁴CPP measurements of any cycle on the two cruises. In contrast, cycle P0810-5 had the highest relative contribution of active

transport ($86\% \pm 4\%$ of total export at the 95% CI). P0810-5 was on the coastal (i.e. high biomass) side of a strong frontal feature with high rates of primary productivity and large standing stocks of zooplankton.

Although these rates of active transport are higher than reported in many studies, they are fully consistent with mesozooplankton community dynamics in the CCE. The model suggests that total epipelagic mesozooplankton consumption on phytoplankton, protists, detritus, and other mesozooplankton ranged from $361 - 2966 \text{ mg C m}^{-2} \text{ d}^{-1}$ (median: $1006 \text{ mg C m}^{-2} \text{ d}^{-1}$). Vertically stratified day-night net tows showed that 35% - 86% (median: 57%) of the mesozooplankton community was vertically migrating to depth each day and that most of these vertical migrants were copepods and euphausiids (Stukel et al., 2013d). Our model results indicate that only 20% - 23% of respiration and 16% - 34% of excretion by vertical migrants occurred at depth. None of these assumptions are particularly aggressive. Furthermore, our results (Figure 2.9) are consistent with estimates of DVM in the zooplankton derived from the model of Archibald et al. (2019), if specific dynamics of the CCE are taken into account (e.g., zooplankton consume nearly all of NPP, Landry et al. 2009; microphytoplankton are negligible contributors to sinking flux, Stukel et al. 2013). Our estimates of the total export ratio 19% - 44% are also consistent with typical f -ratio estimates (new production to total export) in our study region, which varied from 0.23 to 0.40 (Krause et al., 2015a). Our results thus do not arise from unusual parameterizations but instead may reflect the fact that estimates of active export using standard metabolism calculated from Ikeda et al. (1985; 2001) may be conservative underestimates.

Our results also reflect realistic coupling between the epipelagic and mesopelagic communities. Model results suggested that the carbon demand was equal to <1% - 4% (median: 1.1%) of NPP for mesopelagic fish, 1% - 7% (median: 3%) of NPP for predatory gelatinous zooplankton, 8% - 22% (median: 14%) of NPP for resident mesopelagic zooplankton, and 6% - 19% (median: 11%) of NPP for mesopelagic bacteria. These mesopelagic carbon demands must be met by carbon flux from the surface layer, the most likely sources of which are sinking particle flux (which we experimentally measured using two independent approaches) and active transport. While it is possible that both sediment traps and ^{238}U - ^{234}Th disequilibrium underestimated sinking carbon flux, the inverse analysis offers compelling evidence that active

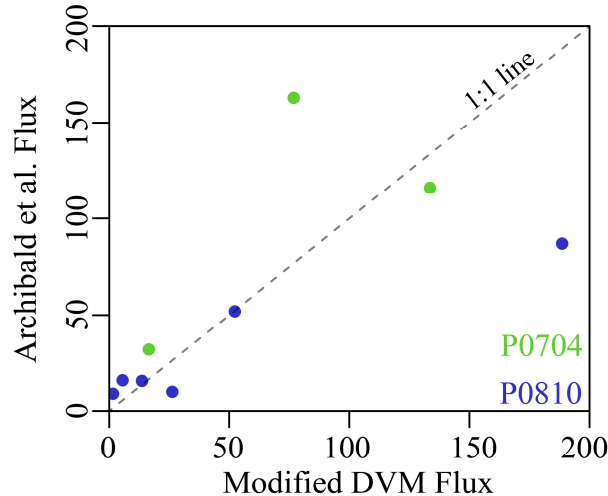


Figure 2.9. Comparison between modeled mesozooplankton DVM flux without mesopelagic mortality and the predicted flux from Archibald et al. (2019) with CCE-specific parameterization following Stukel et al. (2015a). Cruises are as colored (P0704 = green, P0810 = blue) and dashed line is a 1:1 reference line. Fluxes are shown in $\text{mg C m}^{-2} \text{d}^{-1}$.

transport is more likely to support mesopelagic fish and gelatinous predator communities.

Although sinking particles can efficiently support bacterial production (as they are likely directly colonized by particle-attached bacteria), many fish and gelatinous zooplankton are predators that feed more on living organisms than on the sinking fecal pellets that typically dominate particle flux in the CCE. For these planktivorous organisms, sustaining their metabolism through a food chain supported by sinking particles would likely require one (if not more) trophic levels to separate them from the export source, depending on whether the sinking particles are consumed by filter- or flux-feeding zooplankton or by microbes (Stukel et al., this issue). Thus, sustaining the high carbon demand of mesopelagic myctophids with sinking particles requires substantially more total carbon flux than does sustaining it via active transport of the myctophids' prey.

Mesopelagic sources of mortality have implications for the fitness of vertical migrators. It is often assumed that DVM is ecologically advantageous when the costs associated with not feeding during the day and actively swimming to depth are offset by the benefits of reduced predation pressure and/or reduced metabolism at colder mesopelagic temperatures (Bianchi et al., 2013a; Hansen and Visser, 2016a; Morozov and Kuzenkov, 2016). Our model suggests that mortality normalized to ingestion is similar across all mesozooplankton compartments and across a wide range of ecosystem states (SMZ: 24% - 26%, LMZ: 22% - 25%, vmSMZ: 21% - 25%, vmLMZ: 25% - 27%, dSMZ: 21% - 23%, dLMZ: 19% - 23%). Even though vmSMZ experience

similar predation to SMZ and dSMZ, approximately half of the predation on vertically migrating zooplankton takes place in the mesopelagic, thereby transferring carbon to depth despite the fact that their excretion and respiration occur primarily in the epipelagic.

The comparable mortality experienced by vertically-migrating mesozooplankton in the mesozooplankton may seem counterintuitive in light of extensive research suggesting that the adaptive advantage of DVM may be to reduce predation (Ohman and Romagnan, 2016; Bandara et al., 2018). However in the CCE, it is not particularly surprising when the large abundances of myctophids, gonostomatids, and other mesopelagic fish are considered. Davison et al. (2013, 2015) demonstrated high biomass of these fish comprising both vertically-migrating and mesopelagic resident communities. Mesozooplankton may thus face as high, if not higher, predator abundance at mesopelagic depths than in the epipelagic, although colder temperatures and reduced irradiance may diminish predation rates at depth. DVM may remain advantageous as a lifestyle because if these organisms were present at the surface during the day then they might experience substantially greater predation than in the mesopelagic.

Sensitivity Analysis and Ecological Connections

The ecosystems generated in the 9 model runs were as varied as the cruise measurements: including observations from dynamic coastal blooms to quiescent oligotrophic communities. All 9 cycles had significantly elevated NPP compared to the observed ^{14}C PP (Figure 2.3; Figure A1) with 95% CI from the MCMC random walk. Whether this result can be considered a model bias or is derived from possible systematic differences between ^{14}C PP and true net primary production (Peterson, 1980; Lefevre et al., 1997; Marra, 2009; Milligan et al., 2014) is not known. Compared to shorter ^{14}C labeling experiments (e.g. dawn-to-dusk, 8h, pulse-chase), the 24 hour incubations used here are generally thought to measure NPP rates directly (Milligan et al., 2015); however, long-term incubations are susceptible to biases introduced by heterotrophic processes and DOC excretion (Laws et al., 2000c; Dickson et al., 2001). Since rapid consumption of net primary productivity by grazers, cell lysis, and excretion of DOC (all of which are explicitly included in the LIEM) will reduce the apparent ^{14}C -bicarbonate uptake rates, ^{14}C PP rates may be biased low, especially when turnover times are short. In fact, when comparing dilution-based growth rates with 24h ^{14}C PP incubations in the equatorial Pacific, Landry et al. (2011) found that ^{14}C PP estimates needed to be adjusted upwards by 29% on

average. An alternative explanation may stem from a bias in the MCMC approach used. Since the random walk is strictly required to yield solutions where flows are positive through the “mirror” algorithm, the region of permitted solutions is non-symmetric and may favor the broader solution-space of high NPP solutions (as noted in Stukel et al., 2012). A thorough investigation into the potential biases of the ^{14}C CPP method of the MCMC solution algorithm are beyond the scope of this study, but the impact of a potential bias in modeled NPP are discussed below.

To test the model’s sensitivity to the misfit with ^{14}C CPP and to confirm that our results were not driven by a potential bias in the model, the LIEM was rerun assuming that ^{14}C CPP uncertainty was 1/10th of the actual estimated uncertainty (i.e., 0.6% relative uncertainty). The model-observation misfit increased by nearly 2.5x with vmSMZ and SMZ grazing rates, myctophid metabolic estimates, and sediment trap export all reduced by $\sim 2 \Sigma$ relative to the standard model run. This result shows that the model needed to increase NPP in the standard model run in order to match the observed mesozooplankton grazing rate and myctophid metabolic requirements. However, the proportion of export resulting from active transport remained relatively unchanged. It varied from 106 to 641 mg C m⁻² d⁻¹ across the cycles (compared to 162 to 707 mg C m⁻² d⁻¹ in the standard model run). This suggests that our primary conclusions about export flux were not contingent on elevated model NPP.

Because bacterial activity in the mesopelagic was not measured, we set a high upper and low minimum bounds for bacterial production. For the minimum bound on mesopelagic BP, we chose an attenuation coefficient of $\alpha = 1.47$ (Yokokawa et al., 2013). This resulted in model-determined mesopelagic bacterial carbon demand that may have been lower than true *in situ* values. Other reported values for the attenuation of BP in the mesopelagic include slopes of $\alpha = 1.15$ (Tanaka and Rassoulzadegan, 2004) and 1.03 (Gasol et al., 2009), which would result in 25% and 36% higher estimates of mesopelagic BP, respectively. When the minimum mesopelagic bacterial production estimates were halved ($\alpha = 0.64$; Eq. 1), the model responded by increasing NPP by +2% (inter-cycle median) and total export flux by 11%. Since passive particle flux is constrained by observations, passive flux increased by 0% - 12% (median: 4%) while active transport by mesozooplankton increased by 0% - 56% (median: 26%). Active transport by nekton was also elevated (0% - 14%, median: 10%). Model-observation misfit increased by an average of 17% with notable changes in NPP (+0.42 Σ), sediment trap flux

(+0.34 Σ) and Thorium-234 flux (+0.22 Σ).

The standard model results were also robust to changes in other observations. When the nekton metabolic estimates were halved, export by vmMYC was reduced by 51% (inter-cycle median), a change of $< 5 \text{ mg C m}^{-2} \text{ d}^{-1}$, while other forms of export were unchanged. Increasing the upper limit of mesozooplankton GGE from 30% to 40% led to a $\sim 20\%$ increase in mesozooplankton active transport and no change in nekton-derived active flux or passive flux.

Zooplankton basal respiration rates have been shown to be suppressed under low-oxygen conditions (Ekau et al., 2010; Seibel, 2011), such as those seen in the midwater oxygen minimum zones (OMZ) often encountered below the productive Eastern boundary current upwelling biomes (Chavez and Messié, 2009; Bettencourt et al., 2015). During our study periods, water-column dissolved oxygen concentrations fell below $44.7 \mu\text{M}$ (0.5 ml/l), indicating hypoxic conditions (Helly and Levin, 2004; Gilly et al., 2013), between 271 m and 470 m water depth (Figure A3). Notably, most of the zooplankton captured in our study were found at depths shallower than 300 m. While there are questions remaining with regard to how mesozooplankton respiration rates would be affected by the intermediate oxygen depletion observed in our study (Teuber et al., 2013; Kiko et al., 2016), the model results are largely insensitive to a possible reduction in basal metabolism. In particular, the respiration rates of the mesopelagic organisms in the model were consistently higher than the basal metabolic constraint placed on them (typically $>2x$). Including ecological implications of the OMZ directly would be a valuable contribution to the field that necessitates a more depth-resolved model due to the importance of vertical gradients in oxygen and temperature.

Linear Inverse Models

LIEMs are powerful tools for assimilating diverse *in situ* measurements and constraints with a food web perspective. The use of a two-layer model (Jackson and Eldridge, 1992) is particularly powerful because it allows information from the mesopelagic to constrain epipelagic food web flows and vice versa. Compared to most previously published LIEMs, the model presented here includes many more *in situ* rate measurements, made possible by the suite of contemporaneous rate measurements made during quasi-Lagrangian experiments. When constrained by fewer rate measurements (Dubois et al., 2012; van Oevelen et al., 2012; Sailley et al., 2013), the LIEM solution relies more heavily on greater than/less than constraints derived

from biomass measurements, leading to correspondingly higher uncertainty. This highlights a need for studies that simultaneously quantify the activity of many different plankton functional groups.

Since a LIEM is fundamentally a data-regression technique, our results are emergent from (A) our observations, (B) the assumptions used (e.g. GGE), and (C) the ecosystem structure of the model. Thus, we believe the resulting model solutions to be descriptive of the dominant *in situ* processes in the CCE LTER study region. However, it is important to note that there were large uncertainties associated with some model flows, and that these could be quantified using the MCMC approach (Supp. Table 2). We thus highly recommend the MCMC approach (Kones et al., 2009; van den Meersche et al., 2009), which has been shown to be robust in its ability to recover ecosystem rates relative to the L-2 minimum norm (Stukel et al., 2012a; Saint-béat et al., 2013). Even more important is its ability to generate confidence intervals that realistically represent the uncertainties in model outputs with respect to both measurements and under-determinacy of the model. For instance, for cycle P0810-6, we found that the 95% confidence interval for HNF ingestion of detritus was 5 - 127 mg C m⁻² d⁻¹, providing no real knowledge of whether or not this connection was an important part of the ecosystem. However, for Cycle P0810-5, we found that mesopelagic mesozooplankton predation on small vertical migrators was 233 - 423 mg C m⁻² d⁻¹ (95% CI), indicating a higher degree of confidence that this flow was substantial at this location. Investigation of the confidence intervals can thus inform which conclusions can be considered robust. Developing even better-resolved ecosystem models likely requires incorporation of more diverse measurement types, such as ¹⁵N isotopic data (Stukel et al., 2018a).

The Biological Carbon Pump and Mesopelagic Flux Attenuation

Reports of active transport by vertically migrating biota have long suggested that these organisms can transport a globally significant amount of carbon to depth. However, most early studies suggested that active transport was substantially less important than passive flux of sinking particles (Morales, 1999; Davison et al., 2013; Steinberg and Landry, 2017a). At the oligotrophic BATS station off Bermuda, Dam et al. (1995) found that respiration by mesozooplankton augmented the passive carbon flux at 150 m by 18% – 70%. Also at BATS, Steinberg et al. (2000) reported a significant vertical transfer of nitrogen by zooplankton,

including dissolved organic nitrogen (DON). In fact, vertical migrators were found to perform 15% - 66% of the total nitrogen transport. Hansen and Visser (2016a) estimated that across the North Atlantic active transport by mesozooplankton may constitute 27% of total export out of the surface mixed layer. In addition to zooplankton, vertical migrations by micronekton can also lead to significant export fluxes (Hernandez-Leon et al.; Angel and Pugh, 2010; Davison et al., 2013). Using biomass estimates and metabolic relationships, Davison et al. (2013) found micronekton contributions of $22 - 24 \text{ mg C m}^{-2} \text{ d}^{-1}$ (or 15% - 17% of estimated passive export) in the northeast Pacific at 150 m water depth. In the North Pacific Subtropical Gyre, Al-Mutairi and Landry (2001) estimated that active transport due to zooplankton respiration was responsible for carbon flux equal to 18% of passive flux at 150 m. Using a conservative approach, Longhurst (1990) estimated that active export by zooplankton DVM was 13% - 58% that of passive flux at 150 m when accounting for respiration alone in subtropical waters, which is similar to our results where the LIEM suggests that mesozooplankton respiration at depth is 9% - 113% (median: 34%) that of passive export at 100 m. Global modeling estimates have indicated that active transport may be responsible for 14% (Archibald et al., 2019) or 15 to 40% (Bianchi et al., 2013) increases in carbon export out of the euphotic zone relative to sinking particles alone. More recent results have suggested increased importance for active transport, potentially rivaling that of passive flux. In the Costa Rica Dome, a region with high mesozooplankton biomass like the CCE, Stukel et al. (2018b) identified active transport by zooplankton DVM as responsible for 21-45% of total euphotic zone export. Hernández-León et al. (this issue) found that active transport was equal to one quarter of passive flux in oligotrophic regions, but was 2-fold higher than passive flux in eutrophic areas of the tropical and subtropical Atlantic. Our results that total active transport (zooplankton and nekton) may be responsible for 18% - 84% (median: 42%) of total carbon export at 100 m in the CCE are thus somewhat higher than found in most studies, but consistent with recently published values for high zooplankton biomass regions. Furthermore, our results are in line with other biogeochemical and ecological expectations (e.g., mesopelagic carbon demand, euphotic zone new production, mesozooplankton energy partitions). We thus suggest that active transport in high biomass regions may be more important, in fact, than some previous studies suggest, and we recommend focused research to investigate the potentially conservative assumptions made in previous studies that rely on standard (rather than active) estimates of zooplankton metabolic rates.

Within the mesopelagic, zooplankton also play an important biogeochemical role in the attenuation of particle flux (Buesseler and Boyd, 2009; Steinberg et al., 2008; Stukel et al., this issue) and in effecting elemental cycling (Kiko et al., this issue; Robinson et al., 2010). Our results suggest that mesozooplankton detritivory accounted for the consumption of 57% - 71% of sinking particles from the epipelagic, with bacterially-mediated remineralization of the majority of the remainder (i.e. mesopelagic export efficiency is $< 10\%$). Notably, 3 of the 4 cycles with the lowest proportion of detritivory and the largest proportion of carnivory in the resident mesopelagic zooplankton were during upwelling cycles. This is opposite to the findings of Wilson et al. (2010), who observed increases in fatty-acid biomarkers associated with carnivory at station Aloha relative to K2 and attributed the increase to the lower primary productivity at station Aloha. Our result that zooplankton rely more heavily on carnivory in the mesopelagic agrees with fecal pellet characteristic analyses and fatty acid biomarkers measured by Wilson et al. (2008) and Wilson et al. (2010), respectively. However, given the advective nature of an eastern boundary current and frequency of non-steady state conditions, it is difficult to generalize from our results to the rest of the Pacific. Clearly additional studies are necessary.

Conclusions

The LIEM used here incorporated numerous *in situ* measurements made during quasi-Lagrangian experiments in the CCE in order to constrain carbon flows through the ecosystem. These observations were made in water parcels spanning a wide range of conditions from highly productive upwelling regions to an oligotrophic offshore domain and consistently found that active transport of carbon by mesozooplankton was important to supplying the mesopelagic carbon demand. The model suggests that, relative to total export, gravitational settling contributes 12% - 55% (median: 37%) and subduction contributes 2% - 32% (median: 14%) of carbon flux. This finding has implications for the interpretation of sediment trap and ^{234}Th disequilibrium measurements and for helping to reconcile the long-studied imbalance in the mesopelagic carbon budget. The LIEM also highlights the central importance of zooplankton in marine food webs and biogeochemistry. Excretion by vertical migrants is important for meeting bacterial carbon demand, while predation on vertical migrants supports mesopelagic resident fish communities. Our analysis comprises a unique, fully resolved phytoplankton-to-fish coupled food web of the epipelagic and mesopelagic ocean. Nevertheless, substantial uncertainties

remain, and targeted studies are necessary to validate the suggested relationships *in situ* and to test their applicability across the global ocean.

CHAPTER 3

LATERAL ADVECTION SUPPORTS NITROGEN EXPORT IN THE OLIGOTROPHIC OPEN-OCEAN GULF OF MEXICO

Introduction

This chapter is an original research article and submission to Nature Communications with the following coauthors, who were invaluable to the project: committee member Angela N. Knapp, Michael R. Landry, Karen E. Selph, fellow lab member Taylor A. Shropshire, Rachel Thomas, and my doctoral advisor Michael R. Stukel. As such, the format has been modified to fit this dissertation.

In contrast to its productive coastal margins, the open-ocean Gulf of Mexico (GoM) is notable for highly stratified surface waters with extremely low nutrient and chlorophyll concentrations. Field campaigns in 2017 and 2018 indicate low rates of turbulent mixing, which combined with oligotrophic nutrient conditions, give very low estimates of diffusive flux of nitrate into the euphotic zone ($< 1 \mu\text{mol N m}^{-2} \text{d}^{-1}$). Estimates of local N_2 -fixation are similarly low. In comparison, measured export rates of sinking particulate organic nitrogen (PON) from the euphotic zone are 2 – 3 orders of magnitude higher (i.e. 462 – 1144 $\mu\text{mol N m}^{-2} \text{d}^{-1}$). We reconcile these disparate findings with regional scale dynamics inferred independently from remote-sensing products and a regional biogeochemical model and find that laterally sourced organic matter is sufficient to support $>90\%$ of open-ocean nitrogen export in the GoM. Particularly for small ocean areas like the GoM that are closely bordered by productive coasts, lateral transport needs to be considered in studies of biogeochemical balances.

Conventionally, primary production is partitioned between new and regenerated production based on the source of inorganic nitrogen (Harrison et al., 1987a): new production (NP) is fueled by N input from external sources (e.g. upwelled nitrate or N_2 -fixation) while regenerated production (RP) comes from the internal recycling of nitrogen (e.g. ammonium). While RP often supports the vast majority of total primary production in open-ocean ecosystems, new nitrogen sources (NP) are necessary to support N export because the mass fluxes into and out of a system must balance when integrated over sufficiently large spatiotemporal scales. While the NP and RP dichotomy is well established in the simple biogeochemical metric of the f -ratio ($=\text{NP}/(\text{NP}+\text{RP})$), direct measurement of NP is complicated by the complexities of nitrogen

cycling. For example, the most common NP measurement technique, nitrate uptake incubations, assumes negligible rates of nitrification (i.e. ammonium oxidation into nitrate) within the euphotic zone. Nitrification, which produces nitrate from ammonium and thus cannot support NP, however, is known to be an important process (Dore and Karl, 1996; Wankel et al., 2007; Yool et al., 2007; Martens-Habbena et al., 2009), especially in oligotrophic waters where ammonium concentrations can exceed those of nitrate. Additionally, strong gradients in organic matter concentrations between coastal and offshore environments provide significant lateral transport potential. Through lateral transport, nutrients and organic matter can be carried into the offshore region yet cannot be not well partitioned into NP or RP. Modeling studies have suggested that net offshore fluxes can be an important addition to regional N balances, supporting 24 – 80 % of total export in subtropical gyres (Williams and Follows, 1998; Letscher et al., 2016). However, lateral transport is difficult to constrain definitively because the spatiotemporal scales of advection are usually poorly matched to those of direct field measurements.

While numerous biogeochemical budgets have been reported for the shallow shelves of the GoM (Xue et al., 2013; Fichot et al., 2014; Fennel and Laurent, 2018; Laurent et al., 2018), fewer studies have focused on the oceanic region that covers approximately 66 % of the GoM surface area. Data presented here were collected during two field campaigns of *Bluefin Larvae in Oligotrophic Ocean Foodwebs: Investigating Nutrients to Zooplankton in the GoM* (BLOOFINZ-GoM) program targeting the central GoM spawning grounds of the endangered Atlantic Bluefin tuna (Domingues et al., 2016; Landry et al., 2019). Major constituents of the euphotic zone community were assessed for five Lagrangian process studies (Landry et al., submitted; Stukel et al., submitted; Yingling et al., submitted; Knapp et al., submitted), allowing us to compile comprehensive biogeochemical budgets. Here, we combine these *in situ* measurements with independent remote-sensing observations and a biogeochemical model to evaluate the relative roles of locally upwelled nitrate, N₂-fixation, and lateral transport in supporting N export from oligotrophic oceanic waters of the GoM.

Methods

Sampling Plan and Environmental Sampling

Data were collected during two cruises in the Northern Gulf of Mexico conducted in May 2017 and April/May 2018. Each cruise began with a bongo survey of water parcels that were identified by remote sensing as having favorable SST and vorticity (Domingues et al., 2016) for larval Atlantic Bluefin Tuna (ABT). At selected locations, a sediment trap array was deployed and a Lagrangian experiment was initiated. Over the following 3 – 4 days, the water parcel was repeatedly sampled for biogeochemical properties and incubations were conducted to measure process rates. Throughout an experiment, profiles of temperature and salinity were taken through the upper 200 m 3 – 4 times per day. Additionally, PAR profiles were conducted at least once per Lagrangian experiment around local noon. Ambient nutrient concentrations were determined from samples collected daily from 6 depths throughout the euphotic zone (same depths as incubations were conducted). The concentrations of nitrate+nitrite were measured using a chemiluminescent method, while concentrations of NH_4^+ were measured using the fluorescent OPA method. See Knapp et al. (submitted) for details.

Trichodesmium Abundance and N_2 Fixation

Trichodesmium abundance was assessed as reported in Selph et al. (Ref (Selph et al., submitted)). Briefly, 6.6 L samples from 6 depths (2 - 50 m) were collected and filtered through inline 8- μm , 47-mm filters daily. Filters were frozen in petri dishes (-80°C), stored, and thawed prior to chlorophyll extractions in 90% acetone. Fluorescence was then determined on a 10-AU (Turner Designs) fluorometer equipped with Chl filters. Additional, preserved filters (2% paraformaldehyde) were taken for microscopic analysis and enumeration of *Trichodesmium* trichomes and biovolume. Chlorophyll-specific N_2 -fixation rates were calculated based on the photo-fixation model of Breitbarth et al. (2008) based on culture work conducted at temperatures (i.e. 26°C) and photoperiods (i.e. 12 h) consistent with *in situ* conditions observed.

Productivity & Nutrient Dynamics

Rates of net primary production (NPP) and nitrate uptake were measured at 6 depths spanning the euphotic zone each day of a Lagrangian experiment. Incubation bottles (2.7 L) were filled by Niskin rosette and then with $\text{H}^{13}\text{CO}_3^-$ and/or $^{15}\text{NO}_3^-$. Bottles were then incubated in mesh bags attached to an *in situ* drift array (Landry et al., 2009a) for 24 hours—drift array was deployed and recovered pre-dawn, typically ~0500 local time. Upon recovery, incubation bottles were immediately filtered onto precombusted GF/F. Samples were kept at -80°C until analysis. In addition to *in situ* incubations, a series of deck-board experiments were conducted for 4 - 6 hours to measure vertical patterns and diel variability in nitrate and ammonium uptake (Yingling et al., submitted). Samples were analyzed at the UC Davis stable isotope facility. Nutrient uptake rates and associated uncertainty were calculated as in Stukel (2020).

Thorpe Scale Analysis

Profiles of vertical diffusivity (K_z) were calculated by Thorpe scale analysis (Gargett and Garner, 2008) of CTD-derived density profiles. Thorpe scale analysis estimates turbulent mixing parameters (i.e. vertical eddy diffusivity, K_z) based on the number and size of observed density inversions. Raw Seabird data files were processed based on the recommendations of Gargett and Garner (2008). Resulting profiles of K_z were averaged across all casts during a Lagrangian experiment using the geometric mean. Nitrate fluxes were then calculated using the observed vertical nutrient gradients and vertical diffusivity (Eq. 1).

$$F_z = -K_z \left(\frac{d[\text{NO}_3^-]}{dz} \right) \quad \text{Eq. 1}$$

Zooplankton Abundance, Biomass, and Migrant Excretion

Zooplankton were collected daily from paired day-night tows with a 1-m diameter ring net (200- μm mesh) towed obliquely through the euphotic zone (Landry et al., submitted). The tow contents were filtered through stacked Nitex screens of 5, 2, 1, 0.5 and 0.2-mm Nitex mesh to produce 5 size classes, and carbon, nitrogen, and dry mass for each size class was determined. Active nitrogen transport by daytime excretion of diel migrating mesozooplankton at mesopelagic depths were calculated from the equations of Ikeda (1985b), the biomass

differences between paired day and night tows (size-fractioned migrant carbon), the average C values of individual animals in each migrant size fraction (Landry et al., 2001) and the mean temperature in the 300-500 m depth range (10 ~ 12 °C).

Export Production

Each sediment trap deployment consisted of three cross-members with 12 Particle Interceptor Tubes (Knauer et al., 1979b) per depth. Trap depths were determined from CTD fluorescence profiles with one cross member below the mixed layer and within the euphotic zone (60 m), one at the base of the euphotic zone (110 – 130 m) and one at 230 m. The sediment trap array included a 3-m x 1-m holey sock drogue at 15 m depth (Stukel et al., 2013a). Sediment trap tubes were filled with a poisoned brine solution. After recovery, the overlying seawater siphoned off to within 3 cm of the brine interface. The samples were then filtered through 100 µm filter which was manually inspected under a stereomicroscope (25X magnification) to remove zooplankton “swimmers”. After washing the >100 µm non-swimmer fraction back in, whole tube contents were filtered onto a precombusted GF/F for C and N isotopes.

Nitrogen Isotopic Signatures of New and Export Production

Mass balance requires that the nitrogen $\delta^{15}\text{N}$ isotopic signature of export equals the isotopic signature of the source nitrogen. N_2 -fixation supplies nitrogen with a $\delta^{15}\text{N}$ of approximately -2 – 0 ‰ (Minagawa and Wada, 1986; Carpenter et al., 1997) and vertical mixing of subsurface nitrate would maintain the subsurface isotopic signature: 2.0 – 3.8 ‰ (Knapp et al., submitted). Exported nitrogen (sinking + active) was observed to have a $\delta^{15}\text{N}$ of ~ 2.9 – 5 ‰.

Remote-Sensing Estimates of Transport

Eight-day composites of surface POC concentrations estimated from the Moderate Resolution Imaging Spectroradiometer (MODIS Aqua & Terra) were retrieved from the National Aeronautical and Space Administration’s (NASA) data repository (NASA Ocean Biology Processing Group, 2017, 2018) for each May 2000-2019. We assumed that particles had Redfield stoichiometry (106:16, C:N, mol:mol). Remote sensing fields were binned to 8-km x 8-km resolution prior to analysis to reduce noise. Regional circulation was prescribed from OSCAR

(Ref (ESR, 2009)), a data-assimilative, remote-sensing data product with 1/3rd degree spatial and 5-day temporal resolution. OSCAR circulation fields were mapped onto the remote-sensing grid using bilinear spatial interpolation and linear temporal interpolation. Fluxes between each grid cell were then calculated for each remote-sensing field (n = 80). The total net flux into the control volume were divided by the area of the control volume for comparison to vertical N flux measurements. Results are shown for the control volume as defined in Figure 1a.

NEMURO-GOM Estimates of Transport

The biogeochemical model NEMURO-GoM was used to provide a consistent three-dimensional perspective on nutrient uptake dynamics in the study region. The model consists of 29 z-layers with a vertical resolution of 10 m in the upper 150 m and ~4-km horizontal resolution. NEMURO-GOM is run offline within the MIT general circulation model and forced by daily averaged flow fields obtained from a data assimilative HYbrid Coordinate Ocean Model GoM simulation. The model has been extensively validated against nutrient, biomass, and rate measurements and fully resolves a simple nitrogen cycle with 11 state variables consisting of two phytoplankton and three zooplankton functional groups(Shropshire et al., 2020). Vertical mixing in the model is parameterized based on a nonlocal K-profile parameterization (KPP) mixing scheme which is based on a bulk Richardson number approach that quantifies the importance of stratification and destabilizing shear(Large et al., 1994). Daily model output for May of 1993 – 2012 were analyzed (n = 571) with flux integrations performed for the same control volumes as used for the remote sensing estimations (Figure 1a). Mesoscale eddies were identified in daily averaged model flow fields using the algorithm of Laxenaire et al. (Ref. (Laxenaire et al., 2018)) which utilizes surface velocities along closed contours of SSH to define eddy boundaries. Lateral eddy flux was determined by calculating the net flux into the control column for all model grid cells that were identified as located within an eddy (i.e. enclosed SSH contour with the greatest velocity).

Field Observations and Dynamics

Most (62 – 79 %) net primary production (NPP) occurred in the upper euphotic zone (UEZ; 0 – 60 m) with a surface maximum of 270 – 550 $\mu\text{mol C m}^{-3} \text{ d}^{-1}$. In the lower euphotic

zone (LEZ; 60 – 130 m) including the deep chlorophyll maximum (DCM), NPP declined to $\sim 100 \mu\text{mol C m}^{-3} \text{ d}^{-1}$. Nitrate uptake rates were not strongly depth-dependent, with maximum rates typically between 20 and 60 m and vertically integrated rates of $0.44 - 1.40 \text{ mmol N m}^{-2} \text{ d}^{-1}$ in UEZ and $0.26 - 2.05 \text{ mmol N m}^{-2} \text{ d}^{-1}$ in LEZ. f -ratios were $0.04 - 0.14$ (mean: 0.07) in the UEZ and $0.03 - 0.44$ (mean: 0.14) for the LEZ. Although nitrification was not directly measured, ammonium-specific rates from other oligotrophic studies ($0.02 - 0.5 \text{ d}^{-1}$; Yool et al., 2007) and references within) imply median nitrate sources of 1 and $30 \text{ nmol N L}^{-1} \text{ d}^{-1}$, respectively. Both nitrate (defined herein as nitrate + nitrite) and ammonium were generally $<100 \text{ nM}$ throughout the euphotic zone, with nitrate concentrations between the detection limit ($\sim 10 \text{ nM}$) and 50 nM in the UEZ (Figure 3.1a). Nitrate concentrations remained depressed well below the LEZ, with $2.5 - 12 \mu\text{M}$ concentrations at 150 m indicating subduction or nutrient uptake at very low light. Ammonium averaged 60 nM^{18} with no depth trend in the euphotic zone (Figure 3.2a). UEZ chlorophyll- a was consistently below 0.2 mg m^{-3} (Figure 3.1b), and UEZ integrated nitrogen pools did not vary significantly throughout the Lagrangian experiments (Figure 3.2c-e).

Gravitational export of organic matter from the UEZ (Stukel et al., submitted) (at 60 m) ranged from $590 - 1530 \mu\text{mol N m}^{-2} \text{ d}^{-1}$ and generally decreased with depth ($460 - 1140 \mu\text{mol N m}^{-2} \text{ d}^{-1}$ at the base of the euphotic zone; $190 - 400 \mu\text{mol N m}^{-2} \text{ d}^{-1}$ at 200 m ; Figure 3.1d, 3.4a). UEZ export was 164% (range: $90 - 330 \%$) that of LEZ, indicating significant consumption of sinking particles within the LEZ. Furthermore, isotopic enrichment of sinking nitrogen with depth (range: $0.35 - 2.01 \text{ ‰}$) indicates active reworking of particles within the euphotic zone.

Active export of euphotic zone N due to ammonium excretion of migratory zooplankton at depth ranged from $20 - 172 \mu\text{mol N m}^{-2} \text{ d}^{-1}$ (mean: $71 \mu\text{mol N m}^{-2} \text{ d}^{-1}$; Figure 3.4b). This underestimates *in situ* active transport since organic excretion and zooplankton mortality at depth are not considered.

Cellular abundances of *Trichodesmium* (Selph et al., submitted), a dominant diazotroph in the GoM, ranged from $0 - 19 \text{ trichomes L}^{-1}$, which based on a photo-fixation model (Breitbarth et al., 2008), implies maximum N_2 -fixation rates of between 0 and $0.38 \text{ nmol N L}^{-1} \text{ d}^{-1}$ and vertically integrated fixation rates of $0.4 - 2.8 \mu\text{mol N m}^{-2} \text{ d}^{-1}$ and $0.4 - 2.8 \mu\text{mol N m}^{-2} \text{ d}^{-1}$ in the UEZ and LEZ (Figure 3.4d), respectively. While lower than in some other regions (Mulholland et al., 2019; Tang et al., 2019), such rates are consistent with Northern GoM

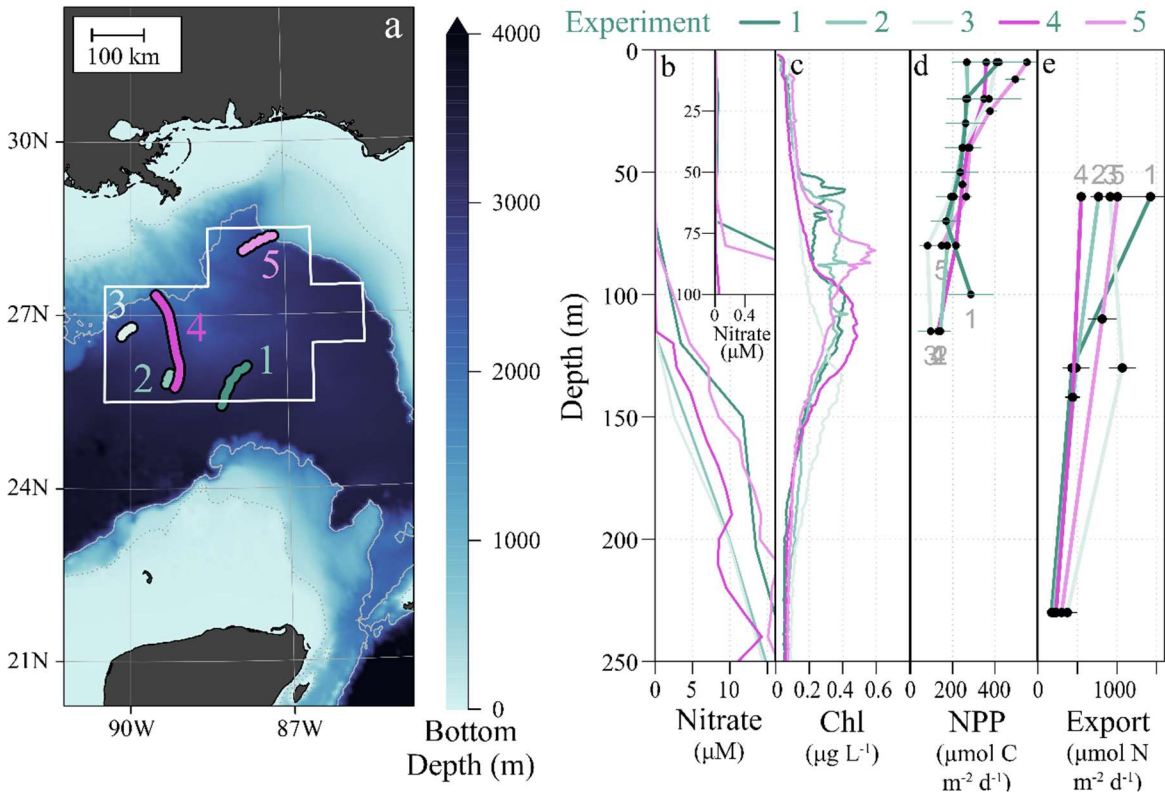


Figure 3.1. Overview of *in situ* data. Study locations in the central GoM (colored drift trajectories) with a white outline indicating the integration volume from surface to 55 m considered as representative of the eastern Central GoM (depths >2000 m, outside the general flow of the Loop Current). (a) Vertical profiles of nitrate concentrations with inset detailing low surface concentrations. (b) Vertical profiles of chlorophyll concentrations as recorded by calibrated fluorometer. (c) Vertical profiles of NPP and (d) vertical profiles of particulate nitrogen export at three depths (UEZ, LEZ, 200 m). Colors correspond to Lagrangian experiments, and error bars indicate ± 1 SD of means for measurements during experiments.

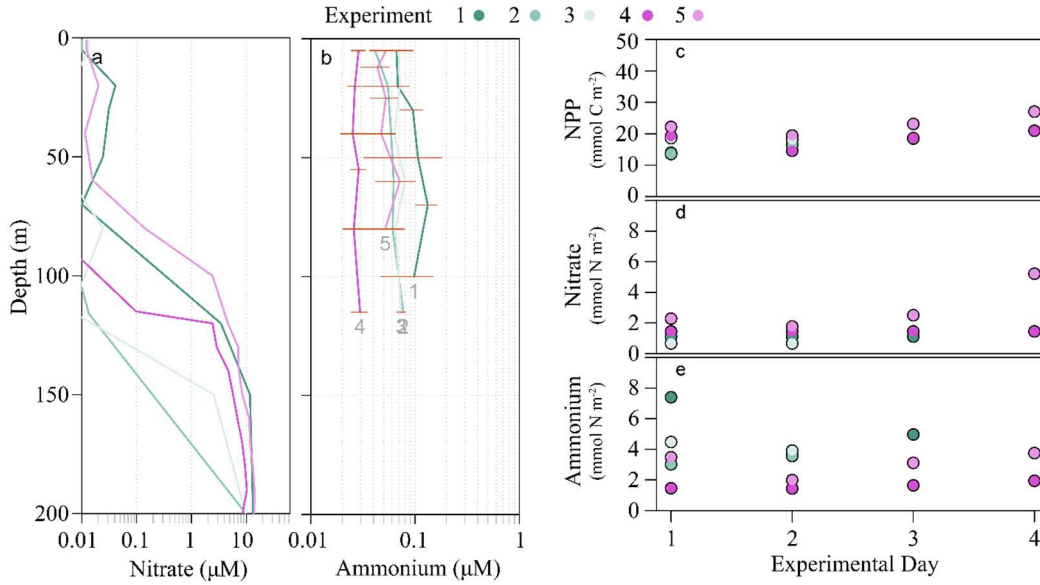


Figure 3.2. Vertical nutrient profiles and daily UEZ rates and inventories. (a-b) Nitrate and ammonium profiles averaged by Lagrangian experiment. (c-e) Timeseries of UEZ-integrated NPP and inventories of nitrate and ammonium for each day of an experiment.

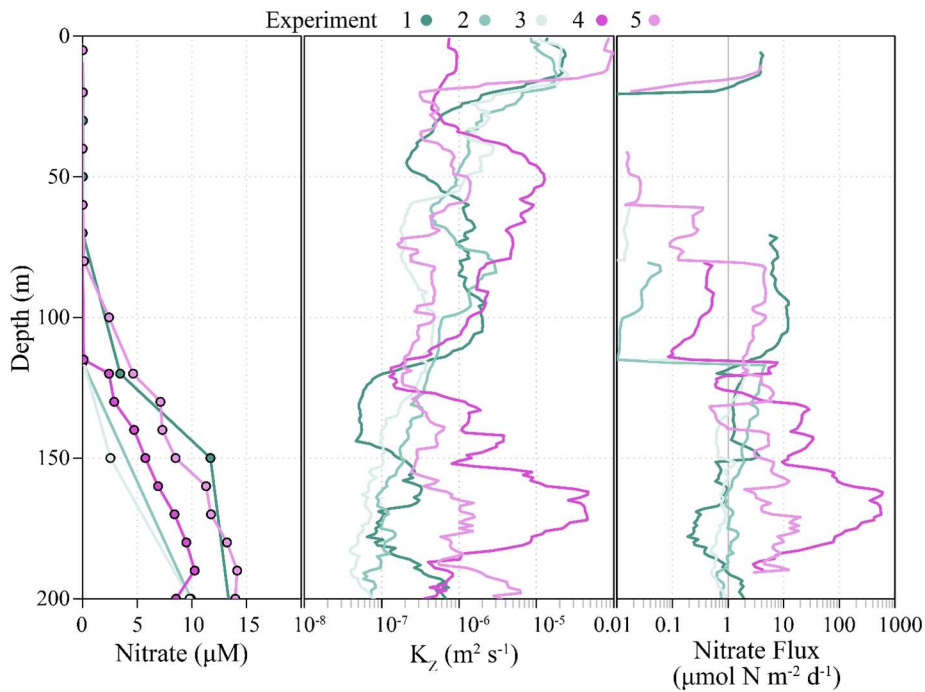


Figure 3.3. Calculation of vertical mixing of nitrate. (a) Vertical profiles of nitrate concentrations, (b) vertical eddy diffusivity, and (c) calculated nitrate flux. Values shown were averaged for each Lagrangian experiment.

findings (Knapp et al., submitted; Holl et al., 2007) and the low cell densities observed. Furthermore, the isotopic signature of sinking particulate N (i.e. $\delta^{15}\text{N}$) was nearly identical to that of subsurface nitrate (Knapp et al., submitted), leaving little room in the $\delta^{15}\text{N}$ budget for N_2 fixation (Appendix B).

Thorpe-scale analysis of vertical eddy diffusivity in the LEZ ranged from 10^{-6} to $10^{-4} \text{ m}^2 \text{ s}^{-1}$, which, combined with the small observed gradients in NO_3^- concentration, yields LEZ flux estimates of $0.01 - 1 \mu\text{mol N m}^{-2} \text{ d}^{-1}$ (Figure 3.4c; Figure 2.3). UEZ nitrate gradients were ~ 0 , constraining vertical nitrate fluxes to $\ll 0.01 \mu\text{mol N m}^{-2} \text{ d}^{-1}$ (Figure 3.3). Although vertical diffusivities can vary significantly in space and time, the stratification strength and vertical diffusivities for our field study are consistent with independent estimates from NEMURO-GOM (Figure 3.5) and with previously reported values (Haskell et al., 2015; Whitt et al., 2019).

As vertical mixing of nitrate and nitrogen fixation individually provide $<1\%$ of sinking nitrogen on average in our Lagrangian experiments, locally generated NP is clearly insufficient in balancing the measured rates of PON export. A significant role of lateral transport of organic material is suggested by the rapid horizontal displacements in our drifter experiments and the strong coastal-offshore productivity gradients in the GoM (Figure 3.5). We tested this hypothesis with independent approaches of satellite remote-sensing products and a biogeochemical model tuned to the open-ocean GoM.

Lateral Supply of Bioavailable Nitrogen

MODIS Aqua (NASA Ocean Biology Processing Group, 2017) and Terra (NASA Ocean Biology Processing Group, 2018) remote-sensing products provide spatial POM data to infer lateral gradients in the GoM. Combined with a remote-sensing circulation product, OSCAR (ESR, 2009), we calculate lateral fluxes of particulate organic nitrogen (PON) in the UEZ. Independently, results from a 3D, nitrogen-currency ecosystem model (NEMURO-GOM; Shropshire et al., 2019) are used to resolve lower trophic level dynamics in the open-ocean GoM.

The interannual median UEZ transport of PON (i.e. organisms and detritus) into the central GoM zone (Figure 3.1a, 3.7) is estimated to be $1150 \mu\text{mol N m}^{-2} \text{ d}^{-1}$ (IQR: $610 - 1530 \mu\text{mol N m}^{-2} \text{ d}^{-1}$) and $1165 \mu\text{mol N m}^{-2} \text{ d}^{-1}$ (IQR: $700 - 1725 \mu\text{mol N m}^{-2} \text{ d}^{-1}$) by remote-sensing and NEMURO-GOM, respectively. Both estimates (Figure 3.7) are larger than the median sediment trap-derived UEZ export of $980 \mu\text{mol N m}^{-2} \text{ d}^{-1}$ (range: $587 - 1526 \mu\text{mol N m}^{-2} \text{ d}^{-1}$),

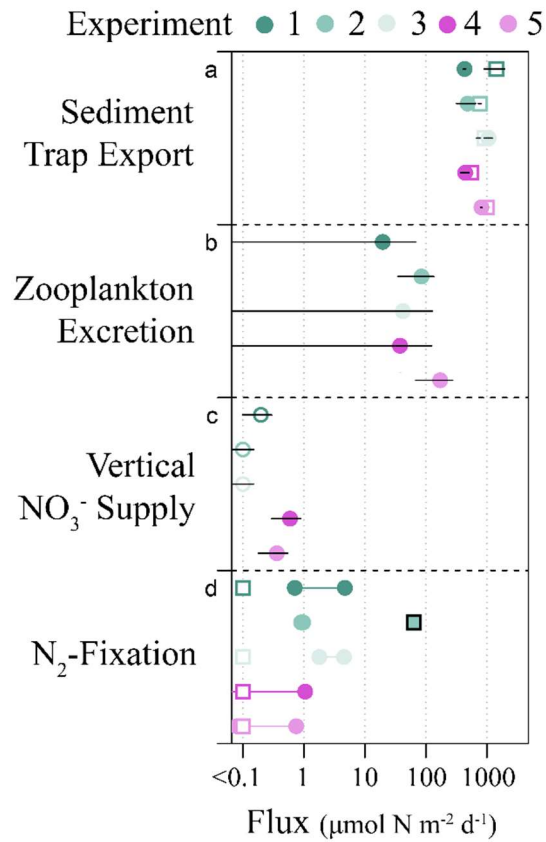


Figure 3.4. Summary of observed euphotic zone nitrogen fluxes from the oligotrophic GoM. (a) Sediment trap fluxes include export at the base of the UEZ and the LEZ (closed circles) (b) Zooplankton excretion below the euphotic zone. (c) Vertical mixing of nitrate into the LEZ. Mixing into UEZ not shown (~ 0). (d) N_2 fixation rates modeled from observed *Trichodesmium* biomass (circles) and from $\delta^{15}\text{N}$ -based budgets for the entire euphotic zone as reported in Knapp et al.¹⁸. Fluxes $< 0.1 \mu\text{mol N m}^{-2} \text{d}^{-1}$ are shown on left as open symbols.

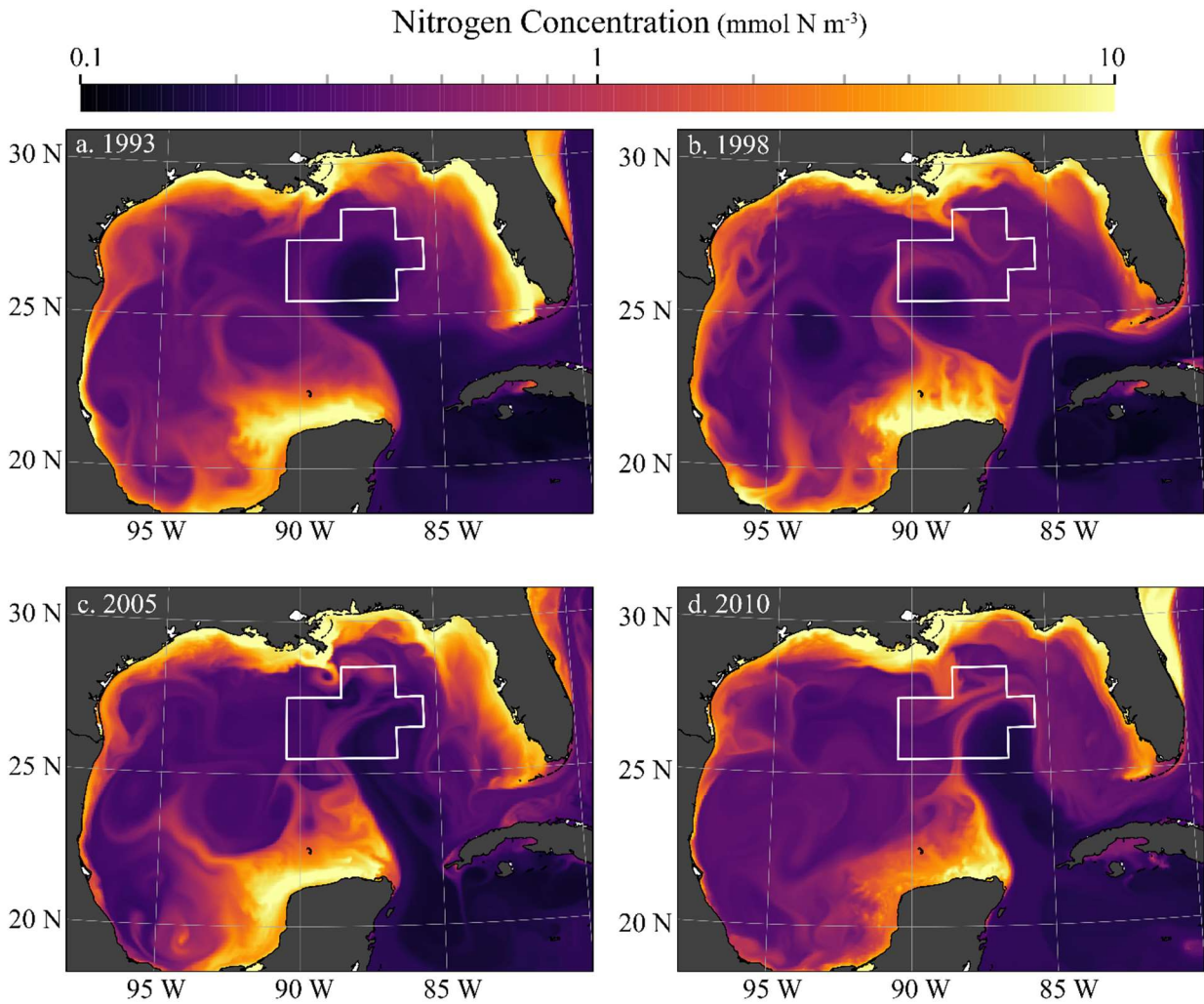


Figure 3.5. Map of GoM with UEZ nitrogen concentrations (NEMURO-GOM). Data are monthly averages for each respective year for depths 0 – 55 m depth and include all nitrogen containing state variables.

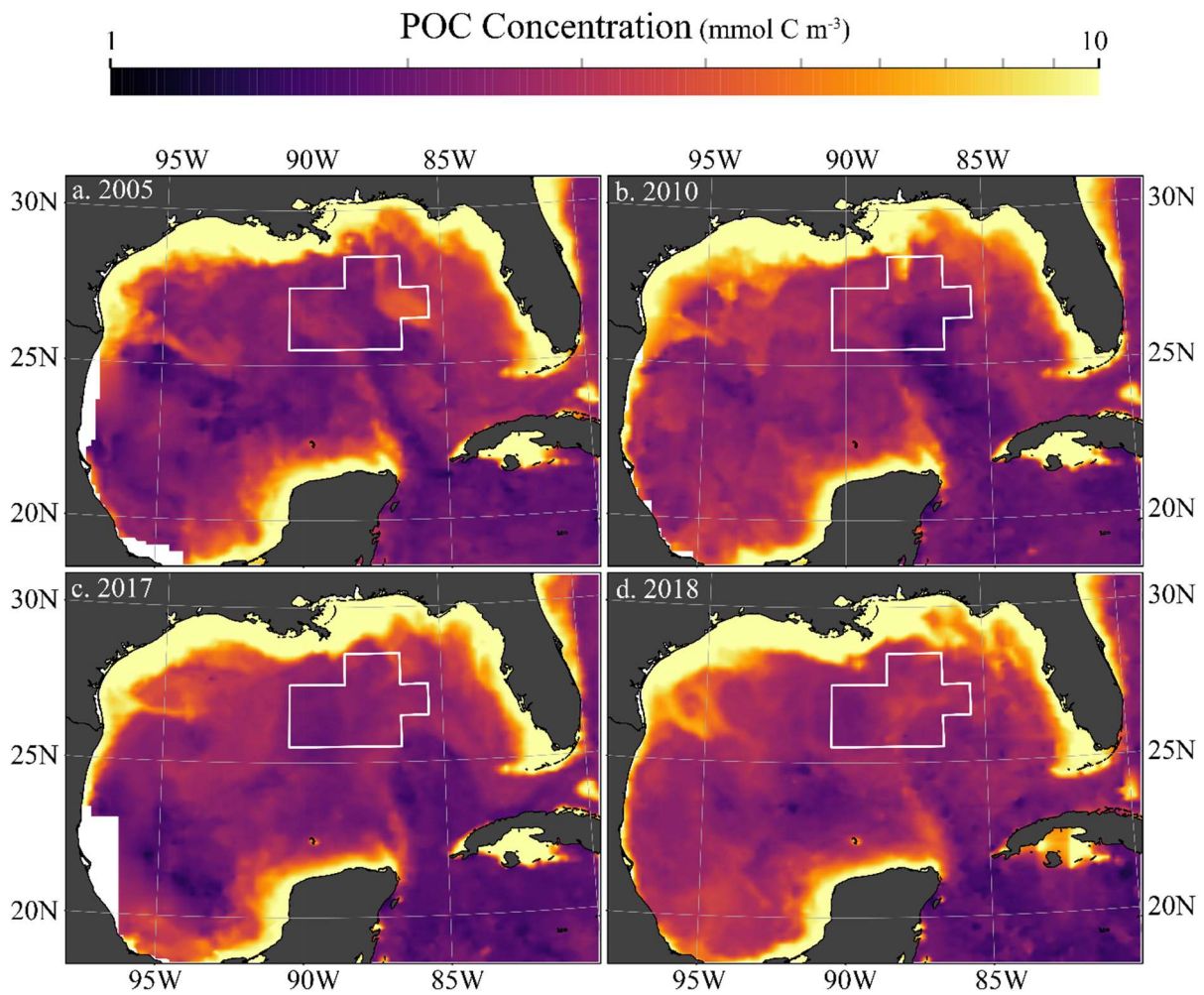


Figure 3.6. Map of GoM with surface POC inventories (MODIS). Data are 8-day composites for mid-May with 8 km lateral resolution. Years are as indicated.

and also greater than the LEZ export of $520 \mu\text{mol N m}^{-2} \text{d}^{-1}$ (range: $462 - 1144 \mu\text{mol N m}^{-2} \text{d}^{-1}$). DON contributed an additional $-8 - 46 \%$ to total UEZ lateral transport within NEMURO-GOM in any given day (Figure 3.7). Taken together, these results clearly show that net lateral transport of organic matter is of sufficient magnitude to support open-ocean export in the GoM.

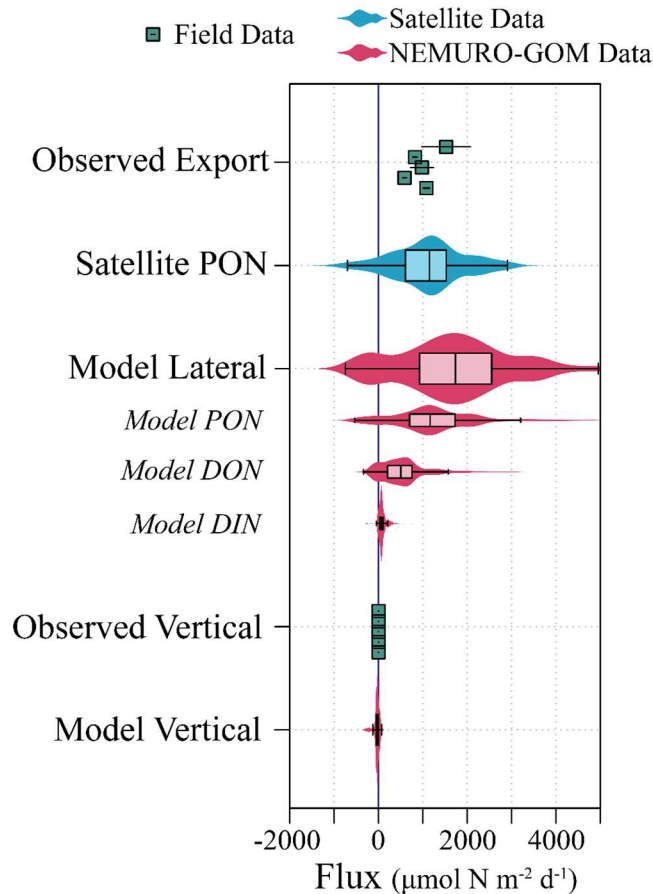


Figure 3.7. Comparison of lateral nitrogen supply to observed export production in the UEZ. Satellite lateral PON flux was calculated from 8-day composite MODIS Terra/Aqua imagery during the month of May (2002 – 2019) with flow fields prescribed by OSCAR circulation. NEMURO-GOM fluxes were calculated separately for PON, DON and DIN and summed for total lateral fluxes. NEMURO-GOM vertical fluxes are integrated for the UEZ and include upwelling and turbulent mixing but not export by sinking particles. Positive flux values indicate net input into the integration volume. Flux values are normalized to lateral area.

Circulation patterns in NEMURO-GOM suggest that the open-ocean GoM is predominately a downwelling region and thus an organic nitrogen sink. In the absence of significant vertical input of subsurface nitrate into the LEZ or recently fixed nitrate into the UEZ, particulate N export can only be supported by either lateral transport or a non-steady state

drawdown of bioavailable nitrogen. Since the latter was not observed during any of our 5 Lagrangian experiments (Figure 3.2c-e), lateral input must be responsible for ~100 % of export out of the UEZ and >90 % of export out of the LEZ (Figure 3.8). While episodic transport events such as storms have been shown to be relevant in other regions (Klein and Coste, 1984; Rumyantseva et al., 2015), the impact of such transient processes on the N balance of open-ocean GoM is less clear due to (a) the deep euphotic zone depths observed (70 - 130 m) and (b) the lack of appreciable subsurface nitrate. Such second-order processes are likely more important near the shelves where nitracline and mixed layer depths are closer. What is clear is the prevalence of mesoscale eddies formed through instabilities in the Loop Current (Oey et al., 2013) (Figures 3.5 & 3.6). Previous studies have found that through both enhanced surface velocities and long persistence such mesoscale features can transport large volumes of water onto and off of the shelf (Sahl et al., 1997; Toner, 2003; Barkan et al., 2017).

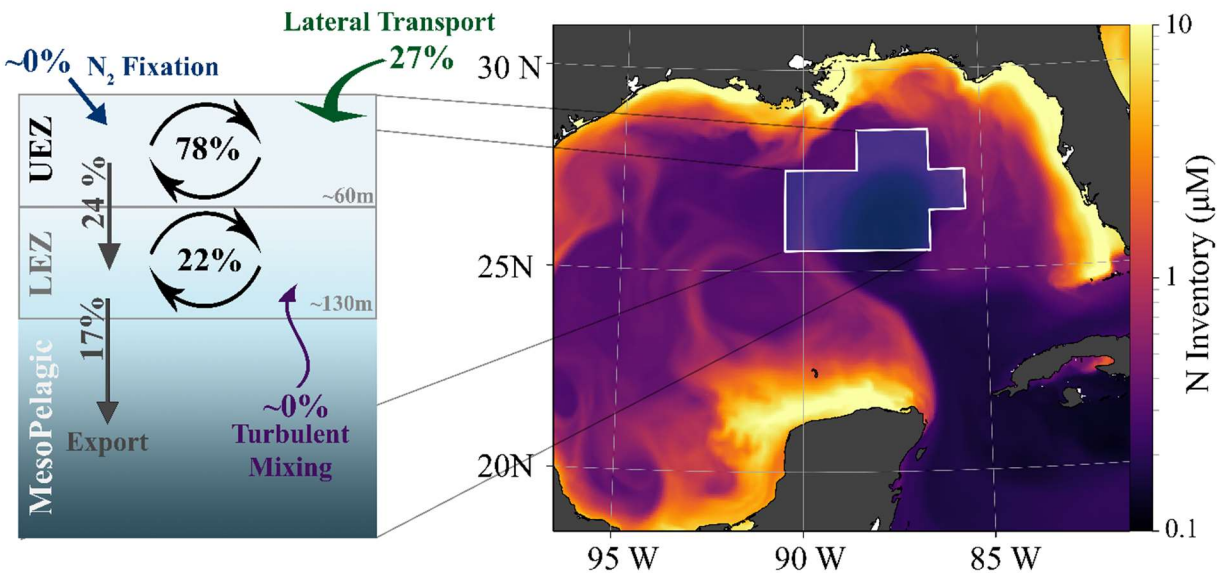


Figure 3.8. Schematic of transport mechanisms and fluxes of the NE GoM. (left) Arrows and values and fluxes observed or estimated from model relative to euphotic zone NPP. (right) A 3D depiction of the NE GoM illustrating possible sources and sinks of bioavailable nitrogen in the oligotrophic euphotic zone.

Since the oligotrophic GoM has previously been compared to the mid-ocean gyres due to similar biogeochemical properties (e.g. DCM, oligotrophic, low biomass) (Selph et al., submitted; Gomez et al., 2018; Shropshire et al., 2020), it may be reasonable to consider the applicability of our results to these oceanic regions. However, the small GoM (relative to open-

ocean gyres) has strong circulation (time scales of weeks instead of months-years), which implies greater lateral connectivity than within the mid-ocean gyres. Consequently, lateral PON fluxes are likely weaker in gyres and may be compensated, in part, by greater DON flux contributions. In this regard, upwelling-associated DON inputs have been shown to supply gyre interiors through lateral advection, entrainment, and mixing (Oschlies, 2002; Roussenov et al., 2006; Torres-Valdés et al., 2009), and based on model results may support 40 – 70 % of export production in the North Atlantic gyre (Torres-Valdés et al., 2009). Furthermore, export efficiency (i.e. export/NPP) is lower in the subtropical gyres (~5%) than measured in our study (11% - 25%) indicating a reduced lateral input requirement to support gyre export. Taken together, these analyses suggest that lateral transport of organic matter could potentially be a dominant source of external N in the oligotrophic gyres, as it is in the GoM.

Conclusions

Our results highlight the importance of inter-disciplinary and integrative process studies for constraining biogeochemical fluxes. Among still unresolved issues, it not clear whether the laterally transported organic matter was originally supported by nitrate from the shelf, from upwelling at the shelf break, from upwelling associated with mesoscale features, or from some combination of these. Furthermore, extrapolating our results to other time periods and conditions (e.g., winter) in the GoM should be done with caution and appropriate field measurements. Nevertheless, our results clearly highlight the importance of accounting for contributions of lateral transport to carbon and nitrogen budgets in oligotrophic ocean regions and the role that horizontal mesoscale currents have in supporting vulnerable open-ocean GoM ecosystems.

CHAPTER 4

SPATIAL AND INTERANNUAL VARIABILITY IN EXPORT EFFICIENCY AND THE BIOLOGICAL PUMP IN AN EASTERN BOUNDARY CURRENT UPWELLING SYSTEM WITH SUBSTANTIAL LATERAL ADVECTION

Introduction

This chapter corresponds to an original research article published in Deep-Sea Research Part II in 2018 with the following coauthors, who were invaluable to the project: Ralf Goericke, Mati Kahru, Hajoong Song, and my doctoral advisor Michael R. Stukel.

The biological carbon pump (BCP), a mechanism whereby atmospheric CO₂ is fixed into organic matter by marine phytoplankton and transported into the deep ocean, is responsible for the removal of 5 – 13 Pg C yr⁻¹ from the atmosphere (Laws et al., 2000a, 2011b; Henson et al., 2011c). Future changes in the BCP could thus cause a substantial perturbation to the global carbon cycle. Unfortunately, our ability to predict such changes is hampered by the large uncertainty in the current magnitude of the BCP and by the dearth of studies that have assessed interannual variability in particle flux out of the euphotic zone. While important contributions have been made by time series studies in the oligotrophic North Pacific and Sargasso Sea (Church et al., 2013; Lomas et al., 2013), there remains a critical need for research focusing on process-oriented quantification of interannual variability in the BCP, especially in dynamic coastal regions.

The BCP consists of several distinct processes including sinking, vertical mixing and subduction of organic matter, and active transport by vertically-migrating organisms (Ducklow et al., 2001; Steinberg and Landry, 2017b). For this study, only gravitationally mediated flux of particulate organic carbon (POC) is considered (hereafter termed “export”). Globally, both net primary production (NPP) and export are contingent on a variety of chemical, physical and biological processes (Ducklow et al., 2001; Turner, 2015) such as nutrient availability (Cermeño et al., 2008), heterotrophic bacterial abundance (del Giorgio and Duarte, 2002b), and water column stability (Sarmiento et al., 1998). Uncertainties in the global budget thus stem from complex and region-specific relationships between net primary productivity (NPP) and export production. Satellite observations provide a unique platform from which synoptic, global time

series can be calculated given the use of suitable models. However, while current export models have the ability to estimate broad spatial patterns in export, they struggle to predict intra-regional variability in export efficiency (Stukel et al., 2015b). Remote sensing models for export production typically encapsulate either specific mechanisms (e.g., aggregation of microphytoplankton, mesozooplankton grazing, or mineral ballasting; (Armstrong et al., 2002), (Siegel et al., 2014c)) or generalized empirical relationships (e.g., (Dunne et al., 2005b; Laws et al., 2011b)). In comparison, models of NPP have enjoyed success in predicting regional patterns (Kahru et al., 2009) thanks to both strong coupling between NPP and other ecosystem variables and to an extensive *in situ* dataset to which to compare the models. Improved regional models are clearly a prerequisite for reducing the uncertainty within global budgets and allowing for more accurate predictions of the marine carbon cycle under different climate change scenarios.

The California Current Ecosystem (CCE) is an eastern boundary current ecosystem with both coastal boundary and wind-stress curl upwelling, and substantial offshore advection influenced by Ekman transport. Spatial gradients in export efficiency (defined herein as the ratio of export to NPP) in the CCE (Stukel et al., 2011, 2013b) do not agree with the patterns predicted by some common export models which assume negligible horizontal advection or strong local coupling between NPP and export production (Dunne et al., 2005b). The combination of large horizontal gradients in POC, Chl-*a*, and biomass (Ohman et al., 2013; Goericke and Ohman, 2015) with strong surface currents requires consideration of spatiotemporal decoupling in water column processes (Olivieri and Chavez, 2000; Plattner, 2005). In fact, within the CCE-LTER dataset there is an inverse relationship between export efficiency as measured by sediment traps and ¹⁴CPP (Stukel et al. 2013; Morrow et al. this issue), a pattern inconsistent with general expectations that are incorporated into many remote-sensing models of export production.

In this paper, we first investigate mechanistic relationships between water column processes and carbon export measured during Lagrangian experiments conducted on a series of CCE LTER cruises. These cruises were planned to sample different sources of ecosystem variability including onshore-offshore productivity gradients, ENSO phases, and seasonal climatological patterns. We then develop an empirical model to predict export and export efficiency across these different conditions. The model is then compared to several alternative formulations each representing a specific hypothesis. The model is applied to remote sensing

measurements to calculate regional maps of export efficiency and export production and compared with previously published model results. Of particular importance are the regional patterns of export production and export anomalies from 1998 through 2016 (including the 2014-2015 warm anomaly and the 2015-16 El Niño).

Methods

Cruise Data

Data used to parameterize the model came from five cruises of the California Current Ecosystem Long Term Ecological Research (CCE LTER) program: P0605 (May 2006), P0704 (April 2007), P0810 (October 2008), P1408 (August 2014), and P1604 (April 2016). Each cruise was designed to quantify ecosystem rates within homogenous water parcels representing different regions of the CCE (Fig. 4.1). This was accomplished through a quasi-Lagrangian drifter framework over 2-5 day periods ((Landry et al., 2009b, 2012b)) involving sediment traps, an *in situ* incubation array, and repeated water column surveys. In each case selection of water parcels for drifter deployment was guided by free-fall Moving Vessel Profiler surveys (Ohman et al., 2012b). Key measurements used in this study include primary production (H^{14}CO_3 -uptake (Morrow et al.) his issue) and gravitational particle export (sediment traps and ^{238}U - ^{234}Th disequilibrium, Stukel et al. 2011; (Stukel et al., 2012b); (Stukel et al., 2013b)). The present study makes use of results from 22 Lagrangian experiments, including 63 days of drifting sediment trap deployments (8 – 22 tubes per deployment), 542 ^{234}Th : ^{238}U measurements and 602 primary production measurements. Bulk rates and associated errors for the 2-5 day Lagrangian experiments (hereafter ‘cycles’) were calculated through averaging these profiles for each experimental cycle (Table 1).

The Lagrangian framework provides contemporaneous measurements of multiple ecosystem variables over short biological timescales, thereby providing a snapshot of the ecosystem state within defined water parcels. The five cruises were designed to sample a wide range of physical and biogeochemical gradients within the CCE domain: sea surface temperature ranged from 12.2°C to 19.8°C, NPP ranged from 119 $\text{mg C m}^{-2} \text{d}^{-1}$ to 4170 $\text{mg C m}^{-2} \text{d}^{-1}$, and sediment trap export at 100 m ranged from 32 to 299 $\text{mg C m}^{-2} \text{d}^{-1}$ (for data source, see Section

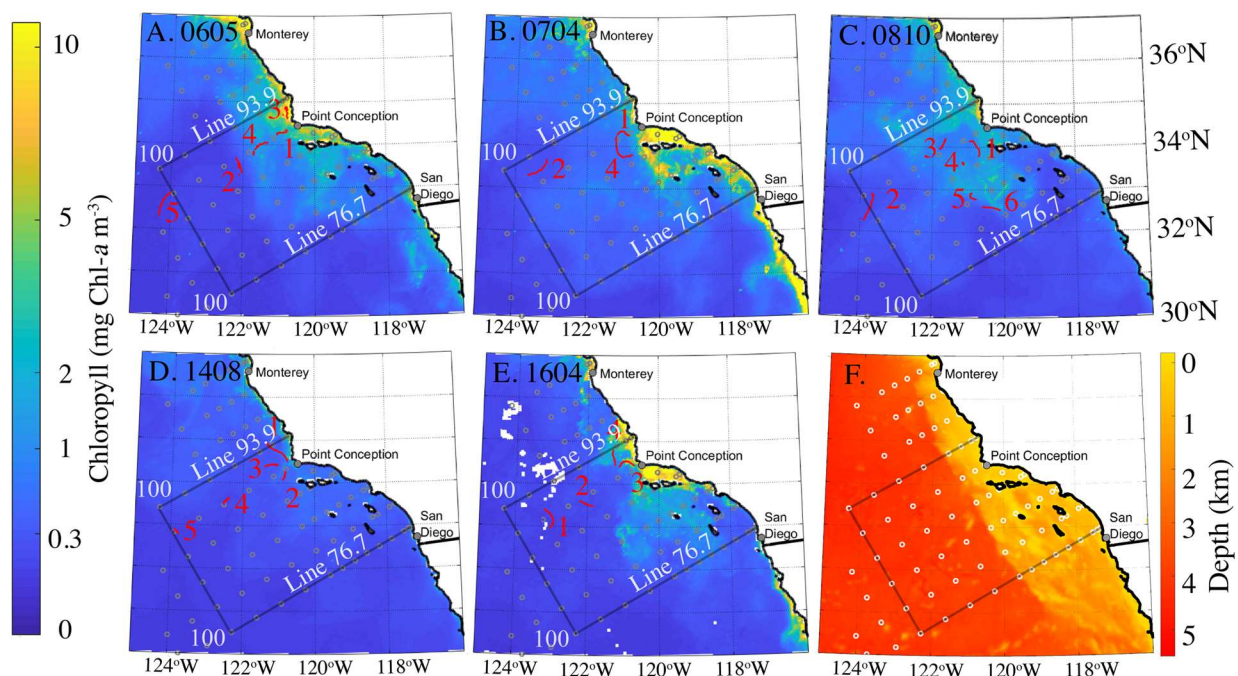


Figure 4.1. CCE LTER Domain and Drifter Tracks. Each panel is a map of CCE domain (box outline) along with the CalCOFI survey grid (gray circles in A-E; white circles in F) and drifter tracks (numbered red lines) for each cycle: A. P0605, B. P0704, C. P0810, D. P1408, E. P1604. F. Bathymetric map of the study region. SSChl-*a* concentrations are shown in the shading for A-E while depth is shown in F.

Table 4.1. Environmental conditions, water column parameters and sediment trap fluxes for each cruise cycle. NPP, Chl-*a*, POC are integrated over the euphotic zone. Export was calculated based on sediment trap derived flux and normalized to the base of the euphotic zone using a remineralization correction: $Export = SedTrap * \exp((Z_{SedTrap} - Z_{eu}) \cdot 0.0063)$. Export during P0605 cycles (*) was based on ^{234}Th : ^{238}U disequilibrium profiles and not sediment traps. Data is available from the CCE Datazoo site.

Cruise/Cycle	Distance Offshore (km)	NPP (mg C m ⁻² d ⁻¹)	Chl (mg Chl- <i>a</i> m ⁻²)	POC (mg C m ⁻²)	SST (C)	SedTrap Depth (m)	SedTrap (mg C m ⁻² d ⁻¹)	Euphotic Depth (m)	Export (mg C m ⁻² d ⁻¹)
CCE-P0605-2	109	522 (9)	27 (3)	4730 (280)	14.6	--	--	78	72 (12) *
CCE-P0605-4	14	1442 (252)	50 (10)	5400 (870)	14.8	--	--	32	133 (13) *
CCE-P0605-5	63	458 (153)	31 (8)	4880 (750)	16.4	--	--	63	76 (19) *
CCE-P0704-1	26	1215 (829)	67 (21)	5300 (1550)	12.4	100	144 (6)	42	207 (9)
CCE-P0704-2	175	573 (84)	31 (7)	5120 (340)	14.2	100	32 (3)	65	40 (4)
CCE-P0704-4	50	2295 (916)	74 (13)	6730 (960)	12.4	100	170 (20)	49	234 (28)
CCE-P0810-1	41	551 (180)	55 (41)	5140 (1900)	17	50	112 (17)	41	119 (18)
CCE-P0810-2	220	478 (31)	23 (2)	4040 (530)	16.9	100	69 (6)	58	89 (8)

Table 4.1. Continued.

Cruise/Cycle	Distance Offshore (km)	NPP (mg C m ⁻² d ⁻¹)	Chl (mg Chl- <i>a</i> m ⁻²)	POC (mg C m ⁻²)	SST (C)	SedTrap Depth (m)	SedTrap (mg C m ⁻² d ⁻¹)	Euphotic Depth (m)	Export (mg C m ⁻² d ⁻¹)
CCE-P0810-3	70	888 (79)	40 (3)	4500 (1390)	15.9	60	120 (6)	41	136 (7)
CCE-P0810-4	70	672 (85)	80 (21)	9250 (1550)	16	50	216 (2)	28	248 (3)
CCE-P0810-5	127	1670 (307)	66 (9)	5600 (420)	15.0	60	127 (14)	29	155 (17)
CCE-P0810-6	177	316 (41)	21 (3)	3020 (290)	17.2	60	112 (12)	58	114 (13)
CCE-P1408-1	24	386 (106)	117 (33)	9700 (2050)	16.8	60	159 (3)	30	192 (4)
CCE-P1408-2	42	320 (9)	56 (10)	7670 (1480)	16.8	60	124 (7)	35	145 (8)
CCE-P1408-3	52	280 (10)	31 (3)	5160 (350)	18.6	60	111 (7)	44	123 (7)
CCE-P1408-4	200	119 (10)	20 (2)	3520 (350)	19.1	70	51 (2)	56	56 (2)
CCE-P1408-5	355	132 (5)	18 (1)	3620 (390)	19.8	100	42 (1)	75	50 (1)
CCE-P1604-1	278	220 (55)	31 (2)	5010 (710)	17.5	100	72 (4)	73.5	85 (4)
CCE-P1604-2	174	261 (63)	27 (1)	4140 (110)	15.3	97	40 (2)	86	43 (2)
CCE-P1604-3	55	865 (228)	52 (8)	6730 (2030)	13.4	57	120 (5)	43	131 (5)
CCE-P1604-4	18	1658 (339)	116 (19)	13750 (4400)	14.4	47	251 (4)	16	305 (5)

4). The cycle locations spanned the dominant ecological gradient in the region from coastal upwelling to offshore oligotrophic (Fig. 4.1). While the P0605, P0704, and P0810 cruises all occurred during El Niño neutral conditions (hereafter “cool” years), the P1408 and P1604 cruises occurred during anomalously warm SST periods coinciding with an anomalous warming pattern in the northeast Pacific during 2014-2015 and the 2015-16 El Niño, respectively (Bond et al., 2015; Di Lorenzo and Mantua, 2016; Jacox et al., 2016). Within this study, the CCE domain is defined by the standard CCE control volume: the bounding box formed by CalCOFI line 76.7 out to Station 76.7-100 and line 93.9 out to Station 93.9-100 (Fig. 4.1). This volume is a practical boundary for spatial integrations.

Primary productivity during each cycle was measured through *in situ* H¹⁴CO₃ incubations conducted at 6-8 depths spanning the euphotic zone. Water samples were transferred from a Niskin bottle into polycarbonate incubation bottles using silicon tubing. Incubations were conducted in either 4L polycarbonate bottles (P0605, P0704, P0810) or triplicate 250 mL bottles (P1408 and P1604). Dark bottle incubations were conducted to correct for non-photosynthetic bicarbonate utilization and/or adsorption onto particles. All samples were incubated on our

Lagrangian array at the depth from which they were sampled. After approximately 24 hours, incubations were retrieved and filtered onto GF/F filters, placed in liquid scintillation cocktail, and counted for ^{14}C activity. Vertically-integrated primary production was determined by trapezoidal integration.

We used drifting VERTEX-style sediment traps with an 8:1 aspect ratio (height:diameter) topped by a baffle constructed from smaller tubes with a similar 8:1 aspect ratio (Knauer et al., 1979c). During each experimental cycle (except on cruise P0605), cross frames consisting of 8 or 12 trap tubes were deployed at 100 m (sometimes an additional cross frame was deployed at 50-60 m depending on the maximum extent of the euphotic zone estimated at sea by CTD fluorescence). All trap deployments were deeper than the mixed layer depth. Tubes were filled with a hypersaline, poisoned brine solution (0.4% formaldehyde final concentration). Upon recovery, the overlying seawater was gently siphoned before the samples were split for analysis using a Folsom splitter: C and N were measured with a CHN analyzer or isotope ratio mass spectrometer, C: ^{234}Th ratios were determined as described below, and pigments (Chl-*a* and pheopigments) were measured by the acidification method. See Stukel et al. (2013) and Morrow et al. (this issue) for more details.

Measured export was normalized to the base of the euphotic zone by assuming exponential decrease in export flux with depth: $f_{exp} = f_{sedtrap} \cdot \exp(\gamma \Delta d)$ where γ is the remineralization length coefficient (averaging 0.0063 m^{-1} in the shallow CCE; (Stukel et al., 2015b) and Δd is the separation between the base of the euphotic zone (defined as the 1% light level averaged over multiple CTD casts for each cycle) and the sediment trap depth (typically either 50m, 60m or 100m). This led to a maximum change of 44% in measured export (Cycle P0704-1) and an average change of 15% across entire dataset. P0605 data (based only on ^{234}Th since sediment traps were not utilized; see below) was not corrected in this manner. Instead ^{234}Th : ^{238}U disequilibrium was integrated over the euphotic depth.

During all cruises, ^{234}Th : ^{238}U disequilibrium measurements were taken using the standard small volume method (Benitez-Nelson et al., 2001b; Pike et al., 2005a). Vertical ^{234}Th profiles were then used in a steady-state export model (Savoie et al., 2006b) with C: ^{234}Th ratios determined from $>50\text{-}\mu\text{m}$ particles collected by *in situ* pumping (McLane Industries) at 100 m for P0605 and from particles collected in the sediment trap on subsequent cruises.

Remote Sensing Products

Merged satellite data products for SST, Chl-*a*, NPP, and POC have been developed for the CCE-LTER domain (<http://www.wimsoft.com/CC4km.htm>). The Chl-*a* product is empirically optimized for this region (Kahru et al., 2012, 2015) and merged from multiple sensors (OCTS 1996-1997, SeaWiFS 1997-2010, MERIS 2002-2012, MODIS-Aqua 2002-present, and VIIRS 2012-present) with a spatial resolution of 4 km. NPP is based on the derived Chl-*a* and multi-sensor merged PAR data using a modified VGPM model (Kahru et al., 2009). Monthly composited average fields were used throughout to reduce gaps due to cloud cover. Regional maps of the diffuse attenuation coefficient ($K_{D,490}$) were retrieved from the NASA ocean color website (<https://oceancolor.gsfc.nasa.gov/>) with the same spatial and temporal scales.

Model Framework & Hydrodynamic Model

The goal of this paper is to develop a model that can be used to predict interannual variability in export flux in the CCE. It is crucial that such a model be capable of capturing intra-regional variability in export. We make the assumption that functional relationships between ecosystem processes and physical drivers are consistent within the region, thus we can make a “space-for-time” assumption and utilize the broad spatial variability across the region to elucidate relationships between export under different productivity regimes. This assumption is supported by results showing that the functional relationships between export, primary productivity, and mesozooplankton grazing remained similar between El Niño neutral phases, the 2014-2015 North Pacific warming event and subsequent 2015-2016 El Niño, and across seasons (Morrow et al., this issue). We analyzed an empirical relationship between export and various ecological drivers which led to a parameterization tuned for the CCE region. A linear functional form was used as there was no evidence that a different form would be better suited. A type II ordinary least squares (type II OLS) regression was used when applying the model for prediction while a type II major axis (type II MA) regression was used to assess the relationships within the cruise data.

The relationship between regional advection and SST was quantified using a 1/10th degree Regional Ocean Modeling System (ROMS) simulation, which was run for a three-month

period ending with the cruise period (hereafter “3-month run”). Initial and boundary conditions for the ROMS simulation were from the CCS 31-year historical reanalysis (<http://oceanmodeling.ucsc.edu/reanalccs31/>) for the time period prior to 2010 and the near-real-time CCS estimation (<http://oceanmodeling.ucsc.edu/ccsnrt/>) for dates after 2010. Atmospheric forcings were derived from Coupled Ocean/Atmospheric Mesoscale Prediction System (COAMPS). The 3-month run model was compared to a one-month duration 4DVARs data-assimilative ROMS model which was tuned to observed cruise conditions and used the same boundary conditions as above. Since the comparison between the two simulations yielded nearly identical results, the 3-month run was used instead of the 4DVARs model for all cruises (except for P0704 where the 4DVARs model was used) in order to have sufficient run-time for analysis (see below). The ROMS simulation starts approximately 2 months before each cruise and continues until the end of the cruise.

The Larval TRANSport (LTRANS) software package is an offline, Lagrangian particle tracking model designed for integration with ROMS to allow for tracking of particle position and characteristics over time (North et al., 2006). It was used here to track neutrally-buoyant particles within the water column. Initially particles were released at the location and time of each cycle evenly throughout the euphotic zone. The model was run backward in time, thus tracking the history of each water parcel occupied on the five cruises used in this study. The age of the water mass was defined as the median time since each particle had originally entered the euphotic zone. Euphotic depth was calculated from $K_{D,490}$ as in (Tang et al., 2007) and tuned for the CCE region by comparing predicted euphotic depth (1% PAR) to *in situ* measurements: $z_{eu} = \frac{1.54}{K_{D,490}} + 35$.

For each cycle, 10,000 particles were released of which 58% (mean; range: 14—100%) left the euphotic zone during the simulation. Water parcel age was calculated as the median time between when the particles entered the euphotic zone and the cruise cycle occurred. For cycles where less than 50% of the particles exited the euphotic zone during the model run, age was estimated by assuming constant particle exchange between the euphotic zone and the deeper water column: $Age_{predicted} = Age_{obs} \left(\frac{N_{exchanged}}{N_{total}} \right)^{-1}$ where Age_{obs} is the median age of the particles that left the euphotic zone, and $N_{exchanged}$ and N_{total} are number of particles exchanged and in total (i.e. 10,000), respectively. Comparisons between the two hydrodynamic models (3-

month run and the 4DVARs run) showed that contemporaneous velocity fields were highly correlated and led to similar particle trajectories when applied to analogous LTRANS initializations.

Statistical Analysis

Confidence intervals for both types of models (type II OLS and type II MA, *see* 2.3) were calculated through a non-parametric bootstrapping procedure: 10,000 distinct datasets were computed using a random, paired sampling of new (x, y) coordinates based on a normal distribution centered on the observation with a standard deviation equal to measurement uncertainty (σ_x , σ_y). The model was then fit to each dataset resulting in a distribution of the slope and intercept at each value. Model uncertainty is defined to be the 1 SE interval from the bootstrap analysis (68% confidence window for a normal distribution) averaged over the input data set. This metric provides a single number comparison between the variance in the dependent variable over the observed range of the independent variable.

Results and Discussion

Spatial Patterns in Export Production

Observed NPP and export production were highest in the coastal upwelling region (Table 1). However, the *e*-ratio (=export/NPP) followed an inverse relationship with elevated *e*-ratios offshore and low *e*-ratios along the coast (Fig. 4.2 A,B). While most hypotheses regarding ecosystem efficiency predict high *e*-ratios in productive coastal waters (Michaels and Silver, 1988; Buesseler and Boyd, 2009b), the only nearshore water parcels with high *e*-ratios (>25%) in this study were encountered during the P1408 cruise when primary productivity was depressed throughout the CCE.

Indeed, primary productivity even in these nearshore cycles in August 2014 (P1408-1 & 3) exhibited values that were more representative of oligotrophic offshore regions (280-386 mg C m⁻² d⁻¹, Table 1) than conditions typically encountered in the coastal upwelling zone. Across the dataset, we found a strong negative correlation between *e*-ratio and NPP ($P < 0.001$; Fig. 4.3). This confirms prior results derived from independent ²³⁴Th:²³⁸U disequilibrium and sediment

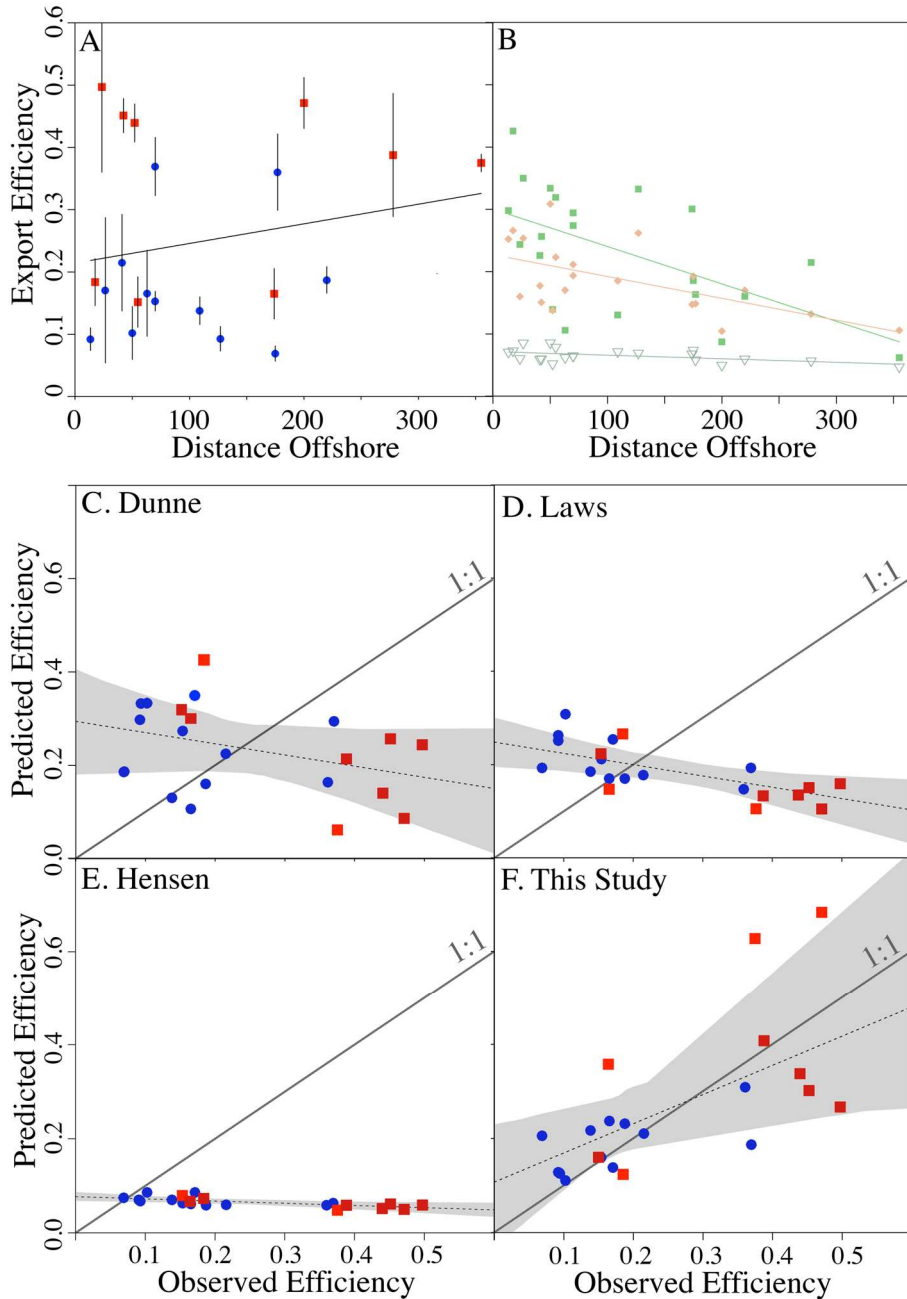


Figure 4.2. A. Plot of observed e-ratios against distance offshore. “Warm” and “Cool” years are shown as red circles and blue squares respectively. Line shows least-squares linear regression. B. Same as in (A) for predicted e-ratios. Points show the Dunne et al. (green squares), Laws et al. (orange squares) and Henson et al. (green open triangles) model predictions along with least-squares linear regressions. C. Plot of predicted e-ratio from Dunne et al. export model against observed e-ratios (same legend as A). Labeled line is 1:1 correspondence. D and E. Same as (C) for the Henson et al. and Laws et al. export models, respectively. F. Same as (C, D, E) for the model proposed in this study. Linear regressions and 95% CI are shown for each of the models (C, D, E, F; grey).

trap methodologies (Stukel et al., 2013b) and agrees with intra-regional variability found in the *e*-ratio to NPP relationship measured in the Gulf of Mexico and Southern Ocean (Maiti et al., 2013b, 2016a).

Most published global export models have utilized SST and NPP and/or sea surface Chl (SSChl) as inputs due to the relatively straightforward algorithms used to determine these variables by satellite. We compared our cruise observations to three prominent global export models and parameterized as in Stukel et al. (Stukel et al., 2015b): Dunne et al. (Dunne et al., 2005b), Laws et al. (Laws et al., 2011b), and Henson et al. (Henson et al., 2011c). Identical remote sensing fields were used throughout. While the magnitude of April-May average export flux in the CCE control volume determined by the Dunne, and by the Laws models (94, and 102 mg C m⁻² d⁻¹, respectively) was in approximate agreement with the observed export values (mean: 131 mg C m⁻² d⁻¹, range: 40 – 305 mg C m⁻² d⁻¹), both modeled *e*-ratio trends departed from observations (Fig. 4.2 C, D, E, F). Both the Laws and Dunne models predicted that the *e*-ratio would be higher in coastal regions as a result of a positive correlation of *e*-ratio with NPP. These assumed relationships between primary production and export efficiency are directly opposite to our observed relationship of an inverse correlation between NPP and *e*-ratio in the CCE (Fig. 4.3). The Henson model (which computes *e*-ratio as a function of temperature) predicted a nearly constant *e*-ratio across the CCE. It is thus clear that these models do not correctly represent intra-regional variability in the *e*-ratio and particle flux. Hence, we suggest that a CCE-specific algorithm is necessary. Here, we make the assumption that spatial variability in ecosystem processes driving export flux can be used as a proxy for temporal variability in these same processes (space-for-time assumption). Independent evidence based on the relationship between sediment trap material and mesozooplankton grazing suggest that carbon export within the CCE is invariant during different climatic regimes (Morrow et al. this issue). Therefore, a single carbon export model should be appropriate for the CCE domain across inter-annual variability.

Observed Temperature and Export Production

Our first step toward estimating export from satellite was to identify suitable predictors of export that can be detected using satellite remote sensing tools. Plausible predictors for export within the CCE include NPP, POC and Chl-*a* concentrations, SST, and distance offshore. All of

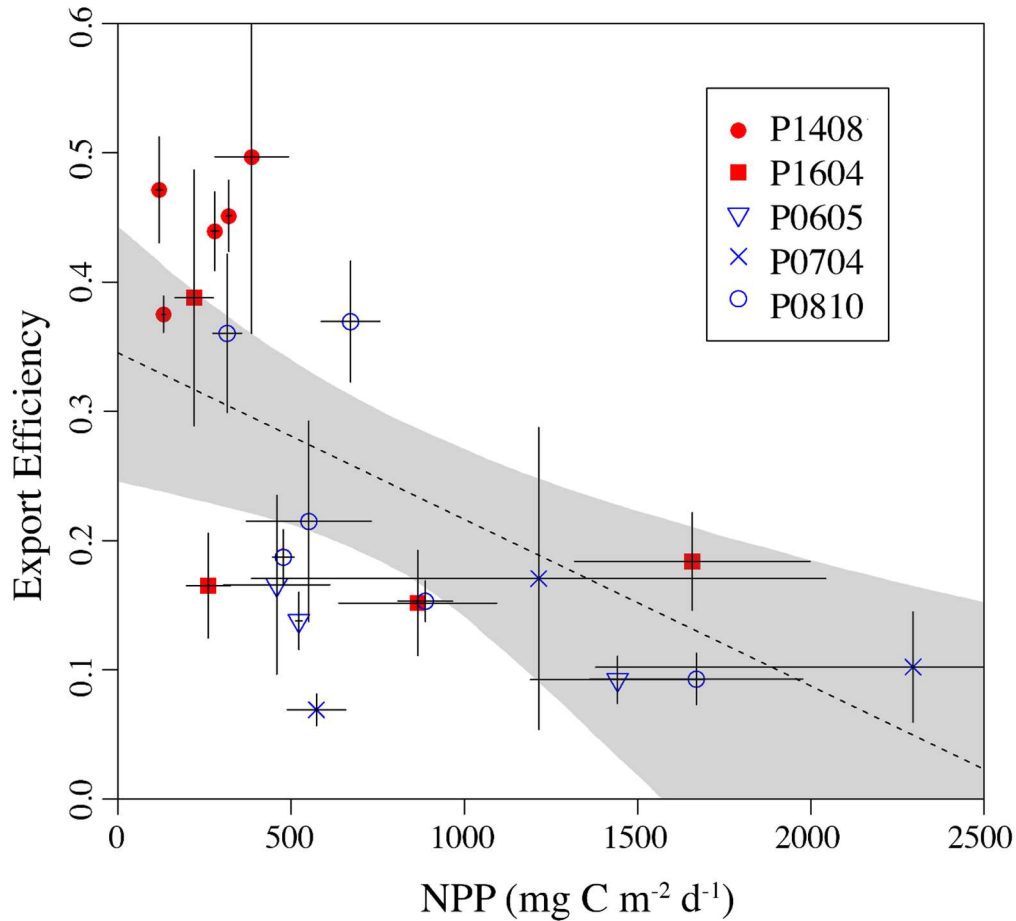


Figure 4.3. Scatterplot of export efficiency against NPP for all cruise cycles. Warm cruise years and cool cruise years are shown in red and blue, respectively; while each cruise is indicated by the indicated symbol. Error bars show 1 SE of measurement uncertainty. Black dashed line is a type II MA linear fit with the 95% confidence interval shown by shading.

these relationships were investigated and NPP and SST were identified as the two strongest predictors of export. A Type II OLS linear regression of *e*-ratio plotted against SST showed a significant positive slope ($P < 0.001$):

$$e\text{-ratio} = 0.056 \times SST - 0.698 \quad (\text{Eq. 1})$$

where the slope was 0.056 ± 0.008 (mean \pm 1 standard error) and the intercept was -0.698 ± 0.122 . The Root Mean Squared Error (RMSE) assessing the model-data misfit was 62.4 with an R^2 of 0.67 (Table 2). Model uncertainty was 29.0% (1 SE). This positive relationship between SST and *e*-ratio was initially surprising. Increased temperature speeds up heterotrophic processes, including remineralization by heterotrophic bacteria and particle consumption by

protists and metazoan zooplankton (Ikeda, 1985c; Laws et al., 2000a; Kirchman et al., 2009; Marsay et al., 2015a). Conversely, cold temperatures in this region are indicative of upwelling and the introduction of nitrate that can support new production and eventual export (Dugdale and Goering, 1967; Eppley and Peterson, 1979). We thus find it unlikely that temperature is a direct driver of increased export efficiency. Rather, we hypothesize that temperature is a proxy for other processes affecting spatial variability in export flux in the CCE, with lateral advection as the most likely process.

Regionally, the relationship between SST and export efficiency (Fig. 4.4) is robust (overlapping relationships were found in both “warm” and “cool” cruise years). As a region with coastal upwelling and Ekman transport, which entrains recently upwelled water and advects it offshore, the positive correlation between SST and *e*-ratio can be explained as a mutual correlation with water mass age. As upwelling occurs, cold, nutrient-rich waters are introduced to the euphotic zone leading to high rates of NPP and biomass accumulation. The dominant advective patterns then move the water parcel offshore while nutrients are drawn down and the water gains heat from the atmosphere. As the nutrients are depleted, phytoplankton production

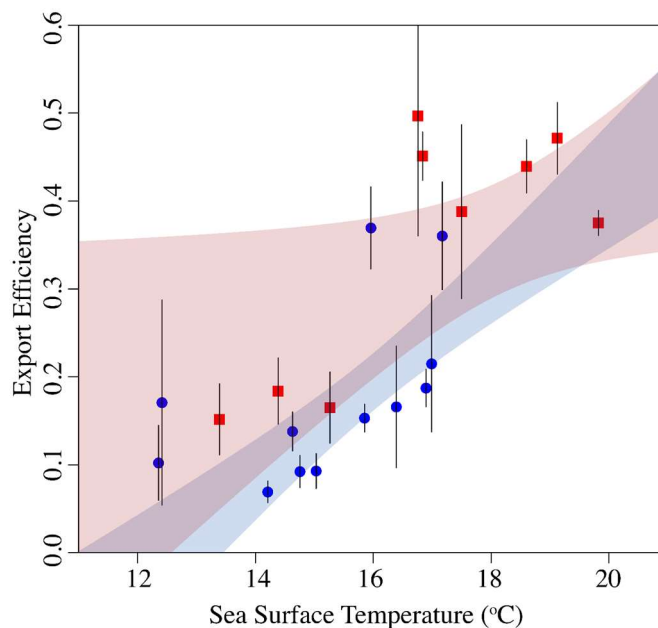


Figure 4.4. Plot of *e*-ratio (Sed Trap Flux / ¹⁴CPP) against SST (°C) for the indicated cruises. Colored bands indicated the 95% confidence intervals on the relationship for just the “warm” cruises (orange; P1604 and P1408) and for all cruises (blue).

Table 4.2. Summary and comparison of model formulations. Statistics were calculated from a type II ordinary least squares regression. Function f is the NPP model shown, function g was applied to the residuals of $f(\text{NPP})$, and f' is a function predicting e -ratio from SST.

Model	Formula	RMSE	R²	Mean Conf. (95 %)
SST	$\text{Export} = \text{NPP} * f(\text{SST})$	62.4	0.67	29.0 %
NPP	$\text{Export} = m * \text{NPP} + \text{offset}$	52.2	0.88	27.3 %
<i>Add 1</i>	$\text{Export} = f(\text{NPP}) + g(\text{SST})$	52.2	0.88	55.4 %
<i>Add 2</i>	$\text{Export} = f(\text{NPP}) + g(\text{Chl-}a)$	38.2	0.93	58.4 %
<i>Add 3</i>	$\text{Export} = f(\text{NPP}) + g(\text{distance})$	47.6	0.90	71.6 %
<i>Add 4</i>	$\text{Export} = f(\text{NPP}) + g(\text{POC})$	35.9	0.94	54.6 %

declines but export production may remain higher than predicted (based on this reduced NPP) as a result of the time lag between particle production and particle export. When combined with offshore Ekman transport, this temporal lag drives a spatial decoupling of export and new production that has been predicted from model results (Olivieri and Chavez, 2000; Plattner, 2005) and observed in field data (Stukel et al., 2011) in the CCE.

We suggest that the relationship between e -ratio and SST is not mechanistic, but instead provides a proxy for the temporal-spatial decoupling between production and export. Due to horizontal advection, coastally produced POC is rapidly transported offshore leading to depressed e -ratios close to shore and elevated e -ratios offshore. Therefore, since temporal lags drive the relationship, we can think of the controlling factor to be the age of water (defined herein as the time since the water parcel was upwelled into the euphotic zone). Upwelled water is approximately a consistent temperature and, importantly, nearly always colder than the ambient atmospheric temperature in the region, leading to positive heat flux into the water (particularly during the spring, summer and fall periods that we sampled). Due to the high heat capacity of the water, mixed-layer and euphotic zone water parcels in the CCE likely reach equilibrium temperature only after a period of weeks to months.

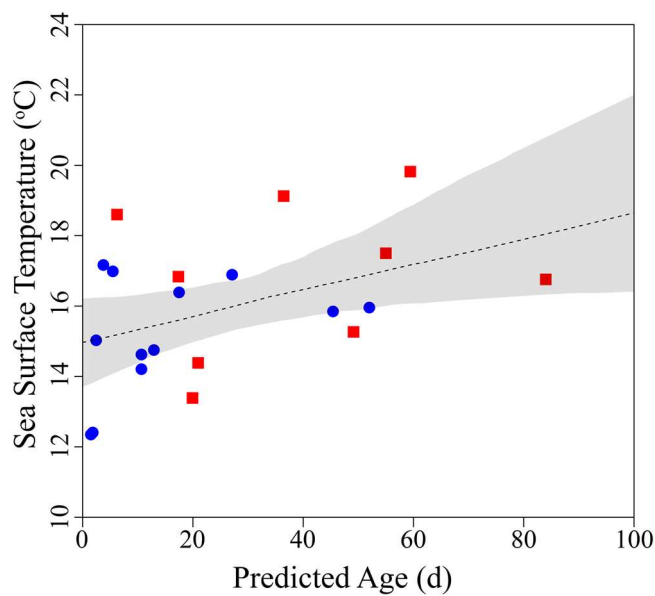


Figure 4.5. Scatterplot showing age of water parcel based on LTRANS-ROMS model results against the measured SST for each cycle of P1604, P1408, P0810 and P0605 (Table 1). Dashed line is type II MA linear regression with 95% confidence interval determined from a bootstrapped jackknife procedure (sample with replacement; shaded region).

To assess the temperature-age relationship, we used results from a physical circulation model (ROMS) to force a particle advection model (LTRANS) that was run backward in time to determine the median length of time since each water parcel that we studied at sea entered the euphotic zone. The results of the LTRANS-ROMS simulation show the fraction of the water that was upwelled versus time for the length of the simulation (see Supp. Table 1). While the distribution of particle ages was quite variable and often multimodal (e.g. distinct events), calculating the age of the water parcel based on the median allows for a robust estimate without relying *a priori* on a particular age distribution. Comparing the LTRANS-calculated age versus SST, we find a significant ($p < 0.01$) positive relationship verifying that SST and age since upwelling covary within the CCE (Fig. 4.5). This supports our supposition that the SST-*e*-ratio relationship is not causal, but instead is a byproduct of the advective nature of the system. The large degree of variance within this dataset may be suggesting that either the SST *e*-ratio relationship is more complicated than this analysis allows for or that the LTRANS simulation fits are over-simplifying an otherwise complex time series of mixing and diffusion. We recommend against using SST as a predictor of interannual variability in export flux in the CCE, because interannual variability in surface temperature can alter the SST-age relationship.

Specifically, we should expect that during warm phases of ENSO or the Pacific Decadal Oscillation or during potentially unrelated warming events, such as the 2014 warm anomaly, surface temperatures at a given water parcel age would be warmer than if initial temperatures were cooler. An SST-based algorithm would thus inflate export estimates during periods when our mechanistic understanding of temperature-respiration relationships suggests we should expect lower export efficiency. In other words, because the SST to *e*-ratio relationship is not causal, we should not expect temporal stationarity to hold for this particular relationship. The likelihood that the age of the water parcel and offshore advection were the ultimate drivers of the SST to *e*-ratio relationship also has important implications for our expectations of NPP to *e*-ratio relationships. If slowly sinking particles are being produced nearshore and advected offshore (or if neutrally-buoyant particles are being produced nearshore and converted into sinking particles by aggregation or compaction into mesozooplankton fecal pellets as they are advected offshore) we should expect that a portion of the NPP in coastal regions serves to support export in offshore regions.

NPP and Export Production

Fundamentally, NPP sets the maximum energy within an ecosystem; therefore, it is a valuable predictor of the magnitude of many ecosystem processes. Without strong evidence to support any specific functional form for the NPP-export relationship, we selected a linear fit (Eq. 2). A type II OLS linear regression with bootstrap error suggested a statistically significant positive relationship (slope = 0.081 ± 0.021) between export and NPP with a significant ($p < 0.001$) positive intercept ($71.9 \pm 19.3 \text{ mg C m}^{-2} \text{ d}^{-1}$).

$$\text{Export} = 0.081 \times \text{NPP} + 71.9 \quad (\text{Eq. 2})$$

This NPP-model had a Root Mean Squared Error (RMSE) of 52.2 with an R^2 of 0.88. Model uncertainty is 37.2%. The non-zero intercept can be interpreted as a background level of well-mixed POC that is produced in the coastal region and sinks slowly. Such an interpretation of the data is supported by an analysis of the sediment trap collected material. When compared to autochthonous phytoplankton production and mesozooplankton grazing, export rates remain elevated leading to positive export even as NPP tends towards zero (Fig. 4.6). Furthermore, this “residual” export is expected to have no pigment content, and thus is likely derived from older, recalcitrant particles (for a detailed analysis see Morrow et al.; this issue). Since the CCE region

is strongly advective, slowly sinking particles may be transported considerable distances before they settle past the depth horizon sampled by the sediment traps. Across the water parcels that we sampled, the median value for the bulk turnover time of POC with respect to sinking (POC standing stock / export) was 56 days, highlighting the potential for extensive advective transport of particles prior to export. Stukel et al. (Stukel et al., 2017b) used sinking rates parameterized from *in situ* data and a particle transport model to estimate that in the CCE, exported POC was produced (on average) 9 to 78 km from where it eventually crossed the 100-m depth horizon.

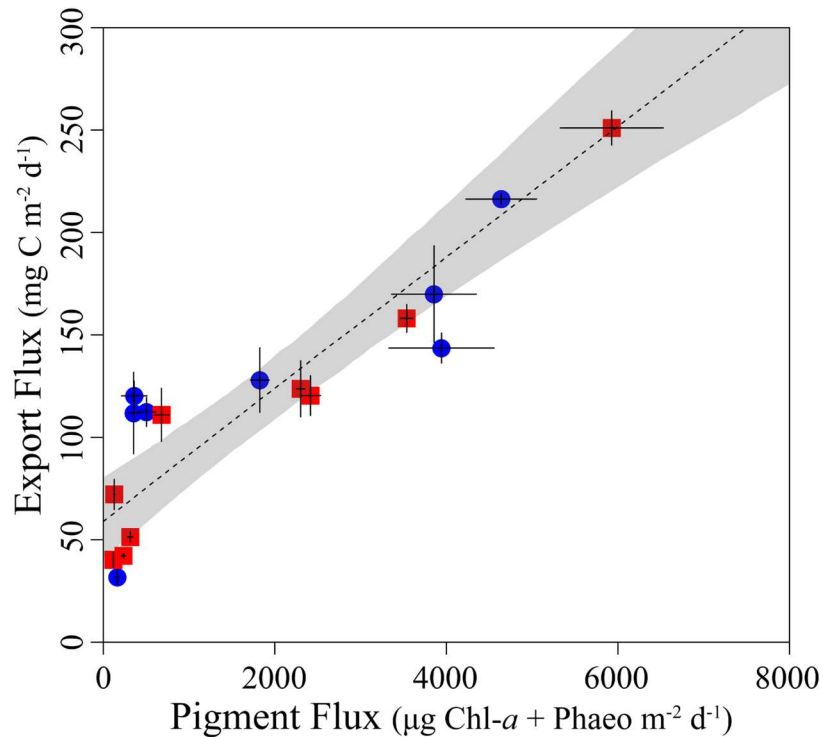


Figure 4.6. Comparison of carbon export flux and bulk pigment fluxes out of the base of the euphotic zone. Pigment flux consists of the sum of Chlorophyll-*a* and phaeopigment flux estimates. Colors and symbols are as in previous figures with red squares representing anomalously warm cruise years and blue circles for anomalously cool cruise years. Error bars show 1 standard error in the measurements. Regression is type II MA regression with 95% confidence intervals shown by shading.

While other commonly used functional relationships guarantee a zero intercept (e.g., power function), the advective nature of the CCE suggests that local export should never decrease to zero. The non-zero intercept can be interpreted as the export due to a class of slowly sinking, non-pigmented POC that becomes well-mixed within the euphotic zone due to a longer residence time compared to quicker settling particles. Importantly, this statistically robust offset

highlights the decoupling between particle production and measured export of these long-lived, slowly sinking particles.

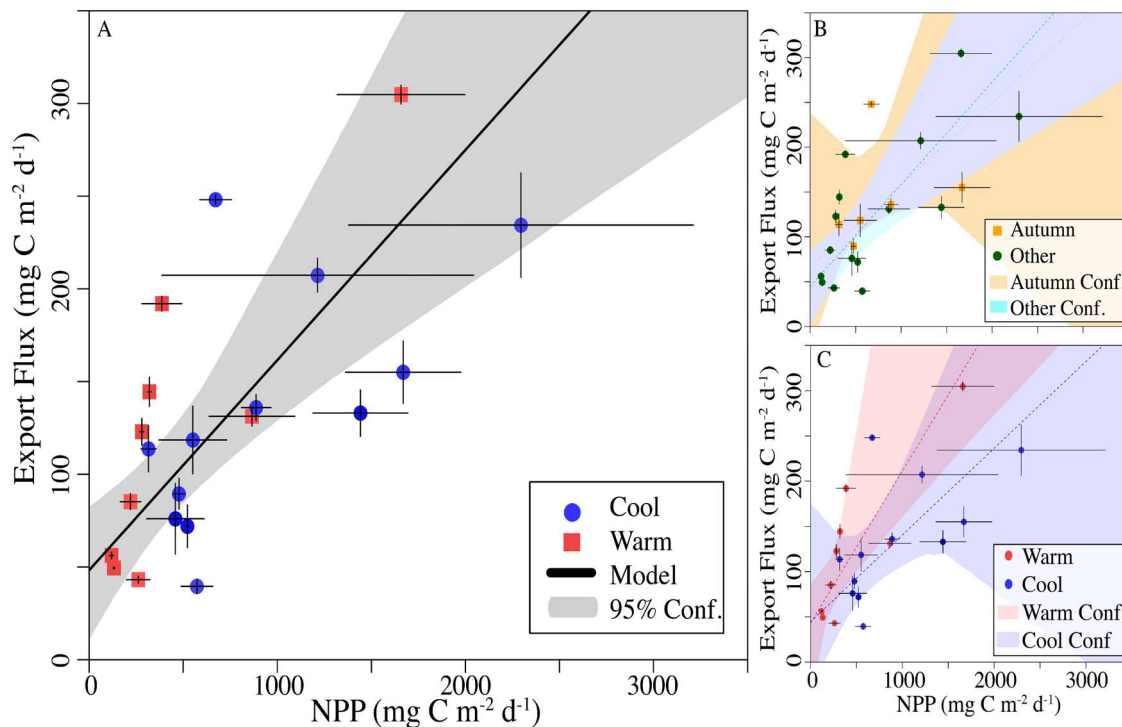


Figure 4.7. A. Export flux vs Net Primary Productivity along with type II major axis regression. Error bars indicate 1 SE of measurement. Grey band is 95% confidence interval for the regression on all data. Red squares indicate data from P1604 and P1408 (i.e. “warm” years) while blue circles indicate all other cruises (P0605, P0704, and P0810; i.e. “cold” years). B. Same as in (A) showing 95% confidence windows for regression on “autumn” (P0810) cruise and the other years only (orange squares and green circles, respectively). C. Same as (A) with 95% confidence windows for warm-year and cool-year cruises (red squares and blue circles, respectively).

To test the applicability of the model under different climatic conditions (i.e., to test the space-for-time assumption), we assessed the relationship’s sensitivity to intra-annual (seasonal), and inter-annual (ENSO cycles) variability. The relationship proved robust across these partitionings of the dataset (Supp. Fig. 2). The 95% confidence interval on the type II linear regressions overlapped significantly in each case and a positive intercept was always found (although the intercept was not always significant at the 95% confidence interval, because fewer data points were available when the data were partitioned, Fig. 4.7).

Export efficiency has been found to be contingent on a number of physical drivers and ecosystem processes including water column structure, species composition, and the composition of the POC itself. The linear relationship proposed here implies that across the domain a constant proportion of primary productivity is exported as rapidly sinking particles (i.e., the slope of the regression). This is likely a generalization of a more complex relationship that varies in space and time. Hence, the empirical model (Eq 2) was also compared against several additional formulations involving both physical and ecosystem metrics including distance offshore, SST, and concentrations of POC and Chl-*a* (Table 2).

While the NPP model (Eq. 2) explains 88% of the variance in the sediment trap flux measurements (Table 2), several extensions of the model were tested using measurements with remote sensing proxies (Supp. Fig. 2). Additional variance in the flux measurements was accounted for by regressing on the residuals of the NPP model (Supp. Fig. 2). This additional explanatory power is balanced by a corresponding increase in model uncertainty. By including SST in the NPP model, model uncertainty increased from 27.3% to 55.4% without gaining any explanatory power ($R^2 = 0.88$). This lends further support to our supposition that the strong relationship between SST and *e*-ratio was in fact caused by the offshore advection of POC, which is already accounted for by our base NPP model (Eq. 2).

The inclusion of Chl-*a* led to an increase of explanatory power (0.93) and an increase in model uncertainty (from 27.3% to 58.4%). Similarly, adding POC led to an increased R^2 value (0.94) with an increase in uncertainty (to 54.6%). This suggests that the inclusion of these parameters is potentially useful as it reflects biomass and hence is likely related to where on the temporal sequence (i.e. new production and biomass accumulation → maximum biomass → net biomass decrease and high *e*-ratio) a particular water parcel is located. POC and Chl-*a* concentrations may thus reflect, in part, the accumulated amount of refractory biomass in the system. However, the increased uncertainty suggests that the addition of these parameters is not justified for use in a predictive model. Each additional parameter increases the risk of overfitting the model and thereby reducing its utility when extended to other parts of our regional domain. We believe a 2-parameter model is most suitable when compared to the size of the dataset ($n=22$).

Interannual Variability in Satellite-Derived Export Production

Figure 4.8 shows April-May anomalies in export production calculated from satellite data using Eq. 2. Regional annually-averaged export production dropped from a climatological mean of $109.7 \text{ mg C m}^{-2} \text{ d}^{-1}$ to $100.3 \text{ mg C m}^{-2} \text{ d}^{-1}$ during the peak of the 2015-16 El Niño event in 2015, a decrease of 8.6%, with the largest anomalies taking place in the coastal zone (15.3% decrease; Table 4.3; Supp. Table 2). Similarly, in spring 1998 (during the 1997-98 El Niño), export production dropped by 7.1% regionally, with coastal zone export dropping 14.0%. These decreases in particle export were accompanied by concomitant decreases in NPP that were ultimately caused by reduced coastal upwelling (Kahru et al., 2018a). While the decreased export was seen throughout the region during the 1998 El Niño, the region north of Point Conception actually experienced above-average modeled springtime NPP and export during the 2014-2015 warm anomaly and 2015-2016 El Niños. (Fig. 4.8). Whether this increase reflected different upwelling patterns driven by substantial differences in the physical processes associated with each El Niño (Jacox et al., 2016) is beyond the scope of this manuscript.

A full time-series of reconstructed export production in the CCE from 1998 to 2017 (Fig. 4.9) shows a substantial decline in export in all seasons during the 2014-2015 warm anomalies and the 2015-2016 El Niño relative to the preceding decade, particularly in the productive coastal upwelling region that drives much of the variability in export flux in the CCE. Such a result is not surprising, given the increased stratification, decreased nutrient concentrations, and decreased phytoplankton biomass observed region-wide (McClatchie et al., 2016).

Caveats, Future Research, and Other Mechanisms of Export

The model embedded within Eq. 4.2 reflects a hypothesis about the processes driving particle flux in the CCE. Specifically, it suggests that there are two classes of sinking particles; a slowly-sinking recalcitrant particle class that reflects allochthonous particle production and is impacted by substantial horizontal advection, and a rapidly-sinking particle class that is reflective of autochthonous particle production in the water immediately above the sediment trap. Results of other studies (Stukel et al. 2013; Morrow et al. this issue) suggest that the latter particle class is primarily composed of sinking mesozooplankton fecal pellets, while the former

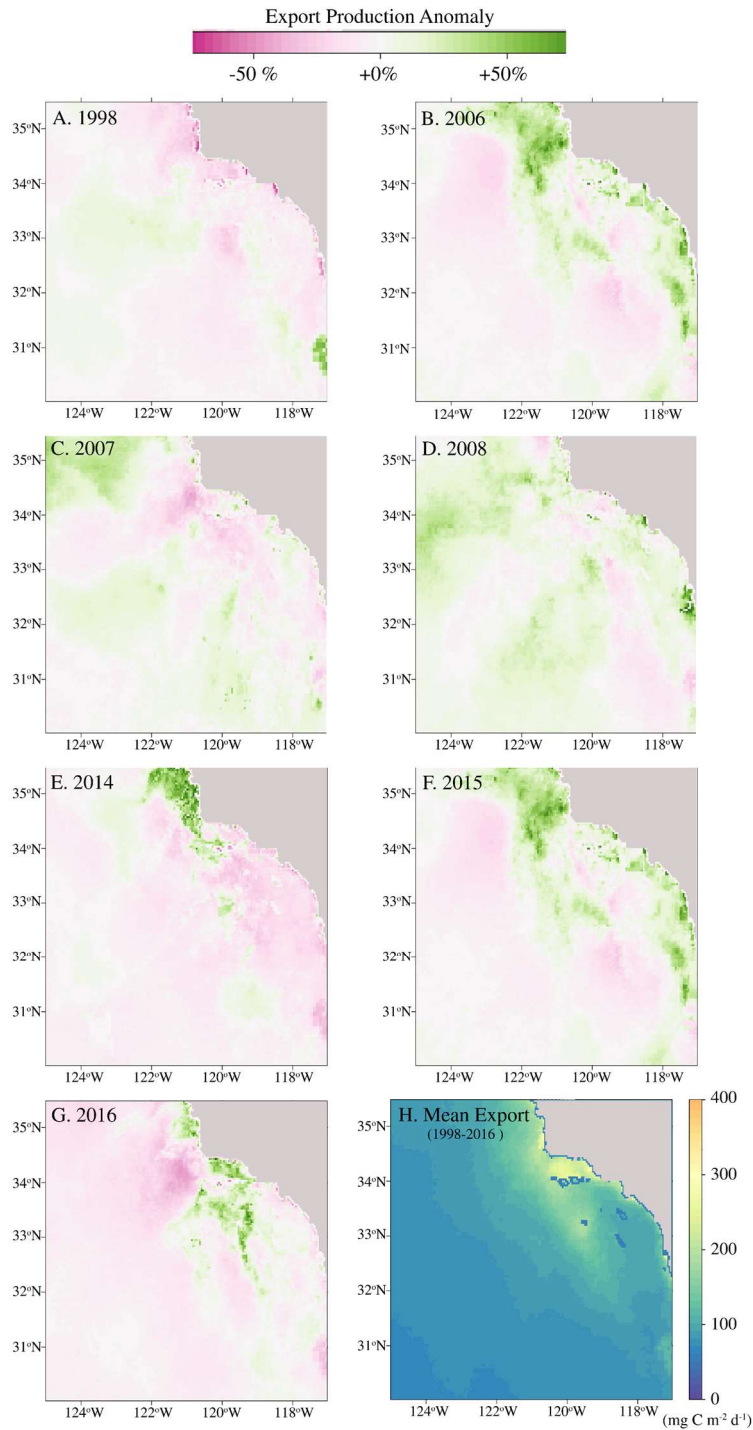


Figure 4.8. Spatial map of export production anomaly (%) for April & May of the indicated year across the CCE domain based on the NPP model. Climatological values were calculated from averaging export between 1998 and 2016. (A) 1998, (B) 2006, (C) 2007, (D) 2008, (E) 2014, (F) 2015, (G) 2016. H. Spatial map of climatological April-May carbon export production (1998-2016 mean; $\text{mg C m}^{-2} \text{d}^{-1}$).

Table 4.3. Summary of CCE regional model results for select years. Shown are the modeled export production ($\text{mg C m}^{-2} \text{d}^{-1}$) for the region (entire CCE Domain), the coastal zone (< 150km offshore) and the Offshore zone (>250 km offshore) and averaged for the indicated year. Export efficiency is shown in the parentheses.

Year	Regional	Coastal Zone	Offshore
1998	101.9 (27%)	127.6 (19%)	93.2 (35%)
1999	107.3 (25%)	130.5 (18%)	99.0 (30%)
2006	111.7 (23%)	160.6 (15%)	98.1 (30%)
2007	114.2 (22%)	146.9 (16%)	105.8 (25%)
2008	115.4 (21%)	151.4 (15%)	105.7 (25%)
2014	106.0 (25%)	133.7 (15%)	97.2 (36%)
2015	100.28 (29%)	125.6 (19%)	95.4 (33%)
2016	108.2 (24%)	152.7 (15%)	98.9 (30%)

is likely marine snow comprised of degraded POM of unknown origin. The robustness of this relationship with regards to seasonal or interannual variability in the CCE gives us some confidence in its applicability to estimate interannual variability in export flux. However, it is important to consider that the underlying hypothesis (i.e., export driven by a combination of longer-lived particles and autochthonous production) could be represented by other functional forms. For instance, perhaps the export of longer-lived particles (which are likely derived disproportionately from the high productivity regions near the coast) is not constant but decreases slightly with distance from shore. Indeed, when considered on longer spatial scales, such a scenario is almost certainly true - otherwise we would expect much higher export ratios in the oligotrophic subtropical gyre than are actually measured (Neuer et al., 2002; Church et al., 2013). Furthermore, it is possible that the production of rapidly-sinking particles is not a constant fraction of NPP, but instead shows a quadratic or power law relationship to NPP. Such a relationship might be expected given trophic shifts from protozoan grazers to mesozooplankton grazers when primary productivity is principally attributable to large phytoplankton. The ability

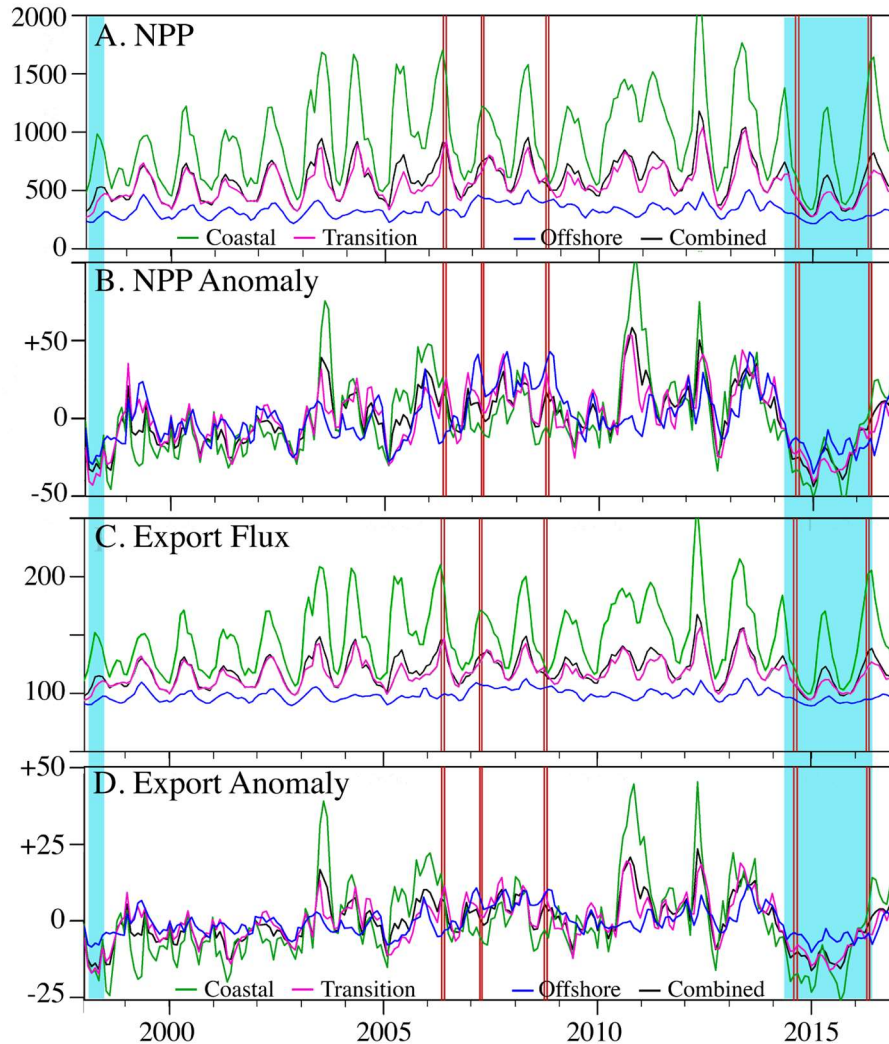


Figure 4.9. A) Time series of NPP ($\text{mg C m}^{-2} \text{d}^{-1}$) within the CCE domain (black), the coastal CCE waters (green), the transitional CCE waters (magenta) and the offshore CCE waters (blue). (B) Same as A with NPP normalized (% anomaly) to the climatological mean from 1998 to 2016. (C) Same as A with export flux as calculated from the model (Eq. 4.2). (D) Same as C with export normalized (% anomaly) to the 1997-2016 climatological mean. Vertical red lines indicate each CCE-LTER cruise, while blue shaded regions are the 1997-98 and 2015-16 El Niños.

to resolve a more complex model, however, will require substantially more simultaneous export and NPP measurements across the CCE.

Despite the above discussion, there are conceptual reasons to be confident that the true underlying relationship may not deviate too far from Eq. 2. First, while it might be assumed that increased Ekman transport during upwelling-favorable conditions would lead to increased particle transport offshore and hence a higher export of long-lived particles offshore, increased

Ekman transport is typically accompanied by increased subduction. Thus, water parcels may spend less time at the surface and the decreased age of the water parcels may offset increased advective transport. It is thus likely that the increased Ekman transport does not drive a substantial increase in the gravitational sinking flux of recalcitrant particles, but instead leads to increased rates of POC subduction (Levy et al., 2013a; Stukel et al., 2017b). Second, although it is commonly assumed that the production of labile particles should increase faster than primary production (Michaels and Silver, 1988; Laws, 2004; Siegel et al., 2014c), these models often assume steady state. In a temporally dynamic, spatially heterogeneous ocean with substantial horizontal advection, non-steady state impacts can substantially modify the NPP-export relationship. Most importantly, while we find a shift from grazing by mesozooplankton in upwelling regions to grazing by protists in oligotrophic areas, this is often accompanied by a shift in the growth:grazing balance. In coastal regions, with abundant nutrients and large diatoms, growth often exceeds grazing and the community has net biomass accumulation. In offshore regions, grazing typically exceeds growth as phytoplankton biomass declines and hence total grazing is higher than would be expected from NPP measurements. A simple trophic model used to estimate fecal pellet production from *in situ* measurements in the CCE actually estimated a higher ratio of fecal pellet production:NPP in the offshore region where protists dominated because of this growth:grazing imbalance (Stukel et al., 2011). It is thus possible that spatial variability in growth:grazing ratios offset spatial variability in protist:mesozooplankton grazing.

Another surprising result of our analyses relates to the balance between new and export production in warm versus neutral ENSO phases. Increased upwelling during cold years introduces additional nitrate into surface waters, leading to increased primary production and an increased f -ratio (new production / total production). Thus, if new production is balanced by sinking particle flux as postulated by Eppley & Peterson (1979), we would anticipate increased e -ratios during cold years, which is the opposite of the prediction derived from Eq. 2 and supported by our *in situ* measurements. However, new production and net community production (the balance of photosynthesis and ecosystem respiration, which is functionally similar to new production) are substantially higher in the CCE than export flux (Harrison et al., 1987b; Stukel et al., 2011, 2013b). While increased upwelling during cool ENSO phases should drive increased f -ratios in the region, these increased f -ratios are likely balanced not by increased export of sinking particles, but by an increase in other export processes (e.g., subduction and active transport;

(Song et al., 2012). Stukel et al. (Stukel et al., 2017a) found that subduction of suspended or slowly sinking particles was a substantial export term in the CCE, and that the aforementioned decreases in Ekman transport during warm years likely leads to decreased subduction throughout the region. Furthermore, mesoscale features (fronts and eddies) have been linked to substantial increases in subduction rates in the CCE (Stukel et al., 2017a) and the frequency of sea-surface fronts was substantially lower during the 2014-2016 marine heat wave (Kahru et al. this issue). Active transport in the CCE is primarily driven by vertically migrating euphausiids and copepods (Stukel et al., 2013b). These crustaceans generally have lower biomass during warm ENSO phases and the 2014-2016 marine heat wave (Lilly and Ohman; Lavaniegos and Ohman, 2007); Lilly and Ohman, this issue), suggesting decreased active transport during warm ENSO phases. Taken together, these results suggest that during El Niños, new production decreases substantially, as does active transport and passive flux of particles by subduction, while export of sinking particles shows a more moderate decline.

Our results highlight the importance of intensive, process-oriented studies and the development of region-specific algorithms for determining interannual variability in export flux. However, they also make it clear that much work remains. What is the origin, sinking speed, and remineralization rate of long-lived POM? Does mesozooplankton grazing control the production of rapidly sinking particles, or are particle formation rates and sinking speeds modulated by other processes (e.g., Fe-limitation, (Brzezinski et al., 2015)? Do these results (derived from homogeneous water parcels) apply to dynamic frontal regions where export seems to be enhanced in the CCE (Krause et al., 2015b; Stukel et al., 2017a)? Does recalcitrant POM flux explain inverse relationships between NPP and *e*-ratio measured in other regions (Maiti et al., 2013b, 2016a)? Are our results applicable to other upwelling systems, such as the Equatorial Pacific? Future progress will require spatially-resolved time-series of export flux, novel biogeochemical (McDonnell et al., 2015; Bishop et al., 2016) and ecological (Amacher et al., 2013) sampling approaches capable of assessing the mechanisms driving export flux, and new synthetic modeling approaches capable of combining such diverse observational data into predictive models of carbon flux (Jackson and Burd, 2015; Coles et al., 2017).

CHAPTER 5

DECOUPLING OF PRIMARY PRODUCTION AND EXPORT PRODUCTION: SYNTHESIZING OBSERVATIONS FROM A MESOSCALE FILAMENT

Introduction

This chapter corresponds to an original research article in preparation for submission.

Coastal filaments are mesoscale and sub-mesoscale features that commonly form in eastern boundary upwelling systems (EBUS), such as Benguela, NW Africa, California, and Peruvian margin systems (Chavez and Messié, 2009), wherein wind-driven upwelling draws cold, dense water up to the surface. This water is then transported offshore by Ekman flow and subsequently interacts with warmer surface waters leading to the formation of instabilities and the generation of filaments and eddies. While eddies are mesoscale features that can persist for months to years and travel 1000's of km (Lee and Coward, 2003; Mathis et al., 2007; Toniazzo et al., 2010; Thompson et al., 2014; Guyennon et al., 2015), filaments are stochastic features that often last weeks to months and travel offshore ~100's of km (Nagai et al., 2015). Both phenomena are important vectors for transporting coastal water offshore and may carry with them elevated levels of nutrients (Mathis et al., 2007), coastal organisms (Bucklin et al., 1989; Harrison et al., 2013) and pollution (Hjermann et al., 2007).

Previous studies have shown that mesoscale advective features can provide a significant source of nutrients to the offshore domain (Nagai et al., 2015) when compared to *in situ* vertical mixing; yet, in general, these features have been understudied by oceanographic voyages. Since marine productivity is limited by nutrient availability throughout most of the euphotic zone, the flux of nutrients within a filament may help support offshore pelagic ecosystems, and, through enhanced export of organic matter, offshore benthic communities. In addition to the transport of dissolved constituents, filaments can effectively transport coastal organisms out into the open ocean (Bucklin, 1991), which can impact species diversity and population genetics. By linking the offshore domain and coastal waters, filaments spatially decouple nutrient sources from downstream productivity and respiration. The ecological response to changing conditions drives a series of community shifts starting from coastal blooms of diatoms and ending with nutrient depleted waters dominated by cyanobacteria and picoeukaryotes. This progression is likely

modulated by environmental conditions and physical forcings (e.g. temperature, mixing) as well as by multiple intersecting ecological processes (e.g. time scale of phytoplankton growth and nutrient drawdown; community successional patterns).

The formation, propagation and decay of mesoscale features occurs nearly continuously in the region off of California's Point Conception during Spring and Fall upwelling seasons (Kelly et al., 1998; Marchesiello et al., 2003). Here the supply of upwelled nutrients supports the expansive and productive sardine and anchovy fisheries. Due to the frequent occurrence of mesoscale features in the California Current region, it provides a valuable study site for determining the impact these large-scale disturbances have on planktonic communities and the resulting impacts to biogeochemical cycles. By following the flow of a filament, we can observe biogeochemical transitions over a month-long period as recently upwelled water is advected offshore and nutrients are drawn down. Here we develop and use a Lagrangian particle model to determine the spatiotemporal decoupling between NPP and export production associated with the filament.

The model presented below includes four distinct particle processes including (1) production, (2) sinking, (3) remineralization, and (4) mesozooplankton grazing and fecal pellet production. Our goal is to develop a simple model that can mechanistically track particles with realistic sinking speeds that are consistent with *in situ* measurements while 3D advection leads to lateral decoupling of export production along the filament. We use the model to quantify the importance of the filament and lateral transport more generally in shaping observed sediment trap fluxes. Comparisons between locations within the filament and outside the filament show that particles within the filament experience much greater across-shore transports (up to 95 km on average) and lateral decoupling between particle production and export relative to those outside.

Materials & Methods

Field Data

Field data were collected through a Lagrangian sampling platform. Initially a regional survey was conducted using a towed CTD instrument (Seasoar, Chelsea Instruments) in order to identify the location and extent of the filament and provide data for developing a data-assimilating circulation model (see below). Once completed, a small scale survey was conducted

using a moving vessel profiler (MVP) to more accurately identify water parcels of interest. After that, a surface-tethered sediment trap was deployed with a 1×3-m drogue at 15 m, which was used to track the water parcel over the next 3 – 4 days within a moving reference frame. A series of 5 Lagrangian experiments (or “cycles”) were conducted, of which 4 full cycles were performed during which standing stock measurements (e.g. POC, nutrients, Chlorophyll) and biological incubations (e.g. dilution experiments; Landry et al., 2009) were conducted. In addition, an extra sediment trap experiment was conducted in order to track a water parcel of interest while the ship performed a Lagrangian experiment elsewhere in the filament. Cycle *upwelling* (hereafter “Cycle U”) was performed close to the filament’s upwelling region. Cycle *filament 1* (“F1”) was performed further offshore in the core of the filament. At the end of Cycle F1, an additional sediment trap array was deployed (Cycle *filament 2*; “F2”) for the duration of Cycle *mixing* (“M”) and retrieved just prior to the start of Cycle *filament 3* (“F3”). Cycle M was characterized by diffusive mixing between the filament and the surrounding water masses, and hence provides information about filament interactions with non-filament waters. The final cycle, Cycle F3, took place at the terminus of the filament and where the sediment trap for Cycle F2 was collected. Thus, Cycles U, F1, F2, and F3 provide near-continuous Lagrangian observations during the duration of the filament.

Net Primary Production – NPP was calculated from Chl, light, and nutrients as in (Stukel et al., 2019a) (<https://oceaninformatics.ucsd.edu/datazoo/catalogs/ccelter/datasets>). Estimates from this algorithm agreed well with independent dilution-based estimates of NPP made on the cruise (Kranz et al., 2020). In addition to direct observations, remotely sensed NPP (8-d composite, MODIS Aqua) was retrieved from the NASA Oceancolor web portal (NASA Ocean Biology Processing Group, 2017).

Particulate Organic Carbon – Samples for particulate organic carbon (POC) were collected during each day of a cycle at the same depths as NPP (i.e. spanning the euphotic zone) with two additional samples taken from below the euphotic zone. Water was immediately filtered onto precombusted 25-mm GF/F filters (Whatman) and stored at -80°C until processing on land by a CHN analyzer.

Chlorophyll – Chl concentrations were collected daily from 6 depths spanning the euphotic zone (same depths as euphotic zone POC samples) and immediately filtered onto 25-

mm GF/F filters. Samples were extracted in test tubes with 7 mL of 90% acetone for 24 hours at -20°C. Chlorophyll-a fluorescence was then measured using a calibrated 10AU (Turner Industries) fluorometer (i.e. acidification method; Strickland and Parsons, 1972). Similar to NPP, remotely sensed Chl (8-d composite, MODIS Aqua) data was also retrieved from the NASA Ocean Color web portal (NASA Ocean Biology Processing Group, 2017).

Export Production – We used drifting VERTEX-style sediment traps with an 8:1 aspect ratio (height:diameter) topped by a baffle constructed from smaller tubes with a similar 8:1 aspect ratio (Knauer et al., 1979d). During each experimental cycle, three cross frames consisting of 8 or 12 trap tubes were typically deployed at the base of the euphotic zone (~1% PAR), 100 m, and 150 m. Tubes were filled with a hypersaline, poisoned brine solution (0.4% formaldehyde final concentration). Upon recovery, the overlying seawater was gently siphoned before the samples were split for analysis using a Folsom splitter. C and N were measured with an elemental analyzer interfaced to an isotope ratio mass spectrometer (UC Davis), C:²³⁴Th ratios were determined as described below, and pigments (i.e. Chl-*a* and phaeopigments) were measured by the acidification method. See Stukel et al. (2013) and Morrow et al. (2018) for more details.

Particle Model and Hydrodynamics

To investigate spatiotemporal decoupling between particle production, chlorophyll, and export, we developed a particle production and export model (Table 5.1). The model contains 10,000 particle classes, each with a distinct sinking velocity between 0.001 m d⁻¹ and 1000 m d⁻¹. Particle creation takes place at each timestep and depth (t and z, respectively) and in direct proportion to NPP with sinking speeds determined from a power law relationship (Stukel et al., 2018e) (Eq. 1) of one parameter: β .

$$NSS(z, t, i) = NPP(z, t) \frac{s_i^\beta}{\int_{s.min}^{s.max} s^\beta ds} \quad (\text{Eq. 1})$$

Particle distributions are driven by four distinct processes within the model: (1) production, (2) remineralization, (3) mesozooplankton grazing, and (4) sinking. Remineralization of particles takes place for all particle types at a constant rate (λ , d⁻¹) while grazing (G, mg C m⁻³ d⁻¹) is parameterized by a saturating functional relationship of observed Chlorophyll (CHL, mg Chl m⁻³), a maximum grazing rate (γ), a minimum threshold for grazing (ϵ , mg Chl m⁻³), and a

half saturation constant (K , mg Chl m^{-3}) (Eq. 2). Grazing transforms particles of one sinking class, I , into particles of another class with an assumed log-normal distribution. Based on previous work, mesozooplankton fecal pellets in the CCE typically sink at roughly 60 – 300 $m d^{-1}$ (Stukel et al., 2019d). Their sinking velocities were approximated by a log-normal distribution with $\mu = 4.6$ and $\sigma = 0.5$ (median = 100 $m d^{-1}$). In addition, 70% of the grazed carbon is lost to respiration or incorporation into mesozooplankton biomass based on mesozooplankton absorption efficiencies (Steinberg and Landry, 2017c). Grazing parameters were determined empirically based on previous CCE LTER mesozooplankton gut pigment measurements (Morrow et al., 2018; Ohman, unpub.) throughout the filament. Sinking occurs continuously for all particles based on their sinking speed class.

$$G(z, t, i) = \underbrace{PC(z, t, i)/CHL(z, t)}_{POC:Chl \text{ ratio}} \cdot \underbrace{(CHL(z, t) - \epsilon) \cdot \gamma / (CHL(z, t) + K - \epsilon)}_{\text{fraction of Chl grazed per timestep}} \cdot \Delta t \quad (\text{Eq. 2})$$

Based on this formulation, the particle concentration (PC , mg C $m^{-3} d^{-1}$) and export rate (EX , mg C $m^{-2} d^{-1}$) can be calculated for any time or depth based on Eq. 3 and 4, respectively, with filter functions Eq. 5A-D.

$$PC(z', t', i) = \sum_{z \leq z'} \sum_{t \leq t'} \underbrace{(NSS(z, t, i) - G(z, t, i))}_{\text{net particle production}} \cdot \underbrace{e^{-\lambda(t'-t)}}_{\text{remineralization}} \cdot H_1 \cdot H_2 \cdot \Delta t \cdot \Delta z \quad (\text{Eq. 3})$$

$$EX(z', t', i) = \sum_{z \leq z'} \sum_{t \leq t'} \underbrace{(NSS(z, t, i) - G(z, t, i))}_{\text{net particle production}} \cdot \underbrace{e^{-\lambda(t'-t_*)}}_{\text{remineralization}} \cdot H_3 \cdot H_4 \cdot \Delta t \cdot \Delta z \quad (\text{Eq. 4})$$

$$H_1 = H((z' - z) - S_i \cdot (t' - t)) \quad (\text{Eq. 5A})$$

$$H_2 = H(S_i \cdot (t' - t) - (z' - z - \Delta z)) \quad (\text{Eq. 5B})$$

$$H_3 = H(S_i \cdot (t' - t) - (z' - z)) \quad (\text{Eq. 5C})$$

$$H_4 = H(t' - t^* - \Delta t) \quad (\text{Eq. 5D})$$

Where, z' and t' are the current time and depth of interest, Δt and Δz are the grid resolution, $t_* = (z' - z)/S$ and H is the Heaviside step function:

$$H(x) = \begin{cases} 0, & \text{for } x < 0 \\ 1, & \text{for } x \geq 0 \end{cases}$$

A 1-D version of the model was used to determine parameters by comparing *in situ* observations of POC and Export from cycles U, F1, F2, and F3 with model results. As input to the model, *in situ* NPP and Chl values were first gridded to a 1 m by 1 d spatiotemporal grid including a two week spin-up period and encompassing the entire cruise and the water column down to 200 m. Values for β and λ were objectively determined based on a grid search to minimize the sum of the squared normalized residuals ($SSNR = \sum(obs - model)^2 / \sigma_{obs}^2$). Since $G(z, t, i)$ and $PC(z, t, i)$ are codependent, the system must be solved iteratively for all preceding timesteps (i.e. $t < t'$).

Table 5.1. Description and values of model parameters. Quantities determined by grid search optimization or directly from field data are noted as such.

Parameter	Value	Description	Units
β	1.5 (grid search)	Power law sinking speed slope	unitless
S_{min} & S_{max}	0.001 & 1000	Minimum and maximum sinking speeds	$m d^{-1}$
ϵ	0.08 (field data)	Grazing threshold	$mg\ Chl\ m^{-3}$
γ	10.3 (field data)	Maximum grazing rate	$mg\ Chl\ m^{-3}$ d^{-1}
K	1.88 (field data)	Grazing half saturation constant	$mg\ Chl\ m^{-3}$

Table 5.1. Continued

Parameter	Value	Description	Units
λ	0.20 (grid search)	Detrital Remineralization Rate	d^{-1}
H1	Eq. 5A	Test that particle is above horizon	unitless
H2	Eq. 5B	Test that particle is below horizon	unitless
H3	Eq. 5C	Test that particle has sank past	unitless
H4	Eq. 5D	Test that particle has not sank past	unitless
NSS	Eq. 1	Normalized Sinking Spectrum	unitless
G	Eq. 2	Mesozooplankton Grazing	mg C m^{-3}
PC	Eq. 3	Particle Concentration	mg C m^{-3}
EX	Eq. 4	Export	mg C m^{-2} d^{-1}
Δt	1	Temporal resolution of 1D model	d
Δz	1	Spatial resolution of 1D model	m

NPP and Chl was prescribed in the 3D model using remote sensing estimates (8-d MODIS Aqua; NASA Ocean Biology Processing Group, 2017) and were assumed constant during the model run as a mean state approximation (and due to poor remote sensing coverage during this period). Particles were initialized based on the optimized parameterization for β (Eq. 1). NPP and Chl were assumed constant within the euphotic zone (z_{eu}), which was estimated as in (Kelly et al., 2018): $z_{\text{eu}} = 1.54 / K_{\text{d},490} + 35$, where $K_{\text{d},490}$ is the diffuse attenuation coefficient at 490 nm, also retrieved from MODIS Aqua 8-d composites (NASA Ocean Biology Processing Group, 2017). Hydrodynamic circulation was prescribed by a regional, data-assimilative ocean model (ROMS). ROMS circulation was optimized through an iterative data-assimilation method (4DVARs) using vertical profiles of temperature and salinity taken during the P1706 cruise.

Particles were then advected using 6-hourly, averaged velocity fields. By coupling to a hydrodynamic circulation model to determine (A) the location of particle export relative to observed particle production and (B) the location of particle formation relative to observed particle export.

Model sensitivity was evaluated for both variations in parameters (i.e. sequentially modify each parameter by a small amount and compare model-data misfit) and for sensitivity to initial conditions. All code used is freely available at <https://github.com/tbrycekelly/TAPPE/>.

Results

Field Data from Lagrangian Cycles

Euphotic zone depths (1% incident radiation; 1% I_0) were consistently shallower than 40 m and occasionally deeper than the surface mixed layer (Table 5.2). Surface nutrients decreased nearly continuously throughout the field campaign irrespective of mixed layer depth highlighting the dominant role of biological uptake in controlling nutrient concentrations. Cycle U is notable for extremely high, and increasing, chlorophyll inventories (mean: 265 mg Chl-*a* m⁻²) and productivity with a community dominated by diatoms (S.A. Kranz, pers. communication). Cycle B1 maintained high productivity even as chlorophyll inventories and net community production declined (Kranz et al., 2020). Productivity measurements were not made during Cycle F2. Cycle F3 had significant residual surface nitrate (3.0 μ M) relative to Cycle M (1.7 μ M) and very low Chlorophyll inventories and NPP, likely indicative of high grazing pressure. Cycle M was identified as a region of mixing between the filament waters ($S \sim 33.6$) and California Current waters ($S \sim 33.25$; Auad et al., 2011) and had the lowest surface nutrients (1.7 μ M) and lower NPP than Cycles U and F1 but twice those of Cycle F3 (Table 5.2). We note that the lowest vertically integrated NPP (Cycle F3: 45 mmol C m⁻² d⁻¹) was more than double the NPP of an “oligotrophic” study site (Table 5.2; 18 mmol C m⁻² d⁻¹).

The production-respiration balance of Cycles F1, F3, and M was close to net zero according to net community production (Kranz et al., 2020) suggesting a balance in growth:grazing and/or nutrient limitation. Through grow-out experiments, evidence for mild iron-limitation in the phytoplankton community were observed during Cycle F1 (Forsch et al., in

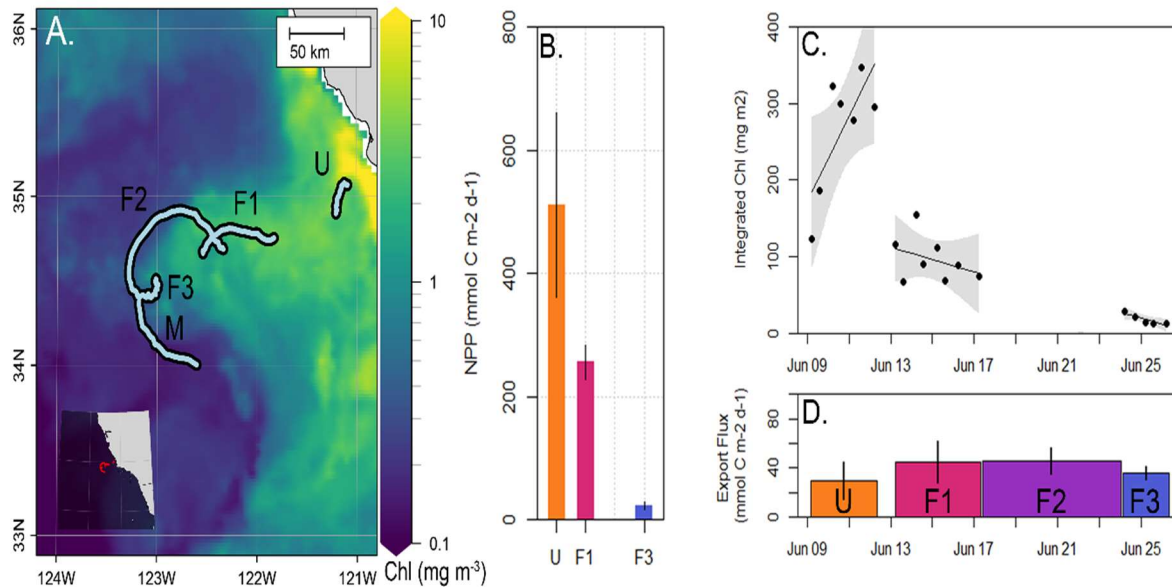


Figure 5.1. Map of study region (A) colored with MODIS AQUA SSChl (mg Chl m^{-3}) for the month of June, 2017. Overlaid are drift tracks for the 5 Lagrangian Cycles. (B) Cycle averaged rate of NPP for U, F1, and F3. (C) observed chlorophyll inventories throughout the cruise. Rate of change in chlorophyll inventories for each cycle are shown by type-I linear regression with 95% confidence intervals (shading). (D) Cycled averaged export production as measured in trap closest to euphotic zone depth. All error bars indicate 95% confidence interval.

prep), with support from measured variable fluorescence (i.e. F_v/F_m ; Kranz et al., 2020). No such evidence was found for the other cycles.

Export production at the base of the euphotic zone ranged from 29 – 47 $\text{mmol C m}^{-2} \text{d}^{-1}$, with the highest euphotic zone export during cycles F1 and M (45 and 47 $\text{mmol C m}^{-2} \text{d}^{-1}$, respectively; Table 2). To place these numbers in context, the P1706 cycles were 5 of the top 7 highest export events observed across 37 cycles of the CCE-LTER dataset (Figure 5.2). Even considering the extremely high rates of NPP observed during P1706, the lack of a significant trend between NPP and EF is evident as NPP varied by >1000 % while euphotic zone export flux varied by no more than 60% (Figure 5.2A; Table 5.2). Observed e-ratios (e-ratio = euphotic zone sediment trap export / vertically integrated NPP) ranged from 5 – 80 % with an inverse relationship to NPP (given export was relatively constant).

Transfer efficiency (i.e. the ratio of carbon flux at depth, here 150 m, normalized to carbon flux at the base of the euphotic zone) was consistently high relative to the historical CCE LTER dataset. The highest transfer efficiencies (67 % and 72 %) were observed for Cycles U

Table 5.2. Summary of experimental conditions during each cycle. All values were averaged across all profiles taken during the cycle. Gross primary production and NCP values are from Kranz et al. (2020). *Values for “typical” coastal bloom and oligotrophic cycles were from previous CCE process studies from a 2008 costal cycle and an offshore 2016 cycle (P1604-4 and P1604-2, respectively). †Range indicates 95% confidence interval. **Values estimated as the mean of Cycle F1 and Cycle F3.

	<i>Cycle U</i> <i>Upwelling</i>	<i>Cycle F1</i> <i>Mid-stage</i>	<i>Cycle F2</i> <i>Mid-stage</i>	<i>Cycle F3</i> <i>Late-stage</i>	<i>Cycle M</i> <i>Mixing</i>	<i>Typical</i> <i>Coastal</i> <i>Bloom*</i>	<i>Typical</i> <i>Oligotrophic*</i>
<i>Surface NO₃⁻ (μM)</i>	6.8	7.9	5.5**	3.0	1.7	2.0	0.1
<i>Int. Chl-a (mg m⁻²)</i>	265 ± 80	96 ± 30	n.d.	18 ± 6.8	60 ± 33	66 ± 9	27 ± 1
<i>Euphotic Zone Depth (m)</i>	13	22	29**	35	38	16	86
<i>ML Depth (m)</i>	20	27	20**	12	18	14	70
<i>ML Temperature (°C)</i>	12.8	12.8	13.7**	14.6	14.8	15.3	15.3
<i>ML gross primary production (mmol C m⁻² d⁻¹)</i>	799 ± 158	530 ± 97	n.d.	31 ± 1	96 ± 20	n.d.	n.d.
<i>Vertically Integrated NPP† (mmol C m⁻² d⁻¹)</i>	564 (234 – 1184)	242 (113 – 484)	n.d.	45 (21 – 90)	108 (50 – 218)	126 (80 – 173)	18 (9 – 27)
<i>Net Community Production (mmol C m⁻² d⁻¹; NCP_{inst})</i>	77.8	-14.2	n.d.	0.0	-10.5	16.4	6.0
<i>Gravitational Export (mmol C m⁻² d⁻¹)</i>	29 ± 7.5	45 ± 8.5	46 ± 5	36 ± 3	46.5 ± 26	21 ± 0.3	3.5 ± 0.2

and F3, respectively. Elevated transfer efficiencies are not surprising in productive CCE water parcels since fecal pellets can form a significant proportion (i.e. ~100 %) of gravitational export (Stukel et al., 2013c), yet such high transfer efficiency for cycle F3 is interesting. As previously noted, elevated grazing pressure is consistent with the high concentration of residual nitrate observed in Cycle F3. Cycle M, where filament water was mixing with offshore, low nutrient water, showed the strongest vertical export attenuation with only 14% of euphotic zone export making it to 150 m. This high flux attenuation suggests that water column structure (possibly including mesopelagic flux feeders, e.g. Stukel et al., 2019b) may be an important factor modulating transfer efficiency; although due to sharp spatial gradients present in that cycle, interpretation of the available data is challenging.

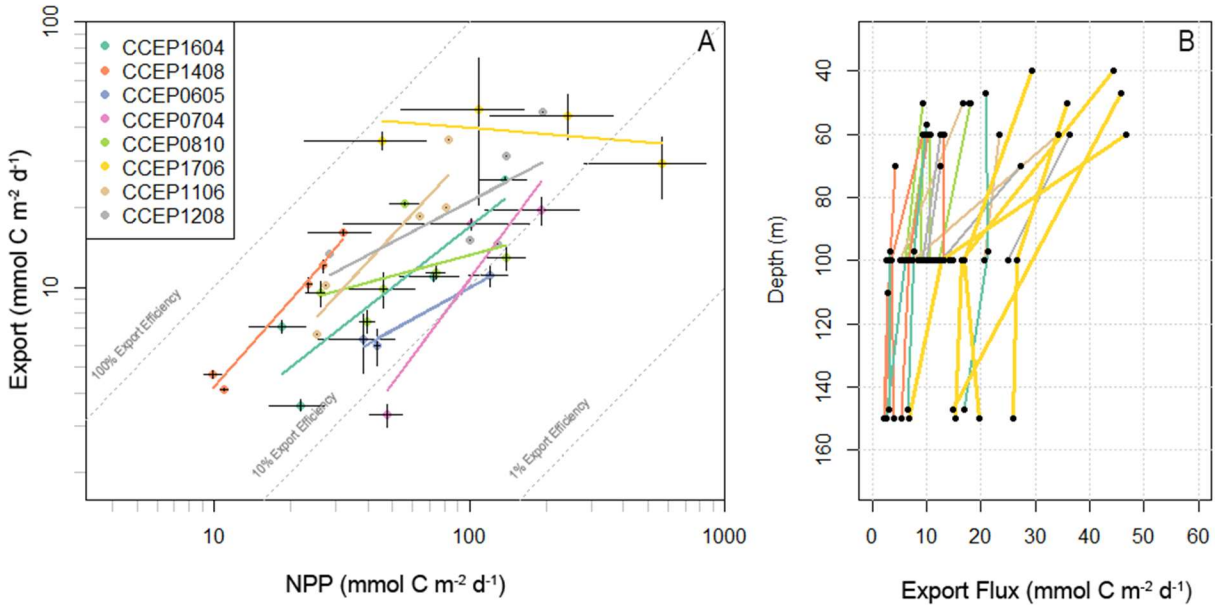


Figure 5.2. (A) Relationships between NPP and EF in the CCE region for each CCE LTER process study. A linear type-1 regression is shown separately for each cruise. Error bars shown are ± 1 standard error of an observation. **(B) Vertical profiles of gravitationally settling flux measured by PIT-style sediment trap.** Black lines correspond to the indicated cycles of CCEP1706 while all previous CCE-LTER sediment trap deployments are in grey.

Particle Production Model

Parameters for the particle production model (beta and lambda) were objectively determined from 101 POC and 11 export observations taken from Cycles U, F1 – 3: $\beta = -1.5$ and $\lambda = 0.20$ (Figure D.1). The grazing parameters (γ , ϵ , and K) were determined *a priori* based on the entire CCE LTER dataset. To spin-up the model, rates of *in situ* NPP were extrapolated to two weeks prior to the cruise. This allowed POC inventories to build up prior to data-matchups and is used as the base case in the sensitivity tests (below). Modeled export ratio (i.e. model export / vertically integrated NPP at a specific time), the model analog to e-ratio, varied from 0.45 – 1.05 at the base of the euphotic zone yielding a narrower range, and higher values, compared to field observations (i.e. 0.05 – 0.80 e-ratio), which is not surprising given the simplified model architecture. Modeled POC showed a larger concentration range compared to observations (Figure D.1) with a clear temporal pattern with overestimated POC in Cycles U and F1 and too little POC concentrations in the model for Cycles F2 and F3. This mismatch is likely driven by the fact that our model implicitly assumes that functional relationships (e.g., sinking speeds, grazing) remain constant along the filament; in reality changes in community

composition and physiological status of phytoplankton and zooplankton will impact sinking rates. While sinking particles have a range of lability and composition (e.g. Marsay et al., 2015), which is important in determining remineralization and consumption rates, modeled processes are invariant to the temporal progression of the system and do not include effects such as the accumulation of refractory POC after a bloom. While such a process can be explicitly included, constraints for such an approach are lacking (Anderson and Tang, 2010). Our simpler model approach requires less assumptions and appears to provide reasonable estimates of particle sinking speeds and spatial patterns of export efficiency.

Additionally, the 1D model parameterization consistently underestimated export for Cycle F3 and generally underestimated flux attenuation with depth. Considering the large range in observed primary production rates, it is not surprising that the model was unable to match export across the four cycles (i.e. U, F1 – 3) and instead recovered average export across all observations (Figure D.1). Without additional fecal pellet processes, such as fragmentation (Cavan et al., 2017) or flux feeder interception (Stukel et al., 2019d), mesozooplankton fecal pellets did not attenuate quickly enough relative to their sinking speed to accurately recreate the observed vertical patterns of flux. Conversely, non-fecal pellets did not sink quickly enough to significantly impact vertical patterns of export before remineralization occurred (e.g. turnover time for particles was 3.4 d for $\lambda = 0.2 \text{ d}^{-1}$). This agrees with prior observations in the CCE which suggest that in productive regions (e.g., the filament) fecal pellets dominate sinking export flux (Morrow et al., 2018). Sinking speed of export increased with depth (Figure 5.3) below the euphotic zone (i.e. zone of particle formation) from $\sim 110 \text{ m d}^{-1}$ to $\sim 128 \text{ m d}^{-1}$ at 150 m reflecting the attenuation of slowly settling particles (through remineralization) and subsequent enrichment of both faster settling detritus and fecal pellets with depth.

Three-Dimensional Particle Advection and Export

Coupling the particle production model to a 3D Lagrangian model permitted direct simulation of particle production and export dynamics within the filament. We determined the probable source locations for the material collected in the sediment traps. On average particles were advected 30 – 100 km prior to leaving the euphotic zone but typically traveled less than 10 additional km prior to reaching 150 m due to the combined effects of fast settling velocities

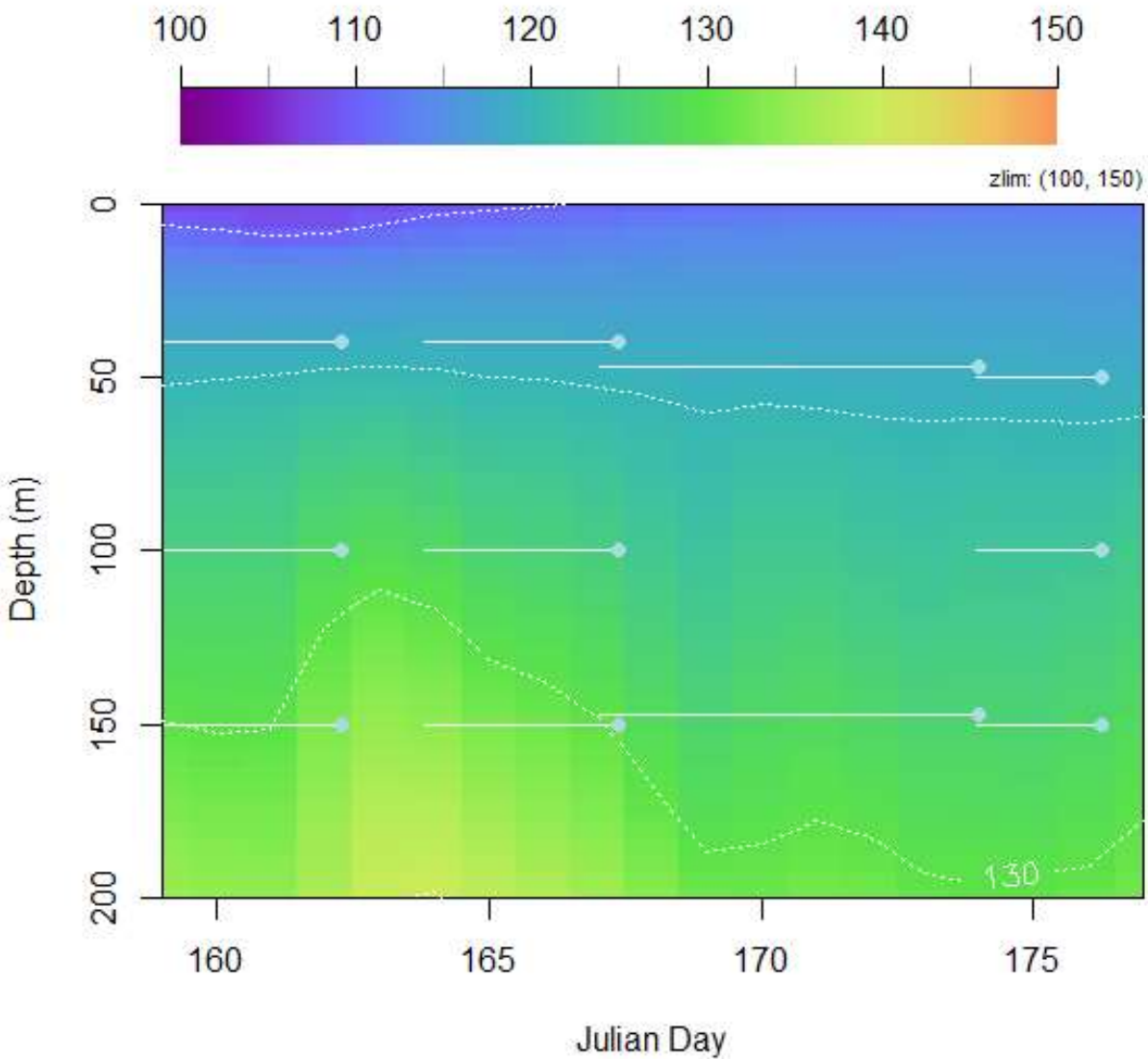


Figure 5.3. Waterfall diagram showing the mean sinking speed of exported particles in the 1D model. Solid lines indicate depth and duration for sediment trap deployments for cycles U, F1, F2, and F3. Contours show 10 m d^{-1} increments.

associated with deeper-reaching particles ($\sim 118 \text{ m d}^{-1}$ at 40 m to 128 m d^{-1} at 150 m) and slower advective velocities at depth. Indeed, median lateral speeds in the surface mixed layer were 0.25 m s^{-1} (IQR: $0.13 - 0.33 \text{ m s}^{-1}$) but decreased to 0.16 m s^{-1} (IQR: $0.10 - 0.25 \text{ m s}^{-1}$) at 150 m. Median lateral transports of euphotic zone export increased between cycles F1 ($\sim 30 \text{ km}$) and F2 ($\sim 100 \text{ km}$). Additionally, the distribution of lateral transport distances indicate that the later cycles were partially composed of particle that traveled $> 50 \text{ km}$ whereas earlier cycles were almost entirely composed of particles produced $< 50 \text{ km}$ away (Figure 5.5).

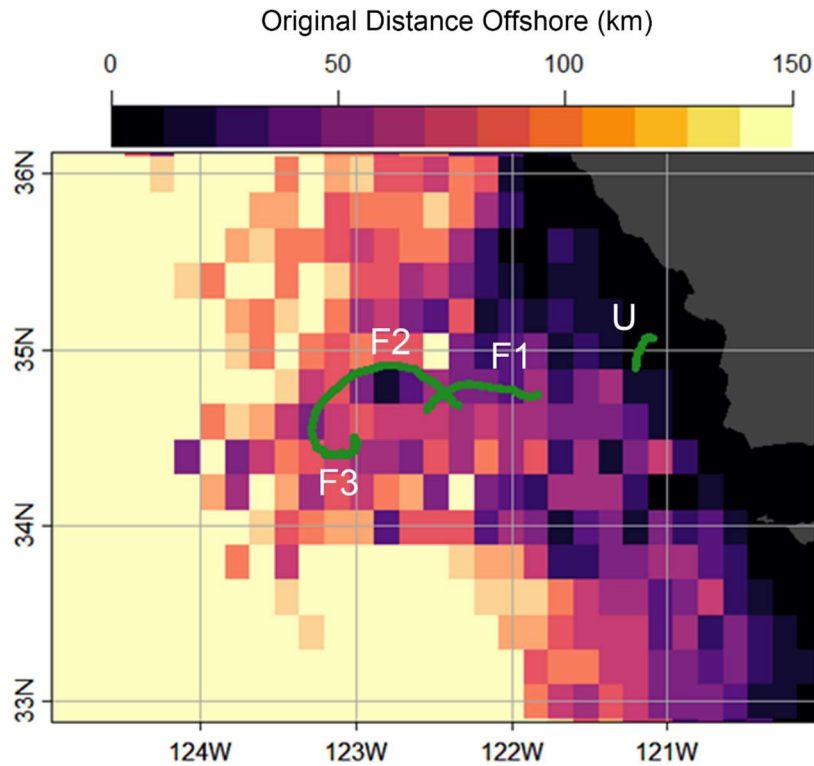


Figure 5.4. Original distance offshore of particles exported past 150 m. Darker colors indicate particles that started closer to shore while bright colors shown particles that began far offshore.

The model indicates that export within the filament consists of particles formed much closer to the coast relative to surrounding water masses (Figure 5.4). For example, Cycle F2 took place ~ 130 km offshore yet the particles were formed a median distance of 58 km offshore (IQR: 25 – 93 km) indicating a net *offshore* advection of 73 km. Contrast this with particles initialized just 1 degree north with an average offshore distance of 136 km. This “virtual sediment trap” would have been comprised of particles that were formed 142 km offshore (IQR: 112 – 177 km), a net *onshore* advection of 6 km. The extent of lateral transport and net offshore transport varied between cycles, with cycles U and F1 being transported primarily along-shore (from the north) while F2 (see above) and F3 (median: 95 km, IQR: 92 – 99 km) were laterally advected across-shore substantial distances. Exported particles in two test locations, which were not influenced by the filament (Figure 5.5E, F), show substantial differences in the distribution of lateral transports with a bimodal distribution for inshore particles and a median transport distance of 20 km while the offshore, non-filament particles were advected further (38 km). As previously noted, there was not a substantial difference in lateral transport for particles captured

at different depths. For example, particles captured at 200 m on Cycle F3 traveled an additional 1 km on average over particles captured at the base of the euphotic zone during the same cycle.

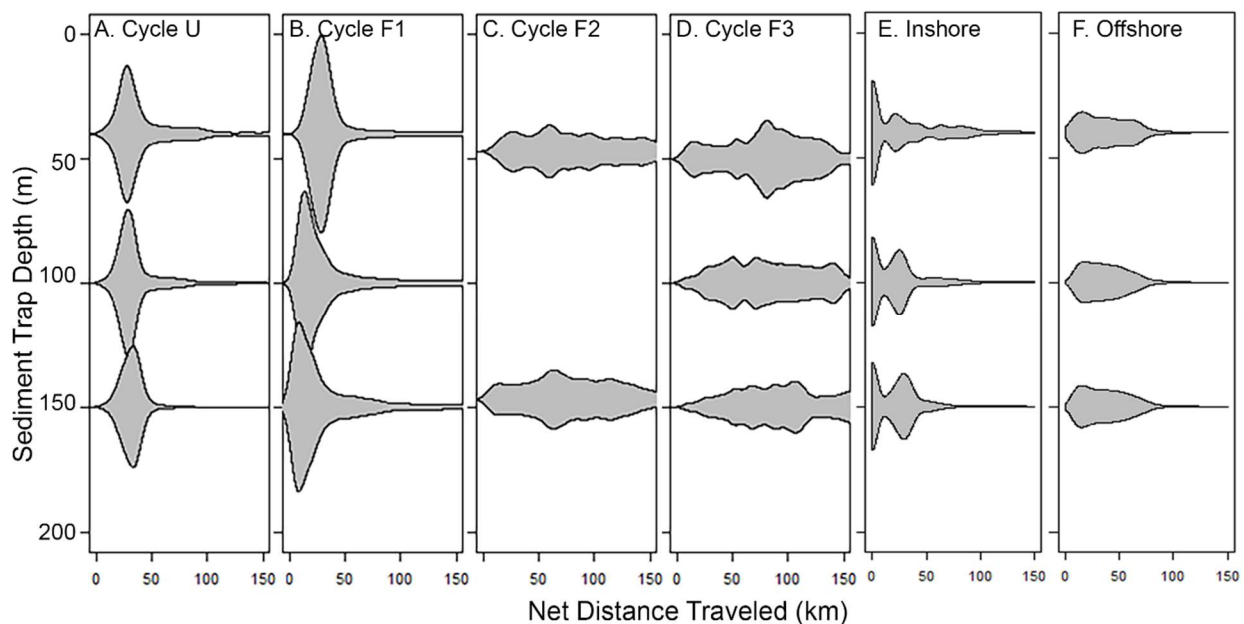


Figure 5.5. Distribution of net lateral distance traveled by particles collected in each sediment trap deployment for the indicated cycle and depth. Additionally, 2 non-filament locations were investigated (E) Inshore and (F) Offshore.

Model Sensitivity and Controlling Parameters

The model was not sensitive to values of beta since the predominate export pathway was through fecal pellets, and not through sinking detritus (a 10% change in beta corresponds to <5% change in POC concentrations and <3 % change in export). In contrast, remineralization rate (λ) impacted all model properties and was an important (and linear) control for model export ratio and POC concentrations.

Within the model, remineralization impacts all particles (fecal pellets and non-fecal pellets) uniformly with time. This is a simplification of several biotic processes including bacterial remineralization, microzooplankton respiration, and viral lysis. Since separately constraining these individual processes is not feasible given a paucity of observational data for these independent processes, grouping each of them into a simple functional relationship seems appropriate. Considering just the non-fecal pellet particles in the model, which consist of phytoplankton, nano- and microzooplankton, porous detritus, and aggregates, the comparison of specific model rates to observations quickly becomes difficult. For example, protistan

zooplankton ingestion will remineralize organic matter at a quantifiable rate based on metabolic efficiency and dilution-based grazing rates. Yet in the model there is no particle type distinction beyond fecal pellet and non-fecal pellet, so such a rate would need to be adjusted for by the phytoplankton to POC ratio, which is both highly variable (Selph et al., submitted; Li et al., 2010) and difficult to measure (Kemp, 1993). Similar analytical approaches would be required to explicitly constrain rates from the other respiratory processes in the ecosystem and to compare against λ . Nevertheless, these rapid remineralization processes ($\lambda = 0.2$) seem consistent with ecosystem function as elucidated by *in situ* measurements. For instance, the median protistan grazing rate on phytoplankton was 0.3 d^{-1} (M. Landry, unpub.).

In addition to model parameters, initial conditions impact POC and export. We tested the impacts of different initial conditions (relative to the standard model run) in three different ways: (1) zero condition where no model spin up is performed, (2) high condition where high rates of NPP were used to spin up the model for two weeks prior to the cruise, and (3) suspended condition where the model was initialized with elevated levels of slowly sinking POC prior to the cruise. When the zero condition was used, the optimized model was less skilled with larger model-data misfits with too little export in later cycles. A similar pattern was observed with the suspended condition, which was largely controlled by mesozooplankton grazing and fecal pellet production. The model was relatively insensitive to the high condition yielding similar model parameters and model-data misfits. This is likely due to the particle residence time under these parameter values (2 – 4 d).

Discussion

Carbon Export Production in the CCE

NPP has been shown to be a useful predictor of export within the CCE (Kelly et al., 2018); yet carbon export production was remarkably consistent across cycles (Table 5.2; Figure 5.2A) even as NPP varied by over an order of magnitude leading to a strong inverse relationship between NPP and export efficiency (i.e. export efficiency increases from 5 – 77 % across our Lagrangian experiments). This invariance in export flux likely results from a combination of *in situ* processes (e.g. grazing, community shifts, and physiological changes) and physical decoupling (e.g. vertical gradients in lateral advection) over timescales of days. Similar inverse patterns in export efficiency have been noted previously. Maiti and colleagues (2013) observed a

strong inverse relationships in the Southern Ocean and proposed a reevaluation of global export models to account for non-linear relationships between primary production and export. More recently Maiti and colleagues (2016) note a general disagreement between established export algorithms (e.g. Dunne et al., 2005; Laws et al., 2011) and *in situ* observations within the Gulf of Mexico. Kelly et al. (2018) investigated export efficiencies within the California Current Ecosystem and suggested that the regional inverse relationship between export efficiencies and primary production stems from a spatiotemporal decoupling between particle production and particle export due, in part, to the strong surface currents found in this region. Temporal decoupling has more recently been invoked by Laws and Maiti (2019) to explain the significant negative correlation between NPP and export efficiency at Station ALOHA and in the Southern Ocean. They found that the temporal mismatch between NPP and observed export could explain the discrepancy and recommend temporally averaging data over periods longer than ~5 days. Stukel and Barbeau (2020) provide evidence for a different form of export decoupling stemming from the ecological changes brought about by nutrient stoichiometry and nutrient limitation. They found that nutrient concentrations and stoichiometry were a better predictor of export than NPP was in the CCE. Here, nutrient-derived decoupling occurs as a result of iron stress in diatoms whereby heavily mineralized diatoms ballast export material (Thomalla et al., 2008). Ultimately, each of these studies argue for a regional perspective that should include spatiotemporal decoupling and the recognition of site-specific drivers relevant to setting export efficiency (e.g., NPP, temperature, nutrient stoichiometry, advection).

While active carbon transport via diel vertical migration was not considered in this model (yet can be substantial in the CCE; e.g. Kelly et al., 2019), we did find that mesozooplankton play an important role in setting the length scales of lateral decoupling between NPP and export through fecal pellet production. Previous studies have recognized the quantitative importance of fecal pellets in setting the mean depth of exported material (Wilson et al., 2008, 2013), but fewer studies have commented on implications for lateral transport of sinking particles. Furthermore, we note a temporal lag between NPP and grazing within the model. This result is directly analogous to the double integration hypothesis (Di Lorenzo and Ohman, 2013), which postulates that zooplankton abundance integrates phytoplankton growth which itself integrates physical forcings. Similarly, since modeled POC is a temporal integration of production – losses (Eq. 3), grazing will lag primary production. Consequently, due to finite sinking speeds, fecal pellet

export will lag grazing. This simple chain of decoupling is a mechanism that remote sensing models (e.g., Siegel et al. 2014) ignore: peak export production is not contemporaneous with peak primary production but rather lags it (Kahru et al., 2019; Laws and Maiti, 2019).

The model illustrates the disproportionate role fecal pellets play in determining the overall connectivity between the euphotic zone and the mesopelagic. By sinking substantially faster than other particles, modeled fecal pellet export collocates export across many depth horizons in a way that other particles in the model do not. We found here that particles were advected 30 – 100 km as they slowly settled out of the euphotic zone or were grazed by mesozooplankton. Yet in contrast to this substantial decoupling, we found that particle export at 200 m is nearly collocated with export shallower in the water column due to a combination of higher sinking speeds (sinking speeds increase with depth) and weaker currents. Previous studies have documented the increase in settling velocity with depth (Berelson, 2001; Villa-Alfageme et al., 2016), which has important ramifications for mesopelagic flux transport and likely influences zooplankton feeding strategies at depth.

Impact of Mesoscale Filament on Export

According to the model, median across-shore transport due to the filament varied by location and ranged from around 30 km closer to the coast (Cycle U) to nearly 100 km within the core of the filament and further offshore (Cycle F1 and F2). These net transports are consistent with previously reported decoupling length scales of 100 – 300 km through across-shore transport (Plattner et al., 2005; Nagai et al., 2015). For example, Plattner et al. (2005) investigated spatial decoupling between new production and export production using a simple NPZD model coupled to ROMS in the California Current region and found a complex mosaic of export production due to coastal upwelling and mesoscale physical features. They note that although new production monotonically decreased with distance offshore, export peaked between 10 and 80 km offshore. Following this, Nagai et al. (2015) used a higher resolution ROMS model coupled to a more sophisticated biogeochemistry model to again investigate filament transports in the California Current region. They noted frequent occurrence of upwelling-associated filaments within their model, which, in conjunction with westward propagating eddies, formed an important regional conveyor belt for nutrients and organic matter subsidizing more than 10% of the offshore organic matter inventory. In contrast to eddies with a

mean advective speed of 2 cm s^{-1} (Nagai et al., 2015), filaments more rapidly transport water offshore (e.g. maximum advective speeds exceed 50 cm s^{-1} during P1706) and have been shown to be effective coastal transport vectors in a variety of settings (Kelly et al., 1998; Harrison et al., 2013; Capet et al., 2014), yet are temporally less persistent physical phenomena lasting weeks to months (Nagai et al., 2015).

Through both filaments and eddies, across-shore transport of organic matter can be a significant loss term for coastal ecosystems and has even been found to exceed losses by vertical particle fluxes (e.g. Harrison et al., 2013). Indeed, eddy-driven transport has been long studied in the pelagic due to its important biogeochemical role (Mathis et al., 2007; Laxenaire et al., 2018). Additionally, through entrainment, mixing, and advection of coastal waters offshore, filaments and other mesoscale interactions can provide an important nutrient subsidy for oligotrophic ecosystems (Duarte et al., 2013) and may even support the majority of export production in some systems (Kelly et al., in prep). Finally, filaments and mesoscale features, which are common in EBUS, may modulate benthic flux in the offshore domain, where episodic flux events have been shown to constitute nearly 50% of total flux (Smith et al., 2018).

Comparison to Other Model Approaches

In contrast to the model presented here, which contains particles with sinking speeds that span 6 orders of magnitude, biogeochemical models typically partition particles to just a couple particle types with fixed sinking speeds. By doing so, these models remove important modes of variability in POC concentrations and distributions. One area where this aspect is particularly relevant is for assessing lateral and vertical transport distances. Eulerian models do not permit easy estimations over transport distances without the injection of virtual tracers into specific grid cells due to the use of state variables. This contrasts strongly with Lagrangian approaches with explicit representation of particles, transports, and transport distributions such as in Figure 5. The distribution of transport distances permits more accurate estimation of export location and more accurate predictions of the biogeochemical impact that export has.

Compared with the present model, which includes four distinct processes, higher complexity models include additional particle processes, which have been shown to be important in other study areas (e.g. Stemmann et al., 2004). For example, Burd et al. (2000) explicitly models changing particle size classes due to aggregation and disaggregation and uses size-

fractionated POC and Thorium-234 to validate against. For application to the CCE where mesozooplankton biomass can be quite substantial (Landry et al., 1994), such aggregate models are more difficult to reconcile with food-web processes which are inherently non-aggregative (biotic interactions rarely preserve particle properties such as size). Whereas the present model does not distinguish between physical properties besides sinking speed, it does include ecosystem processes that are particularly important in this study region. Nevertheless, a particle aggregation type of model (e.g. Burd et al., 2000) is potentially powerful when adequately constrained because it permits a mass-balanced, mechanistic approach to particle processes that are difficult to formulate in other frameworks. The drawback to size class structured particle models is the complexity in validating and constraining POC properties such as porosity, excess density, and drag. Since most field measurements are on bulk properties (e.g. total mass) there are often many more free parameters than constraints to the model. Instead, it may be insightful to compare the results for a sinking speed model, such as the current one, with *in situ* size spectra to directly examine changes to the size-sinking speed relationship. Such data could be a powerful constraint and improve the power law relationship currently assumed in primary production (Eq. 1).

In addition to resolving processes important to the CCE, the present model is distinct from many previous particle export models (Clegg and Whitfield, 1990; Murnane et al., 1990; Stemmann et al., 2004; Lerner et al., 2016), which are not Lagrangian. Indeed, many particle models are dependent on particle density and thus are solved in 1D configurations (and often at steady-state) and would be difficult to implement—and a challenge to run computationally—in 2D or 3D. While restricting the types of particle behaviors, the current model uses readily available remote sensing products to provide environmental conditions for the particles and thus remove costly particle-particle interactions. An Eulerian, biogeochemical model could provide similar environmental properties including space and time varying zooplankton populations (Shropshire et al., 2020) in a coupled fashion, but such an approach is beyond the scope of the present discussion.

Linking Particle Transport to *In Situ* or Remote-Sensing Particle Observations

While the physical properties of sinking particles have been a topic of interest since early sediment trap studies (e.g. Kleerekoper, 1953; Gardner, 1980), our skill in predicting particle

properties *a priori* remains poor. Previous particle studies have generally used particle size spectra to estimate particle abundances for different size classes, and then to use trends between particle size and sinking speeds to estimate flux (Guidi et al., 2008; Iversen and Robert, 2015). While this may be a practical approach for leveraging *in situ* optical systems to estimate particle export when direct measurements are not feasible, such methods have been difficult to generalize (e.g. Fender et al., 2019). Indeed, the heterogeneity of sinking and suspended particles may effectively obfuscate simple relationships between size and sinking speed (Iversen and Lampitt, in press; Stukel et al., 2014). Our present modeling approach avoids these issues by explicitly grouping particles based on sinking speed rather than size; and although this approach is extremely helpful in reducing the number of assumptions made, it does not provide a convenient measurement analog for validation (sinking speed spectrum is not a common measurement). In the future, it may prove useful to combine optical-based estimates of particle abundance, size, and settling velocities, with the Lagrangian approach we use here, to more thoroughly investigate particle transport and transformation through the ocean interior.

An alternate approach to remote-sensing of export variability is based on correlations with satellite-observable properties. Existing satellite-derived data products of export utilize an Eulerian reference frame which implicitly assumes that export will be collocated to primary production (Laws et al., 2000b, 2011c; Dunne et al., 2005a; Henson et al., 2011a; Siegel et al., 2014a), even in regions where lateral advection is known to be important (e.g. EBUS). By combining simple models of regional circulation (e.g. OSCAR; ESR, 2009) and a Lagrangian export model, realistic patterns of export could be discerned. Indeed, such a mechanistic approach could be better capable of predicting changes to the BCP under climate change where relationships between traditional environmental predictors (e.g. temperature) and export may fundamentally change. While the current Lagrangian model is optimized for the specific ecosystem drivers of the CCE (i.e. mesozooplankton fecal pellet production), the processes included have been found to be important generally, albeit likely requiring a distinct parameterization.

Conclusions

Productivity was strongly impacted by the presence of the filament with elevated rates of NPP and enhanced carbon export throughout the filament core. The invariance of carbon export to

primary productivity (Figure 5.2A) highlights the importance of spatial decoupling even within a shallow euphotic zone (~40 m). We parameterized a novel particle production and export model using *in situ* observations to explicitly quantify decoupling between particle production and export and positively identified the filament as a region of enhanced lateral transports, net across-shore transport, and export decoupling. Although advection within the filament led particles during some cycles to be transported > 100 km before exiting the euphotic zone, variations in net transport distance with depth was extremely low due to a combination of higher sinking speeds and weaker lateral currents at depth. While the present work has focused on the biogeochemical impact of a single coastal filament, such mesoscale features are not only pervasive in the greater California Current system but likely have similar impacts on particle advection, transport, and decoupling processes.

CHAPTER 6

CONCLUSIONS

Over the previous four chapters we have investigated variability in carbon export production and the efficiency of the BCP. We have shown the substantial role that mesozooplankton can play in actively transporting organic matter to depth through respiration, excretion, and, most importantly, mortality. We have documented how lateral export in the Gulf of Mexico can supply nutrients and organic matter to oligotrophic area thereby supporting more than 90% of the vertical export. Then, we identified regional dynamics that are crucial in modulating export production and export efficiency. Finally, we have directly quantified vertical decoupling between particle production (via NPP) and gravitational settling through the development of a novel particle model. Through this diverse collection of studies, we now have a more detailed understanding of carbon export drivers in the ocean and how they impact the BCP (Figure 6.1).

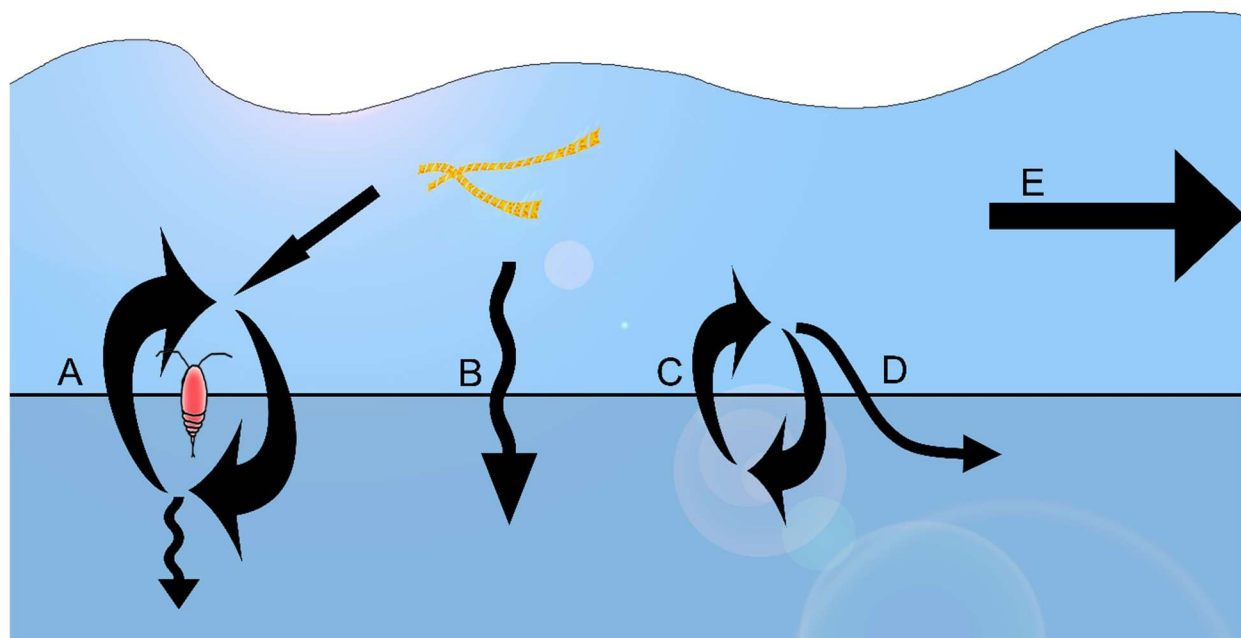


Figure 6.1. Overview of carbon export pathways: (A) active transport, (B) gravitational settling, (C) mixing, (D) subduction, and (E) lateral transport.

Review

We addressed several essential questions in this work and used novel tools to unravel the idiosyncrasies of ecosystem connection to the BCP.

To investigate the biogeochemical connections between epipelagic and mesopelagic ecosystems, we leveraged a data-assimilation technique that could (a) account for inaccuracy and uncertainty in our observations, (b) accurately resolve the ecosystem structure as we understand it, and (c) work for an under-constrained system. Compared to previous literature that only considered (or could constrain) gravitational sinking flux and/or mesozooplankton excretion (del Giorgio and Duarte, 2002a; Steinberg et al., 2008; Burd et al., 2010; Henson et al., 2011b; Hannides et al., 2015), we applied a whole-ecosystem approach and allowed for various paths of connection between the euphotic and twilight zones (Figure 6.1) including gravitational sinking, subduction, and active transport through respiration, excretion, and mortality. A linear inverse ecosystem model (van Oevelen et al., 2010; LIEM) was well suited to the task of synthesizing the available data (including observations, metabolic constraints, and missing data) and determining a statistical ensemble of possible ecosystems. This tool resulted in the discovery that active biological transport accounts for up to 84% (between 18% and 84%) of export in the CCE ecosystem. While the amount of active biological transport is larger than estimated in previous literature (Bianchi et al., 2013b; Hansen and Visser, 2016b; Archibald et al., 2019a), our approach agrees with previous discrepancies between sinking flux and mesopelagic metabolic uptake (Burd et al., 2010) by highlighting the importance of “cryptic” forms of export.

By analyzing a simple mass-balance assessment of the oligotrophic Gulf of Mexico determined from *in situ* measurements, we noted an imbalance in one-dimensional analysis of the system: our observed particulate nitrogen flux was 1 – 2 order of magnitude larger than expected vertical inputs of nitrate or N₂ fixation. Since the Gulf of Mexico generally has much higher energy than the ocean gyres, we hypothesized that our missing input term could be lateral supply (Figure 6.1E) from more productive areas, such as from the shelf break. To determine the quantity of organic matter being transported into the central Gulf of Mexico, we used two independent modelling approaches. The first used remote sensing of particulate organic carbon (POC) and currents based on satellite altimetry to calculate the flow of material into and out of a control-volume box. The second used output from a 3D, biogeochemical model (Shropshire et al., 2020) that modeled the ecosystem and the 3D transport of water around the Gulf of Mexico.

Not only did these two modelling approaches agree remarkably well on the net transport of organic matter, but their estimates matched our own observations for a “missing” input of nutrients into the system. Through these approaches we determined lateral advection was a significant source of nitrogen to these oligotrophic ecosystems, which may be an important dynamic to resolve when forecasting the effects of climate change in this region.

We once again turned to remote sensing and hydrodynamic models to investigate the relationship between export production and primary production across an extensive dataset collected off the coast of California (Chapter 4). Throughout this region, El Niño state is an important physical driver which impacts nutrient availability (Jiménez-Quiroz et al., 2019), primary production (Kahru et al., 2018b), and zooplankton populations (Lilly and Ohman, 2018); and so we hypothesized that such a strong physical forcing on the system would impact regional export efficiencies and the relationships between primary production and export. Through a combination of remote sensing and field data, we were unable to find a significant change in the underlying relationships between export production and El Niño. Instead the data pointed to water parcel age since upwelling as a significant driver of export efficiency regionally. This secondary hypothesis was validated with a Lagrangian particle model (i.e. a model that follows virtual particles as they are transported within the model), wherein we were able to test how circulation and time influenced export efficiency.

Finally, we applied these tools once again to a new dataset, which followed a mesoscale filament as it transported coastal waters offshore. Due to the strong currents and the spatial relationships between our observations (instead of tracking several independent water masses we instead tracked one water mass for nearly 2 weeks), the dataset was suitable for testing hypotheses regarding the spatiotemporal decoupling between particle production and euphotic zone export. Here we developed a novel particle model to resolve particle sinking speeds from the time of production until they were exported to depth or respired. By resolving the relationships between sinking speed, depth, and ecosystem processes (such as fecal pellet production), we are able to determine how decoupling in the water column influenced our field measurements (especially gravitational settling) and to provide an improved physical context for interpreting field data in this dynamic region.

Through this body of work, we added substantially to the understanding of the BCP by investigating the connectivity of the ecosystem and environment to carbon export. This was

accomplished through the collection and synthesis of new datasets and by the development and implementation of new tools. By integrating models and observations, hypotheses across many spatiotemporal scales can be tested including (a) that mesozooplankton can provide an important carbon subsidy to the mesopelagic through diel vertical migration, (b) that lateral connectivity in the Gulf of Mexico can supply bioavailable nitrogen to oligotrophic waters, (c) that El Niño modifies the relationship between the environment and export efficiency (hypothesis rejected), and (d) decoupling between particle production and export substantially modifies the properties of sinking particles and the interpretation of *in situ* sediment trap data.

Additional Contributions

In addition to the results described within, there have been several other avenues of research during the course of my graduate career.

Biogeochemistry and Export Production

Net Community Production – In a series of manuscripts looking at the balance between photosynthesis and respiration (i.e. net community production), we assessed the applicability of O₂:Ar methods to an Eastern boundary current upwelling domain and investigated diurnal periodicity in this highly productive area (Wang et al., 2020b). These results were then leveraged in a comparison of multiple, independent productivity measurements (Kranz et al., 2020). This work illustrated the value and need for a standardized toolkit from which to process the continuous, often idiosyncratic, data required for the O₂:Ar method; therefore, an open source pipeline was developed for use by the community and consists of a simplified graphical interface and a customizable command line interface (Kelly et al., in prep).

Optical Systems – Using data collected from 7 cruises in the CCE we developed a new parameterization between the particle size spectra as measured by an Underwater Video Profiler and measured particle export (Fender et al., 2019). We found that our parameterization was dramatically different from previous parameter sets from other locations and reinforces the importance of *in situ*, regional ecology in setting relationships between size spectra and sinking particle flux.

Remote Sensing – As an extension to Chapter 4, Mati Kahru investigated the functional relationship and temporal decoupling between remotely sensed primary productivity and measured particle export (Kahru et al., 2019). We found that the highest correlation between NPP and export occurred ~ 7 day apart suggesting that gravitational settling flux may consist of particles produced many days prior to the actual export.

Trace Metals – In addition to carbon, our export work has expanded to include some of the first direct observations of bioavailable trace element (e.g. Fe, Mn, Cu, Zn) export from the euphotic zone (Morton et al., in prep). In addition, a novel particle model was designed to model small scale transport and geochemical alteration (including dissolution and scavenging) of particles in and below the sea-surface microlayer (Ebling et al. in prep).

Modeling Approaches – Following the application of the linear inverse ecosystem model (LIEM) used in Chapter 2, we developed a novel LIEM implementation that could be used to assimilate ecosystem rate measurements and isotopic signatures (Stukel et al., 2018b). Contrary to previous studies that included isotopic information, our implementation did not require complete and accurate knowledge of the isotopic signature in all members of the ecosystem—a set of measurements that are almost never available in pelagic ecosystems.

Continuing the modeling work, several manuscripts were published based on the water column ^{234}Th tracer. Simply put, ^{234}Th concentrations in the water column are inversely proportional to the rate of sinking particles so that when ^{234}Th concentrations are low, export is high. The first publication investigated the ecological and biogeochemical predictors for the carbon to ^{234}Th ratio (i.e. $\text{C}:\text{}^{234}\text{Th}$) and found two empirical relationships with high predictive value (Stukel et al., 2019c). The second manuscript investigated a mechanistic model to explain changes in $\text{C}:\text{}^{234}\text{Th}$ in response to environmental considerations (Stukel and Kelly, 2019).

Broader Ecosystem Connections

Within the same special issue where the second chapter of this dissertation was published, another article was published wherein the growth and grazing relationship between phytoplankton and zooplankton was inspected and the resulting impact on the biological pump was assessed (Morrow et al., 2018b). Finally, through a NOAA RESTORE Act grant, a number of collaborators and I performed a thorough study of the nutrient dynamics and ecological connectivity within the oligotrophic Gulf of Mexico from nutrients on up to bluefin tuna larvae.

This project has led to several publications on a range of topics including nutrient cycling (Knapp et al., submitted), a linear inverse estimation of the ecosystem (Stukel et al., submitted), nutrient uptake rates and objective determination of model phytoplankton parameterizations (Yingling et al., submitted) and several on community composition, production, and export (Landry et al., submitted; Selph et al., submitted; Stukel et al., submitted).

Future Work

Autonomous Platforms

It is an understatement to say that the development and utilization of autonomous sampling platforms is a burgeoning area of oceanography. With programs such as ARGO well on their way towards near-continuous ocean monitoring, and programs like BioARGO just on the horizon, it is worth considering how these programs will impact our understanding and approach towards the BCP. Already we have seen autonomous platforms provide invaluable data on ocean circulation (Oke and Schiller, 2007), ocean acidification (Juranek et al., 2011), and even biogeochemical modeling (Wang et al., 2020a); but how can they directly complement measurements of export?

A great number of papers have investigated the problem of estimating sinking particle flux from optical measurements. Some approaches have used the *in situ* particle size spectrum (e.g. UVP; Guidi et al., 2008) in an attempt to relate particle abundance, sinking velocity, and mass, while others have developed *in situ* platforms to measure the size and encounter rate of particles (e.g. CFE; Bourne et al., 2018). While at times insightful, the general consensus is that many of the results resist generalization (Fender et al., 2019). While a particular approach works well for one study, it is non-trivial to apply the same approach to another study site or the same study site at another time (e.g. Fender et al., 2019). As with many early studies, datasets are often quite limited (even if not always small) due to the paucity of sampling performed and the limited geographical areas they tend to be collected in. Yet, with additional process studies and a substantial increase in observations (via a platform like ARGO, for example) significant progress can be made towards predicting gravitational settling flux from images.

Zooplankton and the BCP

A common thread through many of these chapters is the disproportional impact zooplankton have on modulating the biological carbon pump. While not always central to the stories of the preceding chapters, zooplankton directly modify, attenuate, and produce sinking particle flux (Morales, 1999; Steinberg et al., 2002; Stukel et al., 2013a, 2019d). Indeed, entire special issues (e.g. Kiko et al., 2020) have been dedicated to their important, and often poorly constrained, role in establishing the efficiency of the BCP. Thus, future advances in modeling zooplankton abundance and activities (e.g. grazing, respiration, mortality) on a global scale will provide a new generation of food-web-based export models. For example, Shropshire et al. (2020) has shown that traditional biogeochemical models can be improved by explicitly utilizing zooplankton biomass and rate measurements as validation tools. Such a model illustrates the value of zooplankton models, and although focused on the Gulf of Mexico, it demonstrates the feasibility of global zooplankton models. Using satellites instead of biogeochemical models, the “zooplankton from space” project seeks to quantify zooplankton dynamics through a hybrid ecosystem and remote sensing approach. Such projects may be the first step in resolving global distributions of zooplankton and zooplankton grazing and the resulting impact on regional export production.

General Recommendations

Having worked with a wide range of datasets and model output, and having collected a number of these data during my 239 days at sea, I would like to outline a few recommendations about the current state, and future progress, of BCP observations.

A common theme across several of the preceding chapters has been the importance of lateral processes in modulating and modifying biogeochemical properties and metrics, such as export efficiency. Although lateral dynamics can be a challenge to infer from both traditional Eulerian sampling plans and from adaptive Lagrangian platforms, spatial interactions between water masses, ecosystems, and geochemistry often complicate interpretations and can compete with the in situ processes we are measuring and obfuscate patterns. Through improvements in physical modeling approaches (and advancements in computing power) the valuable context of circulation can be—and is—accessible to everyone.

Finally, the necessity of additional oceanographic timeseries cannot be overstated, and this is specifically true for timeseries of export measurements. With the exception of moored sediment traps, long term export measurements are not available in most of the ocean. While autonomous platforms may one day replace the need for labor intensive sediment trap deployments and recoveries, until then we need substantially more datasets to draw upon when attempting to discern regional or interannual changes in export production. In general, oceanography needs for more process studies since “a single rate measurement is worth 1000 standing stock measurements” (paraphrased from Peter Franks).

APPENDIX A

LINEAR INVERSE ECOSYSTEM MODEL CONSTRAINTS

Table A1. Measurement constraints used in the LIEM. Values given show the mean (μ) and 1 SD (σ) for each cycle except for min/max constraints which are blank. Marked values (*) were assumed values calculated from cycles of the same classification. All values are given in $\text{mg C m}^{-2} \text{d}^{-1}$.

Quantity		P07.1		P0704-2		P0704-4		P0810-1		P0810-2		P0810-3		P0810-4		P0810-5		P0810-6	
		μ	σ	μ	σ	μ	σ	μ	σ	μ	σ	μ	σ	μ	σ	μ	σ	μ	σ
1	C-14PP	1233	74	587	35	2314	139	554	33	484	29	893	54	674	40	1672	100	325	19
2	Delta PHY	-322	209	18	253	-80	602	538	1680	-1	50	-76	166	-399	4771	-325	173	-5	62
3	Microzooplankton Grazing	659	238	717	135	1282	225	472	301	243	51	357	74	277	41	498	48	138	43
4	SMZ Grazing	2249	1132	123	37	856	652	21	9	90	26	199	53	48*	21*	836*	688*	85*	37*
5	LMZ Grazing	93	87	42	18	123	55	18	12	14	9	66	26	21*	15*	51*	55*	19*	14*
6	vmSMZ Grazing	2092	907	137	44	669	499	50	30	110	34	249	113	72*	50*	753*	538*	101*	47*
7	vmLMZ Grazing	232	171	42	18	132	42	19	11	20	10	51	25	19*	14*	95*	101*	22*	16*
8	SMZ + LMZ Grazing	2342	1077	166	57	979	763	35	31	104	44	265	65	67*	38*	887*	668*	104*	61*
9	vmLMZ + vmSMZ Grazing	2306	1137	203	82	622	238	86	42	165	11	336	163	107*	70*	809*	650*	150*	41*
10	Sed Trap @ 100m	144	13	32	6	170	41	74	11	69	13	78	7	149	36	127	22	107	5
11	Thorium @ 100m	77	11	32	10	121	45	32	60	51	29	18	22	46	38	53	13	54	8
12	Fecal Pellet Flux @ 100m	135		4		54		4		8		5		35		14		4	
13	Minimum Subduction	39		47		25		11		33		13		26		10		31	
14	Maximum Subduction	79		55		45		33		47		15		51		19		59	
15	Epi Bacterial Prod (0-100m)	66	27	22	12	53	30	240	137	80	17	148	21	351	60	400	37	101	8
16	Min dBAC BP	16		5		8		16		13		14		27		102		21	
17	Max dBAC BP	52		16		27		52		41		45		89		336		69	
18	Deep NM Resp (dMYC)	2.8	5.5	3.4	1.0	2.2	0.7	4.6	2.2	3.6	1.7	3.8	0.8	3.8	4.4	6.7	0.9	7.3	1.8
19	Deep NM Poop (dMYC)	1.2	2.4	1.5	0.5	1.0	0.3	2.1	1.0	1.6	0.7	1.7	0.4	1.7	1.9	3.0	0.4	3.3	0.8
20	Deep NM Mort (dMYC)	2.8	5.5	3.4	1.1	2.2	0.7	4.7	2.3	3.7	1.7	3.9	0.8	3.9	4.4	6.8	1.0	7.4	1.8
21	Epi VM Resp (vmMYC)	7.5	14.7	2.8	2.2	12.2	4.8	12.0	2.8	2.8	0.6	14.5	4.1	8.0	4.8	8.9	1.0	5.5	2.0
22	Deep VM Resp (vmMYC)	9.5	18.6	3.5	2.8	15.5	6.0	14.9	3.4	3.0	0.7	16.9	5.0	9.7	6.0	10.6	0.8	6.2	2.1
23	Deep VM Poop (vmMYC)	5.1	10.0	1.9	1.5	8.3	3.2	8.1	1.9	1.8	0.4	9.5	2.8	5.3	3.3	5.9	0.5	3.5	1.3
24	Deep VM Mort (vmMYC)	6.0	11.7	2.2	1.8	9.8	3.8	9.5	2.2	2.1	0.5	11.1	3.2	6.3	3.8	6.9	0.6	4.1	1.5

Table A2. Mesozooplankton biomass and minimum respiration estimates used in the LIEM. Respiration is given in mg C m⁻² d⁻¹ and biomass in mg C m⁻².

Quantity	<i>P0704-1</i>	<i>P0704-2</i>	<i>P0704-4</i>	<i>P0810-1</i>	<i>P0810-2</i>	<i>P0810-3</i>	<i>P0810-4</i>	<i>P0810-5</i>	<i>P0810-6</i>
Epipelagic Min Resp (SAR)	8.0	8.6	8.0	0.0	0.0	0.0	0.0	8.9	0.0
SMZ Min Resp	24.4	5.1	20.6	4.8	26.3	18.0	36.3	31.6	27.3
vmSMZ Min Resp	5.3	0.4	5.5	16.4	3.3	8.6	0.0	21.5	0.0
dSMZ Min Resp	2.6	2.6	5.7	9.4	2.5	7.1	1.1	14.5	3.3
LMZ Min Resp	7.0	3.3	11.9	5.5	10.4	5.7	7.8	3.0	5.8
vmLMZ Min Resp	19.9	1.5	63.2	24.7	14.9	50.9	11.1	64.2	11.8
dLMZ Min Resp	3.2	5.4	6.7	20.4	7.6	13.3	4.9	31.3	13.5
GEL Min Resp	0.2	0.1	0.1	0.3	0.7	0.2	0.0	0.0	0.7
dGEL Min Respiration	0.4	0.1	0.5	0.4	1.1	0.3	0.1	0.4	0.8
SMZ Biomass	654	106	511	106	833	509	1249	1891	1346
vmSMZ Biomass	104	33	115	722	127	282	0	1120	0
dSMZ Biomass	499	280	715	968	307	834	111	1430	381
LMZ Biomass	424	173	478	971	586	1126	867	938	1763
vmLMZ Biomass	557	347	5175	993	1557	9859	1681	6122	1671
dLMZ Biomass	5928	2839	5702	7180	1818	3579	1395	7134	3942

Detailed Methods

LIEM Approach

The MCMC approach begins with an initial solution that fits the equalities and inequalities (we started with the L_2 solution, e.g. (Vézina and Piatt, 1988)). A bounded random walk is then performed using the open source library *limSolve* (Soetaert et al., 2017). During each step of the random walk, a tentative solution is first produced. For this tentative solution to be accepted and for the random walk to continue from this new point, the inequality constraints need to be assessed to ensure all conditions are met. If the tentative solution lies outside the bound of an inequality constraint, the solution is reflected back into the valid solution space (i.e. mirror algorithm). The tentative solution is assessed using a weighted sum of squared residuals (SSR) between the model's solution and the *in situ* measured values including measurement uncertainty (Eq. 1).

$$prob(x) = e^{-\frac{1}{2}\sigma^{-2}(Ax-b)^T(Ax-b)} \quad (\text{Eq 1})$$

where σ is the measurement uncertainty and $Ax - b$ is the model-predicted *in situ* values.

A stochastic algorithm uses the ratio of the tentative solution's probability (i.e. $prob(x_{n+1})$) and the previous solution's probability to determine if the tentative solution should be accepted (Eq. 2). If the solution is accepted, then the random walk procedure repeats from this new solution; but if it isn't, then the random walk procedure will start again from the previous solution.

$$\frac{prob(x_{n+1})}{prob(x_n)} \geq rand(0 \rightarrow 1) \quad (\text{Eq 2})$$

The random walk was performed for 200 million steps following a burn-in period of 20 million steps (code adapted from Van den Meersche et al., 2009). The burn-in period allowed the model to move away from the initial solution before sampling for the final solution set. Since the optimal acceptance ratio for high dimensional MCMCs has been reported to be around 25% (Roberts et al., 1997; Roberts and Rosenthal, 2001), the jump length for each cycle was adjusted to approximate that acceptance ratio for the sake of efficiency and consistency across cycles. The random walk solution is then subsampled yielding 10,000 solutions that fit the equality and inequality constraints while approximating the measurement constraints. The mean and 95% confidence intervals of these sets were used to determine the maximum likelihood solution and

uncertainty for each output variable. When discussing ranges in flow values across multiple cycles, the values shown are the range in the mean solution for each cycle unless otherwise indicated.

Supplemental Equations

The following 24 equations are for the mass balance within the model:

$$\Delta PHY = gppTOphy - phyTOres - phyTOhnf - phyTOmic - phyTOsmz - phyTOlmz - phyTOsdt - phyTOdoc - phyTOvmsmz - phyTOvmlmz$$

$$\Delta HNF = 0 = phyTOhnf - hnfTOmic - hnfTOsmz - hnfTOres - hnfTOsdt - hnfTOdoc + bacTOhnf + sdtTOhnf + ldtTOhnf - hnfTOvmsmz$$

$$\Delta MIC = 0 = phyTOmic + hnfTOmic - micTOres - micTOsmz - micTOlmz - micTOsdt - micTOdoc + bacTOmic + sdtTOmic + ldtTOmic - micTOvmsmz - micTOvmlmz$$

$$\Delta SMZ = 0 = phyTOsmz + hnfTOsmz + micTOsmz - smzTOlmz - smzTOsar - smzTOres - smzTOsdt - smzTOdoc + ldtTOsmz - smzTOvmlmz$$

$$\Delta vmSMZ = 0 = phyTOvmsmz + hnfTOvmsmz + ldtTOvmlmz + micTOvmsmz - vmsmzTOlmz - vmlmzTOvmlmz_{deep} - vmsmzTOsar - vmsmzTOres - vmsmzTOsdt - vmsmzTOdoc - vmsmzTOdres - vmsmzTOddoc - vmsmzTOdsdt - vmsmzTOdlmz + dhnfTOvmsmz + dmicTOvmsmz + dldtTOvmsmz - vmsmzTOvmlmz_{epi}$$

$$\Delta LMZ = 0 = phyTOlmz + micTOlmz + smzTOlmz - lmzTOgel - lmzTOvmmyc - lmzTOsar - lmzTOres - lmzTOldt - lmzTOdoc + ldtTOlmz + vmsmzTOlmz$$

$$\Delta vmLMZ = 0 = phyTOvmlmz + micTOvmlmz + smzTOvmlmz + vmsmzTOvmlmz_{deep} + ldtTOvmlmz - vmlmzTOgel - vmlmzTOvmyc_{epi} - vmlmzTOsar - vmlmzTOres - vmlmzTOldt - vmlmzTOdoc - vmlmzTOdres - vmlmzTOdgel - vmlmzTOvmmyc_{deep} - vmlmzTOdmyc + dsmzTOvmlmz + dmicTOvmlmz + dldtTOvmlmz + vmsmzTOvmlmz_{epi} - vmlmzTOddoc - vmlmzTOldt$$

$$\Delta GEL = 0 = lmzTOgel - gelTOres - gelTOdoc - gelTOpoop - gelTOhtl + vmlmzTOgel$$

$$\begin{aligned}
\Delta v m M Y C = 0 &= l m z T O v m m y c - v m m y c T O r e s - v m m y c T O d o c - v m m y c T O p o o p \\
&\quad - v m m y c T O h t l + d l m z T O v m m y c - v m m y c T O d r e s - v m m y c T O d d o c \\
&\quad - v m m y c T O p o o p_{m e s o} - v m m y c T O h t l + v m l m z T O v m m y c_{e p i} \\
&\quad + v m l m z T O v m m y c_{d e e p} \\
\Delta S A R = 0 &= s m z T O s a r + l m z T O s a r - s a r T O r e s - s a r T O d o c - s a r T O p o o p - s a r T O h t l \\
&\quad + v m s m z T O s a r + v m l m z T O s a r \\
\Delta B A C = 0 &= d o c T O b a c - b a c T O r e s - b a c T O h n f - b a c T O m i c \\
\Delta S D T = 0 &= p h y T O s d t + h n f T O s d t + m i c T O s d t + s m z T O s d t - s d t T O h n f - s d t T O m i c \\
&\quad - s d t T O d o c - s d t T O d s d t_{g r a v i t y} + v m s m z T O s d t - s d t T O d s d t_{s u b d u c t} \\
\Delta L D T = 0 &= l m z T O l d t - l d t T O h n f - l d t T O m i c - l d t T O s m z - l d t T O l m z - l d t T O d o c \\
&\quad - l d t T O d l d t_{g r a v i t y} - l d t T O s m s m z - l d t T O v m l m z + v m l m z T O l d t \\
&\quad - l d t T O d l d t_{s u b d u c t} \\
\Delta D O C = 0 &= p h y T O d o c + h n f T O d o c + m i c T O d o c + s m z T O d o c + l m z T O d o c + g e l T O d o c \\
&\quad + v m m y c T O d o c + s a r T O d o c + s d t T O d o c + l d t T O d o c - d o c T O b a c \\
&\quad + v m s m z T O d o c + v m l m z T O d o c \\
\Delta d H N F = 0 &= d b a c T O d h n f + d s d t T O d h n f + d l d t T O d h n f - d h n f T O v m s m z \\
&\quad - d h n f T O r e s - d h n f T O d d o c - d h n f T O d s d t - d h n f T O d m i c \\
&\quad - d h n f T O d s m z \\
\Delta d M I C = 0 &= d h n f T O d m i c - d m i c T O r e s - d m i c T O d d o c - d m i c T O d s d t - d m i c T O d s m z \\
&\quad - d m i c T O d l m z + d b a c T O d m i c + d s d t T O d m i c + d l d t T O d m i c \\
&\quad - d m i c T O v m s m z - d m i c T O v m l m z \\
\Delta d S M Z = 0 &= d h n f T O d s m z + d m i c T O d s m z - d s m z T O d r e s - d s m z T O d d o c \\
&\quad - d s m z T O d s d t - d s m z T O d l m z + d l d t T O d s m z - d s m z T O v m l m z \\
\Delta d L M Z = 0 &= d m i c T O d l m z + d s m z T O d l m z - d l m z T O r e s - d l m z T O d d o c - d l m z T O d l d t \\
&\quad - d l m z T O d g e l - d l m z T O v m m y c + d l d t T O d l m z + v m s m z T O d l m z \\
\Delta d G E L = 0 &= d l m z T O d g e l - d g e l T O d r e s - d g e l T O d d o c - d g e l T O p o o p - d g e l T O h t l \\
&\quad + v m l m z T O d g e l \\
\Delta d M Y C = 0 &= d l m z T O d m y c - d m y c T O d r e s - d m y c T O d d o c - d m y c T O p o o p \\
&\quad - d m y c T O h t l + v m l m z T O d m y c \\
\Delta d B A C = 0 &= d d o c T O d b a c - d b a c T O d h n f - d b a c T O d m i c - d b a c T O d d o c
\end{aligned}$$

$$\begin{aligned} \Delta dSDT = 0 = & sdtTOdsdt_{gravity} + dhnfTOdsdt + dmicTOdsdt + dsmzTOdsdt \\ & - dsdtTOdhnf - dsdtTODmic - dsdtTOddoc - dsdtTOext \\ & + vmsmzTOdsdt + sdtTOdsdt_{subduct} \end{aligned}$$

$$\begin{aligned} \Delta dLDT = 0 = & ldtTOldt_{gravity} + vmlmzTOldt + dlmzTOldt - dldtTOdhnf \\ & - dldtTOMIC - ldtTODsmz - dldtTOddoc - dldtTOext - dldtTOvmsmz \\ & - dldtTOvmlmz + ldtTOldt_{subduct} \end{aligned}$$

$$\begin{aligned} \Delta dDOC = 0 = & vmlmzTOddoc + dhnfTOddoc + dmicTOddoc + dsmzTOddoc \\ & + dlmzTOddoc + dgeltTOddoc + vmmycTOddoc + dmycTOddoc \\ & + dsdtTOddoc + dldtTOddoc - ddocTOdbac + vmsmzTOddoc \end{aligned}$$

Supplemental Figures and Tables

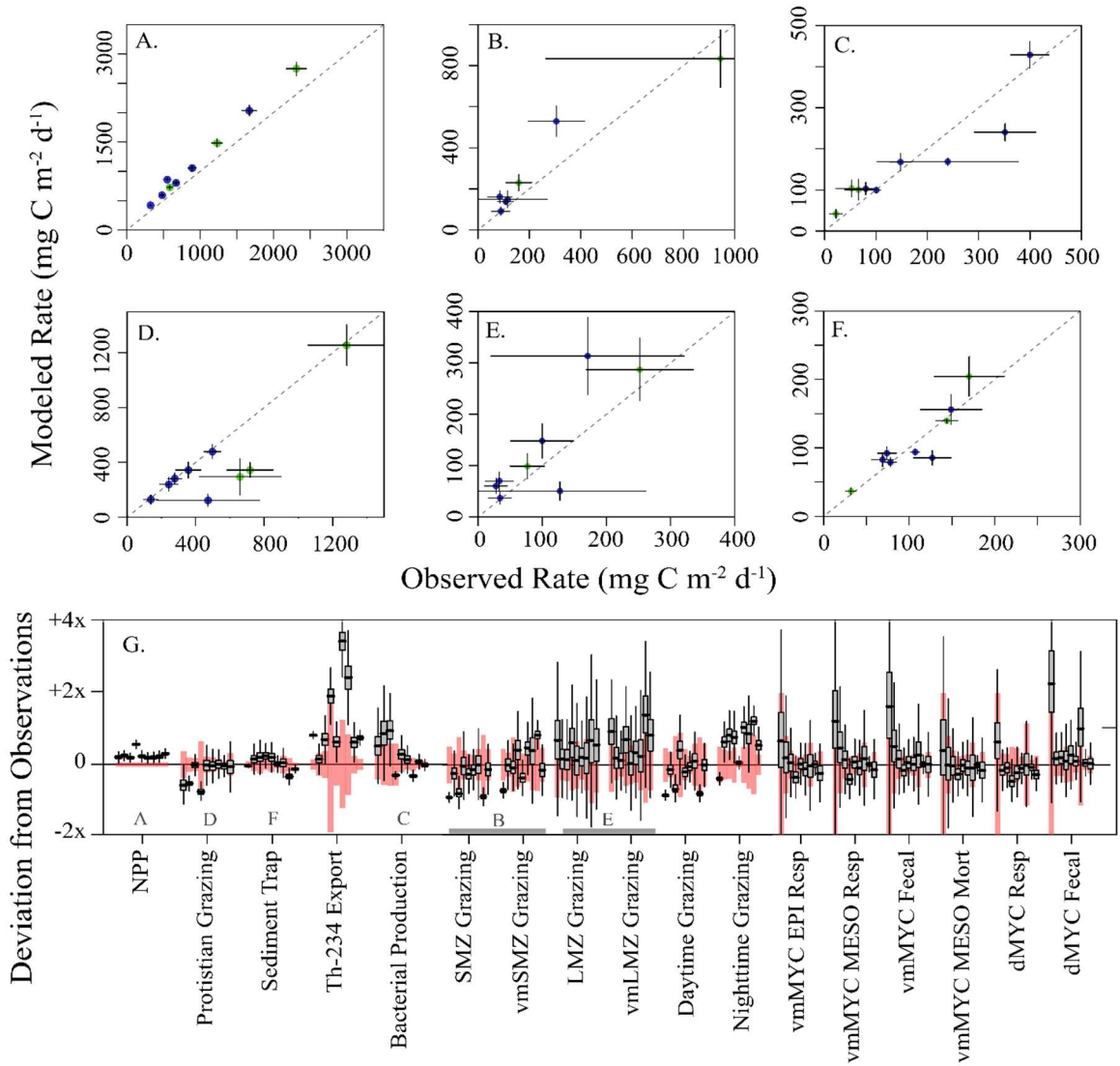


Figure A1. Selected modeled rates versus observations: (A) primary productivity and export, (B) small mesozooplankton grazing, (C) epipelagic bacterial production, (D) protistian zooplankton grazing, (E) large mesozooplankton grazing, and (F) sediment trap export at 100m. Dashed line in each panel is a 1:1 reference line and error bars show 1 SD. (G) Box and whisker plot of relative model deviations from observations for each cycle (box shows inter-quartile range and whiskers to 95% CI). The cycles are shown in chronological order for each equation, and observations are as labeled. The red shading shows 1 SD of the observation (i.e. σ_{obs}).

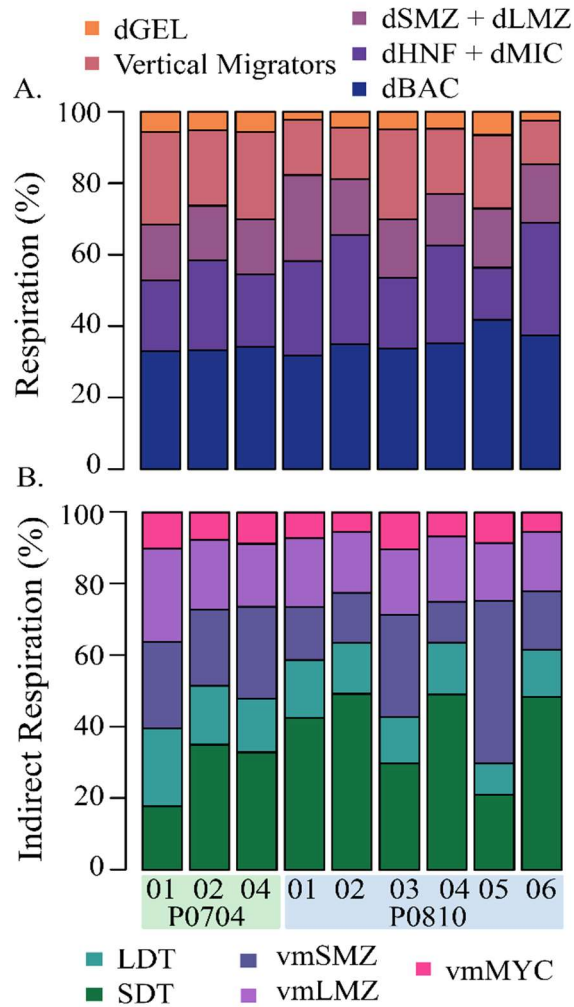


Figure A2. A) Proportion of mesopelagic respiration carried out by each category of mesopelagic organism. (B) Relative proportion of mesopelagic respiration supplied by each of the export pathways: passive transport by SDT and LDT, active transport by vmSMZ, vmLMZ, and vmMYC. Each were calculated from the indirect analysis.

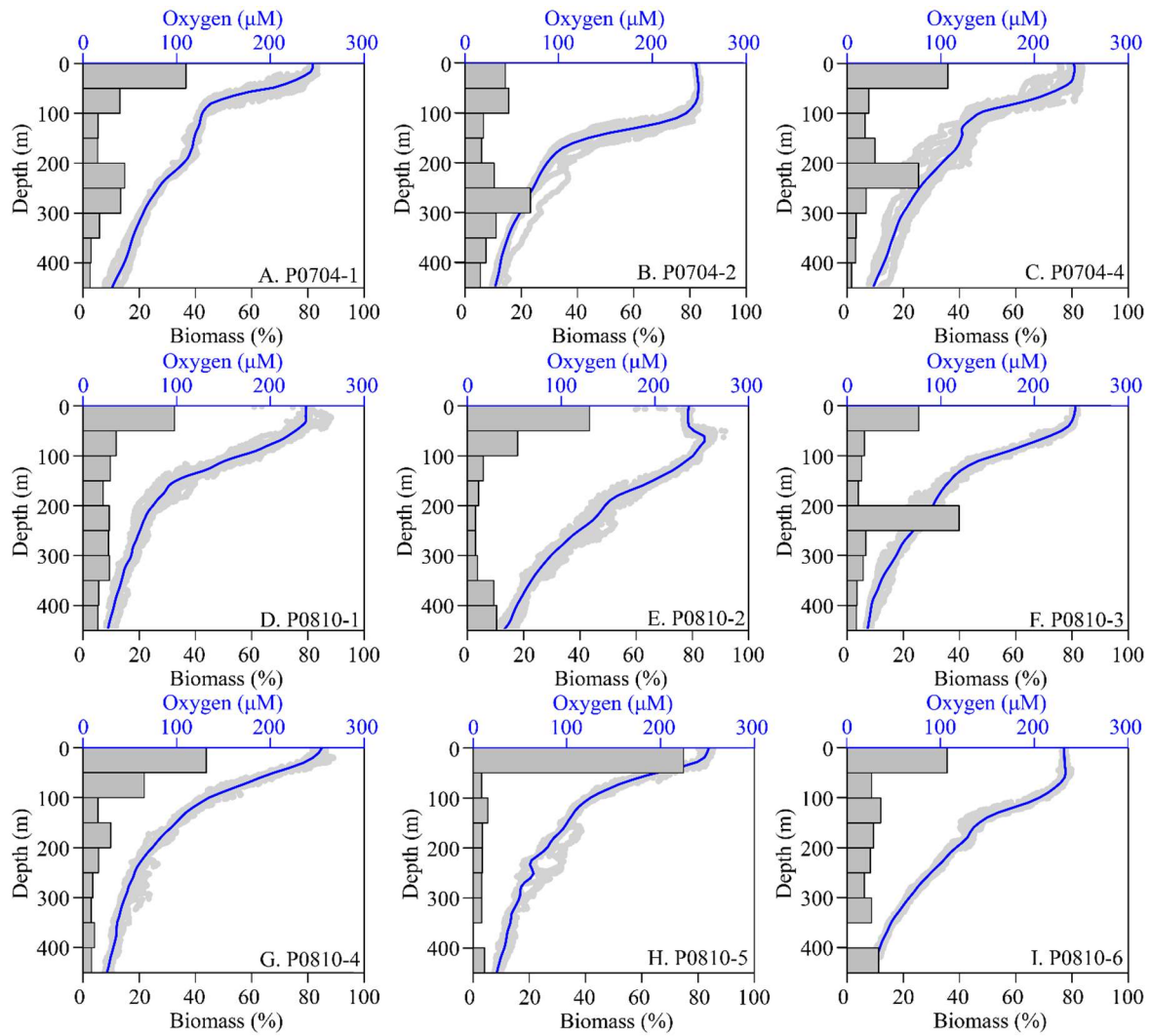


Figure A3. Vertical Distribution of mesozooplankton biomass and dissolved oxygen (DO) concentrations. Bars shown the fraction of total mesozooplankton biomass captured at that depth (MOCNESS, 202 μm mesh) averaged over each cycle. Blue line shows a loess smoothing of the raw oxygen data (grey). Cycles are as indicated.

Table A3. Input equations for the model and the associated organisms where G = grazing, R = respiration, D = detritus production, E = excretion of DOC, GPP = gross primary production, and NPP = net primary production. Subscript x signifies organism x, and epi and meso signify the epipelagic or mesopelagic flux, respectively. Measured constraints and mass balance constraints are provided in Appendix A. Activity specific constraints for vertically migrating mesozooplankton include epipelagic and mesopelagic temperatures (T_{epi} and T_{meso} , respectively) and $a = 0.0648^{\circ}\text{C}^{-1}$ (Ikeda, 1985a).

	#	Equation	Organism (where X=)
GGE	1a	$0.90 \cdot G_x > R_x + D_x + E_x$	MIC, HNF, dMIC, dHNF, SMZ, vmSMZ, dSMZ, LMZ, vmLMZ, dLMZ, Gel, dGEL
	1b	$0.60 \cdot G_x < R_x + D_x + E_x$	
Bacterial Growth Efficiency	2a	$0.95 \cdot G_x > R_x + D_x + E_x$	BAC, dBAC
	2b	$0.70 \cdot G_x < R_x + D_x + E_x$	
Assimilation Efficiency	3a	$0.50 \cdot G_x > D_x$	HNF, dHNF, MIC, dMIC, SMZ, vmSMZ [†] , dSMZ, LMZ, vmLMZ [†] , dLMZ, GEL, dGEL
	3b	$0.10 \cdot G_x < D_x$	
Excretion	4a	$0.10 \cdot G_x < E_x$	HNF, dHNF, MIC, dMIC, SMZ, vmSMZ, dSMZ, LMZ, vmLMZ, dLMZ, GEL, dGEL
	4b	$R_x < E_x$	
	4c	$\frac{E_{x,epi}}{E_{x,meso}} > \frac{\exp(a \cdot T_{epi})}{\exp(a \cdot T_{meso})}$	vmSMZ, vmLMZ
Phytoplankton Excretion	5a	$E_x > 0.02 NPP$	PHY
	5b	$E_x < 0.55 NPP$	
Respiration from Biomass	6a	$R_x > \textit{in situ estimate}$	SMZ, vmSMZ, dSMZ, LMZ, vmLMZ, dLMZ, GEL, dGEL
	6b	$\frac{R_{x,epi}}{R_{x,meso}} > \frac{\exp(a \cdot T_{epi})}{\exp(a \cdot T_{meso})}$	
Respiration from Ingestion	7	$R_x > 0.20 \cdot I_x$	HNF, dHNF, MIC, dMIC, SMZ, vmSMZ, dSMZ, LMZ, vmLMZ, dLMZ, GEL, dGEL
Phytoplankton Respiration	8a	$R_x > 0.10 \cdot GPP$	PHY
	8b	$R_x < 0.55 \cdot GPP$	
	13b	(subducted detritus) < maximum	

Table A3. Continued.

Phytoplankton Excretion + Resp	9a	$E_x + R_x > 0.29 GPP$	PHY
	9b	$E_x + R_x < 0.62 GPP$	
Deep Bacterial Production	10a	$I_x - R_x > BP \text{ minimum}$	dBAC
	10b	$I_x - R_x < BP \text{ maximum}$	
Fecal Pellet Flux	11	(LDT to dLDT) > minimum	LDT, dLDT
Vertical Migrations	12	(GEL to dGEL) > minimum	GEL, dGEL
Subduction	13a	(subducted detritus) > minimum	SDT, dSDT, LDT, dLDT

APPENDIX B

SUPPLEMENTAL DISCUSSION ON LATERAL TRANSPORT IN THE GOM

Constraining the Source of Laterally Transported Organic Matter

In this study, we investigated lateral advection using a hydrodynamic model and remote sensing data products and found a significant association between mesoscale circulation and large-scale transport into the central GoM study region. Furthermore, estimated net lateral transport appears to balance observed nitrogen export—an export term otherwise unbalanced by *in situ* processes. The remote sensing and model products, however, do not place strong constraints on the source material, nor the transformation processes, from which the laterally transported nitrogen is derived. Whether this bioavailable nitrogen is sourced from (1) subsurface nitrate, (2) N₂-fixation, or (3) terrestrial sources remains unresolved, yet several patterns are evident through this study and others.

Geographically, the source regions of the laterally advected nitrogen can be broadly identified based on a mean state approximation (Figures 3.5, 3.6). A substantial proportion of lateral transport is carried through the southern boundary of the control box, which is likely derived from entrainment and localized upwelling associated with the interaction of the Campeche Bank and Loop Current (Merino, 1997; Otis et al., 2019) (Figures 3.8, 3.5, 3.6).

Applying an eddy detection algorithm (Laxenaire et al., 2018) to NEMURO-GOM, net fluxes associated with eddies were small (mean: 44 $\mu\text{mol N m}^{-2} \text{d}^{-1}$) relative to average net flux (1165 $\mu\text{mol N m}^{-2} \text{d}^{-1}$). This, however, is likely due to our criteria for an eddy, which implies no lateral divergence (i.e. closed stream function) and thus excludes phenomenon such as filaments and jets that often form on the edges of eddies (Nagai et al., 2015). Although mesoscale eddies, which are shed by the Loop Current (Oey et al., 2013; Zhong and Bracco, 2013), only carry a small proportion (~4%) of the net lateral transport, they likely force surrounding flow fields (Sahl et al., 1997) that may contribute significant flux over short durations (compared to the Loop Current). Nevertheless, additional data are necessary to determine both the delivery mechanisms and sourcing mechanisms responsible for the lateral N transport in the GoM.

Nitrogen isotopic signatures (i.e. $\delta^{15}\text{N}$) carry with them information about their original sources (e.g. subsurface nitrate: 2 – 4 ‰ vs N_2 -fixation: -2 – 0 ‰), albeit continuously modified by biological processes (Casciotti, 2016). The mass-balance constraints for nitrogen and ^{15}N , as presented, are consistent with upwelled, laterally sourced nitrate (Howe et al., 2020) and with the conclusion reached by Knapp et al. (submitted), who investigated the (in)significance of N_2 -fixation in these oligotrophic waters using a ^{15}N mass-balance approach. This isotopic approach strongly constrains biogeochemical dynamics, especially when informed by broad-scale circulation patterns as was done here. As with all end-member analyses, we note that it is not possible to positively associate export material (3 – 5 ‰) with a unique combination of end-members due to the wide range of isotopic signatures for riverine (6 – 8 ‰) (BryantMason et al., 2013) atmospheric (-5 – 4 ‰) (Dillon and Chanton, 2005), and biotic (-2 – 0 ‰) sources of nitrogen. However, without a significant source of sufficiently low $\delta^{15}\text{N}$ (i.e. $\ll 3\text{‰}$), coastal water cannot be a significant source of organic matter to the oligotrophic GoM. Finally, previous studies have come to mixed conclusions on the degree of connectivity between the shelf environment and the pelagic GoM (Zhong and Bracco, 2013; Barkan et al., 2017; Otis et al., 2019). Combined with the present questions regarding the source of the laterally transported N, process studies in the pelagic GoM are necessary to thoroughly investigate these shelf-basin interactions.

Implications on Vertical Connectivity

Given that the LEU was disproportionately responsible for nitrate uptake (Yingling et al., submitted), although supporting only 21 – 38 % of NPP, one might conclude that export production is centered within the LEU and that export production may thus be supported by episodic fluxes of nitrate at depth. However, observations of export flux strongly refute such a hypothesis. Particle flux out of the UEZ exceeded that of the LEU implicating the LEU as a zone of net remineralization and not of particle formation. This vertical partitioning of export production illustrates the potential problems of including the entire euphotic zone into a single mass-budget. Performing an identical mass-budget for the entire euphotic zone reduces the substantial mismatch between *in situ* nitrogen sources and sinks by averaging across areas of particle production and heterotrophic consumption yet, importantly, does not change the overall conclusions regarding the role of lateral transport (Figure B1). Indeed, vertical integrations of

lateral flux become increasingly sensitive to depth due to the large inventory of subsurface nitrate and spatial variability in euphotic zone depth. Integrating NEMURO-GOM to 135 m (comparable to the depth of most sediment trap deployments) does not significantly change lateral PON, DON or vertical flux values (Figure 3.7) but does substantially augment lateral DIN fluxes. By restricting our primary analysis to the UEZ, we not only get a clearer picture of euphotic zone nitrogen requirements (e.g. export flux at 60 m) but also mitigate sensitivities associate with depth integrations in regions of large vertical gradients.

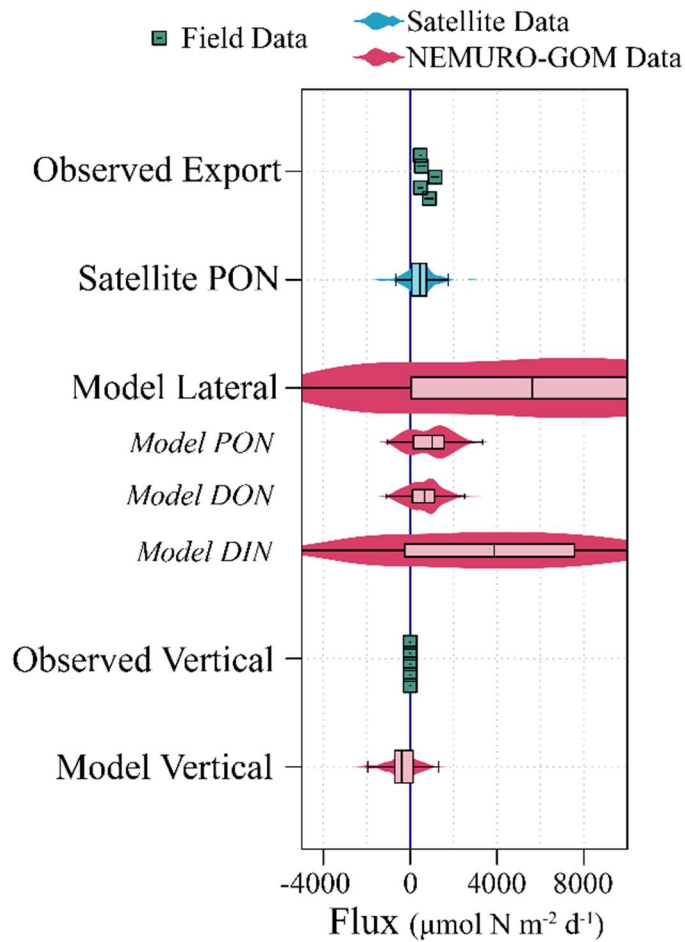


Figure B1. Comparison of lateral nitrogen supply to observed export production for entire euphotic zone (UEZ + LEZ). Observed export was at the base of the euphotic zone. Satellite lateral PON and NEURO-GOM fluxes were calculated as in Figure 3.7. NEMURO-GOM vertical fluxes are integrated to 135 m (UEZ + LEZ) and include upwelling and turbulent mixing but not export by sinking particles. Positive flux values indicate net input into the integration volume. Flux values are normalized to lateral area.

APPENDIX C

SUPPLEMENT TO CHAPTER 4

Table C1. Summary of results from LTRANS particle simulation including the estimated age, fraction of particles that left the euphotic zone and the method used to calculate the age (“median” = median of all particle ages; “interpolation” = linear interpolation based on the fraction of particles with known ages and the total number of particles).

Cruise/Cycle	Estimated Age (days)	Particles Exchanged (%)	Method Used
CCE-P0605-2	9.59	87	Median
CCE-P0605-4	12.94	98	Median
CCE-P0605-5	17.51	99	Median
CCE-P0704-1	1.84	37	Extrapolation
CCE-P0704-2	10.66	27	Extrapolation
CCE-P0704-4	1.50	99	Median
CCE-P0810-1	2.60	80	Median
CCE-P0810-2	11.41	82	Median
CCE-P0810-3	45.33	54	Median
CCE-P0810-4	22.20	47	Extrapolation
CCE-P0810-5	2.23	96	Median
CCE-P0810-6	3.77	99	Median
CCE-P1408-1	83.60	24	Extrapolation
CCE-P1408-2	17.36	37	Extrapolation
CCE-P1408-3	6.22	27	Extrapolation
CCE-P1408-4	36.45	74	Median
CCE-P1408-5	57.40	59	Median
CCE-P1604-1	54.77	13	Extrapolation
CCE-P1604-2	46.05	51	Median
CCE-P1604-3	2.34	95	Median
CCE-P1604-4	20.93	95	Median

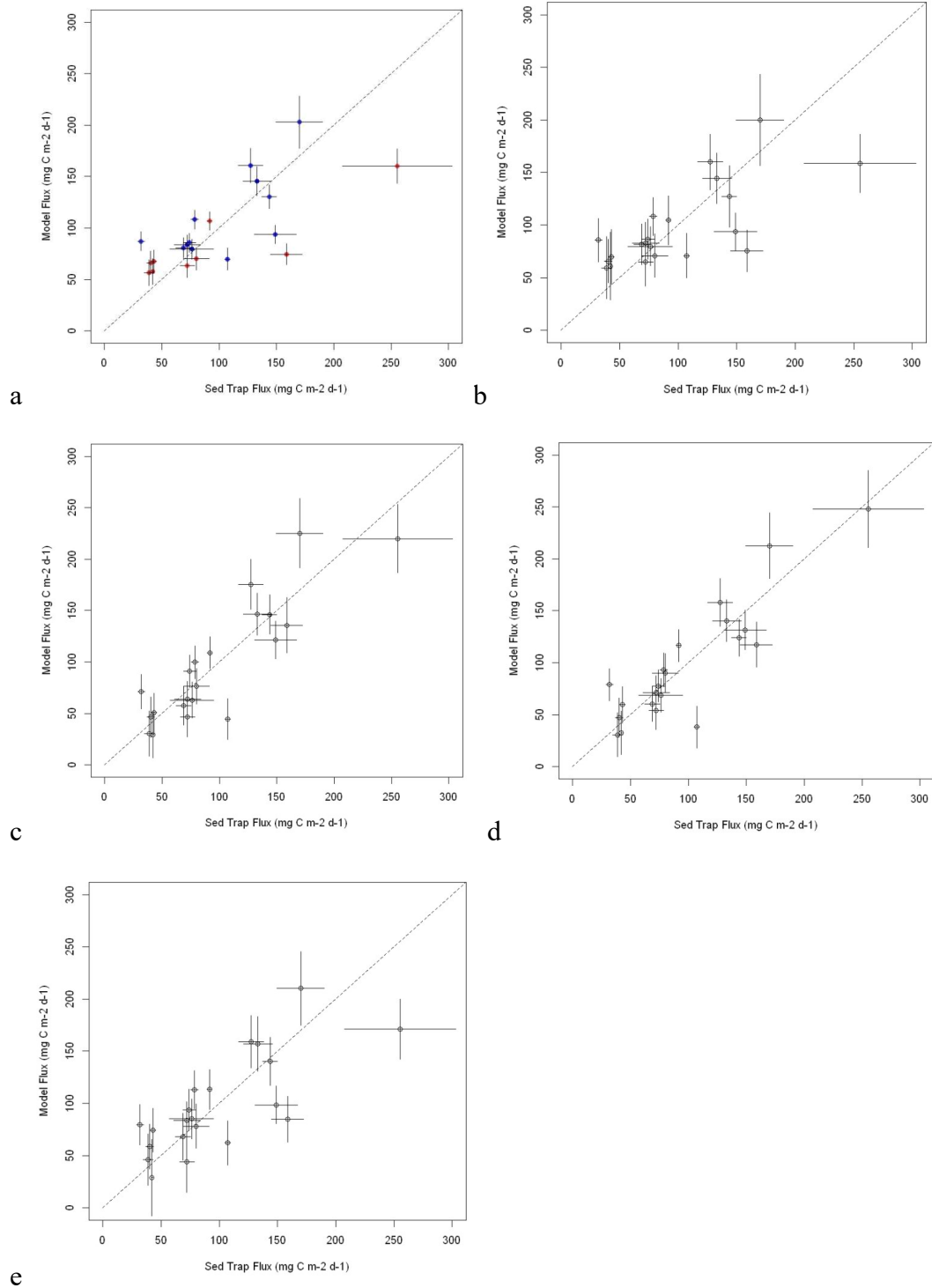


Figure C1. Plots of each modification of the empirical NPP model. Lines indicate 1 SE of the measurement or model prediction. Models: (a) NPP. (b) NPP + SST. (c) NPP + Chl-*a*. (d) NPP + POC. (e) NPP + Distance Offshore.

Table C2. Modeled NPP, Export and export efficiency for the CCE domain derived from remote sensing fields for the indicated years.

Date	Regional		Coastal Zone		Transition Zone		Offshore Zone	
	Export	Export Efficiency	Export	Export Efficiency	Export	Export Efficiency	Export	Export Efficiency
1998	101.93	0.27	127.55	0.19	103.85	0.26	93.21	0.35
1999	107.26	0.25	130.55	0.18	115.49	0.21	98.98	0.30
2000	105.24	0.26	133.87	0.17	111.52	0.23	96.25	0.32
2001	105.05	0.26	133.99	0.17	110.68	0.23	96.21	0.32
2002	106.72	0.25	138.13	0.17	114.45	0.22	97.12	0.31
2003	111.83	0.23	159.49	0.15	117.82	0.21	97.76	0.31
2004	110.65	0.23	151.58	0.15	121.33	0.20	97.36	0.31
2005	109.67	0.23	156.75	0.15	111.66	0.23	95.56	0.33
2006	111.65	0.23	160.55	0.15	120.93	0.20	98.09	0.30
2007	114.24	0.22	146.91	0.16	124.35	0.19	105.79	0.25
2008	115.38	0.21	151.40	0.15	122.70	0.20	105.68	0.25
2009	109.99	0.23	145.74	0.16	115.11	0.22	100.08	0.29
2010	115.85	0.21	166.47	0.14	123.41	0.19	97.51	0.31
2011	114.60	0.22	165.04	0.14	120.26	0.20	99.20	0.29
2012	113.33	0.22	162.92	0.14	123.73	0.19	100.99	0.28
2013	116.35	0.21	168.56	0.14	127.22	0.19	102.44	0.27
2014	105.97	0.25	133.72	0.18	112.86	0.22	97.24	0.31
2015	100.28	0.29	125.56	0.19	102.80	0.27	92.77	0.36
2016	108.24	0.24	157.71	0.15	115.42	0.21	95.41	0.33

APPENDIX D

SUPPLEMENTAL TO CHAPTER 5

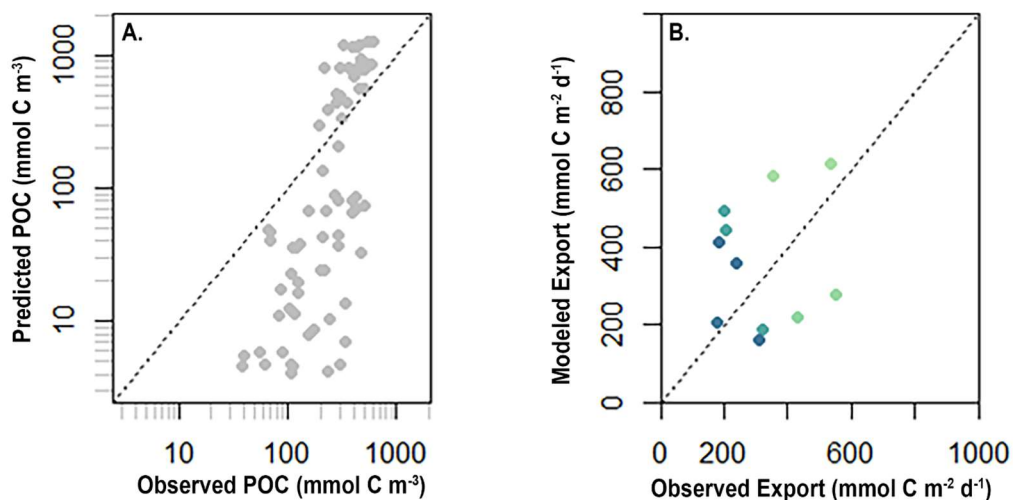


Figure D1. Comparison plots between model and observations for (A) POC and (B) Export.
Dashed line is 1:1.

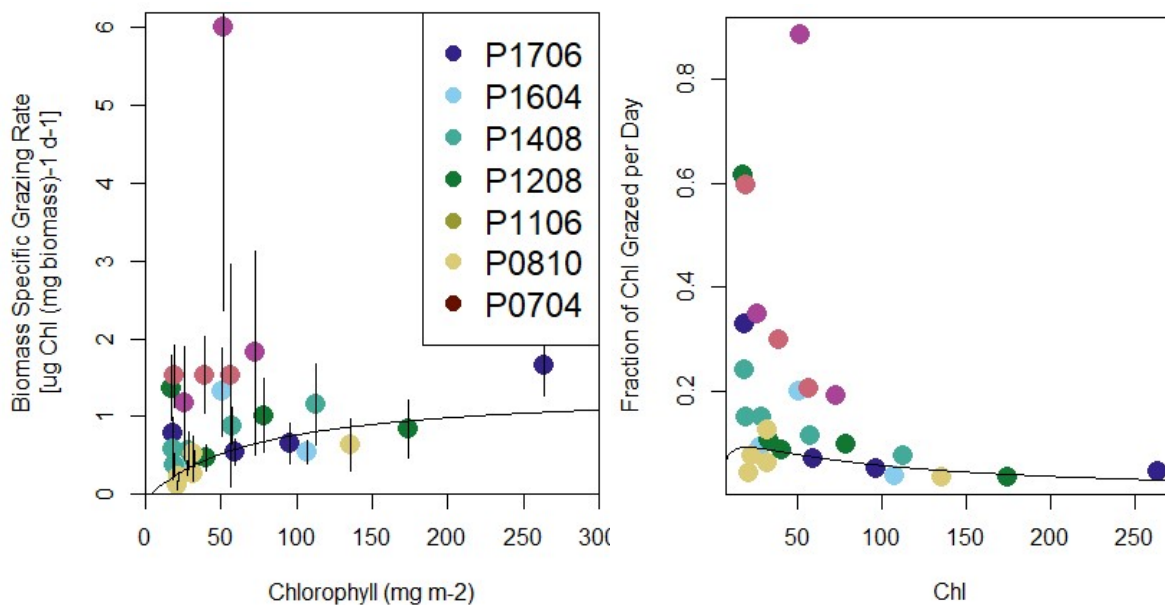


Figure D2. Mesozooplankton grazing rates vs. chlorophyll for the indicated CCE LTER process cruises. Line indicates best fit for grazing model parameters. Error bars show observational uncertainty.

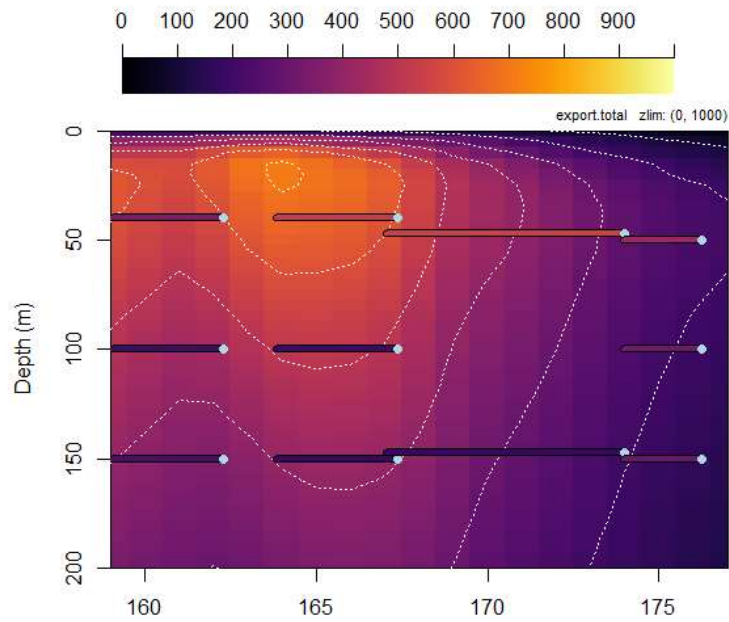


Figure D3. Modeled export flux in 1D model with sediment trap deployments for Cycles U, F1 – F3 overlaid in the same scale ($\text{mmol C m}^{-2} \text{d}^{-1}$). Contours are shown for every 100 $\text{mmol C m}^{-2} \text{d}^{-1}$ increment.

REFERENCES

- Al-Mutairi, H., and Landry, M. R. (2001). Active export of carbon and nitrogen at station ALOHA by diel migrant zooplankton. *Deep-Sea Res. Part II Top. Stud. Oceanogr.* 48, 2083–2103. doi:10.1016/S0967-0645(00)00174-0.
- Amacher, J., Neuer, S., and Lomas, M. (2013). DNA-based molecular fingerprinting of eukaryotic protists and cyanobacteria contributing to sinking particle flux at the Bermuda Atlantic time-series study. *Deep-Sea Res. Part II Top. Stud. Oceanogr.* 93, 71–83. doi:10.1016/j.dsr2.2013.01.001.
- Anderson, T. R., Martin, A. P., Lampitt, R. S., Trueman, C. N., Henson, S. A., and Mayor, D. J. (2018). Quantifying carbon fluxes from primary production to mesopelagic fish using a simple food web model. *ICES J. Mar. Sci.* doi:10.1093/icesjms/fsx234.
- Anderson, T. R., and Tang, K. W. (2010). Carbon cycling and POC turnover in the mesopelagic zone of the ocean: Insights from a simple model. *Deep Sea Res. Part II Top. Stud. Oceanogr.* 57, 1581–1592. doi:10.1016/j.dsr2.2010.02.024.
- Angel, M. V., and Pugh, P. R. (2010). Quantification of diel vertical migration by micronektonic taxa in the northeast Atlantic. *Hydrobiologia*, 1–5. doi:10.1023/A.
- Archibald, K. M., Siegel, D. A., and Doney, S. C. (2019a). Modeling the Impact of Zooplankton Diel Vertical Migration on the Carbon Export Flux of the Biological Pump. *Glob. Biogeochem. Cycles* 33, 181–199. doi:10.1029/2018GB005983.
- Archibald, K. M., Siegel, D. A., and Doney, S. C. (2019b). Modeling the impact of zooplankton diel vertical migration on the carbon export flux of the biological pump. *Glob. Biogeochem. Cycles*. doi:10.1029/2018GB005983.
- Armstrong, R. A., Lee, C., Hedges, J. I., Honjo, S., and Wakeham, S. G. (2001). A new, mechanistic model for organic carbon fluxes in the ocean based on the quantitative association of POC with ballast minerals. *Deep Sea Res. Part II Top. Stud. Oceanogr.* 49, 219–236. doi:10.1016/S0967-0645(01)00101-1.
- Armstrong, R. A., Lee, C., Hedges, J. I., Honjo, S., and Wakeham, S. G. (2002). A new, mechanistic model for organic carbon fluxes in the ocean based on the quantitative association of POC with ballast minerals. *Deep-Sea Res. Part II Top. Stud. Oceanogr.* 49, 219–236. doi:10.1016/S0967-0645(01)00101-1.
- Auad, G., Roemmich, D., and Gilson, J. (2011). The California Current System in relation to the Northeast Pacific Ocean circulation. *Prog. Oceanogr.* 91, 576–592. doi:10.1016/j.pocean.2011.09.004.

- Aumont, O., Maury, O., Lefort, S., and Bopp, L. (2018). Evaluating the Potential Impacts of the Diurnal Vertical Migration by Marine Organisms on Marine Biogeochemistry. *Glob. Biogeochem. Cycles* 32, 1622–1643. doi:10.1029/2018GB005886.
- Baker, C. A., Estapa, M. L., Iversen, M., Lampitt, R., and Buesseler, K. (2020). Are all sediment traps created equal? An intercomparison study of carbon export methodologies at the PAP-SO site. *Prog. Oceanogr.* 184, 102317. doi:10.1016/j.pocean.2020.102317.
- Bandara, K., Varpe, Ø., Ji, R., and Eiane, K. (2018). A high-resolution modeling study on diel and seasonal vertical migrations of high-latitude copepods. *Ecol. Model.* 368, 357–376. doi:10.1016/j.ecolmodel.2017.12.010.
- Barkan, R., McWilliams, J. C., Molemaker, M. J., Choi, J., Srinivasan, K., Shchepetkin, A. F., et al. (2017). Submesoscale Dynamics in the Northern Gulf of Mexico. Part II: Temperature–Salinity Relations and Cross-Shelf Transport Processes. *J. Phys. Oceanogr.* 47, 2347–2360. doi:10.1175/JPO-D-17-0040.1.
- Benitez-Nelson, C. R., Buesseler, K. O., Van Der Loeff, M. R., Andrews, J., Ball, L., Crossin, G., et al. (2001a). Testing a new small-volume technique for determining ²³⁴Th in seawater. in *Journal of Radioanalytical and Nuclear Chemistry*, 795–799. doi:10.1023/A:1010621618652.
- Benitez-Nelson, C. R., Buesseler, K. O., van der Loeff, M. R., Andrews, J., Ball, L., Crossin, G., et al. (2001b). Testing a new small-volume technique for determining Th-234 in seawater. *J. Radioanal. Nucl. Chem.* 248, 795–799. doi:10.1023/A:1010621618652.
- Berelson, W. M. (2001). Particle settling rates increase with depth in the ocean. *Deep Sea Res. Part II Top. Stud. Oceanogr.* 49, 237–251. doi:10.1016/S0967-0645(01)00102-3.
- Bettencourt, J. H., López, C., García, E. H., Montes, I., Sudre, J., Dewitte, B., et al. (2015). Boundaries of the Peruvian Oxygen Minimum Zone shaped by coherent mesoscale dynamics. *Nat. Geosci.* 8, 937–940. doi:10.1038/ngeo2570.
- Bianchi, D., Stock, C., Galbraith, E. D., and Sarmiento, J. L. (2013a). Diel vertical migration: Ecological controls and impacts on the biological pump in a one-dimensional ocean model. *Glob. Biogeochem. Cycles* 27, 478–491. doi:10.1002/gbc.20031.
- Bianchi, D., Stock, C., Galbraith, E. D., and Sarmiento, J. L. (2013b). Diel vertical migration: Ecological controls and impacts on the biological pump in a one-dimensional ocean model. *Glob. Biogeochem. Cycles* 27, 478–491. doi:10.1002/gbc.20031.
- Bishop, J. K. B., Fong, M. B., and Wood, T. J. (2016). Robotic observations of high wintertime carbon export in California coastal waters. *Biogeosciences* 13, 3109–3129. doi:10.5194/bg-13-3109-2016.
- Bond, N. A., Cronin, M. F., Freeland, H., and Mantua, N. (2015). Causes and impacts of the 2014 warm anomaly in the NE Pacific. *Geophys. Res. Lett.* 42, 3414–3420. doi:10.1002/2015GL063306.

- Bourne, H. L., Bishop, J. K. B., Wood, T. J., Loew, T. J., and Liu, Y. (2018). Carbon Flux Explorer Optical Assessment of C, N and P Fluxes. 27.
- Boyd, P. W., and Trull, T. W. (2007). Understanding the export of biogenic particles in oceanic waters: Is there consensus? *Prog. Oceanogr.* 72, 276–312. doi:10.1016/j.pocean.2006.10.007.
- Breitbarth, E., Wohlers, J., Kläs, J., LaRoche, J., and Peeken, I. (2008). Nitrogen fixation and growth rates of *Trichodesmium* IMS-101 as a function of light intensity. *Mar. Ecol. Prog. Ser.* 359, 25–36. doi:10.3354/meps07241.
- Brun, P., Stamieszkin, K., Visser, A. W., Licandro, P., Payne, M. R., and Kiørboe, T. (2019). Climate change has altered zooplankton-fuelled carbon export in the North Atlantic. *Nat. Ecol. Evol.* 3, 416–423. doi:10.1038/s41559-018-0780-3.
- BryantMason, A., Xu, Y. J., and Altabet, M. (2013). Isotopic signature of nitrate in river waters of the lower Mississippi and its tributary, the Atchafalaya. *Hydrol. Process.* 27, 2840–2850. doi:10.1002/hyp.9420.
- Brzezinski, M. A., Krause, J. W., Bundy, R. M., Barbeau, K. A., Franks, P., Goericke, R., et al. (2015). Enhanced silica ballasting from iron stress sustains carbon export in a frontal zone within the California Current. *J. Geophys. Res. C Oceans* 120, 4654–4669. doi:10.1002/2015JC010829.
- Bucklin, A. (1991). Population genetic responses of the planktonic copepod *Metridia pacifica* to a coastal eddy in the California Current. *J. Geophys. Res.* 96, 14799. doi:10.1029/91JC01209.
- Bucklin, A., Rienecker, M. M., and Mooers, C. N. K. (1989). Genetic tracers of zooplankton transport in coastal filaments off northern California. *J. Geophys. Res.* 94, 8277. doi:10.1029/JC094iC06p08277.
- Buesseler, K. O., and Boyd, P. W. (2009a). Shedding light on processes that control particle export and flux attenuation in the twilight zone of the open ocean. *Limnol. Oceanogr.* 54, 1210–1232. doi:10.4319/lo.2009.54.4.1210.
- Buesseler, K. O., and Boyd, P. W. (2009b). Shedding light on processes that control particle export and flux attenuation in the twilight zone of the open ocean. *Limnol. Oceanogr.* 54, 1210–1232. doi:10.4319/lo.2009.54.4.1210.
- Burd, A. B., Hansell, D. A., Steinberg, D. K., Anderson, T. R., Arístegui, J., Baltar, F., et al. (2010). Assessing the apparent imbalance between geochemical and biochemical indicators of meso- and bathypelagic biological activity: What the @\$#! is wrong with present calculations of carbon budgets? *Deep-Sea Res. Part II Top. Stud. Oceanogr.* 57, 1557–1571. doi:10.1016/j.dsr2.2010.02.022.
- Burd, A. B., Moran, S. B., and Jackson, G. A. (2000). A coupled adsorption aggregation model of the POC/Th ratio of marine particles. 18.

- Capet, A., Mason, E., Rossi, V., Troupin, C., Faugère, Y., Pujol, I., et al. (2014). Implications of refined altimetry on estimates of mesoscale activity and eddy-driven offshore transport in the Eastern Boundary Upwelling Systems: CAPET ET AL. *Geophys. Res. Lett.* 41, 7602–7610. doi:10.1002/2014GL061770.
- Carlson, C. A., Ducklow, H. W., and Michaels, A. F. (1994). Annual flux of dissolved organic carbon from the euphotic zone in the northwestern Sargasso Sea. *Nature* 371, 405–408. doi:10.1038/371405a0.
- Carpenter, E. J., Harvey, H. R., Fry, B., and Capone, D. G. (1997). Biogeochemical tracers of the marine cyanobacterium *Trichodesmium*. *Deep Sea Res. Part Oceanogr. Res. Pap.* 44, 27–38. doi:10.1016/S0967-0637(96)00091-X.
- Casciotti, K. L. (2016). Nitrogen and Oxygen Isotopic Studies of the Marine Nitrogen Cycle. *Annu. Rev. Mar. Sci.* 8, 379–407. doi:10.1146/annurev-marine-010213-135052.
- Cavan, E. L., Henson, S. A., Belcher, A., and Sanders, R. (2017). Role of zooplankton in determining the efficiency of the biological carbon pump. *Biogeosciences* 14, 177–186. doi:10.5194/bg-14-177-2017.
- Cermeño, P., Dutkiewicz, S., Harris, R. P., Follows, M., Schofield, O., and Falkowski, P. G. (2008). The role of nutricline depth in regulating the ocean carbon cycle. *Proc. Natl. Acad. Sci. U. S. A.* 105, 20344–20349. doi:10.1073/pnas.0811302106.
- Chavez, F. P., and Messié, M. (2009). A comparison of Eastern Boundary Upwelling Ecosystems. *Prog. Oceanogr.* 83, 80–96. doi:10.1016/j.pocean.2009.07.032.
- Choy, C. A., Popp, B. N., Hannides, C. C. S., and Drazen, J. C. (2015). Trophic structure and food resources of epipelagic and mesopelagic fishes in the north pacific subtropical Gyre ecosystem inferred from nitrogen isotopic compositions. *Limnol. Oceanogr.* 60, 1156–1171. doi:10.1002/lno.10085.
- Church, M. J., Lomas, M. W., and Muller-Karger, F. (2013). Sea change: Charting the course for biogeochemical ocean time-series research in a new millennium. *Deep-Sea Res. Part II Top. Stud. Oceanogr.* 93, 2–15. doi:10.1016/j.dsr2.2013.01.035.
- Clegg, S. L., and Whitfield, M. (1990). A generalized model for the scavenging of trace metals in the open ocean—I. Particle cycling. *Deep Sea Res. Part Oceanogr. Res. Pap.* 37, 809–832. doi:10.1016/0198-0149(90)90008-J.
- Cohen, J. H., and Forward, R. B. (2009). Zooplankton Diel Vertical Migration — A Review of Proximate Control. *Ocean. Mar Biol Annu Rev* 47, 77–109. doi:10.1201/9781420094220-5.
- Coles, V. J., Stukel, M. R., Brooks, M. T., Burd, A., Crump, B. C., Moran, M. A., et al. (2017). Ocean biogeochemistry modeled with emergent trait-based genomics. *Science* 358, 1149–1154. doi:10.1126/science.aan5712.

- Conover, R. J. (1966). ASSIMILATION OF ORGANIC BY ZOOPLANKTON. *Limnol. Oceanogr.* 11, 338–345.
- Dam, H. G., and Peterson, W. T. (1988). The effect of temperature on the gut clearance rate constant of planktonic copepods. *J. Exp. Mar. Biol. Ecol.* 123, 1–14. doi:10.1016/0022-0981(88)90105-0.
- Dam, H. G., Roman, M. R., and Youngbluth, M. J. (1995). Downward export of respiratory carbon and dissolved inorganic nitrogen by diel-migrant mesozooplankton at the JGOFS Bermuda time-series station. *Deep-Sea Res. Part I* 42, 1187–1197. doi:10.1016/0967-0637(95)00048-B.
- Davison, P. C., Checkley, D. M., Koslow, J. A., and Barlow, J. (2013). Carbon export mediated by mesopelagic fishes in the northeast Pacific Ocean. *Prog. Oceanogr.* 116, 14–30. doi:10.1016/j.pocean.2013.05.013.
- Davison, P., Lara-Lopez, A., and Anthony Koslow, J. (2015). Mesopelagic fish biomass in the southern California current ecosystem. *Deep-Sea Res. Part II Top. Stud. Oceanogr.* 112, 129–142. doi:10.1016/j.dsr2.2014.10.007.
- del Giorgio, P. A., and Cole, J. J. (1998). BACTERIAL GROWTH EFFICIENCY IN NATURAL AQUATIC SYSTEMS. *Annu. Rev. Ecol. Syst.* 29, 503–541. doi:10.1146/annurev.ecolsys.29.1.503.
- del Giorgio, P. A., and Duarte, C. M. (2002a). Respiration in the open ocean. *Nature* 420, 379–384. doi:10.1038/nature01165.
- del Giorgio, P. A., and Duarte, C. M. (2002b). Respiration in the open ocean. *Nature* 420, 379–384. doi:10.1038/nature01165.
- Di Lorenzo, E., and Mantua, N. (2016). Multi-year persistence of the 2014/15 North Pacific marine heatwave. *Nat. Clim. Change* 6, 1042–1047. doi:10.1038/nclimate3082.
- Di Lorenzo, E., and Ohman, M. D. (2013). A double-integration hypothesis to explain ocean ecosystem response to climate forcing. *Proc. Natl. Acad. Sci.* 110, 2496–2499. doi:10.1073/pnas.1218022110.
- Dickson, M.-L., Orchardo, J., Barber, R. T., Marra, J., McCarthy, J. J., and Sambrotto, R. N. (2001). Production and respiration rates in the Arabian Sea during the 1995 Northeast and Southwest Monsoons. *Deep Sea Res. Part II Top. Stud. Oceanogr.* 48, 1199–1230. doi:10.1016/S0967-0645(00)00136-3.
- Dillon, K. S., and Chanton, J. P. (2005). Nutrient transformations between rainfall and stormwater runoff in an urbanized coastal environment: Sarasota Bay, Florida. *Limnol. Oceanogr.* 50, 62–69. doi:10.4319/lo.2005.50.1.0062.
- Domingues, R., Goni, G., Bringas, F., Muhling, B., Lindo-Atichati, D., and Walter, J. (2016). Variability of preferred environmental conditions for Atlantic bluefin tuna (*Thunnus*

- thynnus*) larvae in the Gulf of Mexico during 1993-2011. *Fish. Oceanogr.* 25, 320–336. doi:10.1111/fog.12152.
- Dore, J. E., and Karl, D. M. (1996). Nitrification in the euphotic zone as a source for nitrite, nitrate, and nitrous oxide at Station ALOHA. *Limnol. Oceanogr.* 41, 1619–1628. doi:10.4319/lo.1996.41.8.1619.
- Duarte, C. M., Regaudie-de-Gioux, A., Arrieta, J. M., Delgado-Huertas, A., and Agustí, S. (2013). The Oligotrophic Ocean Is Heterotrophic. *Annu. Rev. Mar. Sci.* 5, 551–569. doi:10.1146/annurev-marine-121211-172337.
- Dubois, S., Del Amo, Y., Grami, B., Jude, F., Marquis, E., David, V., et al. (2012). Network analysis of the planktonic food web during the spring bloom in a semi enclosed lagoon (Arcachon, SW France). *Acta Oecologica* 40, 40–50. doi:10.1016/j.actao.2012.02.002.
- Ducklow, H. H. W., Steinberg, D. D. K., Buessler, K., and Buessler, K. O. (2001). Upper ocean carbon export and the biological pump. *Oceanography* 14, 50–58. doi:10.5670/oceanog.2001.06.
- Ducklow, H. W., and Harris, R. P. (1993). Introduction to the JGOFS North Atlantic bloom experiment. *Deep-Sea Res. Part II* 40, 1–8. doi:10.1016/0967-0645(93)90003-6.
- Dugdale, R. C., and Goering, J. J. (1967). Uptake of new and regenerated forms of nitrogen in primary productivity. *Limnol. Oceanogr.* 12, 196–206. doi:10.4319/lo.1967.12.2.0196.
- Dunne, J. P., Armstrong, R. A., Gnanadesikan, A., and Sarmiento, J. L. (2005a). Empirical and mechanistic models for the particle export ratio. *Glob. Biogeochem. Cycles* 19, n/a-n/a. doi:10.1029/2004GB002390.
- Dunne, J. P., Armstrong, R. A., Gnnadesikan, A., and Sarmiento, J. L. (2005b). Empirical and mechanistic models for the particle export ratio. *Glob. Biogeochem. Cycles* 19, 1–16. doi:10.1029/2004GB002390.
- Ekau, W., Auel, H., Pörtner, H.-O., and Gilbert, D. (2010). Impacts of hypoxia on the structure and processes in pelagic communities (zooplankton, macro-invertebrates and fish). *Biogeosciences* 7, 1669–1699. doi:10.5194/bg-7-1669-2010.
- Eppley, R. W., and Peterson, B. J. (1979). Particulate organic matter flux and planktonic new production in the deep ocean. *Nature* 282, 677–680. doi:10.1038/282677a0.
- ESR (2009). OSCAR third degree resolution ocean surface currents. Ver. 1. Available at: <https://doi.org/10.5067/OSCAR-03D01>. [Accessed July 10, 2020].
- Fender, C. K., Kelly, T. B., Guidi, L., Ohman, M. D., Smith, M. C., and Stukel, M. R. (2019). Investigating Particle Size-Flux Relationships and the Biological Pump Across a Range of Plankton Ecosystem States From Coastal to Oligotrophic. *Front. Mar. Sci.* 6, 603. doi:10.3389/fmars.2019.00603.

- Fennel, K., and Laurent, A. (2018). N and P as ultimate and proximate limiting nutrients in the northern Gulf of Mexico: implications for hypoxia reduction strategies. *Biogeosciences* 15, 3121–3131. doi:10.5194/bg-15-3121-2018.
- Fichot, C. G., Lohrenz, S. E., and Benner, R. (2014). Pulsed, cross-shelf export of terrigenous dissolved organic carbon to the Gulf of Mexico. *J. Geophys. Res. Oceans* 119, 1176–1194. doi:10.1002/2013JC009424.
- Forget, G., Campin, J.-M., Heimbach, P., Hill, C. N., Ponte, R. M., and Wunsch, C. (2015). ECCO version 4: an integrated framework for non-linear inverse modeling and global ocean state estimation. *Geosci. Model Dev.* 8, 3071–3104. doi:10.5194/gmd-8-3071-2015.
- Franks, P. J. S. (2002). NPZ models of plankton dynamics: Their Construction, coupling to physics, and application. *J. Oceanogr.* 58, 379–387. doi:10.1023/A:1015874028196.
- Friedlingstein, P., Jones, M. W., O’Sullivan, M., Andrew, R. M., Hauck, J., Peters, G. P., et al. (2019). Global Carbon Budget 2019. *Earth Syst. Sci. Data* 11, 1783–1838. doi:10.5194/essd-11-1783-2019.
- Gardner, W. (1980). Sediment trap dynamics and calibration: a laboratory evaluation. *J. Mar. Res.* 38.
- Gargett, A., and Garner, T. (2008). Determining Thorpe Scales from Ship-Lowered CTD Density Profiles. *J. Atmospheric Ocean. Technol.* 25, 1657–1670. doi:10.1175/2008JTECHO541.1.
- Gasol, J. M., Alonso-Sáez, L., Vaqué, D., Baltar, F., Calleja, M. L., Duarte, C. M., et al. (2009). Mesopelagic prokaryotic bulk and single-cell heterotrophic activity and community composition in the NW Africa-Canary Islands coastal-transition zone. *Prog. Oceanogr.* 83, 189–196. doi:10.1016/j.pocean.2009.07.014.
- Gilly, W. F., Beman, J. M., Litvin, S. Y., and Robison, B. H. (2013). Oceanographic and Biological Effects of Shoaling of the Oxygen Minimum Zone. *Annu. Rev. Mar. Sci.* 5, 393–420. doi:10.1146/annurev-marine-120710-100849.
- Goericke, R., and Ohman, M. D. (2015). Introduction to CCE-LTER: Responses of the California Current Ecosystem to climate forcing. *Deep Sea Res. Part II Top. Stud. Oceanogr.* 112, 1–5. doi:10.1016/j.dsr2.2014.12.001.
- Gomez, F. A., Lee, S.-K., Liu, Y., Hernandez Jr., F. J., Muller-Karger, F. E., and Lamkin, J. T. (2018). Seasonal patterns in phytoplankton biomass across the northern and deep Gulf of Mexico: a numerical model study. *Biogeosciences* 15, 3561–3576. doi:10.5194/bg-15-3561-2018.
- Gontikaki, E., van Oevelen, D., Soetaert, K., and Witte, U. (2011). Food web flows through a sub-arctic deep-sea benthic community. *Prog. Oceanogr.* 91, 245–259. doi:10.1016/j.pocean.2010.12.014.

- Gorsky, G., Ohman, M. D., Picheral, M., Gasparini, S., Stemmann, L., Romagnan, J.-B., et al. (2010). Digital zooplankton image analysis using the ZooScan integrated system. *J. Plankton Res.* 32, 285–303. doi:10.1093/plankt/fbp124.
- Guidi, L., Jackson, G. A., Stemmann, L., Miquel, J. C., Picheral, M., and Gorsky, G. (2008). Relationship between particle size distribution and flux in the mesopelagic zone. *Deep Sea Res. Part Oceanogr. Res. Pap.* 55, 1364–1374. doi:10.1016/j.dsr.2008.05.014.
- Guyennon, A., Baklouti, M., Diaz, F., Palmieri, J., Beuvier, J., Lebaupin-Brossier, C., et al. (2015). New insights into the organic carbon export in the Mediterranean Sea from 3-D modeling. *Biogeosciences* 12, 7025–7046. doi:10.5194/bg-12-7025-2015.
- Hannides, C. C. S., Drazen, J. C., and Popp, B. N. (2015). Mesopelagic zooplankton metabolic demand in the North Pacific Subtropical Gyre. *Limnol. Oceanogr.* 60, 419–428. doi:10.1002/lno.10032.
- Hansen, A. N., and Visser, A. W. (2016a). Carbon export by vertically migrating zooplankton: an optimal behavior model. *Limnol. Oceanogr.* 61, 701–710. doi:10.1002/lno.10249.
- Hansen, A. N., and Visser, A. W. (2016b). Carbon export by vertically migrating zooplankton: an optimal behavior model: Optimal vertical migration and carbon export. *Limnol. Oceanogr.* 61, 701–710. doi:10.1002/lno.10249.
- Harrison, C., Siegel, D., and Mitarai, S. (2013). Filamentation and eddy–eddy interactions in marine larval accumulation and transport. *Mar. Ecol. Prog. Ser.* 472, 27–44. doi:10.3354/meps10061.
- Harrison, W. G., Platt, T., and Lewis, M. R. (1987a). *f*-Ratio and its relationship to ambient nitrate concentration in coastal waters. *J. Plankton Res.* 9, 235–248.
- Harrison, W. G., Platt, T., and Lewis, M. R. (1987b). F-ratio and its relationship to ambient nitrate concentration in coastal waters. *J. Plankton Res.* 9, 235–248. doi:10.1093/plankt/9.1.235.
- Haskell, W. Z., Kadko, D., Hammond, D. E., Knapp, A. N., Prokopenko, M. G., Berelson, W. M., et al. (2015). Upwelling velocity and eddy diffusivity from ⁷Be measurements used to compare vertical nutrient flux to export POC flux in the Eastern Tropical South Pacific. *Mar. Chem.* 168, 140–150. doi:10.1016/j.marchem.2014.10.004.
- Helly, J. J., and Levin, L. A. (2004). Global distribution of naturally occurring marine hypoxia on continental margins. *Deep Sea Res. Part Oceanogr. Res. Pap.* 51, 1159–1168. doi:10.1016/j.dsr.2004.03.009.
- Henson, S. A., Sanders, R., Madsen, E., Morris, P. J., Le Moigne, F., and Quartly, G. D. (2011a). A reduced estimate of the strength of the ocean’s biological carbon pump. *Geophys. Res. Lett.* 38, n/a-n/a. doi:10.1029/2011GL046735.

- Henson, S. A., Sanders, R., Madsen, E., Morris, P. J., Le Moigne, F., and Quartly, G. D. (2011b). A reduced estimate of the strength of the ocean's biological carbon pump. *Geophys. Res. Lett.* 38, 10–14. doi:10.1029/2011GL046735.
- Henson, S. A., Sanders, R., Madsen, E., Morris, P. J., Le Moigne, F., and Quartly, G. D. (2011c). A reduced estimate of the strength of the ocean's biological carbon pump. *Geophys. Res. Lett.* 38, 10–14. doi:10.1029/2011GL046735.
- Henson, S. A., Yool, A., and Sanders, R. (2015). Variability in efficiency of particulate organic carbon export: A model study. *Glob. Biogeochem. Cycles* 29, 33–45. doi:10.1002/2014GB004965.
- Hernandez-Leon, S., Olivar, M. P., Puelles, M. L., Bode, A., Castellon, A., Lopez-Perez, C., et al. doi:10.1029/2018GB006098.
- Hjermann, D., Melsom, A., Dingsor, G. E., and Durant, J. M. (2007). Fish and oil in the Lofoten–Barents Sea system: synoptic review of the effect of oil spills on fish populations. *Mar Ecol Prog Ser*, 17.
- Holl, C. M., Villareal, T. A., Payne, C. D., Clayton, T. D., Hart, C., and Montoya, J. P. (2007). *Trichodesmium* in the western Gulf of Mexico: ¹⁵N₂-fixation and natural abundance stable isotopic evidence. *Limnol. Oceanogr.* 52, 2249–2259. doi:10.4319/lo.2007.52.5.2249.
- Howe, S., Miranda, C., Hayes, C. T., Letscher, R. T., and Knapp, A. N. (2020). The Dual Isotopic Composition of Nitrate in the Gulf of Mexico and Florida Straits. *J. Geophys. Res. Oceans* 125. doi:10.1029/2020JC016047.
- Ikeda, T. (1985a). Metabolic rates of epipelagic marine zooplankton as a function of body mass and temperature. *Mar. Biol.* 85, 1–11.
- Ikeda, T. (1985b). Metabolic rates of epipelagic marine zooplankton as a function of body mass and temperature. 11.
- Ikeda, T. (1985c). Metabolic rates of epipelagic marine zooplankton as a function of body mass and temperature. *Mar. Biol.* 85, 543–552. doi:10.1007/BF00396409.
- Ikeda, T., Kanno, Y., Ozaki, K., and Shinada, A. (2001). Metabolic rates of epipelagic marine copepods as a function of body mass and temperature. *Mar. Biol.* 139, 587–596. doi:10.1007/s002270100608.
- Ito, T., and Follows, M. J. (2003). Upper ocean control on the solubility pump of CO₂. *J. Mar. Res.* 61, 465–489. doi:10.1357/002224003322384898.
- Iversen, M. H., and Lampitt, R. S. (in press). Size does not matter after all: No evidence for a size-sinking relationship for marine snow. *Prog. Oceanogr.* doi:10.1016/j.pocean.2020.102445.

- Iversen, M. H., and Robert, M. L. (2015). Ballasting effects of smectite on aggregate formation and export from a natural plankton community. *Mar. Chem.* 175, 18–27. doi:10.1016/j.marchem.2015.04.009.
- Jackson, G. A., and Burd, A. B. (2015). Simulating aggregate dynamics in ocean biogeochemical models. *Prog. Oceanogr.* 133, 55–65. doi:10.1016/j.pocean.2014.08.014.
- Jackson, G. A., and Eldridge, P. M. (1992). Food web analysis of a planktonic system off Southern California. *Prog. Oceanogr.* 30, 223–251. doi:10.1016/0079-6611(92)90014-Q.
- Jacox, M. G., Hazen, E. L., Zaba, K. D., Rudnick, D. L., Edwards, C. A., Moore, A. M., et al. (2016). Impacts of the 2015–2016 El Niño on the California Current System: Early assessment and comparison to past events. *Geophys. Res. Lett.* 43, 7072–7080. doi:10.1002/2016GL069716.
- Jiménez-Quiroz, M. del C., Cervantes-Duarte, R., Funes-Rodríguez, R., Barón-Campis, S. A., García-Romero, F. de J., Hernández-Trujillo, S., et al. (2019). Impact of “The Blob” and “El Niño” in the SW Baja California Peninsula: Plankton and Environmental Variability of Bahía Magdalena. *Front. Mar. Sci.* 6, 25. doi:10.3389/fmars.2019.00025.
- Juranek, L. W., Feely, R. A., Gilbert, D., Freeland, H., and Miller, L. A. (2011). Real-time estimation of pH and aragonite saturation state from Argo profiling floats: Prospects for an autonomous carbon observing strategy: ESTIMATING PH AND Ω FROM ARGO FLOATS. *Geophys. Res. Lett.* 38, n/a-n/a. doi:10.1029/2011GL048580.
- Juranek, L. W., and Quay, P. D. (2013). Using Triple Isotopes of Dissolved Oxygen to Evaluate Global Marine Productivity. *Annu. Rev. Mar. Sci.* 5, 503–524. doi:10.1146/annurev-marine-121211-172430.
- Kahru, M., Goericke, R., Kelly, T. B., and Stukel, M. R. (2019). Satellite estimation of carbon export by sinking particles in the California Current calibrated with sediment trap data. *Deep Sea Res. Part II Top. Stud. Oceanogr.*, 104639. doi:10.1016/j.dsr2.2019.104639.
- Kahru, M., Jacox, M. G., and Ohman, M. D. (2018a). CCE1: Decrease in the frequency of oceanic fronts and surface chlorophyll concentration in the California Current System during the 2014–2016 northeast Pacific warm anomalies. *Deep Sea Res. Part Oceanogr. Res. Pap.* doi:10.1016/j.dsr.2018.04.007.
- Kahru, M., Jacox, M. G., and Ohman, M. D. (2018b). CCE1: Decrease in the frequency of oceanic fronts and surface chlorophyll concentration in the California Current System during the 2014–2016 northeast Pacific warm anomalies. *Deep Sea Res. Part Oceanogr. Res. Pap.* 140, 4–13. doi:10.1016/j.dsr.2018.04.007.
- Kahru, M., Kudela, R. M., Anderson, C. R., and Mitchell, B. G. (2015). Optimized Merger of Ocean Chlorophyll Algorithms of MODIS-Aqua and VIIRS. *IEEE Geosci. Remote Sens. Lett.* 12, 2282–2285. doi:10.1109/LGRS.2015.2470250.

- Kahru, M., Kudela, R. M., Manzano-Sarabia, M., and Greg Mitchell, B. (2012). Trends in the surface chlorophyll of the California Current: Merging data from multiple ocean color satellites. *Deep-Sea Res. Part II Top. Stud. Oceanogr.* 77–80, 89–98. doi:10.1016/j.dsr2.2012.04.007.
- Kahru, M., Kudela, R., Manzano-Sarabia, M., and Mitchell, B. G. (2009). Trends in primary production in the California Current detected with satellite data. *J. Geophys. Res. Oceans* 114, 1–7. doi:10.1029/2008JC004979.
- Kelly, K. A., Beardsley, R. C., Limeburner, R., Brink, K. H., Paduan, J. D., and Chereskin, T. K. (1998). Variability of the near-surface eddy kinetic energy in the California Current based on altimetric, drifter, and moored current data. *J. Geophys. Res. Oceans* 103, 13067–13083. doi:10.1029/97JC03760.
- Kelly, T. B., Davison, P. C., Goericke, R., Landry, M. R., Ohman, M. D., and Stukel, M. R. (2019). The Importance of Mesozooplankton Diel Vertical Migration for Sustaining a Mesopelagic Food Web. *Front. Mar. Sci.* 6. doi:10.3389/fmars.2019.00508.
- Kelly, T. B., Goericke, R., Kahru, M., Song, H., and Stukel, M. R. (2018). CCE II: Spatial and interannual variability in export efficiency and the biological pump in an eastern boundary current upwelling system with substantial lateral advection. *Deep Sea Res. Part Oceanogr. Res. Pap.* 140, 14–25. doi:10.1016/j.dsr.2018.08.007.
- Kelly, T. B., Knapp, A. N., Landry, M. R., Selph, K. E., Shropshire, T. A., Thomas, R., et al. (in prep). Lateral Advection Supports the Oligotrophic Ecosystem of the Open-Ocean Gulf of Mexico. *Nat. Geosci.*
- Kemp, P. F. ed. (1993). *Handbook of methods in aquatic microbial ecology*. Boca Raton: Lewis Publishers.
- Kiko, R., Hauss, H., Buchholz, F., and Melzner, F. (2016). Ammonium excretion and oxygen respiration of tropical copepods and euphausiids exposed to oxygen minimum zone conditions. *Biogeosciences* 13, 2241–2255. doi:10.5194/bg-13-2241-2016.
- Kiko, R., Hauss, H., Christiansen, S., Faustmann, J., and Rodrigues, E. Zooplankton-mediated fluxes in the Eastern Tropical North Pacific. *Front. Mar. Sci.*
- Kiko, R., Iversen, M. H., Maas, A. E., Hauss, H., and Bianchi, D. eds. (2020). *Zooplankton and Nekton: Gatekeepers of the Biological Pump*. Frontiers Media SA doi:10.3389/978-2-88963-982-3.
- Kirchman, D. L., Morán, X. A. G., and Ducklow, H. (2009). Microbial growth in the polar oceans - role of temperature and potential impact of climate change. *Nat. Rev. Microbiol.* 7, 451–459. doi:10.1038/nrmicro2115.
- Kleerekoper, H. (1953). The Mineralization of Plankton. *J. Fish. Res. Board Can.* 10.

- Klein, P., and Coste, B. (1984). Effects of wind-stress variability on nutrient transport into the mixed layer. *Deep Sea Res. Part Oceanogr. Res. Pap.* 31, 21–37. doi:10.1016/0198-0149(84)90070-0.
- Knapp, A. N., Thomas, R., Stukel, M. R., Kelly, T. B., Landry, M. R., Selph, K. E., et al. (submitted). Constraining the sources of nitrogen fueling phytoplankton and food webs in the Gulf of Mexico using nitrogen isotope budgets. *J. Plankton Res.*
- Knauer, G. A., Martin, J. H., and Bruland, K. W. (1979a). Fluxes of particulate carbon, nitrogen, and phosphorus in the upper water column of the northeast Pacific. *Deep Sea Res. Part Oceanogr. Res. Pap.* 26, 97–108. doi:10.1016/0198-0149(79)90089-X.
- Knauer, G. A., Martin, J. H., and Bruland, K. W. (1979b). Fluxes of particulate carbon, nitrogen, and phosphorus in the upper water column of the northeast Pacific. *Deep Sea Res. Part Oceanogr. Res. Pap.* 26, 97–108. doi:10.1016/0198-0149(79)90089-X.
- Knauer, G. A., Martin, J. H., and Bruland, K. W. (1979c). Fluxes of particulate carbon, nitrogen, and phosphorus in the upper water column of the northeast Pacific. *Deep Sea Res. Part Oceanogr. Res. Pap.* 26, 97–108. doi:10.1016/0198-0149(79)90089-X.
- Knauer, G. A., Martin, J. H., and Bruland, K. W. (1979d). Fluxes of particulate carbon, nitrogen, and phosphorus in the upper water column of the northeast Pacific. *Deep Sea Res. Part Oceanogr. Res. Pap.* 26, 97–108. doi:10.1016/0198-0149(79)90089-X.
- Kones, J. K., Soetaert, K., van Oevelen, D., and Owino, J. O. (2009). Are network indices robust indicators of food web functioning? A Monte Carlo approach. *Ecol. Model.* 220, 370–382. doi:10.1016/j.ecolmodel.2008.10.012.
- Kranz, S. A., Wang, S., Kelly, T. B., Stukel, M. R., Goericke, R., Landry, M. R., et al. (2020). Lagrangian Studies of Marine Production: A Multimethod Assessment of Productivity Relationships in the California Current Ecosystem Upwelling Region. *J. Geophys. Res. Oceans* 125. doi:10.1029/2019JC015984.
- Krause, J. W., Brzezinski, M. A., Goericke, R., Landry, M. R., Ohman, M. D., Stukel, M. R., et al. (2015a). Variability in diatom contributions to biomass, organic matter production and export across a frontal gradient in the California Current Ecosystem. *J. Geophys. Res. Oceans* 120, 1032–1047. doi:10.1002/2014JC010472.
- Krause, J. W., Brzezinski, M. A., Goericke, R., Landry, M. R., Ohman, M. D., Stukel, M. R., et al. (2015b). Variability in diatom contributions to biomass, organic matter production and export across a frontal gradient in the California Current Ecosystem. *J. Geophys. Res. Oceans* 120, 1032–1047. doi:10.1002/2014JC010472.
- Kroes, H. W. (1977). The niche structure of ecosystems. *J. Theor. Biol.* 65, 317–326. doi:10.1016/0022-5193(77)90327-7.

- Landry, M. R., Al-Mutairi, H., Selph, K. E., Christensen, S., and Nunnery, S. (2001). Seasonal patterns of mesozooplankton abundance and biomass at Station ALOHA. *Deep Sea Res. Part II Top. Stud. Oceanogr.* 48, 2037–2061. doi:10.1016/S0967-0645(00)00172-7.
- Landry, M. R., Beckley, L. E., and Muhling, B. A. (2019). Climate sensitivities and uncertainties in food-web pathways supporting larval bluefin tuna in subtropical oligotrophic oceans. *ICES J. Mar. Sci.* 76, 359–369. doi:10.1093/icesjms/fsy184.
- Landry, M. R., Brown, S. L., Rii, Y. M., Selph, K. E., Bidigare, R. R., Yang, E. J., et al. (2008). Depth-stratified phytoplankton dynamics in Cyclone Opal, a subtropical mesoscale eddy. *Deep Sea Res. Part II Top. Stud. Oceanogr.* 55, 1348–1359. doi:10.1016/j.dsr2.2008.02.001.
- Landry, M. R., Lorenzen, C. J., and Peterson, W. K. (1994). Mesozooplankton grazing in the Southern California Bight. II. Grazing impact and particulate flux. *Mar. Ecol. Prog. Ser.* 115, 73–85.
- Landry, M. R., Ohman, M. D., Goericke, R., Stukel, M. R., Barbeau, K. A., Bundy, R., et al. (2012a). Pelagic community responses to a deep-water front in the California Current Ecosystem: Overview of the A-Front Study. *J. Plankton Res.* 34, 739–748. doi:10.1093/plankt/fbs025.
- Landry, M. R., Ohman, M. D., Goericke, R., Stukel, M. R., Barbeau, K. A., Bundy, R., et al. (2012b). Pelagic community responses to a deep-water front in the California Current Ecosystem: Overview of the A-Front Study. *J. Plankton Res.* 34, 739–748. doi:10.1093/plankt/fbs025.
- Landry, M. R., Ohman, M. D., Goericke, R., Stukel, M. R., and Tsyrklevich, K. (2009a). Lagrangian studies of phytoplankton growth and grazing relationships in a coastal upwelling ecosystem off Southern California. *Prog. Oceanogr.* 83, 208–216. doi:10.1016/j.pocean.2009.07.026.
- Landry, M. R., Ohman, M. D., Goericke, R., Stukel, M. R., and Tsyrklevich, K. (2009b). Lagrangian studies of phytoplankton growth and grazing relationships in a coastal upwelling ecosystem off Southern California. *Prog. Oceanogr.* 83, 208–216. doi:10.1016/j.pocean.2009.07.026.
- Landry, M. R., Selph, K. E., Stukel, M. R., Swalethorp, R., Kelly, T. B., Beatty, J., et al. (submitted). Microbial Food Web Dynamics in the Oceanic Gulf of Mexico. *J. Plankton Res.*
- Landry, M. R., Selph, K. E., Taylor, A. G., Décima, M., Balch, W. M., and Bidigare, R. R. (2011). Phytoplankton growth, grazing and production balances in the HNLC equatorial Pacific. *Deep Sea Res. Part II Top. Stud. Oceanogr.* 58, 524–535. doi:10.1016/j.dsr2.2010.08.011.

- Large, W. G., McWilliams, J. C., and Doney, S. C. (1994). Oceanic vertical mixing: A review and a model with a nonlocal boundary layer parameterization. *Rev. Geophys.* 32, 363. doi:10.1029/94RG01872.
- Laurent, A., Fennel, K., Ko, D. S., and Lehrter, J. (2018). Climate Change Projected to Exacerbate Impacts of Coastal Eutrophication in the Northern Gulf of Mexico. *J. Geophys. Res. Oceans* 123, 3408–3426. doi:10.1002/2017JC013583.
- Lavaniegos, B. E., and Ohman, M. D. (2007). Coherence of long-term variations of zooplankton in two sectors of the California Current System. *Prog. Oceanogr.* 75, 42–69. doi:10.1016/j.pocean.2007.07.002.
- Laws, E. (2004). Export flux and stability as regulators of community composition in pelagic marine biological communities: Implications for regime shifts. *Prog. Oceanogr.* 60, 343–354. doi:10.1016/j.pocean.2004.02.015.
- Laws, E. A., D'Sa, E., and Naik, P. (2011a). Simple equations to estimate ratios of new or export production to total production from satellite-derived estimates of sea surface temperature and primary production. *Limnol. Oceanogr. Methods* 9, 593–601. doi:10.4319/lom.2011.9.593.
- Laws, E. A., D'Sa, E., and Naik, P. (2011b). Simple equations to estimate ratios of new or export production to total production from satellite-derived estimates of sea surface temperature and primary production. *Limnol. Oceanogr. Methods* 9, 593–601. doi:10.4319/lom.2011.9.593.
- Laws, E. A., D'Sa, E., and Naik, P. (2011c). Simple equations to estimate ratios of new or export production to total production from satellite-derived estimates of sea surface temperature and primary production: Equations for ef ratios. *Limnol. Oceanogr. Methods* 9, 593–601. doi:10.4319/lom.2011.9.593.
- Laws, E. A., Ducklow, H., and McCarthy, J. J. (2000a). Temperature effects on export production in the open ocean. *Glob. Biogeochem. Cycles* 14, 1231–1246. doi:10.1029/1999GB001229.
- Laws, E. A., Falkowski, P. G., Smith, W. O., Ducklow, H., and McCarthy, J. J. (2000b). Temperature effects on export production in the open ocean. *Glob. Biogeochem. Cycles* 14, 1231–1246. doi:10.1029/1999GB001229.
- Laws, E. A., Landry, M. R., Barber, R. T., Campbell, L., Dickson, M.-L., and Marra, J. (2000c). Carbon cycling in primary production bottle incubations: inferences from grazing experiments and photosynthetic studies using ^{14}C and ^{18}O in the Arabian Sea. 14.
- Laws, E. A., and Maiti, K. (2019). The relationship between primary production and export production in the ocean: Effects of time lags and temporal variability. *Deep Sea Res. Part Oceanogr. Res. Pap.* 148, 100–107. doi:10.1016/j.dsr.2019.05.006.

- Laxenaire, R., Speich, S., Blanke, B., Chaigneau, A., Pegliasco, C., and Stegner, A. (2018). Anticyclonic Eddies Connecting the Western Boundaries of Indian and Atlantic Oceans. *J. Geophys. Res. Oceans* 123, 7651–7677. doi:10.1029/2018JC014270.
- Lee, M.-M., and Coward, A. (2003). Eddy mass transport for the Southern Ocean in an eddy-permitting global ocean model. *Ocean Model.* 5, 249–266. doi:10.1016/S1463-5003(02)00044-6.
- Lefevre, D., Minas, H. J., Minas, M., Robinson, C., Le B. Williams, P. J., and Woodward, E. M. S. (1997). Review of gross community production, primary production, net community production and dark community respiration in the Gulf of Lions. *Deep Sea Res. Part II Top. Stud. Oceanogr.* 44, 801–832. doi:10.1016/S0967-0645(96)00091-4.
- Lerner, P., Marchal, O., Lam, P. J., Anderson, R. F., Buesseler, K., Charette, M. A., et al. (2016). Testing models of thorium and particle cycling in the ocean using data from station GT11-22 of the U.S. GEOTRACES North Atlantic section. *Deep Sea Res. Part Oceanogr. Res. Pap.* 113, 57–79. doi:10.1016/j.dsr.2016.03.008.
- Letscher, R. T., Primeau, F., and Moore, J. K. (2016). Nutrient budgets in the subtropical ocean gyres dominated by lateral transport. *Nat. Geosci.* 9, 815–819. doi:10.1038/ngeo2812.
- Levy, M., Bopp, L., Karleskind, P., Resplandy, L., Ethe, C., and Pinsard, F. (2013a). Physical pathways for carbon transfers between the surface mixed layer and the ocean interior. *Glob. Biogeochem. Cycles* 27, 1001–1012. doi:10.1002/gbc.20092.
- Levy, M., Bopp, L., Karleskind, P., Resplandy, L., Ethe, C., and Pinsard, F. (2013b). Physical pathways for carbon transfers between the surface mixed layer and the ocean interior: PHYSICAL CARBON FLUXES. *Glob. Biogeochem. Cycles* 27, 1001–1012. doi:10.1002/gbc.20092.
- Li, Q. P., Franks, P. J. S., Landry, M. R., Goericke, R., and Taylor, A. G. (2010). Modeling phytoplankton growth rates and chlorophyll to carbon ratios in California coastal and pelagic ecosystems. *J. Geophys. Res.* 115. doi:10.1029/2009JG001111.
- Lilly, L. E., and Ohman, M. D. CCE IV: El Niño-related zooplankton variability in the southern California Current System. *Deep Sea Res. Part Oceanogr. Res. Pap.*
- Lilly, L. E., and Ohman, M. D. (2018). CCE IV El Niño-related zooplankton variability in the southern California Current System. *Deep Sea Res. Part Oceanogr. Res. Pap.* 140, 36–51.
- Liszka, C. M., Manno, C., Stowasser, G., Robinson, C., and Tarling, G. A. (2019). Mesozooplankton Community Composition Controls Fecal Pellet Flux and Remineralization Depth in the Southern Ocean. *Front. Mar. Sci.* 6, 230. doi:10.3389/fmars.2019.00230.
- Lomas, M. W., Bates, N. R., Johnson, R. J., Knap, A. H., Steinberg, D. K., and Carlson, C. A. (2013). Two decades and counting: 24-years of sustained open ocean biogeochemical

- measurements in the Sargasso Sea. *Deep-Sea Res. Part II Top. Stud. Oceanogr.* 93, 16–32. doi:10.1016/j.dsr2.2013.01.008.
- Longhurst, A. R., Bedo, A. W., Harrison, W. G., Head, E. J. H., and Sameoto, D. D. (1990). Vertical flux of respiratory carbon by oceanic diel migrant biota. *Deep Sea Res. Part Oceanogr. Res. Pap.* 37, 685–694. doi:10.1016/0198-0149(90)90098-G.
- Maiti, K., Bosu, S., D'Sa, E. J., Adhikari, P. L., Sutor, M., and Longnecker, K. (2016a). Export fluxes in northern Gulf of Mexico - Comparative evaluation of direct, indirect and satellite-based estimates. *Mar. Chem.* 184, 60–77. doi:10.1016/j.marchem.2016.06.001.
- Maiti, K., Bosu, S., D'Sa, E. J., Adhikari, P. L., Sutor, M., and Longnecker, K. (2016b). Export fluxes in northern Gulf of Mexico - Comparative evaluation of direct, indirect and satellite-based estimates. *Mar. Chem.* 184, 60–77. doi:10.1016/j.marchem.2016.06.001.
- Maiti, K., Charette, M. A., Buesseler, K. O., and Kahru, M. (2013a). An inverse relationship between production and export efficiency in the Southern Ocean. *Geophys. Res. Lett.* 40, 1557–1561. doi:10.1002/grl.50219.
- Maiti, K., Charette, M. A., Buesseler, K. O., and Kahru, M. (2013b). An inverse relationship between production and export efficiency in the Southern Ocean. *Geophys. Res. Lett.* 40, 1557–1561. doi:10.1002/grl.50219.
- Marchesiello, P., McWilliams, J. C., and Shepetchkin, A. (2003). Equilibrium Structure and Dynamics of the California Current System. *J. Phys. Oceanogr.* 33, 31.
- Marra, J. (2009). Net and gross productivity: Weighing in with ¹⁴C. *Aquat. Microb. Ecol.* 56, 123–131. doi:10.3354/ame01306.
- Marsay, C. M., Sanders, R. J., Henson, S. A., Pabortsava, K., Achterberg, E. P., and Lampitt, R. S. (2015a). Attenuation of sinking particulate organic carbon flux through the mesopelagic ocean. *Proc. Natl. Acad. Sci.* 112, 1089–1094. doi:10.1073/pnas.1415311112.
- Marsay, C. M., Sanders, R. J., Henson, S. A., Pabortsava, K., Achterberg, E. P., and Lampitt, R. S. (2015b). Attenuation of sinking particulate organic carbon flux through the mesopelagic ocean. *Proc. Natl. Acad. Sci.* 112, 1089–1094. doi:10.1073/pnas.1415311112.
- Martens-Habbena, W., Berube, P. M., Urakawa, H., de la Torre, J. R., and Stahl, D. A. (2009). Ammonia oxidation kinetics determine niche separation of nitrifying Archaea and Bacteria. *Nature* 461, 976–979. doi:10.1038/nature08465.
- Mathis, J. T., Pickart, R. S., Hansell, D. A., Kadko, D., and Bates, N. R. (2007). Eddy transport of organic carbon and nutrients from the Chukchi Shelf: Impact on the upper halocline of the western Arctic Ocean. *J. Geophys. Res.* 112, C05011. doi:10.1029/2006JC003899.

- McClatchie, S., Goericke, R., Leising, A. W., Auth, T. D., Bjorkstedt, E., Robertson, R., et al. (2016). State of the California Current 2015 – 16: Comparisons With the 1997 – 98 El Niño. *Calif. Coop. Ocean. Fish. Investig. Rep.* 57, 5–61.
- McDonnell, A. M. P., Lam, P. J., Lamborg, C. H., Buesseler, K. O., Sanders, R., Riley, J. S., et al. (2015). The oceanographic toolbox for the collection of sinking and suspended marine particles. *Prog. Oceanogr.* 133, 17–31. doi:10.1016/j.pocean.2015.01.007.
- Merino, M. (1997). Upwelling on the Yucatan Shelf: hydrographic evidence. *J. Mar. Syst.* 13, 101–121.
- Michaels, A. F., and Silver, M. W. (1988). Primary production, sinking fluxes and the microbial food web. *Deep-Sea Res.* 35, 473–490.
- Milligan, A. J., Halsey, K. H., and Behrenfeld, M. J. (2014). HORIZONS:Advancing interpretations of ¹⁴C-uptake measurements in the context of phytoplankton physiology and ecology. *J. Plankton Res.* 37, 692–698. doi:10.1093/plankt/fbv051.
- Milligan, A. J., Halsey, K. H., and Behrenfeld, M. J. (2015). Advancing interpretations of ¹⁴C-uptake measurements in the context of phytoplankton physiology and ecology. *J. Plankton Res.* 37, 692–698. doi:10.1093/plankt/fbv051.
- Minagawa, M., and Wada, E. (1986). Nitrogen isotope ratios of red tide organisms in the East China Sea: A characterization of biological nitrogen fixation. *Mar. Chem.* 19, 245–259. doi:10.1016/0304-4203(86)90026-5.
- Morales, C. E. (1999). Carbon and nitrogen fluxes in the oceans: the contribution by zooplankton migrants to active transport in the North Atlantic during the Joint Global Ocean Flux Study. *J. Plankton Res.* 21, 1799–1808. doi:10.1093/plankt/21.9.1799.
- Morozov, A. Y., and Kuzenkov, O. A. (2016). Towards developing a general framework for modelling vertical migration in zooplankton. *J. Theor. Biol.* 405, 17–28. doi:10.1016/j.jtbi.2016.01.011.
- Morrow, R., Goericke, R., Kelly, T. B., Landry, M. R., Ohman, M. D., Stephens, B. M., et al. Primary Productivity, Mesozooplankton Grazing, and the Biological Pump in the California Current Ecosystem: Variability and Response to El Niño. *Deep-Sea Res. I.*
- Morrow, R. M., Ohman, M. D., Goericke, R., Kelly, T. B., Stephens, B. M., and Stukel, M. R. (2018a). CCE V: Primary production, mesozooplankton grazing, and the biological pump in the California Current Ecosystem: Variability and response to El Niño. *Deep-Sea Res. Part Oceanogr. Res. Pap.* 140, 52–62. doi:10.1016/j.dsr.2018.07.012.
- Morrow, R. M., Ohman, M. D., Goericke, R., Kelly, T. B., Stephens, B. M., and Stukel, M. R. (2018b). CCE V: Primary production, mesozooplankton grazing, and the biological pump in the California Current Ecosystem: Variability and response to El Niño. *Deep Sea Res. Part Oceanogr. Res. Pap.* 140, 52–62. doi:10.1016/j.dsr.2018.07.012.

- Mulholland, M. R., Bernhardt, P. W., Widner, B. N., Selden, C. R., Chappell, P. D., Clayton, S., et al. (2019). High Rates of N₂ Fixation in Temperate, Western North Atlantic Coastal Waters Expand the Realm of Marine Diazotrophy. *Glob. Biogeochem. Cycles* 33, 826–840. doi:10.1029/2018GB006130.
- Murnane, R. J., Sarmiento, J. L., and Bacon, M. P. (1990). Thorium isotopes, particle cycling models, and inverse calculations of model rate constants. *J. Geophys. Res.* 95, 16195. doi:10.1029/JC095iC09p16195.
- Nagai, T., Gruber, N., Frenzel, H., Lachkar, Z., McWilliams, J. C., and Plattner, G.-K. (2015). Dominant role of eddies and filaments in the offshore transport of carbon and nutrients in the California Current System. *J. Geophys. Res. Oceans* 120, 5318–5341. doi:10.1002/2015JC010889.
- NASA Ocean Biology Processing Group (2017). MODIS-Aqua Level 3 Mapped Particulate Organic Carbon Data Version R2018.0. doi:10.5067/AQUA/MODIS/L3M/POC/2018.
- NASA Ocean Biology Processing Group (2018). MODIS-TERRA Level 3 Mapped Particulate Organic Carbon Data Version R2018.0. doi:10.5067/TERRA/MODIS/L3M/POC/2018.
- Neuer, S., Davenport, R., Freudenthal, T., Wefer, G., Llinás, O., Rueda, M.-J., et al. (2002). Differences in the biological carbon pump at three subtropical ocean sites. *Geophys. Res. Lett.* 29, 32-1-32–4. doi:10.1029/2002GL015393.
- North, E. W., Hood, R. R., Chao, S. Y., and Sanford, L. P. (2006). Using a random displacement model to simulate turbulent particle motion in a baroclinic frontal zone: A new implementation scheme and model performance tests. *J. Mar. Syst.* 60, 365–380. doi:10.1016/j.jmarsys.2005.08.003.
- Oey, L.-Y., Ezer, T., and Lee, H.-C. (2013). “Loop Current, Rings and Related Circulation in the Gulf of Mexico: A Review of Numerical Models and Future Challenges,” in *Geophysical Monograph Series*, eds. W. Sturges and A. Lugo-Fernandez, 31–56. doi:10.1029/161GM04.
- Ohman, M. D., Barbeau, K., Franks, P. J. S., Landry, M. R., and Miller, A. J. (2013). Ecological Transitions in a Coastal Upwelling Ecosystem. *Oceanography* 26, 162–173. doi:10.5670/oceanog.2011.65.
- Ohman, M. D., Powell, J. R., Picheral, M., and Jensen, D. W. (2012a). Mesozooplankton and particulate matter responses to a deep-water frontal system in the southern California Current System. *J. Plankton Res.* 34, 815–827. doi:10.1093/plankt/fbs028.
- Ohman, M. D., Powell, J. R., Picheral, M., and Jensen, D. W. (2012b). Mesozooplankton and particulate matter responses to a deep-water frontal system in the southern California Current System. *J. Plankton Res.* 34, 815–827. doi:10.1093/plankt/fbs028.

- Ohman, M. D., and Romagnan, J. B. (2016). Nonlinear effects of body size and optical attenuation on Diel Vertical Migration by zooplankton. *Limnol. Oceanogr.* 61, 765–770. doi:10.1002/lno.10251.
- Oke, P. R., and Schiller, A. (2007). Impact of Argo, SST, and altimeter data on an eddy-resolving ocean reanalysis. *Geophys. Res. Lett.* 34, L19601. doi:10.1029/2007GL031549.
- Olivieri, R. A., and Chavez, F. P. (2000). A model of plankton dynamics for the coastal upwelling system of Monterey Bay, California. *Deep-Sea Res. II* 47, 1077–1106. doi:10.1016/S0967-0645(99)00137-X.
- Omand, M. M., D’Asaro, E. A., Lee, C. M., Perry, M. J., Briggs, N., Cetini, I., et al. (2015). Eddy-driven subduction exports particulate organic carbon from the spring bloom. *Science* 348, 222–225. doi:10.1126/science.1260062.
- Oschlies, A. (2002). Nutrient supply to the surface waters of the North Atlantic: A model study. *J. Geophys. Res.* 107, 3046. doi:10.1029/2000JC000275.
- Otis, D., Le Hénaff, M., Kourafalou, V., McEachron, L., and Muller-Karger, F. (2019). Mississippi River and Campeche Bank (Gulf of Mexico) Episodes of Cross-Shelf Export of Coastal Waters Observed with Satellites. *Remote Sens.* 11, 723. doi:10.3390/rs11060723.
- Peterson, B. J. (1980). PRODUCTIVITY AND THE 14C-CO2 METHOD : A History of the Productivity Problem. *Ecology* 11, 359–385.
- Pike, S. M., Buesseler, K. O., Andrews, J., and Savoye, N. (2005a). Quantification of ²³⁴Th recovery in small volume sea water samples by inductively coupled plasma-mass spectrometry. *J. Radioanal. Nucl. Chem.* 263, 355–360. doi:10.1007/s10967-005-0062-9.
- Pike, S. M., Buesseler, K. O., Andrews, J., and Savoye, N. (2005b). Quantification of ²³⁴Th recovery in small volume sea water samples by inductively coupled plasma-mass spectrometry. *J. Radioanal. Nucl. Chem.* 263, 355–360. doi:10.1007/s10967-005-0062-9.
- Plattner, G.-K. (2005). Decoupling marine export production from new production. *Geophys. Res. Lett.* 32, L11612. doi:10.1029/2005GL022660.
- Plattner, G.-K., Gruber, N., Frenzel, H., and McWilliams, J. C. (2005). Decoupling marine export production from new production. *Geophys. Res. Lett.* 32. doi:10.1029/2005GL022660.
- Powell, J. R., and Ohman, M. D. (2012). Use of glider-class acoustic Doppler profilers for estimating zooplankton biomass. *J. Plankton Res.* 34, 563–568. doi:10.1093/plankt/fbs023.
- Powell, J. R., and Ohman, M. D. (2015). Changes in zooplankton habitat, behavior, and acoustic scattering characteristics across glider-resolved fronts in the Southern California Current System. *Prog. Oceanogr.* 134, 77–92. doi:10.1016/j.pocean.2014.12.011.

- Roberts, G. O., Gelman, A., and Gilks, W. R. (1997). Weak convergence and optimal scaling of random walk Metropolis algorithms. *Ann. Appl. Probab.* 7, 110–120. doi:10.1214/aoap/1034625254.
- Roberts, G. O., and Rosenthal, J. S. (2001). Optimal scaling for various Metropolis-Hastings algorithms. *Stat. Sci.* 16, 351–367. doi:10.1214/ss/1015346320.
- Robinson, C., Steinberg, D. K., Anderson, T. R., Arístegui, J., Carlson, C. A., Frost, J. R., et al. (2010). Mesopelagic zone ecology and biogeochemistry – a synthesis. *Deep Sea Res. Part II Top. Stud. Oceanogr.* 57, 1504–1518. doi:10.1016/j.dsr2.2010.02.018.
- Roussenov, V., Williams, R. G., Mahaffey, C., and Wolff, G. A. (2006). Does the transport of dissolved organic nutrients affect export production in the Atlantic Ocean? *Glob. Biogeochem. Cycles* 20. doi:10.1029/2005GB002510.
- Rumyantseva, A., Lucas, N., Rippeth, T., Martin, A., Painter, S. C., Boyd, T. J., et al. (2015). Ocean nutrient pathways associated with the passage of a storm. *Glob. Biogeochem. Cycles* 29, 1179–1189. doi:10.1002/2015GB005097.
- Sahl, L. E., Wiesenburg, D. A., and Merrell, W. J. (1997). Interactions of mesoscale features with Texas shelf and slope waters. *Cont. Shelf Res.* 17, 117–136. doi:10.1016/S0278-4343(96)00017-9.
- Sailley, S. F., Ducklow, H. W., Moeller, H. V., Fraser, W. R., Schofield, O. M., Steinberg, D. K., et al. (2013). Carbon fluxes and pelagic ecosystem dynamics near two western Antarctic Peninsula Adélie penguin colonies: An inverse model approach. *Mar. Ecol. Prog. Ser.* 492, 253–272. doi:10.3354/meps10534.
- Saint-béat, B., Vézina, A. F., Asmus, R., Asmus, H., and Niquil, N. (2013). The mean function provides robustness to linear inverse modelling flow estimation in food webs : A comparison of functions derived from statistics and ecological theories. *Ecol. Model.* 258, 53–64. doi:10.1016/j.ecolmodel.2013.01.023.
- Samo, T. J., Pedler, B. E., Ball, G. I., Pasulka, A. L., Taylor, A. G., Aluwihare, L. I., et al. (2012). Microbial distribution and activity across a water mass frontal zone in the California Current Ecosystem. *J. Plankton Res.* 34, 802–814. doi:10.1093/plankt/fbs048.
- Sarmiento, J. L., Hughes, T. M. C., Stouffer, R. J., and Manabe, S. (1998). Simulated response of the ocean carbon cycle to anthropogenic climate warming. *Nature* 393, 245–249. doi:10.1038/30455.
- Savoie, N., Benitez-Nelson, C., Burd, A. B., Cochran, J. K., Charette, M., Buesseler, K. O., et al. (2006a). ²³⁴Th sorption and export models in the water column: A review. *Mar. Chem.* 100, 234–249. doi:10.1016/j.marchem.2005.10.014.
- Savoie, N., Benitez-Nelson, C., Burd, A. B., Cochran, J. K., Charette, M., Buesseler, K. O., et al. (2006b). ²³⁴Th sorption and export models in the water column: A review. *Mar. Chem.* 100, 234–249. doi:10.1016/j.marchem.2005.10.014.

- Seibel, B. A. (2011). Critical oxygen levels and metabolic suppression in oceanic oxygen minimum zones. *J. Exp. Biol.* 214, 326–336. doi:10.1242/jeb.049171.
- Selph, K. E., Swalethorp, R., Stukel, M. R., Kelly, T. B., Knapp, A. N., Fleming, K., et al. (submitted). Phytoplankton assemblages in the open ocean water of the Gulf of Mexico during May 2017 and 2018. *J. Plankton Res.*
- Shropshire, T. A., Morey, S. L., Chassignet, E. P., Bozec, A., Coles, V. J., Landry, M. R., et al. (2020). Quantifying spatiotemporal variability in zooplankton dynamics in the Gulf of Mexico with a physical–biogeochemical model. *Biogeosciences* 17, 3385–3407. doi:10.5194/bg-17-3385-2020.
- Siegel, D. A., Buesseler, K. O., Doney, S. C., Sailley, S. F., Behrenfeld, M. J., and Boyd, P. W. (2014a). Global assessment of ocean carbon export by combining satellite observations and food-web models. *Glob. Biogeochem. Cycles* 28, 181–196. doi:10.1002/2013GB004743.
- Siegel, D. A., Buesseler, K. O., Doney, S. C., Sailley, S. F., Behrenfeld, M. J., and Boyd, P. W. (2014b). Global assessment of ocean carbon export by combining satellite observations and food-web models. *Glob. Biogeochem. Cycles* 28, 181–196. doi:10.1002/2013GB004743.
- Siegel, D. A., Buesseler, K. O., Doney, S. C., Sailley, S. F., Behrenfeld, M. J., and Boyd, P. W. (2014c). Global assessment of ocean carbon export by combining satellite observations and food-web models. *Glob. Biogeochem. Cycles* 28, 181–196. doi:10.1002/2013GB004743. Received.
- Smith, K. L., Ruhl, H. A., Huffard, C. L., Messié, M., and Kahru, M. (2018). Episodic organic carbon fluxes from surface ocean to abyssal depths during long-term monitoring in NE Pacific. *Proc. Natl. Acad. Sci.* 115, 12235–12240. doi:10.1073/pnas.1814559115.
- Soetaert, K., Van den Meersche, K., van Oevelen, D., and LAPACK authors (2017). Package “limSolve.” *CRAN*. Available at: <https://cran.r-project.org/package=limSolve>.
- Song, H., Miller, A. J., McClatchie, S., Weber, E. D., Nieto, K. M., and Checkley, D. M. (2012). Application of a data-assimilation model to variability of Pacific sardine spawning and survivor habitats with ENSO in the California Current System. *J. Geophys. Res. Oceans* 117. doi:10.1029/2011JC007302.
- Steinberg, D. K., Carlson, C. A., Bates, N. R., Goldthwait, S. A., Madin, L. P., and Michaels, A. F. (2000). Zooplankton vertical migration and the active transport of dissolved organic and inorganic carbon in the Sargasso Sea. *Deep Sea Res. Part Oceanogr. Res. Pap.* 47, 137–158. doi:10.1016/S0967-0637(99)00052-7.
- Steinberg, D. K., Goldthwait, S. A., and Hansell, D. A. (2002). Zooplankton vertical migration and the active transport of dissolved organic and inorganic nitrogen in the Sargasso Sea. *Deep Sea Res. Part Oceanogr. Res. Pap.* 49, 1445–1461. doi:10.1016/S0967-0637(02)00037-7.

- Steinberg, D. K., and Landry, M. R. (2017a). Zooplankton and the Ocean Carbon Cycle. *Annu. Rev. Mar. Sci.* 9, 413–444. doi:10.1146/annurev-marine-010814-015924.
- Steinberg, D. K., and Landry, M. R. (2017b). Zooplankton and the Ocean Carbon Cycle. *Annu. Rev. Mar. Sci.* 9, 413–444. doi:10.1146/annurev-marine-010814-015924.
- Steinberg, D. K., and Landry, M. R. (2017c). Zooplankton and the Ocean Carbon Cycle. *Annu. Rev. Mar. Sci.* 9, 413–444. doi:10.1146/annurev-marine-010814-015924.
- Steinberg, D. K., Van Mooy, B. A. S., Buesseler, K. O., Boyd, P. W., Kobari, T., and Karl, D. M. (2008). Bacterial vs. zooplankton control of sinking particle flux in the ocean’s twilight zone. *Limnol. Oceanogr.* 53, 1327–1338. doi:10.4319/lo.2008.53.4.1327.
- Stemmann, L., Jackson, G. A., and Gorsky, G. (2004). A vertical model of particle size distributions and fluxes in the midwater column that includes biological and physical processes—Part II: application to a three year survey in the NW Mediterranean Sea. *Deep Sea Res. Part Oceanogr. Res. Pap.* 51, 885–908. doi:10.1016/j.dsr.2004.03.002.
- Straile, D. (1997). Gross Growth Efficiencies of Protozoan and Metazoan Zooplankton and Their Dependence on Food Concentration , Predator-Prey Weight Ratio, and Taxonomic Group. *Limnol. Oceanogr.* 42, 1375–1385.
- Strickland, J. D. H., and Parsons, T. R. (1972). *A Practical handbook of Seawater Analysis*. Fisheries Research Board of Canada.
- Stukel, M., Ohman, M., Benitez-Nelson, C., and Landry, M. (2013a). Contributions of mesozooplankton to vertical carbon export in a coastal upwelling system. *Mar. Ecol. Prog. Ser.* 491, 47–65. doi:10.3354/meps10453.
- Stukel, M. R. (2020). Investigating equations for measuring dissolved inorganic nutrient uptake in oligotrophic conditions. *Ecology* doi:10.1101/2020.08.30.274449.
- Stukel, M. R., Aluwihare, L. I., Barbeau, K. A., Chekalyuk, A. M., Goericke, R., Miller, A. J., et al. (2017a). Mesoscale ocean fronts enhance carbon export due to gravitational sinking and subduction. *Proc. Natl. Acad. Sci.* 114, 1252–1257. doi:10.1073/pnas.1609435114.
- Stukel, M. R., and Barbeau, K. A. (2020). Investigating the Nutrient Landscape in a Coastal Upwelling Region and Its Relationship to the Biological Carbon Pump. *Geophys. Res. Lett.* 47. doi:10.1029/2020GL087351.
- Stukel, M. R., Décima, M., and Kelly, T. B. (2018a). A new approach for incorporating 15N isotopic data into linear inverse ecosystem models with Markov Chain Monte Carlo sampling. *PLoS ONE* 13. doi:10.1371/journal.pone.0199123.
- Stukel, M. R., Décima, M., and Kelly, T. B. (2018b). A new approach for incorporating 15N isotopic data into linear inverse ecosystem models with Markov Chain Monte Carlo sampling. *PLOS ONE* 13, e0199123. doi:10.1371/journal.pone.0199123.

- Stukel, M. R., Décima, M., Landry, M. R., and Selph, K. E. (2018c). Nitrogen and Isotope Flows Through the Costa Rica Dome Upwelling Ecosystem: The Crucial Mesozooplankton Role in Export Flux. *Glob. Biogeochem. Cycles* 32, 1815–1832. doi:10.1029/2018GB005968.
- Stukel, M. R., and Ducklow, H. W. (2017). Stirring Up the Biological Pump: Vertical Mixing and Carbon Export in the Southern Ocean. *Glob. Biogeochem. Cycles* 31, 1420–1434. doi:10.1002/2017GB005652.
- Stukel, M. R., Gerard, T., Kelly, T. B., Knapp, A. N., Laiz-Carrión, R., Lamkin, J. T., et al. (submitted). Plankton food webs of the Gulf of Mexico spawning grounds of Atlantic Bluefin tuna. *J. Plankton Res.*
- Stukel, M. R., Goericke, R., and Landry, M. R. (2019a). Predicting primary production in the southern California Current Ecosystem from chlorophyll, nutrient concentrations, and irradiance. *Ecology* doi:10.1101/590240.
- Stukel, M. R., Kahru, M., Benitez-Nelson, C. R., Décima, M., Goericke, R., Landry, M. R., et al. (2015a). Using Lagrangian-based process studies to test satellite algorithms of vertical carbon flux in the eastern North Pacific Ocean. *J. Geophys. Res. Oceans* 120, 7208–7222. doi:10.1002/2015JC011264.
- Stukel, M. R., Kahru, M., Benitez-Nelson, C. R., Décima, M., Goericke, R., Landry, M. R., et al. (2015b). Using Lagrangian-based process studies to test satellite algorithms of vertical carbon flux in the eastern North Pacific Ocean. *J. Geophys. Res. Oceans* 120, 7208–7222. doi:10.1002/2015JC011264.
- Stukel, M. R., and Kelly, T. B. (2019). The carbon: ^{234}Th ratios of sinking particles in the California current ecosystem 2: Examination of a thorium sorption, desorption, and particle transport model. *Mar. Chem.* 211, 37–51. doi:10.1016/j.marchem.2019.03.005.
- Stukel, M. R., Kelly, T. B., Aluwihare, L. I., Barbeau, K. A., Goericke, R., Krause, J. W., et al. (2019b). The Carbon: ^{234}Th ratios of sinking particles in the California current ecosystem 1: relationships with plankton ecosystem dynamics. *Mar. Chem.*, #pagerange#. doi:10.1016/j.marchem.2019.01.003.
- Stukel, M. R., Kelly, T. B., Aluwihare, L. I., Barbeau, K. A., Goericke, R., Krause, J. W., et al. (2019c). The Carbon: ^{234}Th ratios of sinking particles in the California current ecosystem 1: relationships with plankton ecosystem dynamics. *Mar. Chem.* doi:S0304420318302615.
- Stukel, M. R., Kelly, T. B., Landry, M. R., Selph, K. E., and Swalethorp, R. (submitted). Sinking carbon, nitrogen, and pigment flux within and beneath the euphotic zone in the oligotrophic, open-ocean Gulf of Mexico. *J. Plankton Res.*
- Stukel, M. R., and Landry, M. R. (2010). Contribution of picophytoplankton to carbon export in the equatorial Pacific: A reassessment of food web flux inferences from inverse models. *Limnol. Oceanogr.* 55, 2669–2685. doi:10.4319/lo.2010.55.6.2669.

- Stukel, M. R., Landry, M. R., Benitez-nelson, C. R., and Goericke, R. (2011). Trophic cycling and carbon export relationships in the California Current Ecosystem. *Limnol. Oceanogr.* 56, 1866–1878. doi:10.4319/lo.2011.56.5.1866.
- Stukel, M. R., Landry, M. R., Ohman, M. D., Goericke, R., Samo, T., and Benitez-nelson, C. R. (2012a). Do inverse ecosystem models accurately reconstruct plankton trophic flows? Comparing two solution methods using field data from the California Current. *J. Mar. Syst.* 91, 20–33. doi:10.1016/j.jmarsys.2011.09.004.
- Stukel, M. R., Landry, M. R., Ohman, M. D., Goericke, R., Samo, T., and Benitez-Nelson, C. R. (2012b). Do inverse ecosystem models accurately reconstruct plankton trophic flows? Comparing two solution methods using field data from the California Current. *J. Mar. Syst.* 91, 20–33. doi:10.1016/j.jmarsys.2011.09.004.
- Stukel, M. R., Mislán, K. A. S., Décima, M., and Hmelo, L. (2014). Detritus in the pelagic ocean. *Eco- IX Symp. Proc.*, 49–76.
- Stukel, M. R., Ohman, M. D., Benitez-Nelson, C. R., and Landry, M. R. (2013b). Contributions of mesozooplankton to vertical carbon export in a coastal upwelling system. *Mar. Ecol. Prog. Ser.* 491, 47–65. doi:10.3354/meps10453.
- Stukel, M. R., Ohman, M. D., Benitez-Nelson, C. R., and Landry, M. R. (2013c). Contributions of mesozooplankton to vertical carbon export in a coastal upwelling system. *Mar. Ecol. Prog. Ser.* 491, 47–65. doi:10.3354/meps10453.
- Stukel, M. R., Ohman, M. D., Kelly, T. B., and Biard, T. The roles of filter-feeding and flux-feeding zooplankton as gatekeepers of particle flux into the mesopelagic ocean. *Front. Mar. Sci.*
- Stukel, M. R., Ohman, M. D., Kelly, T. B., and Biard, T. (2019d). The Roles of Suspension-Feeding and Flux-Feeding Zooplankton as Gatekeepers of Particle Flux Into the Mesopelagic Ocean in the Northeast Pacific. *Front. Mar. Sci.* doi:10.3389/fmars.2019.00397.
- Stukel, M. R., Ohman, M. M. D., Benitez-Nelson, C. R. C., and Landry, M. M. R. (2013d). Contributions of mesozooplankton to vertical carbon export in a coastal upwelling system. *Mar. Ecol. Prog. Ser.* 491, 47–65. doi:10.3354/meps10453.
- Stukel, M. R., Song, H., Goericke, R., and Miller, A. J. (2017b). The role of subduction and gravitational sinking in particle export, carbon sequestration, and the remineralization length scale in the California Current Ecosystem. *Limnol. Oceanogr.* doi:10.1002/lno.10636.
- Stukel, M. R., Song, H., Goericke, R., and Miller, A. J. (2018d). The role of subduction and gravitational sinking in particle export, carbon sequestration, and the remineralization length scale in the California Current Ecosystem. *Limnol. Oceanogr.* 63, 363–383. doi:10.1002/lno.10636.

- Stukel, M. R., Song, H., Goericke, R., and Miller, A. J. (2018e). The role of subduction and gravitational sinking in particle export, carbon sequestration, and the remineralization length scale in the California Current Ecosystem: Subduction and sinking particle export in the CCE. *Limnol. Oceanogr.* 63, 363–383. doi:10.1002/lno.10636.
- Tanaka, T., and Rassoulzadegan, F. (2004). Vertical and seasonal variations of bacterial abundance and production in the mesopelagic layer of the NW Mediterranean Sea: Bottom-up and top-down controls. *Deep-Sea Res. Part Oceanogr. Res. Pap.* 51, 531–544. doi:10.1016/j.dsr.2003.12.001.
- Tang, S., Chen, C., Zhan, H., and Xu, D. (2007). Remotely-sensed estimation of the euphotic depth in the northern South China Sea. *Int. Geosci. Remote Sens. Symp. IGARSS*, 917–920. doi:10.1109/IGARSS.2007.4422947.
- Tang, W., Wang, S., Fonseca-Batista, D., Dehairs, F., Gifford, S., Gonzalez, A. G., et al. (2019). Revisiting the distribution of oceanic N₂ fixation and estimating diazotrophic contribution to marine production. *Nat. Commun.* 10, 831. doi:10.1038/s41467-019-08640-0.
- Taylor, A. G., Goericke, R., Landry, M. R., Selph, K. E., Wick, D. A., and Roadman, M. J. (2012). Sharp gradients in phytoplankton community structure across a frontal zone in the California Current Ecosystem. *J. Plankton Res.* 34, 778–789. doi:10.1093/plankt/fbs036.
- Teuber, L., Kiko, R., Séguin, F., and Auel, H. (2013). Respiration rates of tropical Atlantic copepods in relation to the oxygen minimum zone. *J. Exp. Mar. Biol. Ecol.* 448, 28–36. doi:10.1016/j.jembe.2013.06.012.
- Thomalla, S. J., Poulton, A. J., Sanders, R., Turnewitsch, R., Holligan, P. M., and Lucas, M. I. (2008). Variable export fluxes and efficiencies for calcite, opal, and organic carbon in the Atlantic Ocean: A ballast effect in action?: LATITUDINAL VARIABILITY IN EXPORT EFFICIENCY. *Glob. Biogeochem. Cycles* 22, n/a-n/a. doi:10.1029/2007GB002982.
- Thompson, A. F., Heywood, K. J., Schmidtko, S., and Stewart, A. L. (2014). Eddy transport as a key component of the Antarctic overturning circulation. *Nat. Geosci.* 7, 879–884. doi:10.1038/ngeo2289.
- Toner, M. (2003). Chlorophyll dispersal by eddy-eddy interactions in the Gulf of Mexico. *J. Geophys. Res.* 108, 3105. doi:10.1029/2002JC001499.
- Toniazzo, T., Mechoso, C. R., Shaffrey, L. C., and Slingo, J. M. (2010). Upper-ocean heat budget and ocean eddy transport in the south-east Pacific in a high-resolution coupled model. *Clim. Dyn.* 35, 1309–1329. doi:10.1007/s00382-009-0703-8.
- Torres-Valdés, S., Roussenov, V. M., Sanders, R., Reynolds, S., Pan, X., Mather, R., et al. (2009). Distribution of dissolved organic nutrients and their effect on export production over the Atlantic Ocean. *Glob. Biogeochem. Cycles* 23. doi:10.1029/2008GB003389.

- Turner, J. T. (2015). Zooplankton fecal pellets, marine snow, phytodetritus and the ocean's biological pump. *Prog. Oceanogr.* 130, 205–48. doi:10.1016/j.pocean.2014.08.005.
- Van den Meersche, K., Soetaert, K., and van Oevelen, D. (2009). `xsample()`: An R Function for Sampling Linear Inverse Problems. *J. Stat. Softw. Code Snippets* 30, 1–15.
- van den Meersche, K., Soetaert, K., van Oevelen, D., Meersche, K. Van den, Soetaert, K., and Oevelen, D. Van (2009). `xsample()`: An R Function for Sampling Linear Inverse Problems. *Journal of Statistical Software. J. Stat. Softw. Code Snippets* 30, 1–15. doi:10.1002/wics.10.
- van Oevelen, D., Soetaert, K., and Heip, C. (2012). Carbon flows in the benthic food web of the Porcupine Abyssal Plain: The (un)importance of labile detritus in supporting microbial and faunal carbon demands. *Limnol. Oceanogr.* 57, 645–664. doi:10.4319/lo.2012.57.2.0645.
- van Oevelen, D., van den Meersche, K., Meysman, F. J. R., Soetaert, K., Middelburg, J. J., and Vézina, A. F. (2010a). Quantifying food web flows using linear inverse models. *Ecosystems* 13, 32–45. doi:10.1007/s10021-009-9297-6.
- van Oevelen, D., Van den Meersche, K., Meysman, F. J. R., Soetaert, K., Middelburg, J. J., and Vézina, A. F. (2010b). Quantifying Food Web Flows Using Linear Inverse Models. *Ecosystems* 13, 32–45. doi:10.1007/s10021-009-9297-6.
- Vézina, A., and Piatt, T. (1988). Food web dynamics in the ocean. I. Best-estimates of flow networks using inverse methods. *Mar. Ecol. Prog. Ser.* 42, 269–287. doi:10.3354/meps042269.
- Vézina, A., Platt, T., Vezina, A. F., and Platt, T. (1988). Food web dynamics in the ocean. I. Best-estimates of flow networks using inverse methods. *Mar. Ecol. Prog. Ser.* 42, 269–287. doi:10.3354/meps042269.
- Villa-Alfageme, M., de Soto, F. C., Ceballos, E., Giering, S. L. C., Le Moigne, F. A. C., Henson, S., et al. (2016). Geographical, seasonal, and depth variation in sinking particle speeds in the North Atlantic. *Geophys. Res. Lett.* 43, 8609–8616. doi:10.1002/2016GL069233.
- Wang, B., Fennel, K., Yu, L., and Gordon, C. (2020a). Assessing the value of biogeochemical Argo profiles versus ocean color observations for biogeochemical model optimization in the Gulf of Mexico. *Biogeosciences* 17, 4059–4074. doi:10.5194/bg-17-4059-2020.
- Wang, S., Kranz, S. A., Kelly, T. B., Song, H., Stukel, M. R., and Cassar, N. (2020b). Lagrangian Studies of Net Community Production: The Effect of Diel and Multiday Nonsteady State Factors and Vertical Fluxes on O_2/Ar in a Dynamic Upwelling Region. *J. Geophys. Res. Biogeosciences* 125. doi:10.1029/2019JG005569.
- Wankel, S. D., Kendall, C., Pennington, J. T., Chavez, F. P., and Paytan, A. (2007). Nitrification in the euphotic zone as evidenced by nitrate dual isotopic composition: Observations

- from Monterey Bay, California. *Glob. Biogeochem. Cycles* 21.
doi:10.1029/2006GB002723.
- Whitt, D. B., Lévy, M., and Taylor, J. R. (2019). Submesoscales Enhance Storm-Driven Vertical Mixing of Nutrients: Insights From a Biogeochemical Large Eddy Simulation. *J. Geophys. Res. Oceans* 124, 8140–8165. doi:10.1029/2019JC015370.
- Williams, R. G., and Follows, M. J. (1998). The Ekman transfer of nutrients and maintenance of new production over the North Atlantic. *Deep Sea Res. Part Oceanogr. Res. Pap.* 45, 461–489. doi:10.1016/S0967-0637(97)00094-0.
- Wilson, S. E., Ruhl, H. A., and Smith Jr., K. L. (2013). Zooplankton fecal pellet flux in the abyssal northeast Pacific: A 15 year time-series study. *Limnol. Oceanogr.* 58, 881–892. doi:10.4319/lo.2013.58.3.0881.
- Wilson, S. E., Steinberg, D. K., and Buesseler, K. O. (2008). Changes in fecal pellet characteristics with depth as indicators of zooplankton repackaging of particles in the mesopelagic zone of the subtropical and subarctic North Pacific Ocean. *Deep Sea Res. Part II Top. Stud. Oceanogr.* 55, 1636–1647. doi:10.1016/j.dsr2.2008.04.019.
- Wilson, S. E., Steinberg, D. K., Chu, F.-L. E., and Bishop, J. K. B. (2010). Feeding ecology of mesopelagic zooplankton of the subtropical and subarctic North Pacific Ocean determined with fatty acid biomarkers. *Deep Sea Res. Part Oceanogr. Res. Pap.* 57, 1278–1294. doi:10.1016/j.dsr.2010.07.005.
- Xue, Z., He, R., Fennel, K., Cai, W.-J., Lohrenz, S., and Hopkinson, C. (2013). Modeling ocean circulation and biogeochemical variability in the Gulf of Mexico. *Biogeosciences* 10, 7219–7234. doi:10.5194/bg-10-7219-2013.
- Yeber, L., Almeida, C., and Hernández-León, S. (2005). Vertical distribution of zooplankton and active flux across an anticyclonic eddy in the Canary Island waters. *Deep-Sea Res. Part Oceanogr. Res. Pap.* 52, 69–83. doi:10.1016/j.dsr.2004.08.010.
- Yingling, N., Kelly, T. B., Shropshire, T. A., Landry, M. R., Selph, K. E., Knapp, A. N., et al. (submitted). Taxon-Specific Phytoplankton Growth, Nutrient Limitation, and Light Limitation in The Oligotrophic Gulf of Mexico. *J. Plankton Res.*
- Yokokawa, T., Yang, Y., Motegi, C., and Nagata, T. (2013). Large-scale geographical variation in prokaryotic abundance and production in meso- and bathypelagic zones of the central Pacific and Southern ocean. *Limnol. Oceanogr.* 58, 61–73.
doi:10.4319/lo.2013.58.1.0061.
- Yool, A., Martin, A. P., Fernández, C., and Clark, D. R. (2007). The significance of nitrification for oceanic new production. *Nature* 447, 999–1002. doi:10.1038/nature05885.
- Zhong, Y., and Bracco, A. (2013). Submesoscale impacts on horizontal and vertical transport in the Gulf of Mexico: Submesoscale Transport in Gulf of Mexico. *J. Geophys. Res. Oceans* 118, 5651–5668. doi:10.1002/jgrc.20402.

BIOGRAPHICAL SKETCH

Thomas Bryce Kelly

EDUCATION

Florida State University, Earth, Ocean & Atmospheric Sciences; Tallahassee, FL
PhD, Defended Oct. 30, 2020.

Florida State University, Earth, Ocean & Atmospheric Sciences; Tallahassee, FL
MS, Jan. 2015 – 2018.

Boston College, College of Arts and Sciences; Chestnut Hill, MA
Bachelor of Science in Biochemistry, May 2014
Honors Chemistry Program; Minor in Mathematics

WORK EXPERIENCE

University of Alaska Fairbanks, Post-Doctoral Fellow, *currently*.

SKILLS/CERTIFICATIONS

- Sediment Trap deployment and recovery
- Thorium-234 Disequilibrium
- Linear Inverse Modeling; Monte Carlo approaches
- In situ and deckboard incubations
- Lagrangian Particle tracking (inc. LTRANS)
- High Resolution Inductively Coupled Plasma Mass Spectroscopy (HR-ICP-MS)
- R, Julia, FORTRAN

ATTENDED CONFERENCES

- CCE LTER Forum *virtual* (presentation); Ocean Sciences Meeting *San Diego* (presentation); GoMOSES *New Orleans* (poster); Regional Class Research Vessel Workshop *Gulfport*; LTER Meeting *Santa Barbara*; Goldschmidt *Boston* (presentation); Ocean Carbon and Biogeochemistry *Woods Hole*; Southern Biogeochemistry Symposium Tallahassee (organizer); American Geophysical Union *New Orleans* (poster); Southern Biogeochemistry Symposium *Athens FL* (poster); Aquatic Sciences *Honolulu* (poster);

Ocean Science Meeting *New Orleans* (poster); Southern Biogeochemistry Symposium *Atlanta*; ACS *Dallas* (poster); AAAS *Boston* (volunteer); CESS *NYC*; Physcon *Orlando*; Boston Bacterial Conference *Boston*.

PEER REVIEWED AND SUBMITTED PUBLICATIONS

- Kelly, T. B., Knapp, A. N., Landry, M. R., Selph, K. E., Shropshire, T. A., Thomas, R., et al. (submitted) Lateral Advection Supports the Oligotrophic Ecosystem of the Open-Ocean Gulf of Mexico. *Nature Geoscience*.
- Knapp, A. N., Thomas, R., Stukel, M. R., Kelly, T. B., Landry, M. R., Selph, K. E., et al. (submitted) Constraining the sources of nitrogen fueling phytoplankton and food webs in the Gulf of Mexico using nitrogen isotope budgets. *Journal of Plankton Research*.
- Landry, M. R., Selph, K. E., Stukel, M. R., Swalethorp, R., Kelly, T. B., Beatty, J., et al. (submitted) Microbial Food Web Dynamics in the Oceanic Gulf of Mexico. *Journal of Plankton Research*.
- Selph, K. E., Swalethorp, R., Stukel, M. R., Kelly, T. B., Knapp, A. N., Fleming, K., et al. (submitted) Phytoplankton assemblages in the open ocean water of the Gulf of Mexico during May 2017 and 2018. *Journal of Plankton Research*.
- Stukel, M. R., Gerard, T., Kelly, T. B., Knapp, A. N., Laiz-Carrion, R., Lamkin, J. T., et al. (submitted) Plankton food webs of the Gulf of Mexico spawning grounds of Atlantic Bluefin tuna. *Journal of Plankton Research*.
- Yingling, N., Kelly, T. B., Shropshire, T. A., Landry, M. R., Selph, K. E., Knapp, A. N., et al. (submitted) Taxon-Specific Phytoplankton Growth, Nutrient Limitation, and Light Limitation in The Oligotrophic Gulf of Mexico. *Journal of Plankton Research*.
- Kranz, S. A., Wang, S., Kelly, T. B., Stukel, M. R., Goericke, R., Landry, M. R., et al. (2020). Lagrangian Studies of Marine Production: A Multimethod Assessment of Productivity Relationships in the California Current Ecosystem Upwelling Region. *J. Geophys. Res. Oceans* 125. doi:10.1029/2019JC015984.
- Wang, S., Kranz, S. A., Kelly, T. B., Song, H., Stukel, M. R., and Cassar, N. (2020). Lagrangian Studies of Net Community Production: The Effect of Diel and Multiday Nonsteady State Factors and Vertical Fluxes on O₂/Ar in a Dynamic Upwelling Region. *J. Geophys. Res. Biogeosci.* 125. doi:10.1029/2019JG005569.

- Stukel, M. R., Kelly, T. B., Aluwihare, L. I., Barbeau, K. A., Goericke, R., Krause, J. W., et al. (2019). The Carbon:234Thorium ratios of sinking particles in the California current ecosystem 1: relationships with plankton ecosystem dynamics. *Marine Chemistry*. doi:S0304420318302615.
- Stukel, M. R., and Kelly, T. B. (2019). The carbon: 234Thorium ratios of sinking particles in the California current ecosystem 2: Examination of a thorium sorption, desorption, and particle transport model. *Marine Chemistry* 211, 37–51. doi:10.1016/j.marchem.2019.03.005.
- Morton, P. L., Landing, W. M., Shiller, A. M., Moody, A., Kelly, T. D., Bizimis, M., et al. (2019). Shelf Inputs and Lateral Transport of Mn, Co, and Ce in the Western North Pacific Ocean. *Front. Mar. Sci.* 6, 591. doi:10.3389/fmars.2019.00591.
- Kelly, T. B., Davison, P. C., Goericke, R., Landry, M. R., Ohman, M. D., and Stukel, M. R. (2019). The Importance of Mesozooplankton Diel Vertical Migration for Sustaining a Mesopelagic Food Web. *Frontiers in Marine Science* 6. doi:10.3389/fmars.2019.00508.
- Kahru, M., Goericke, R., Kelly, T. B., and Stukel, M. R. (2019). Satellite estimation of carbon export by sinking particles in the California Current calibrated with sediment trap data. *Deep Sea Research Part II: Topical Studies in Oceanography*, 104639. doi:10.1016/j.dsr2.2019.104639.
- Fender, C. K., Kelly, T. B., Guidi, L., Ohman, M. D., Smith, M. C., and Stukel, M. R. (2019). Investigating Particle Size-Flux Relationships and the Biological Pump Across a Range of Plankton Ecosystem States From Coastal to Oligotrophic. *Front. Mar. Sci.* 6, 603. doi:10.3389/fmars.2019.00603.
- Stukel, M. R., Décima, M., and Kelly, T. B. (2018). A new approach for incorporating 15N isotopic data into linear inverse ecosystem models with Markov Chain Monte Carlo sampling. *PLOS ONE* 13, e0199123. doi:10.1371/journal.pone.0199123.
- Morrow, R. M., Ohman, M. D., Goericke, R., Kelly, T. B., Stephens, B. M., and Stukel, M. R. (2018). CCE V: Primary production, mesozooplankton grazing, and the biological pump in the California Current Ecosystem: Variability and response to El Niño. *Deep Sea Research Part I: Oceanographic Research Papers* 140, 52–62. doi:10.1016/j.dsr.2018.07.012.

- Kelly, T. B., Goericke, R., Kahru, M., Song, H., and Stukel, M. R. (2018). CCE II: Spatial and interannual variability in export efficiency and the biological pump in an eastern boundary current upwelling system with substantial lateral advection. *Deep Sea Research Part I: Oceanographic Research Papers* 140, 14–25. doi:10.1016/j.dsr.2018.08.007.
- Tamburini, F., Kelly, T. B., Weerapana, E., and Byers, J. A. (2014). Paper to Plastics: An Interdisciplinary Summer Outreach Project in Sustainability. *Journal of Chemical Education* 91, 1574–1579. doi:10.1021/ed400892t.

Community Activities and Collaboration

- Review for Ocean Dynamics, Journal of Geophysical Research - Oceans, Deep Sea Research Part II, and Limnology & Oceanography.
- Open source software products: <https://github.com/tbrycekelly/>
 - R package for oceanography: TheSource

SHIP TIME

- CCE LTER Rapid Response El Niño cruise (04/16)
- CalCOFI 1611SR Cruise (11/16)
- UNOLS Chief Scientist Training Cruise (12/16)
- BlueFin Tuna Ecology Cruise (05/17)
- CCE LTER Process Cruise (06/17)
- Bluefin Tuna Ecology cruise (05/18)
- New Zealand SalpPoop Cruise (10/18)
- CCE LTER Process Cruise (6/19)
- Palmer LTER Cruise (1/20)

Total Time at Sea – 239 days